

Self-piercing riveting

Related titles:

Advances in brazing: Science, technology and applications
(ISBN 978-0-85709-423-0)

MEMS for automotive and aerospace applications
(ISBN 978-0-85709-118-5)

Corrosion prevention of magnesium alloys
(ISBN 978-0-85709-437-7)

Details of these books and a complete list of titles from Woodhead Publishing can be obtained by:

- visiting our web site at www.woodheadpublishing.com
- contacting Customer Services (e-mail: sales@woodheadpublishing.com; fax: +44 (0) 1223 832819; tel.: +44 (0) 1223 499140 ext. 130; address: Woodhead Publishing Limited, 80, High Street, Sawston, Cambridge CB22 3HJ, UK)
- in North America, contacting our US office (e-mail: usmarketing@woodheadpublishing.com; tel.: (215) 928 9112; address: Woodhead Publishing, 1518 Walnut Street, Suite 1100, Philadelphia, PA 19102-3406, USA)

If you would like e-versions of our content, please visit our online platform: www.woodheadpublishingonline.com. Please recommend it to your librarian so that everyone in your institution can benefit from the wealth of content on the site.

We are always happy to receive suggestions for new books from potential editors. To enquire about contributing to our Welding and other joining technologies series, please send your name, contact address and details of the topic/s you are interested in to francis.dodds@woodheadpublishing.com. We look forward to hearing from you.

The team responsible for publishing this book:

Commissioning Editor: Francis Dodds
Publications Coordinator: Lucy Beg
Project Editor: Kate Hardcastle
Editorial and Production Manager: Mary Campbell
Production Editor: Richard Fairclough
Project Manager: Annette Wiseman, RCL
Copyeditor: Penny Sucharov
Proofreader: Sue Clements
Cover Designer: Terry Callanan

Woodhead Publishing Series in Welding and Other
Joining Technologies: Number 82

Self-piercing riveting

Properties, processing
and applications

Edited by
Andreas Chrysanthou and Xin Sun



Oxford Cambridge Philadelphia New Delhi

Published by Woodhead Publishing Limited,
80 High Street, Sawston, Cambridge CB22 3HJ, UK
www.woodheadpublishing.com
www.woodheadpublishingonline.com

Woodhead Publishing, 1518 Walnut Street, Suite 1100, Philadelphia,
PA 19102-3406, USA

Woodhead Publishing India Private Limited, 303, Vardaan House, 7/28 Ansari Road,
Daryaganj, New Delhi – 110002, India
www.woodheadpublishingindia.com

First published 2014, Woodhead Publishing Limited

© Woodhead Publishing Limited, 2014. The publisher has made every effort to ensure that permission for copyright material has been obtained by authors wishing to use such material. The authors and the publisher will be glad to hear from any copyright holder it has not been possible to contact.

The authors have asserted their moral rights.

This book contains information obtained from authentic and highly regarded sources. Reprinted material is quoted with permission, and sources are indicated. Reasonable efforts have been made to publish reliable data and information, but the authors and the publisher cannot assume responsibility for the validity of all materials. Neither the authors nor the publisher, nor anyone else associated with this publication, shall be liable for any loss, damage or liability directly or indirectly caused or alleged to be caused by this book.

Neither this book nor any part may be reproduced or transmitted in any form or by any means, electronic or mechanical, including photocopying, microfilming and recording, or by any information storage or retrieval system, without permission in writing from Woodhead Publishing Limited.

The consent of Woodhead Publishing Limited does not extend to copying for general distribution, for promotion, for creating new works, or for resale. Specific permission must be obtained in writing from Woodhead Publishing Limited for such copying.

Trademark notice: Product or corporate names may be trademarks or registered trademarks, and are used only for identification and explanation, without intent to infringe.

British Library Cataloguing in Publication Data

A catalogue record for this book is available from the British Library.

Library of Congress Control Number: 2013945031

ISBN 978-1-84569-535-4 (print)

ISBN 978-0-85709-884-9 (online)

ISSN 2052-5532 Woodhead Publishing Series in Welding and Other Joining Technologies (print)

ISSN 2052-5540 Woodhead Publishing Series in Welding and Other Joining Technologies (online)

The publisher's policy is to use permanent paper from mills that operate a sustainable forestry policy, and which has been manufactured from pulp which is processed using acid-free and elemental chlorine-free practices. Furthermore, the publisher ensures that the text paper and cover board used have met acceptable environmental accreditation standards.

Typeset by RefineCatch Limited, Bungay, Suffolk
Printed by Lightning Source

Contents

	<i>Contributor contact details</i>	<i>ix</i>
	<i>Woodhead Publishing Series in Welding and Other Joining Technologies</i>	<i>xi</i>
1	Introduction A. CHRYSANTHOU, University of Hertfordshire, UK	1
1.1	Introduction	1
1.2	Self-piercing riveting (SPR)	2
1.3	Advantages and possible disadvantages of the SPR process	4
1.4	Application of SPR in automotive body applications	5
1.5	Future trends	6
1.6	References	7
Part I	Properties	9
2	Mechanical strength of self-piercing riveting (SPR) E. V. STEPHENS, Pacific Northwest National Laboratory, USA	11
2.1	Introduction	11
2.2	Test types and their relevance	12
2.3	Failure mechanisms	19
2.4	Rivet strength optimization	22
2.5	Self-piercing riveting (SPR) and structural adhesive joining	27
2.6	References	32
3	Fatigue behaviour of self-piercing riveted joints A. CHRYSANTHOU, University of Hertfordshire, UK	33
3.1	Introduction	33
3.2	Comparison between self-piercing riveted and resistance spot-welded joints	34
3.3	Factors that affect the fatigue behaviour of self-piercing riveted joints	35

vi	Contents	
3.4	Fretting fatigue	38
3.5	References	40
4	Corrosion behaviour of self-piercing riveted joints A. CHRYSANTHOU, University of Hertfordshire, UK	41
4.1	Introduction	41
4.2	Background theory of corrosion	42
4.3	Methodology of corrosion studies	46
4.4	Corrosion of self-piercing riveted joints	47
4.5	Corrosion protection of self-piercing rivets and joints	53
4.6	References	54
5	Dynamic strength evaluation/crashworthiness of self-piercing riveted joints X. SUN, Pacific Northwest National Laboratory, USA	56
5.1	Introduction	56
5.2	State-of-the-art review of dynamic tensile tests	58
5.3	Recommended joint dynamic strength testing procedures	63
5.4	Results and discussion	66
5.5	Conclusions	76
5.6	References	77
6	Modelling the strength of self-piercing riveted joints S. FAYOLLE, EDF R&D, France and P.-O. BOUCHARD and K. MOCELLIN, Centre for Material Forming (CEMEF), Mines ParisTech, France	79
6.1	Introduction	79
6.2	Mechanical strength of a self-piercing riveting (SPR) structure	80
6.3	Mechanical behaviour and damage analysis	86
6.4	Numerical modelling	93
6.5	Conclusions and future trends	104
6.6	References	105
Part II	Processing and applications	109
7	Assessing the suitability of materials for self-piercing riveting (SPR) K. MORI, Toyohashi University of Technology, Japan	111
7.1	Introduction	111
7.2	How self-piercing riveting (SPR) joins materials	112
7.3	Joining of similar metals	113
7.4	Joining of dissimilar metals	114

7.5	Finite element simulations of the riveting process	118
7.6	Future trends	120
7.7	References	121
8	Quality control and non-destructive testing of self-piercing riveted joints P. JOHNSON, SBC, University of Shanghai for Science and Technology, People's Republic of China	124
8.1	Introduction	124
8.2	Current technologies	126
8.3	Non-destructive testing (NDT) techniques: computer vision	128
8.4	NDT techniques: ultrasonic testing	146
8.5	Conclusions	147
8.6	References	147
9	Optimization of the strength of self-piercing rivets (SPRs) X. SUN, Pacific Northwest National Laboratory, USA	149
9.1	Introduction	149
9.2	Rivet strength estimation	150
9.3	Rivet strength optimization	159
9.4	Conclusions	169
9.5	References	169
10	Self-piercing riveting (SPR) in the automotive industry: an overview M. W. DANYO, Ford Motor Company, USA	171
10.1	Introduction	171
10.2	Types of self-piercing rivet (SPR)	173
10.3	Uses for SPRs	176
10.4	Product considerations	177
10.5	Manufacturing considerations	178
10.6	Future trends	180
11	Self-piercing riveting (SPR) in automated vehicle construction R. HEWITT, Bentley Motors Ltd, UK	181
11.1	Introduction	181
11.2	Material requirements	183
11.3	Joining techniques	184
11.4	Evaluation of processes	186
11.5	Cost comparisons	186
11.6	Comparable joint performance	192

viii	Contents	
11.7	Specific process opportunities	193
11.8	Process development	194
11.9	Industrial application	197
11.10	Conclusions	205
11.11	Acknowledgements	206
11.12	References	206
	<i>Index</i>	<i>209</i>

Contributor contact details

(* = main contact)

Editors

A. Chrysanthou
School of Engineering and
Technology
University of Hertfordshire
Hatfield, Herts AL10 9AB, UK

E-mail: maeqac@herts.ac.uk

X. Sun
Pacific Northwest National
Laboratory, K6-08
P.O. Box 999
Richland, WA 99352, USA

E-mail: xin.sun@pnnl.gov

Chapters 1, 3 and 4

A. Chrysanthou
School of Engineering and
Technology
University of Hertfordshire
Hatfield, Herts AL10 9AB, UK

E-mail: maeqac@herts.ac.uk

Chapter 2

E. V. Stephens
Pacific Northwest National
Laboratory
902 Battelle Boulevard
Richland, WA 99352, USA

E-mail: elizabeth.stephens@pnnl.gov

Chapters 5 and 9

X. Sun
Pacific Northwest National
Laboratory, K6-08
P.O. Box 999
Richland, WA 99352, USA

E-mail: xin.sun@pnnl.gov

Chapter 6

S. Fayolle
EDF R&D
1 Avenue du Général de Gaulle
92141 Clamart Cedex, France

E-mail: sebastien.fayolle@edf.fr

P.-O. Bouchard* and K. Mocellin
Mines ParisTech
CEMEF – Centre de Mise en Forme
des Matériaux
CNRS UMR 7635
BP 207
1 Rue Claude Daunesse
06904 Sophia Antipolis Cedex,
France

E-mail: pierre-olivier.bouchard@
mines-paristech.fr; katia.mocellin@
mines-paristech.fr

Chapter 7

K. Mori
Department of Mechanical
Engineering
Toyohashi University of Technology
Toyohashi 441-8580, Japan

E-mail: mori@plast.me.tut.ac.jp

Chapter 8

P. Johnson
Department of Engineering
SBC, University of Shanghai for
Science and Technology
1195 Fuxing Zhong Road
Shanghai 200031
People's Republic of China

E-mail: paul.j.johnson@outlook.com

Chapter 10

M. W. Danyo
Ford Motor Company
Product Development Center
20901 Oakwood Blvd.
Dearborn, MI 48124, USA

E-mail: mdanyo@ford.com

Chapter 11

R. Hewitt
Body Assembly, S1
Bentley Motors Ltd
Crewe, Cheshire CW1 3PL, UK

E-mail: richard.hewitt@bentley.co.uk

Woodhead Publishing Series in Welding and Other Joining Technologies

- 1 Submerged-arc welding**
Edited by P. T. Houldcroft
- 2 Design and analysis of fatigue resistant welded structures**
D. Radaj
- 3 Which process? A guide to the selection of welded and related processes**
P. T. Houldcroft
- 4 Pulsed arc welding**
J. A. Street
- 5 TIG and plasma welding**
W. Lucas
- 6 Fundamentals of welding metallurgy**
H. Granjon
- 7 Fatigue strength of welded structures**
S. J. Maddox
- 8 The fatigue strength of transverse fillet welded joints**
T. R. Gurney
- 9 Process pipe and tube welding**
Edited by W. Lucas
- 10 A practical guide to TIG (GTA) welding**
P. W. Muncaster
- 11 Shallow crack fracture mechanics toughness tests and applications**
Conference Proceedings
- 12 Self-shielded arc welding**
T. Boniszewski
- 13 Handbook of crack opening data**
T. G. F. Gray
- 14 Laser welding**
C. T. Dawes
- 15 Welding steels without hydrogen cracking**
N. Bailey and F. R. Coe
- 16 Electron beam welding**
H. Schultz
- 17 Weldability of ferritic steels**
N. Bailey

- 18 Tubular wire welding**
D. Widgery
- 19 Stress determination for fatigue analysis of welded components: Recommendations of IIW Commissions XIII and XV**
Edited by E. Niemi
- 20 The 'local approach' to cleavage fracture**
C. S. Wiesner
- 21 Crack arrest concepts for failure prevention and life extension**
Seminar Proceedings
- 22 Welding mechanisation and automation in shipbuilding worldwide**
R. Boekholt
- 23 Heat treatment of welded steel structures**
D. Croft
- 24 Fatigue design of welded joints and components: Recommendations of IIW Joint Working Group XIII-XV**
Edited by A. Hobbacher
- 25 Introduction to the non-destructive testing of welded joints**
R. Halmslaw
- 26 Metallurgy of basic weld metal**
T. R. Gurney
- 27 Fatigue of thin walled joints under complex loading**
T. R. Gurney
- 28 Handbook of structural welding**
J. F. Lancaster
- 29 Quality assurance in adhesive technology**
A. W. Espie, J. H. Rogerson and K. Ebtehaj
- 30 Underwater wet welding and cutting**
TWI/Paton Electric Welding Institute
- 31 Metallurgy of welding Sixth edition**
J. F. Lancaster
- 32 Computer technology in welding**
Conference Proceedings
- 33 Exploiting advances in arc welding technology**
Conference Proceedings
- 34 Non-destructive examination of underwater welded structures**
V. S. Davey
- 35 Predictive formulae for weld distortion**
G. Verhaeghe
- 36 Thermal welding of polymers**
R. J. Wise
- 37 Handbook of mould, tool and die repair welding**
S. Thompson
- 38 Non-destructive testing of welds**
B. Raj, C. V. Subramanian and T. Jayakumar
- 39 The automotive industry: joining technologies**
TWI
- 40 Power generation: welding applications**
TWI

- 41 **Laser welding**
TWI
- 42 **Fatigue: welding case studies**
TWI
- 43 **Fracture: welding case studies**
TWI
- 44 **The welding workplace**
R. Boekholt
- 45 **Underwater repair technology**
J. Nixon
- 46 **Fatigue design procedure for welded hollow section joints: Recommendations of IIW Subcommittee XV-E**
Edited by X.-L. Zhao and J. A. Packer
- 47 **Aluminium welding**
N. R. Mandal
- 48 **Welding and cutting**
P. T. Houldcroft and J. A. Packer
- 49 **Health and safety in welding and allied processes**
J. Blunt
- 50 **The welding of aluminium and its alloys**
G. Mathers
- 51 **Arc welding control**
P. Julian
- 52 **Adhesive bonding**
R. D. Adams
- 53 **New developments in advanced welding**
Edited by N. Ahmed
- 54 **Processes and mechanisms of welding residual stress and distortion**
Edited by Z. Feng
- 55 **MIG welding guide**
Edited by K. Wenem
- 56 **Cumulative damage of welded joints**
T. R. Gurney
- 57 **Fatigue analysis of welded components: Recommendations of IIW Commissions XIII and XV**
E. Niemi
- 58 **Advanced welding processes**
J. Norrish
- 59 **Fatigue assessment of welded joints by local approaches**
D. Radaj
- 60 **Computational welding mechanics**
Edited by L. E. Lindgren
- 61 **Microjoining and nanojoining**
Edited by Y. N. Zhou
- 62 **Real-time weld process monitoring**
Edited by Y. M. Zhang
- 63 **Weld cracking in ferrous alloys**
Edited by R. Singh

- 64 Hybrid laser-arc welding**
Edited by F. O. Olsen
- 65 A quick guide to welding and weld inspection**
Edited by S. E. Hughes
- 66 Friction stir welding**
Edited by D. Lohwasser and Z. Chen
- 67 Advances in structural adhesive bonding**
Edited by D. Dillard
- 68 Failure mechanisms of advanced welding processes**
Edited by X. Sun
- 69 Advances in laser materials processing**
Edited by J. Lawrence and J. Pou
- 70 Welding and joining of magnesium alloys**
Edited by L. Lui
- 71 Fracture and fatigue of welded joints and structures**
Edited by K. MacDonald
- 72 Minimization of welding distortion and buckling**
Edited by P. Michaleris
- 73 Welding processes handbook Second edition**
K. Weman
- 74 Welding and joining of aerospace materials**
Edited by M. C. Chaturvedi
- 75 Tailor welded blanks for advanced manufacturing**
Edited by B. Kinsey and X. Wu
- 76 Adhesives in marine engineering**
Edited by J. R. Weitzenböck
- 77 Fundamentals of evaluation and diagnostics of welded structures**
A. Nedoseka
- 78 IIW recommendations for the fatigue assessment of welded structures by notch stress analysis**
W. Fricke
- 79 IIW recommendations on methods for improving the fatigue strength of welded joints**
P. J. Haagensen and S. J. Maddox
- 80 Advances in brazing**
Edited by D. P. Sekulic
- 81 Advances in friction-stir welding and processing**
M.-K. Besharati-Givi and P. Asadi
- 82 Self-piercing riveting**
Edited by A. Chrysanthou and X. Sun
- 83 Control of welding distortion in thin plate fabrication: Design support exploiting computational simulation**
T. Gray, D. Camilleri and N. McPherson

A. CHRYSANTHOU, University of Hertfordshire, UK

DOI: 10.1533/9780857098849.1

Abstract: The application of self-piercing riveting in the automotive sector came to prominence in the 1990s when it became one of the joining techniques for aluminium vehicle bodies. This introductory chapter describes the self-piercing riveting process and discusses some of its advantages and applications in automotive vehicles.

Key words: self-piercing riveting (SPR), automotive industry, aluminium alloys.

1.1 Introduction

The use of lightweight materials has always been of interest to the automotive industry. Over the last four decades, there has been an increasing drive to produce lightweight motorcars in order to reduce fuel consumption and vehicle emissions. Events such as the oil crisis of the 1970s and the increase of greenhouse gases in the Earth's atmosphere have been catalytic factors to the need for lighter automotive materials. The high cost of crude oil that has at times exceeded \$125 a barrel in recent years is likely to increase even further the interest in the use of lightweight materials.

The response of the automotive industry has been to introduce new materials for body-in-white applications, including aluminium, polymers and composites. Much of the weight-saving focus has centred on the vehicle body as this accounts for about 30% of the total vehicle weight. In addition to this, the industry has also introduced new steels of higher strength and thinner gauge in order to replace the traditional mild steel in body applications. The introduction of such alternative materials is not simple as the traditional manufacturing processes may not be applicable to them. Thus the introduction of new materials such as aluminium has presented new challenges to the automotive industry in terms of manufacturing, structural properties and performance. While the reliability of resistance spot-welding as a joining method for mild steel vehicle bodies has been unquestionable, the process is not readily applicable to aluminium joints. The reasons for this include:

1. The low melting point of aluminium.
2. The high thermal conductivity of aluminium.

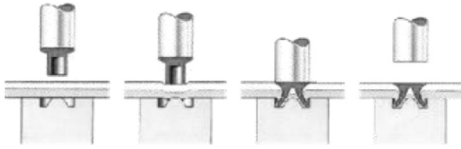
2 Self-piercing riveting

3. The high electrical conductivity of aluminium makes the electrical current requirement high.
4. Being a reactive metal, aluminium reacts and contaminates the copper spot-welding tip, reducing its life.
5. The aluminium oxide layer at the metal surface makes the spot-weld weak and with a low fatigue resistance.

The answer to this manufacturing challenge from the automotive industry was the development of a combination of adhesive bonding and self-piercing riveting. The adhesive, with its load-spreading nature, is the primary joining agent. The self-piercing rivets keep the assembly in position, while the adhesive cures and also act as back-up to prevent catastrophic failure in the event of debonding during performance. The self-piercing riveting technique was developed about half a century ago¹ and was used by the appliance and packaging industry. Self-piercing riveting rose to prominence in the early 1990s when it was adopted by Audi to join structural panels in the all-aluminium Audi A8. This precipitated significant advances in self-piercing riveting technology, including the progression from hydraulically- to electrically-powered equipment and to the development of process monitoring. The HENROB Corporation of Novi, Michigan, has been active in developing self-piercing riveting technology in the USA, UK, Germany and Australia. The company worked in collaboration with Audi in Germany in order to implement this technology in the all-aluminium Audi A8, which was introduced in 1993. Further automotive programmes followed where self-piercing riveting was used in vehicles including the Plymouth Prowler, the BMW 5 series, the Freightliner truck cabs and the Jaguar XJ. In addition to HENROB, several other SPR companies, including Ariel, Bollhoff and Eckhardt, have been involved in automotive applications. A significant progression has been the application of the technique to both space-frame (Audi, Lotus) and monocoque designs (Jaguar). In addition to vehicle body applications, the technique is also used by the automotive industry to join exhaust heat shields, spare wheel supports and battery mountings². The increasing use of the process has led to the need for its further development and has thus attracted interest as an important research topic. The aim of this book is to provide the reader with information on the self-piercing riveting process, the application, behaviour and simulation of the behaviour of self-piercing rivets and on their cost.

1.2 Self-piercing riveting (SPR)

Self-piercing riveting is a cold forming technique that is used to fasten together two or more sheets of materials mechanically with a rivet. As the name of the process suggests, the rivet pierces the top sheet. Joining is achieved by means of the rivet locking into the bottom sheet. The process is schematically illustrated in Fig. 1.1. The technique is divided into the following distinct stages:



1.1 The self-piercing riveting process.

1. The sheets to be joined are clamped together between a blank-holder and an upset die.
2. A semi-tubular rivet is driven under a punch through a feeding system. The punch is driven down using either a hydraulic or electrical system, forcing the rivet down into the material stack.
3. The piercing stage. The rivet shank acts as a shearing punch that pierces into the entire thickness of the top sheet. The lower sheet is pierced only partially until the rivet reacts against the influence of the die.
4. The flaring stage. At this point the rivet flares into the die and forms a mechanical interlock. The applied force causes the lower sheet to undergo plastic deformation and to flow into the die cavity. As a result the lower sheet conforms to the shape of the cavity to form a buttonhole at the bottom.
5. The releasing of the joined sheets.

The process uses relatively large setting forces typically of the order of about 40 MPa. Ideally, the rivet tail should not break through the bottom sheet. SPR joints where the rivet breaks through may have sufficient strength; indeed, this can even exceed the strength of a joint without breakthrough. However, joints with breakthrough are normally unacceptable as the crack in the lower sheet can: (i) compromise fatigue resistance and/or (ii) trap water or moisture and lead to corrosion. The process does not require pre-drilled holes as it is designed to pierce and lock into the materials stack in one single operation. A typical self-piercing riveting machine consists of a C-frame that accommodates the rivet setting mechanism as well as the upset die as shown in Fig. 1.2.



1.2 A self-piercing riveting C-frame.

1.3 Advantages and possible disadvantages of the SPR process

1.3.1 Advantages

Self-piercing riveting has emerged as a joining method for new automotive materials for several reasons, including:

1. Its ability to join together unweldable or difficult to weld materials.
2. It can join together dissimilar materials.
3. Unlike conventional riveting, it does not need pre-drilled holes and exact hole alignment.
4. It causes little or no damage to protective coatings.
5. It produces joints of high strength and of good fatigue resistance.
6. Process monitoring methods are available that can be used as a means of assessing the process quality.
7. The process is simple and can be fully automated. To this end the self-piercing riveting system can be robot-mounted to operate in a flow-line.
8. The cycle time required to make a joint is short (can range from 1 to 4 seconds) and comparable to spot-welding.
9. Unlike spot-welding, the time taken to make a joint does not increase significantly for thicker materials and thicker stacks.
10. The processing tools have a long life (generally in excess of about 200 000 applications).
11. Self-piercing riveting machines are available in a variety of forms: portable, robot-mounted and multi-head machines.
12. Low energy requirement. Self-piercing riveting has gained acceptance as a 'clean' process and compares favourably with more conventional joining techniques in terms of energy requirements.
13. No fume emissions are given off during production, making the process environmentally as well as user friendly.
14. There is no materials waste.
15. The process produces very little noise.
16. The processing costs are lower compared with spot-welding.

1.3.2 Possible disadvantages

There are a number of possible disadvantages associated with the process. These are summarised below:

1. The process requires higher investment costs compared with spot-welding (equipment and tooling costs are higher).
2. The process is only applicable to deformable materials (it cannot be used for brittle materials).

3. The process is double-sided; therefore access to both sides of the stack to be joined is required.
4. The process is not flush as it produces a bulge in the form of a buttonhole (tail-side with about 2–3 mm protrusion) and a rivet head area and these may sometimes not be aesthetically acceptable.
5. There are concerns about potential corrosion problems as a result of self-piercing riveting. These concerns are due to: (i) the potential use of dissimilar materials (for example, high-strength steel alloys are used to join aluminium alloys and this may be a cause of galvanic corrosion); (ii) the joint overlap and the gap between the rivet and the pierced sheet can potentially suffer from differential aeration corrosion (also referred to as crevice corrosion) and (iii) surface irregularities may also lead to differential aeration corrosion. It is therefore important to design against the accumulation of water and moisture to avoid such corrosion problems.
6. Repair of damaged joints with SPR can be impossible as the component may not be accessible from both sides; instead conventional riveting may be used for repairs in such situations.

1.4 Application of SPR in automotive body applications

The drive to reduce vehicle weight and to improve performance has led to the introduction of aluminium alloys for automotive body applications. The low- and medium-volume automotive manufacturers, in particular, have introduced aluminium alloys. While offering great potential, aluminium also introduces a great challenge in meeting the stiffness and noise, vibration and harshness requirements and in using cost-effective manufacturing processes. The self-piercing riveting process was originally developed for applications in the construction and white goods sectors. In the early 1990s, Audi developed the all-aluminium A8 structure. The Audi 8 vehicle body was originally designed to be joined using resistance spot-welding³, but this was observed to be inadequate. In addition to the problems highlighted earlier in this chapter, resistance spot-welding could not satisfy some of the principal requirements including fatigue resistance and crashworthiness. As a consequence, fastening methods such as self-piercing riveting were considered. However, the process had a number of shortcomings, including breakthrough of the rivet tail, distortion of riveted parts and unacceptable gaps in joint seams. In order to solve these problems improvements had to be introduced to the process in the form of new rivet designs and a high-force pre-clamping rivet setter, which have since become standard.

When high-strength steels of a thinner gauge length were introduced to the Volvo FH12 truck cabs in order to reduce their weight, the anticipated increase in the fatigue life of resistance spot-welded joints (in line with the increased strength

of the material) did not materialise. In fact, high-strength steels are more difficult to spot-weld than mild steel because of their higher carbon content, which can lead to embrittlement of the joint. An investigation into the possible use of self-piercing riveting led to a significant increase in the fatigue life of the cab structure. As a result, 42 self-piercing rivet joints were introduced to each cab. According to a TWI study⁴, for the daily production rate of 150 cabs, the equipment costs for self-piercing riveting were \$43 000 higher than for spot-welding. However, self-piercing riveting achieved production cost savings of \$244 000.

Perhaps the most publicised application of self-piercing riveting was in the Jaguar XJ in 2004. The body of the Jaguar XJ was based on a monocoque design and consisted primarily of stampings from aluminium alloys 5754 and 6111. In addition, it included aluminium castings and extrusions as well as high-strength low-alloy steel (HSLA) components. This necessitated the use of about 250 different joint combinations, including 16 different types of rivets. In terms of thickness, the joint combinations ranged from about 1.8 mm to 9 mm. This demonstrates the versatility of the riveting technique. The XJ vehicle structure used a total of about 3180 self-piercing rivets, together with advanced adhesives. The self-piercing rivets were applied using 148 automated robotic servo-electric riveting tools. About 30% of the rivets were applied through the use of 55 manual rivet setting systems. The total weight of the rivets in each car amounted to about 4.5 kg.

1.5 Future trends

The automotive industry has been using self-piercing rivets since the early 1990s. The technique itself has been the subject of several studies within industry, academia and research organisations, while about 130 papers have been published in the open literature. In spite of the interest in the subject and the great amount of test work that has been undertaken, there is still no agreed international test standard for evaluating the static and dynamic behaviour of SPR joints. The most commonly used test configuration has been the single overlap joint because of its simplicity. This joint configuration suffers from substrate bending due to load path eccentricity, which is inherent in this type of joint. As yet there is no standardised specimen configuration, size and test methodology for testing SPR joints. Different researchers have used different specimen sizes in order to test the behaviour of SPR joints and this makes the comparison of data impossible. It appeared at one time that similar test standards to those that are being used for adhesively-bonded joints would be adopted, but this has not yet taken place.

Research studies that have taken place over the last decade have started to forge our understanding of the static and dynamic behaviour of SPR joints. This behaviour is dependent on several factors, among which are the size and geometry of the sample and the rivet, the properties of the materials to be joined and the

rivet, as well as the processing parameters. The wider use of SPR joints will demand the ability of designers to predict their static and dynamic behaviour. The prediction of this behaviour is difficult as it not only depends on the geometric characteristics of the joint, but also on the processing parameters, the sheet material deformation characteristics, the material's plasticity, the resulting residual stresses, etc. The accuracy of the numerical simulation of the behaviour of self-piercing riveted joints has therefore been one of the major challenges over the last decade. Owing to the complexity of the process, it is likely that this will remain so in the foreseeable future. In addition, in order to increase the reliability of self-piercing joints, it is also important to develop easily applicable non-destructive testing techniques that can accurately detect damage and defects during operation of the joints. It is thought that ultrasonic testing⁵ may be a suitable technique to do this, but it will require additional understanding of the variety of defects and the behaviour of complex geometries.

Future research and development is also likely to address the speed of joining, which is dependent on several factors including the materials to be joined, their geometry and the rivet pitch length. It is generally accepted that the current joining speed is roughly about 1 m/min, which is comparable to welding processes. However, this is relatively slow in comparison with the application of adhesives and it is likely that the industry will want to develop a speedier self-piercing riveting process.

1.6 References

1. Pond J B (1972), 'What's new in automotive fastening', *Automotive Ind.*, 147, 32–37.
2. Bollhoff Fastening Ltd, <http://www.boellhoff.de>.
3. LaPensee M L (2003), 'Self-pierce riveting technology: a joining solution for light metals', *Light Met. Age*, 61, 32–34.
4. The Welding Institute, TWI, <http://www.twi.co.uk>.
5. He X, Pearson I and Young K (2008), 'Self-piercing riveting for sheet materials: state of the art', *J. Mater. Process. Technol.*, 199, 27–36.

Mechanical strength of self-piercing riveting (SPR)

E. V. STEPHENS, Pacific Northwest National Laboratory, USA

DOI: 10.1533/9780857098849.1.11

Abstract: Experimental results on static strength evaluations of various SPR populations are presented to compare and contrast the static strength and failure modes of SPR joints joining aluminum alloys and SPR joints joining aluminum and steel, including the test methodologies implemented. The purpose of this chapter is to quantify the static strength levels of these SPR joints under different loading conditions and to provide quantitative measures on the joint strength.

Key words: self-piercing riveting (SPR), SPR of dissimilar metals, SPR joint strength characterization, static failure modes of SPR joints, SPR, and adhesive joining.

2.1 Introduction

Over the years, new and existing joining technologies have been introduced to automotive manufacturers to achieve weight reduction goals. Among these, SPR is recognized as a possible and effective solution for joining body panels and structures, particularly for aluminum parts and dissimilar metals parts. SPR is essentially a cold forming operation, in which a semi-tubular rivet is pressed by a punch into two sheets of material that are supported on a small die. The rivet pierces through the upper sheet and flares into the bottom sheet, thus forming a mechanical interlock between the two sheets. It is important for the automotive design engineers to understand the mechanical behavior of different SPR joints and, furthermore, to incorporate these joint properties in the early design stage using computer aided engineering and design tools.

Although more and more SPR are being used in vehicle assemblies, very limited performance data on SPR have been reported in the open literature. This is particularly true for SPR of dissimilar metals combinations. For example, our literature search on the topic of SPR fatigue yielded only a handful of publications, and the majority of them focused on joints made between aluminum sheets of the same gages. Moreover, almost all of these studies used only one coupon configuration, i.e., lap shear or coach peel. For example, Fu and Mallick¹ examined the fatigue behavior of SPR in 6111-T4 aluminum sheets and studied the effects of different rivet setting pressures on the static and fatigue strength of lap shear samples. Cumulative fatigue tests were also performed and it was found that

Miner's linear damage accumulation law does not apply for SPR fatigue under various amplitude loadings. The loading path with higher load level followed by lower load level appears to improve the fatigue life at the lower load level. However, the loading path in which the lower load level is applied first does not cause a similar effect at the higher load level. Booth *et al.*² studied the static and fatigue strength of SPR and resistance spot-welded (RSW) joints in steel and aluminum. They observed that the SPR fatigue strength was 100% greater than the RSW fatigue strength for lap shear samples.

Since the actual rivet joints in a vehicle can be of multi-material stack up and experience combined and complex loading conditions, any SPR strength characterization must also consider different material combinations and loading conditions. In this chapter, we present experimental results on static strength evaluations of various SPR populations to compare and contrast the static strength and failure modes of SPR joints joining aluminum alloys and SPR joints joining aluminum and steel. The purpose of this chapter is to quantify the static strength levels of these dissimilar SPR joints under different loading conditions and to provide the automotive design engineers with some quantitative measures on the joint strength.

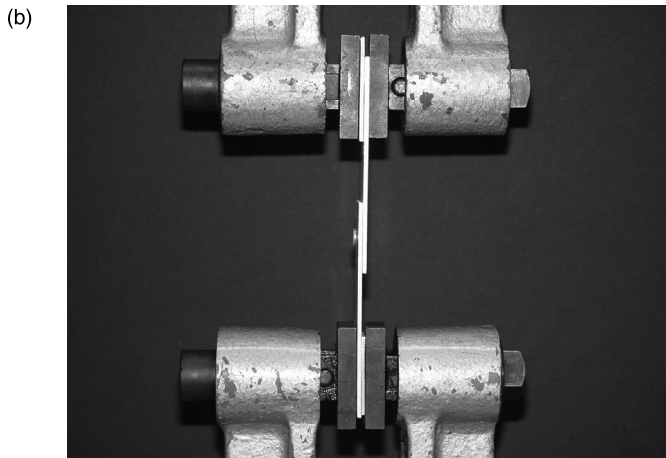
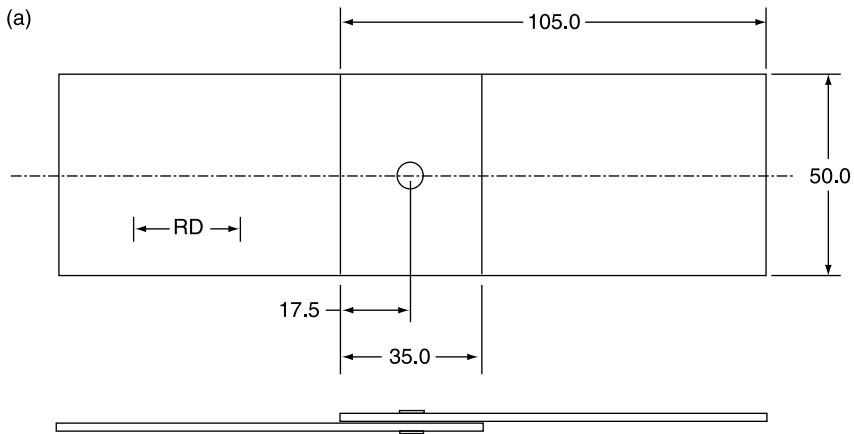
The influence of different material gages, piercing direction and the use of structural adhesives on the static behavior of SPR samples is also investigated. From this perspective, the results presented in this chapter also provide manufacturing engineers with the effects of different manufacturing and processing parameters on the static strength of various SPR joints.

2.2 Test types and their relevance

Uniaxial tension tests are performed to characterize the static joint strength and energy absorption levels of SPR joined materials of both similar and dissimilar combinations. This allows a quick assessment of the joint performance behavior before efforts are spent towards more time intensive evaluations, such as fatigue tests. Lap shear, cross tension and coach peel specimen designs are common specimen configurations used to test the joints in one-directional loading conditions. The SPR sample size used by researchers has tended to vary from one study to another because there are still no agreed test standards for SPR. For the work that is reported in this chapter, lap shear specimens consist of two substrate materials that are typically 105 mm in length and 50 mm in width with a 35 mm overlap of the materials of interest. Although the width of the lap shear specimen may be varied, 50 mm widths have been found to show little degradation of joint strength as the specimen width is reduced^{3,4}. Cross tension specimens are also 105 mm in length and 50 mm in width, where the two materials are joined perpendicular to each other crossing in the center of each material. Coach peel specimens are 105 mm in length and 25.4 mm in width, where the material substrates are bent into an L-shape with a given radius and then joined mirrored

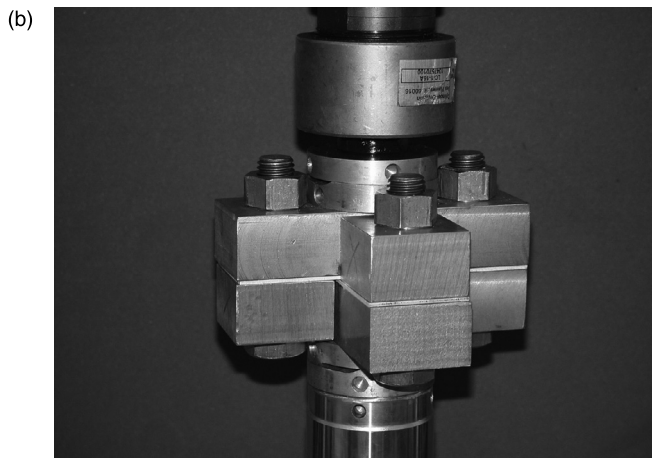
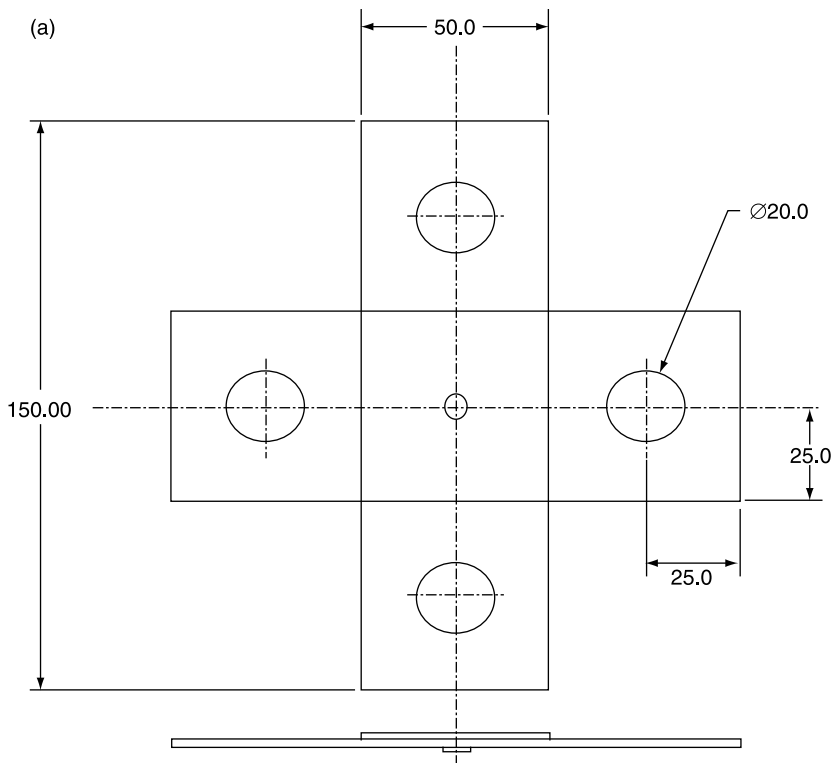
to each other with a minimum overlap of 25.4 mm. For all specimen designs, care is taken in assuring that the rivet is placed at the center of the specimen width. Figures 2.1–2.3 illustrate the coupon design assemblies and each respective assembly in a test fixture.

Typical test parameters for the quasi-static tests of each assembly design include using a closed-looped servo-controlled hydraulic test frame at a rate of 10 mm min^{-1} for lap shear loading conditions and 25 mm min^{-1} for both cross tension and peel loading conditions. A digital data acquisition system should be used to track the load and axial displacement. A minimum of ten specimens are recommended for each assembly design in order to characterize more confidently

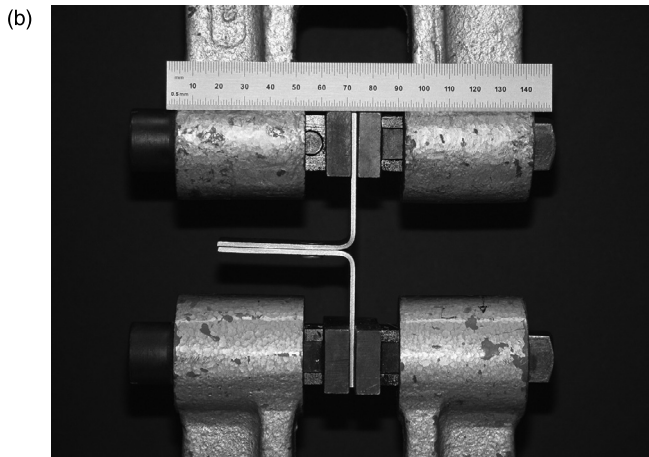
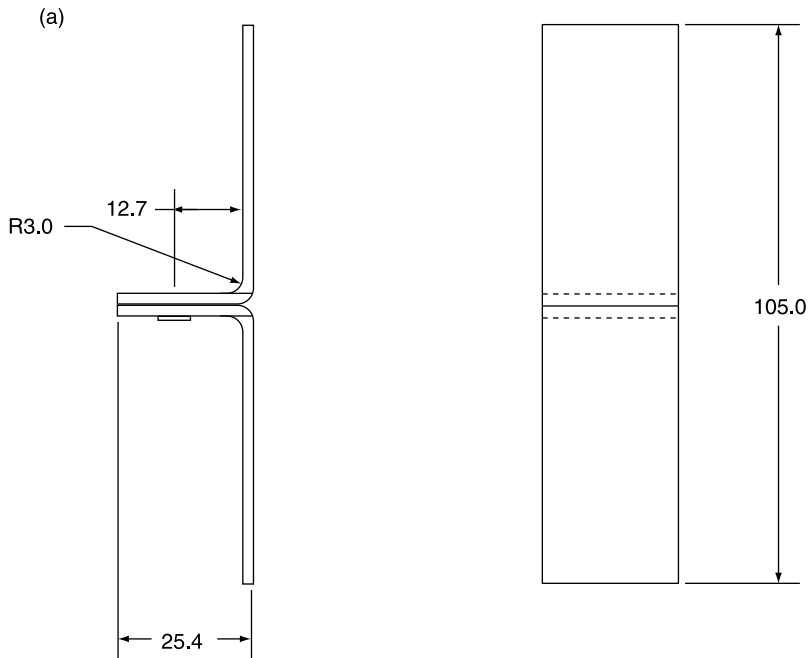


2.1 The lap shear coupon assembly drawing (a), and test fixture (b), used to conduct static tests. All dimensions are in millimeters.

Sunday, February 02, 2014 3:06:13 AM



2.2 The cross tension coupon assembly drawing (a), and test fixture (b), used to conduct static tests. All dimensions are in millimeters.



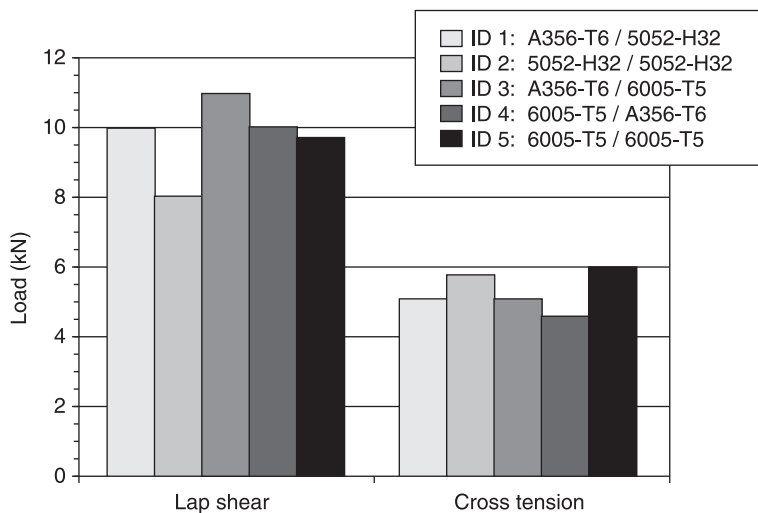
2.3 The coach peel coupon assembly drawing (a), and test fixture (b), used to conduct static tests. All dimensions are in millimeters.

the average peak load results observed. In addition, shims are recommended in the gripped regions of the lap shear assemblies in the test fixture to balance thickness differences. This will minimize coupon bending and ensure alignment of the load path in the joint area.

In this chapter, all joint strength characterization results presented followed these specimen designs and test parameters. To have a better understanding of SPR joint strengths of varying material combinations, Fig. 2.4 shows the lap shear and cross tension test results of single joint SPR assemblies of 3 mm thick AA6005-T5 wrought flat stock extrusion, AA5052-H32 wrought sheet, and A356-T6 cast flat stock in various combinations as described in Table 2.1. These particular materials are used in heavy vehicle applications.

These joint assemblies (joint ID 1 through ID 5) were fabricated with a countersunk rivet 9 mm in length and a rivet shank diameter of 5 mm. Similar pre-clamping pressures (120 bar) and setting pressures (210–235 bar) were used. Greater strengths were observed in the cast to wrought and wrought to cast alloy combinations in comparison with the wrought alloy combinations under lap shear loading. However, in cross tension, the wrought alloy joint combinations exhibited greater strengths in comparison with the cast to wrought and wrought to cast alloy joint populations. Representative load–displacement graphs illustrating this observation are shown in Fig. 2.5. Joint ID 3 (A356-T6/6005-T5) and ID 5 (6005-T5/6005-T5) lap shear and cross tension results are shown.

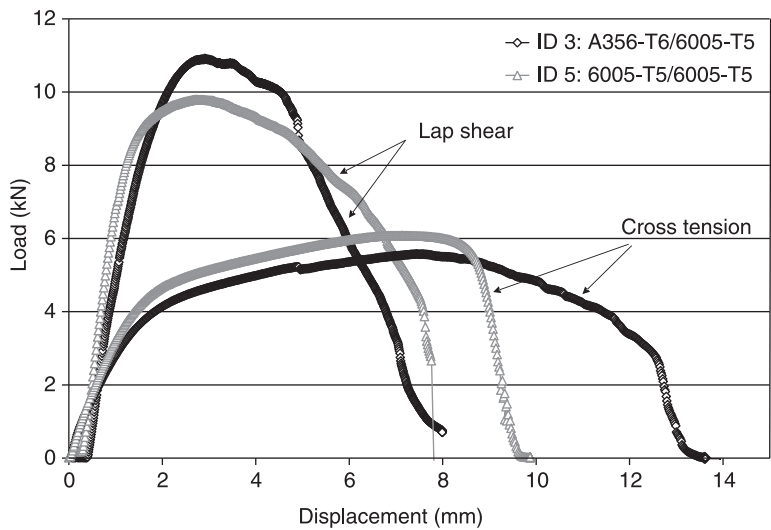
Figure 2.6 illustrates the different strengths observed for dissimilar metal combinations used in automotive applications (joint ID 7 through ID 13). Varying steel alloys such as galvanized, Dual Phase (DP) 600 steel, SAE 1008 steel, and high strength low alloy (HSLA) 350 steel were joined to aluminum alloy 5182-O. These SPR specimen assemblies were fabricated using countersunk rivets with a



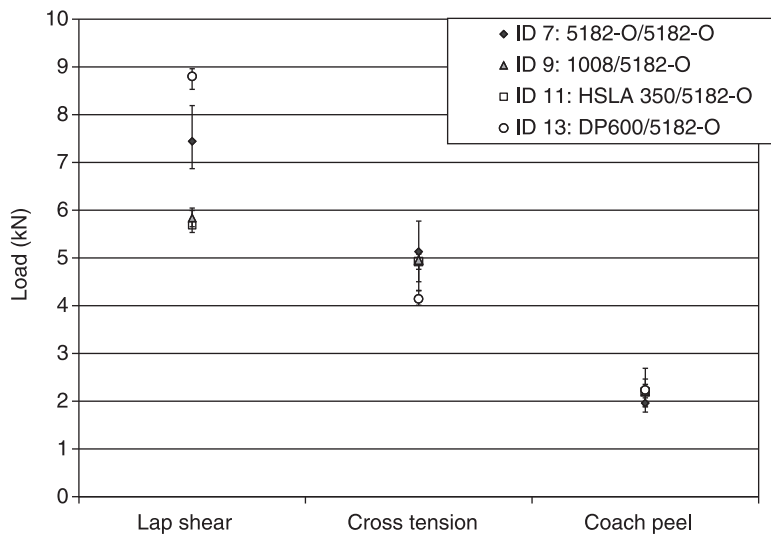
2.4 An illustration of the average static strength results for varying heavy vehicle aluminum cast and wrought alloy SPR joint combinations under lap shear and cross tension loading.

Table 2.1 Joining parameters for single joint SPR specimen assemblies of similar and dissimilar material combinations

SPR joint ID	Top material	Top thickness (mm)	Bottom material	Bottom thickness (mm)	Joint stack (mm)	Rivet length (mm)	Henrob die	Clamp pressure (bar)	Setting pressure (bar)
1	A356-T6	3.0	5052-H32	3.0	6.0	9	A	120	235
2	5052-H32	3.0	5052-H32	3.0	6.0	9	B	120	210
3	A356-T6	3.0	6005-T5	3.0	6.0	9	B	120	235
4	6005-T5	3.0	A356-T6	3.0	6.0	9	A	120	235
5	6005-T5	3.0	6005-T5	3.0	6.0	9	B	120	235
7	5182-O	2.0	5182-O	2.0	4.0	7	C	120	210
9	1008	1.4	5182-O	2.0	3.4	6.5	D	120	210
10	5182-O	2.0	HSLA 350	1.0	3.0	6	D	120	230
11	HSLA 350	1.0	5182-O	2.0	3.0	6	D	120	240
12	5182-O	2.0	DP 600	1.6	3.6	6	D	123	230
12L	5182-O	2.0	DP 600	1.6	3.6	6.5	D	120	240
13	DP 600	1.6	5182-O	2.0	3.6	6.5	D	120	240



2.5 Uniaxial test results for aluminum cast to wrought (ID 3) and wrought alloy (ID 5) SPR joints.



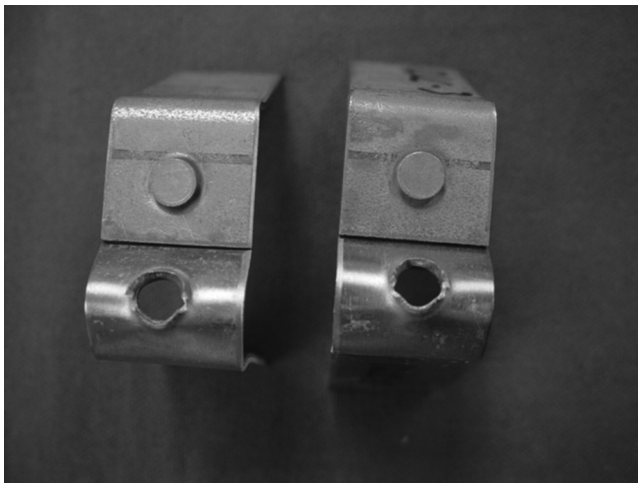
2.6 An illustration of the static strength results for various dissimilar material SPR joint combinations where the bottom material of the joint is 5182-O aluminum.

5 mm rivet shank diameter. The rivet lengths and joining parameters are listed in Table 2.1. The results shown in Fig. 2.6 illustrate the importance of testing the different design configurations because trends observed under one loading condition, such as shear, may not be observed under other loading conditions. For example, SPR joint ID 13 exhibited greater shear strengths in comparison with the other dissimilar metal SPR joint populations. However, under cross tension loading, these same joint assemblies exhibited lower strengths and under coach peel exhibited comparable strengths in comparison with the other aluminum and steel dissimilar joint populations.

2.3 Failure mechanisms

Varying failure modes of the SPR joint may be observed under static loading. Since SPR is a cold-forming-piercing process with plastic deformation occurring around the rivet head and tail, the strength of the joint is primarily determined by the strength of the mechanical interlock between the rivet and the base substrate. Hence, two primary failure modes are typically observed: rivet head pullout and rivet tail pullout.

Rivet head pullout occurs when the rivet head is pulled out from the top material substrate. Figure 2.7 is a representative image of SPR joint assemblies exhibiting rivet head pullout. In this particular figure, coach peel assemblies of joint ID 12 (left assembly) and 12L (right assembly) consisting of 5182-O Al joined to DP 600 are shown. Rivet tail pullout occurs when the rivet tail is pulled out of the



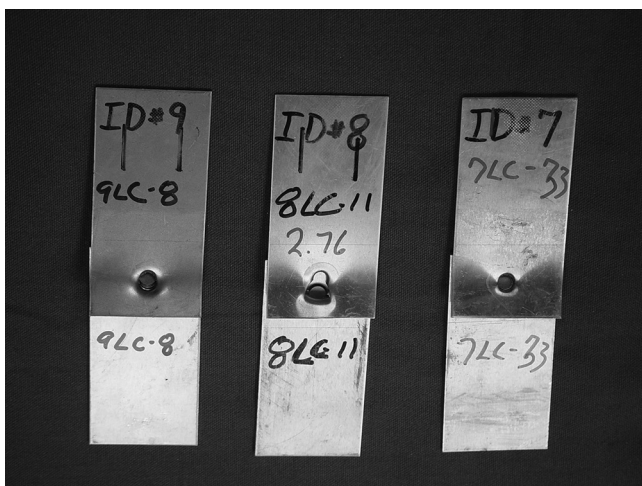
2.7 Representative image of SPR joint assemblies exhibiting rivet head pullout. Images shown are coach peel coupon assemblies after testing.

bottom material substrate. Figure 2.8 is a representative image of SPR joint assemblies exhibiting rivet tail pullout. In this particular figure, lap shear assemblies of joint ID 12 are shown as well.

Under the varying static loading conditions, sheet bending may also be observed, particularly in thin material substrates on the rivet head side, leading to either tearing or shearing of the top sheet material substrate. This allows the rivet head to pull-through as shown in Fig. 2.9. In Fig. 2.9, lap shear assemblies



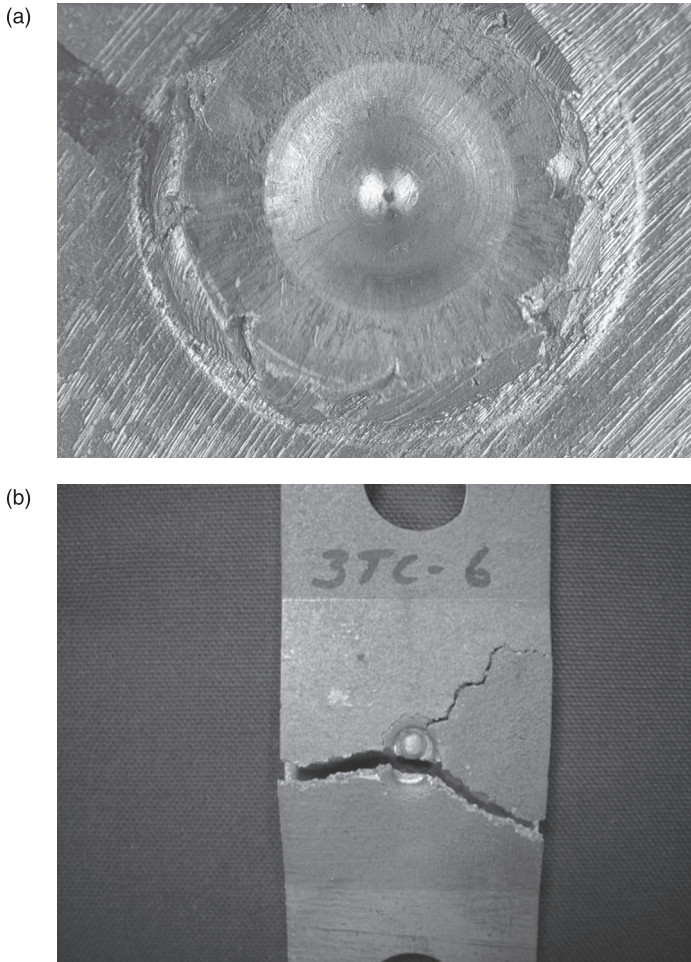
2.8 Representative image of SPR joint assemblies exhibiting rivet tail pullout. Images shown are lap shear coupon assemblies after testing.



2.9 Representative images of SPR joint assemblies exhibiting sheet tearing (outer specimens) allowing rivet head pull-through and sheet shearing (center specimen). Images shown are lap shear coupon assemblies after testing.

of 5182-O joined to 5182-O (right and center assembly) and 1008 steel joined to 5182-O (left assembly) are shown. In the right and center assembly, the 5182-O top material substrate is 2 mm and 1 mm thick, respectively. In the left assembly, the 1008 steel top substrate is 1.4 mm thick. Sheet shearing is observed in the thinner aluminum material substrate.

In addition to the varying SPR failure modes observed, one must be mindful of any potential damage that may occur during the riveting process itself that may influence the integrity of the joint. Rivet shank damage or failure may potentially occur when piercing through a thick and strong material substrate such as DP 600. Tailside damage or cracking may also occur when piercing through materials with low ductility at room temperature such as castings or magnesium. Figure 2.10



2.10 Representative images of a wrought to cast aluminum SPR joint assembly (ID 4) where cracking is observed on the tailside (a) after riveting and subsequent failure of the casting during cross tension loading (b).

shows the tailside of a wrought to cast aluminum SPR joint assembly where cracking is observed after riveting that led to subsequent failure of the casting under cross tension loading.

2.4 Rivet strength optimization

When creating SPR joints, there are factors that may affect the joint strength, such as the rivet length and the riveting piercing direction. Hence, evaluating these factors may aid in optimizing the joint strength for a particular material combination. The following details observations made on the effects of these different joining factors on the strength of the self-piercing rivet joint. The failure modes observed are also noted. Further analysis and understanding of the role of the material substrates, substrate thickness, rivet material and geometry, and die design on the joint strength through rivet optimization is discussed in Chapter 9, along with its anticipated failure mode.

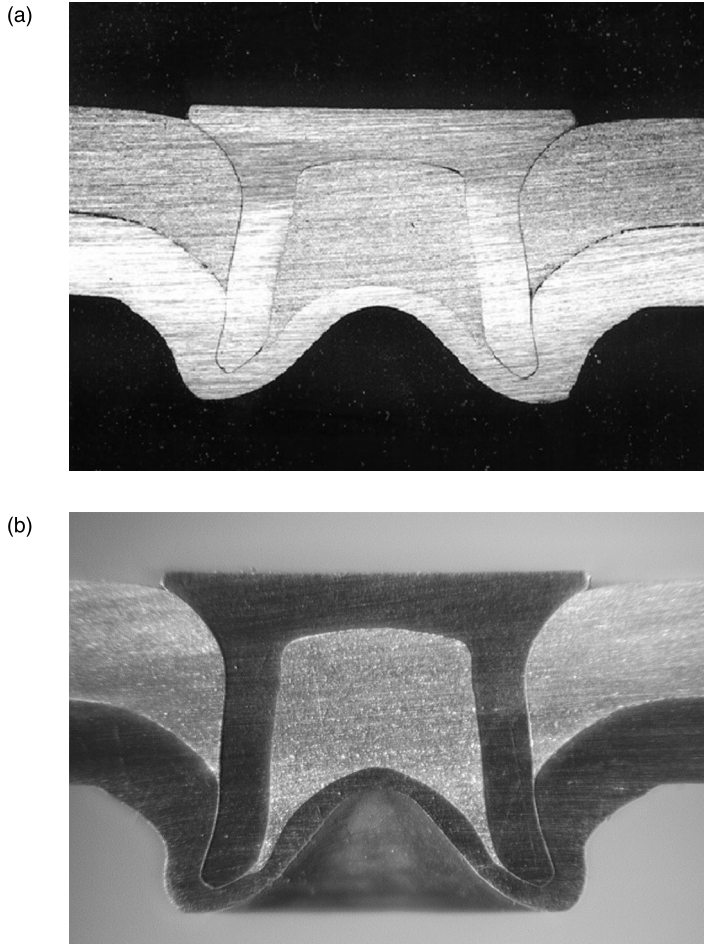
2.4.1 Effect of rivet length

Experiments were performed to investigate the effect of rivet length on the static performance of SPR joints. The rivet length of a 5182-O/DP 600 SPR joint assembly was increased from 6 mm to 6.5 mm. Again, details of the substrate assemblies and joining parameters are listed in Table 2.1. The same countersunk rivet type and die design were used to join the two populations. Similar pre-clamping and setting pressures were also used. An illustration of the SPR cross section is shown in Fig. 2.11, where the longer rivet appears to clinch more material.

Increases in strength and energy absorption were observed in all specimen configurations with the longer rivet (Table 2.2), particularly under cross tension loading. A significant increase in strength (approximately 40 percent) and energy absorption (approximately 250 percent) was observed in the cross tension coupons with the 6.5 mm rivet length. Although the lap shear strengths were comparable, the energy absorption level increased by 77 percent in the longer riveted joints under lap shear loading. The longer rivet appears to contribute to the performance of the joint. Representative load–displacement graphs are illustrated in Fig. 2.12.

2.4.2 Effect of piercing direction

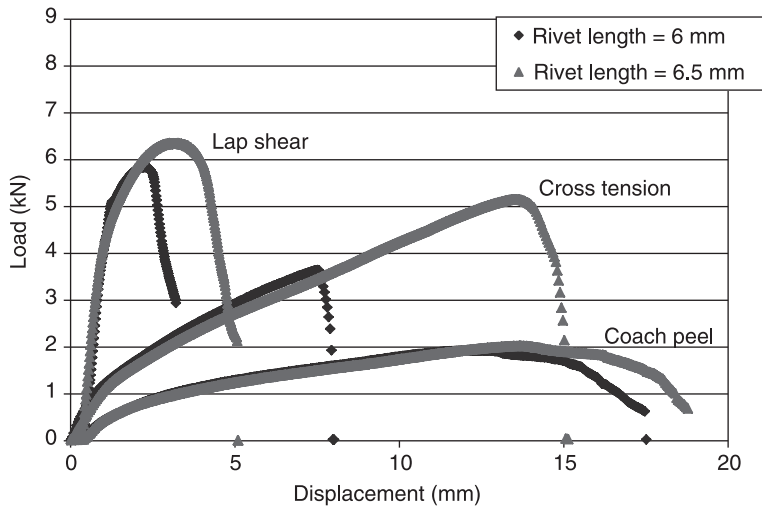
Typically, when riveting materials of different thicknesses and strengths, it is preferable to pierce through the softer or thinner material into the thicker or harder material. However, surprising results were observed when 5182-O and HSLA 350 SPR joint assemblies and 5182-O and DP 600 SPR assemblies were fabricated to evaluate the effect of piercing direction on the static performance of joints. The



2.11 Rivet cross sections for Joint ID 12 with a 6mm rivet (a), and Joint ID 12L with a 6.5mm rivet (b).

Table 2.2 Comparison of the average static strength results of 5182-O joined to DP 600 where the rivet length was increased from 6.0 mm (ID 12) to 6.5 mm (ID 12L)

SPR Joint ID	Lap shear		Cross tension		Coach peel	
	Peak load (kN)	Energy (N mm)	Peak load (kN)	Energy (N mm)	Peak load (kN)	Energy (N mm)
12	6.15	14230	3.70	20331	1.83	22590
<i>Std. dev.</i>	<i>0.13</i>	<i>1490</i>	<i>0.17</i>	<i>3120</i>	<i>0.10</i>	<i>1443</i>
12L	6.37	25190	5.18	51841	2.04	25686
<i>Std. dev.</i>	<i>0.23</i>	<i>1856</i>	<i>0.13</i>	<i>4400</i>	<i>0.08</i>	<i>1390</i>

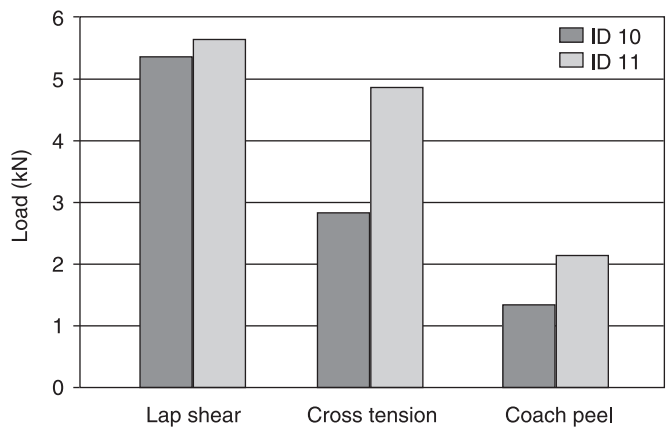


2.12 Uniaxial test results for 5182-O/DP 600 SPR assemblies joined with a 6.0mm rivet (ID 12) and a 6.5mm rivet (ID 12L).

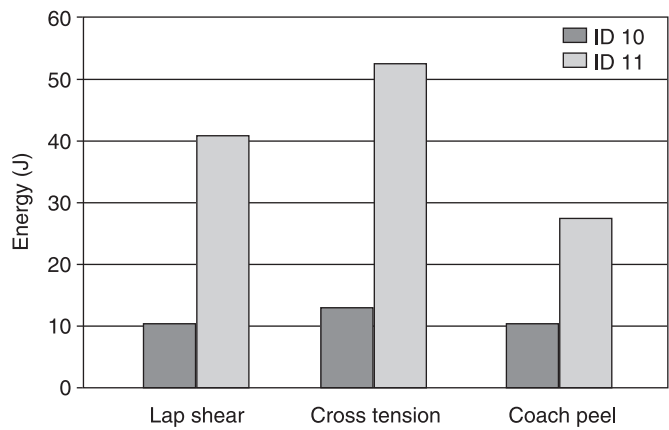
same countersunk rivet, die design, and joining parameters were used to join the dissimilar materials in each population (Table 2.1).

In the 5182 and HSLA 350 SPR joint specimens, an increase in strength and energy absorption was observed when the rivet pierced through the HSLA 350 steel substrate into the softer 5182-O aluminum (ID 11). Although the lap shear strengths of these two populations are comparable, as observed in Fig. 2.13, the cross tension strength in the HSLA 350/5182 SPR assembly increased approximately 70 percent and its coach peel strength increased approximately 58 percent in comparison with piercing through 5182 into the HSLA steel (ID 10). In addition, Fig. 2.14 shows that the energy absorption significantly increased 2.3 to 3.6 times more depending on the loading condition when piercing through the steel substrate into the aluminum substrate. Figure 2.15 shows the cross sections of Joint ID 10 and 11. It is believed that a much better clinched tail end may be attributing to the results observed.

The typical failure mode observed for Joint ID 10 was tail pullout for all static specimen configurations tested. For Joint ID 11, static lap shear specimens had a mixed failure mode of head pullout and sheet shearing, while cross tension specimens exhibited tail pullout, and coach peel specimens exhibited head pullout. Another example of the effects of piercing the direction on the static strength of dissimilar metal joints is illustrated in Fig. 2.16. Here joint ID 12L (5182-O/DP 600) and joint ID 13 (DP 600/5182-O) are compared. Again, the same rivet and die design was used to join the two dissimilar materials in each population. Different strength characteristics were observed. When piercing through the stronger DP 600 material into the softer 5182-O aluminum, greater strengths in

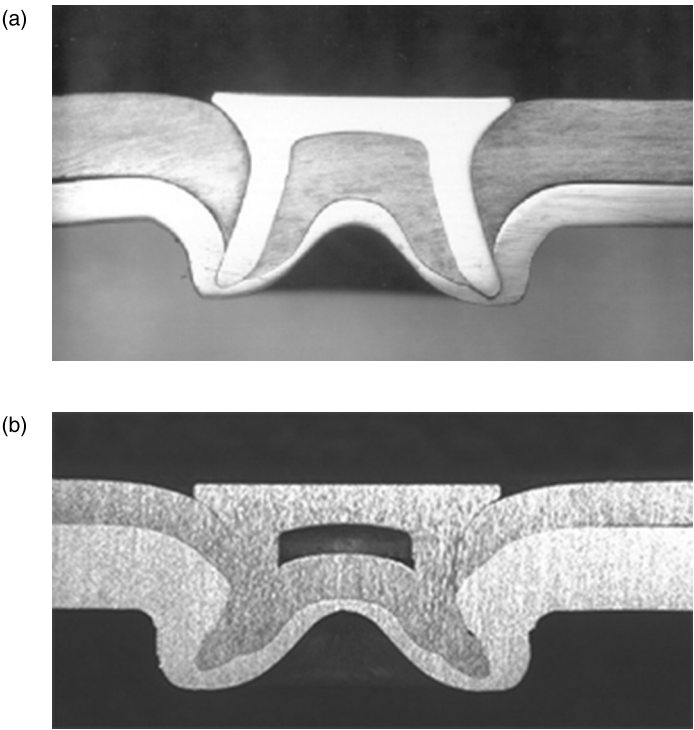


2.13 An illustration of the static peak load results for 5182-O/HSLA 350 (ID 10) and HSLA 350/5182-O (ID 11) comparing piercing direction.

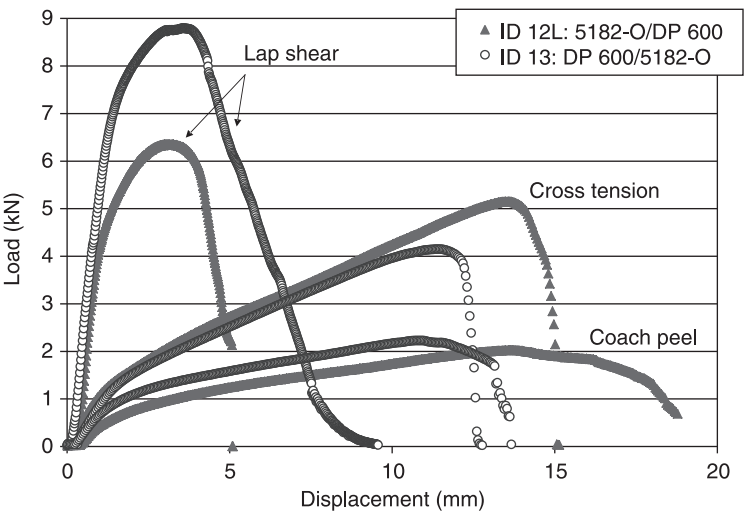


2.14 An illustration of the static tests energy absorption results for 5182-O/HSLA 350 (ID 10) and HSLA 350/5182-O (ID 11) comparing piercing direction.

comparison to the opposite piercing direction are observed in lap shear along with greater displacement to failure. However, under cross tension and coach peel loading, piercing through 5182-O into the DP 600 material (ID 12L) yielded increased strengths and energy absorption levels. The typical failure mode observed for joint ID 12L was head pullout for static lap shear and coach peel specimens, and tail pullout for cross tension specimens. For joint ID 13, static lap shear specimens had a mixed failure mode, and both static cross tension and coach peel specimens exhibited tail pullout.



2.15 Rivet cross sections of joint aluminum and steel assemblies where (a) the rivet is pierced through 5182-O into HSLA 350 (ID 10), and (b) through HSLA 350 into 5182-O (ID 11).

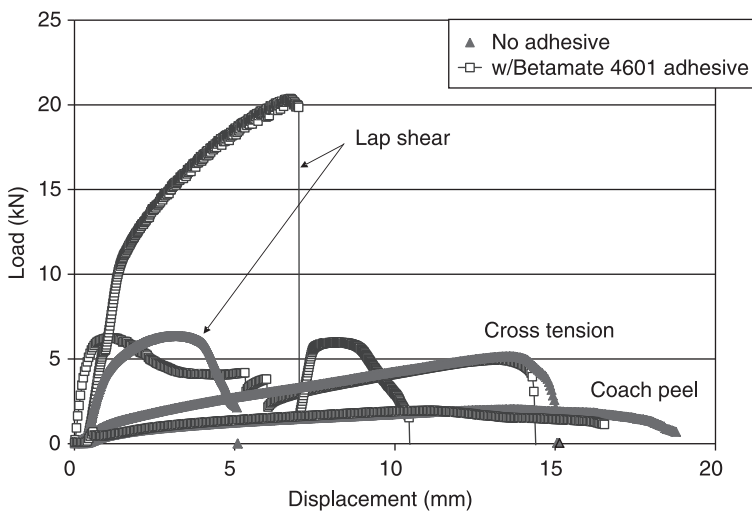


2.16 Uniaxial test results for 5182-O/DP 600 (ID 12L) and DP 600/5182-O (ID 13) SPR joint assemblies comparing the piercing direction.

2.5 Self-piercing riveting (SPR) and structural adhesive joining

Structural bonding is another type of joining technology that is being implemented into vehicle construction with the advent of multi-material vehicles to achieve lightweighting goals. Adhesive bonding may significantly improve the structural stiffness and crash resistance of joined materials by homogenizing the stress distributions throughout the adhesive layer⁵. It increases the load-carrying capacity of the joint and reduces stress concentrations. Not only may it be used alone in vehicle structures, but it may also be used as an extension of existing joining technologies. Hence, the effect of a structural adhesive on the performance of self-piercing rivet dissimilar joint populations was investigated.

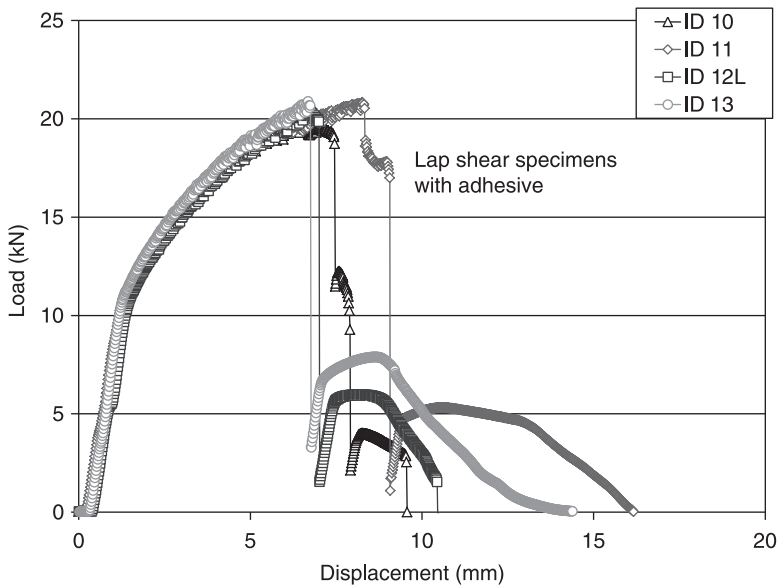
Dow Betamate 4601 adhesive is a crash durable structural adhesive. It is a one component epoxy adhesive intended for bonding of aluminum body structures. Although not optimized for steel structures, this adhesive was applied to the overlap sections of varying SPR joint combinations of dissimilar steel and aluminum substrates (ID 10, 11, 12L and 13) prior to riveting. The completed bond-riveted specimens were then cured at 180°C for 30 minutes, which is consistent with an automotive e-coat oven stage during vehicle assembly. Figure 2.17 illustrates the room temperature static strength results for joint ID 12L with and without the structural adhesive in the varying coupon assemblies. A significant increase in joint strength and displacement to failure was observed in lap shear bond-riveted specimens. The average shear strength increased from



2.17 Uniaxial test results for joint ID 12L (5182-O/DP 600) with and without adhesive in the SPR coupon assemblies.

6.37 to 20.45 kN and the average energy absorption level increased from 25 J to approximately 115 J with the addition of the Betamate adhesive in the SPR joint. Although the peak joint strength did not increase substantially under cross tension loading in the bond-riveted joint, enhancements were observed in energy absorption. The average energy absorption level increased from 52 J to 60 J with the addition of the structural adhesive. The enhancements in strength and absorption energy are evident in the two, uncoupled peak loads observed in the load–displacement graphs in both lap shear and cross tension loading. Once the adhesive failed, the bond-riveted joint then performed similarly to an SPR joint only. These two, uncoupled peak loads were also observed in the other bond-riveted dissimilar material combinations investigated, as shown in Fig. 2.18. In addition, Fig. 2.17 shows that the use of the Betamate 4601 adhesive with the SPR joint in coach peel appeared to have minimal effect. This was also observed in other bond-riveted populations.

The static failure modes for joint ID 12L with and without adhesive also varied under the different loading conditions. Under lap shear loading, rivet head pullout was observed in joint ID 12L specimens without adhesive. However, with the use of the structural adhesive in the joint, rivet tail pullout was observed in the bond-riveted lap shear specimens. Under cross tension loading, tail pullout was observed in joint ID 12L specimens without adhesive. However, head pullout was

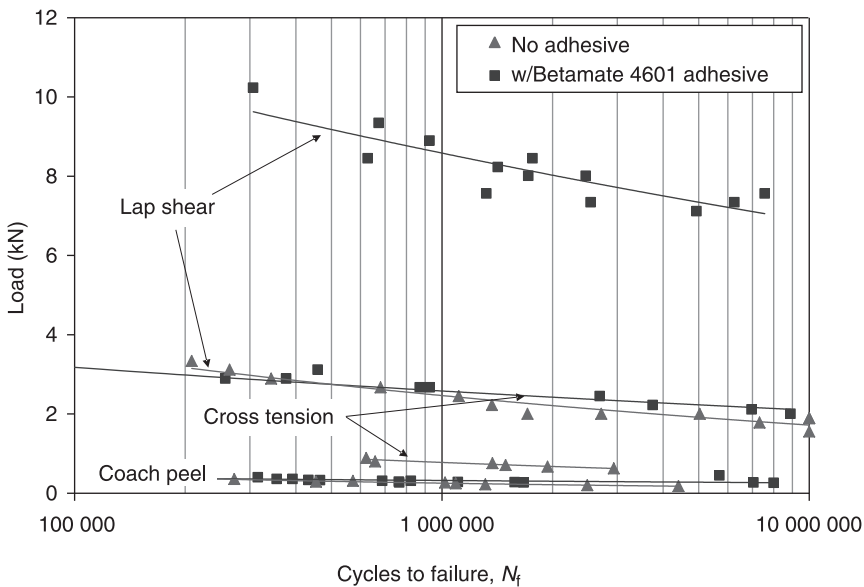


2.18 Lap shear results for joint ID 10, 11, 12L, and 13 with Betamate 4601 adhesive in the SPR coupon assemblies where two peak loads are observed.

observed in the bond-riveted cross tension specimens. No failure mode differences were observed among the joint ID 12L coach peel specimens, regardless of the use of the structural adhesive. Head pullout was observed in all joint ID 12L specimens under coach peel loading.

Fatigue evaluations were also performed on the bond-riveted joint assemblies and their SPR only equivalent. An MTS servo-hydraulic machine was used to test the specimens in load controlled tension-tension with a load ratio of $R=0.1$ and a test frequency of 20 Hz. The fatigue test results showed that the application of a structural adhesive to the SPR joint significantly enhanced the joint durability of the bond-riveted assemblies, in particular for lap shear joints. For the three loading conditions evaluated, lap shear samples with adhesive had the greatest fatigue strength, as shown in Fig. 2.19. Under lap shear loading, the fatigue strength of joint ID 12L with adhesive significantly increased more than 200 percent at 10 million cycles in comparison with the same lap shear joints with no adhesive. A notable increase in fatigue strength under cross tension loading was observed as well. No enhancement in fatigue strength was observed under coach peel loading with the addition of the structural adhesive in the joint.

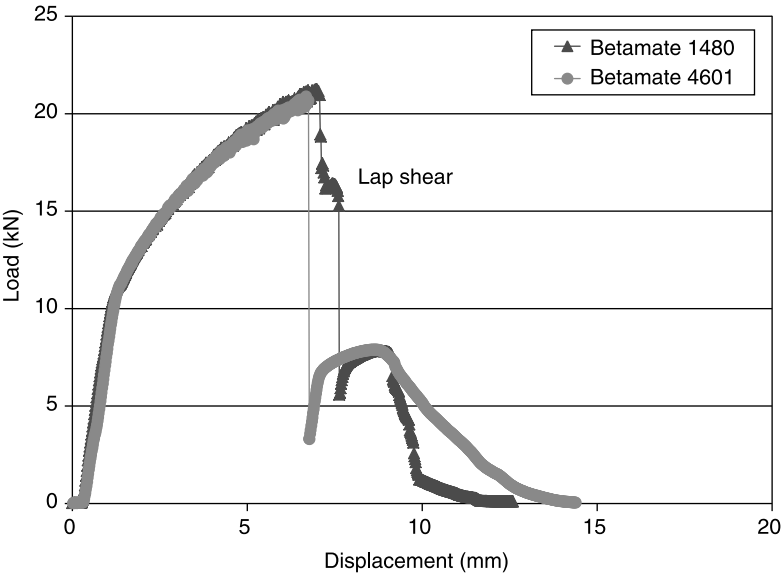
These observations in strength and durability enhancements continued as the effects of different structural adhesives were investigated to evaluate the different adhesion levels of different adhesive systems on dissimilar metal joints. In addition to the Dow Betamate 4601 adhesive, structural adhesive Dow Betamate



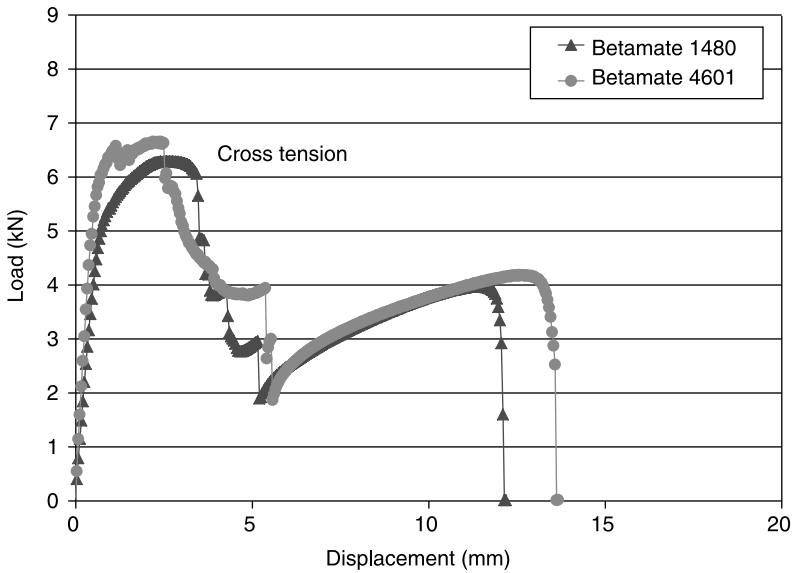
2.19 Fatigue test results for dissimilar metal joint ID 12L (5182-O/DP 600) coupon assemblies with and without Betamate 4601 structural adhesive.

1480 was also applied to the overlap section of joint ID 13 (DP 600/5182-O) prior to riveting. The same curing temperature and duration were employed as the bond-riveted assemblies with 4601 adhesive. Dow Betamate 1480 is also a crash durable adhesive and a one component epoxy that is used in both vehicle structures and hem flanges for closures. Unlike Betamate 4601 adhesive, 1480 is optimized for steel or coated steel surfaces in addition to aluminum substrates in vehicle construction.

Figures 2.20 and 2.21 compare the static performance of joint ID 13 with both structural adhesives for lap shear and cross tension specimen designs, respectively. At room temperature, the two different adhesives yielded similar strengths (first peak on load–displacement graphs) under the varying loading conditions. As in previous observations, a significant increase in joint strength was observed in the lap shear bond-riveted specimens, regardless of adhesive system. Under lap shear loading, the average shear strength increased from 8.80 kN to approximately 21 kN with the use of the structural adhesives in the SPR joint. Under cross tension loading, the average strength increased from 4.14 kN to 6.22 kN with the use of Betamate 1480 adhesive and increased from 4.41 kN to 6.70 kN with the use of Betamate 4601 in the SPR joint. Similar to joint ID 12L specimens with adhesive, greater enhancements were observed in energy absorption under cross tension loading of the bond-riveted joint ID 13 specimens. The average energy absorption levels increased from 32 J to approximately 47 J with the use of Betamate 1480 adhesive and increased from 32 J to 51 J with the use of Betamate 4601.



2.20 Lap shear static test results of joint ID 13 (DP 600/5182-O) with varying structural adhesives in the SPR coupon assemblies.

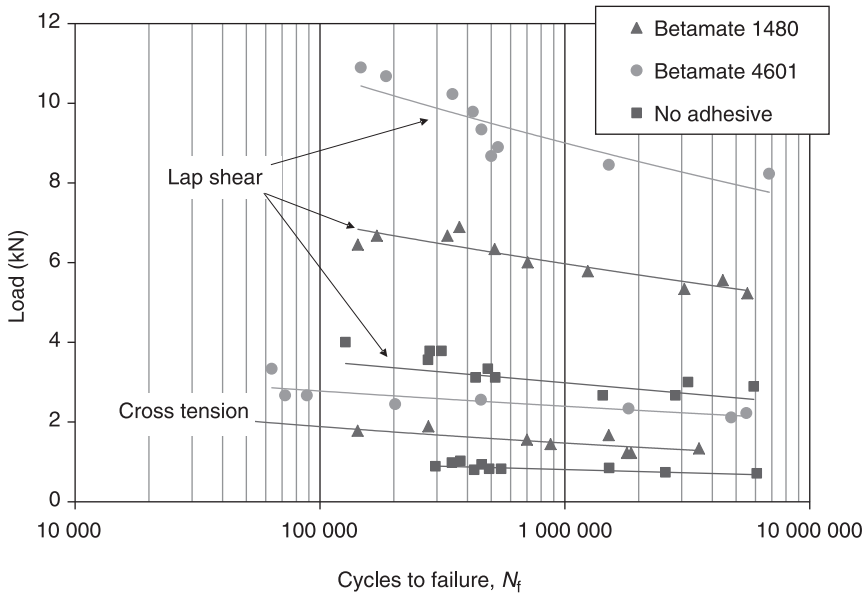


2.21 Cross tension static test results of joint ID 13 (DP 600/5182-O) with varying structural adhesives in the SPR coupon assemblies.

Unlike joint ID 12L bond-riveted specimens, the static failure modes of joint ID 13 specimens with and without adhesive were similar under the different loading conditions. Under lap shear loading, complete rivet pullout was observed in joint ID 13 specimens without adhesive. With the use of Betamate 4601 adhesive in the joint, complete rivet tail pullout with partial head pullout was observed in the bond-riveted lap shear specimens. With the use of Betamate 1480 adhesive in the joint, complete head pullout and partial tail pullout were primarily observed in the bond-riveted lap shear specimens. However, it must also be noted that rivet failure was observed in two of the Betamate 1480 bond-riveted lap shear specimens. Under cross tension loading, all specimens failed via rivet tail pullout, regardless of the adhesive system used and regardless of the presence of adhesive.

In addition, the structural adhesives failed cohesively in the faying surface area surrounding the SPR for both bond-riveted joint ID 12L and ID 13 specimens under the varying static loading conditions. A mixed failure mode (i.e. cohesive and adhesive) was typically observed elsewhere on the faying surface overlap region including delamination of the coated steel surface in some specimens.

In the fatigue evaluations, significant enhancements in joint durability were observed in the lap shear bond-riveted ID 13 specimens, regardless of the adhesive system applied to the SPR joint. These observations are consistent with those observed in joint ID 12L bond-riveted specimens. At 1 million cycles, the fatigue strength increased two to three times that of the equivalent SPR joint with no adhesive depending on the adhesive system applied, as shown in Fig. 2.22. A



2.22 Fatigue test results for dissimilar metal joint ID 13 (DP 600/5182-O) coupon assemblies with and without Betamate 1480 and 4601 structural adhesives.

greater enhancement in joint performance was observed in ID 13 specimens with the 4601 adhesive.

2.6 References

1. Fu M and Mallick P K (2003), 'Fatigue of self-piercing riveted joints in aluminum alloy 6111', *Int. J. Fatigue*, 25(8), 183–9.
2. Booth G S, Olivier C A, Westgate S A, Liebrecht F and Braunling S (2000), 'Self-piercing riveted joints and resistance spot welded joints in steel and aluminum', *Proceedings of the International Body Engineering Conference*, Detroit, MI, SAE Paper No. 2000-01-2681.
3. Vela E, Sun X, Davies R W and Khaleel M A (2002), 'Lap shear coupon design sensitivity study for self-piercing rivets and resistance spot welds', PNNL Technical Report No. 13943, February.
4. Zhou M, Hu S J and Zhang H (1999), 'Critical specimen sizes for tensile-shear testing of steel sheets', *Welding Journal*, 305-s–313-s.
5. Tang H (2010), 'Latest advances in joining technologies for automotive body manufacturing', *Int. J. Vehicle Design*, 54, 1–25.

Fatigue behaviour of self-piercing riveted joints

A. CHRYSANTHOU, University of Hertfordshire, UK

DOI: 10.1533/9780857098849.1.33

Abstract: This chapter addresses the fatigue behaviour of self-piercing riveted joints. Since the process has been used to join aluminium alloy sheets by the automotive industry, the chapter begins with a comparison of the fatigue behaviour of self-piercing rivet joints with resistance spot-welds. The factors that affect fatigue behaviour are then discussed, followed by a description of fretting fatigue and its effects.

Key words: self-piercing riveting (SPR), fatigue behaviour, self-piercing riveted joints, fretting fatigue.

3.1 Introduction

Self-piercing riveting came to prominence in the 1990s when it was used by the automotive industry to join together aluminium alloy panels. The main reason for the application of self-piercing rivets in the automotive sector was that it is difficult to obtain satisfactory resistance spot-welds with aluminium alloys. The early research work on self-piercing rivets had therefore concentrated on comparing the mechanical properties of joints manufactured by the two techniques. In addition to the static strength discussed in Chapter 2, the fatigue life and fatigue strength of different self-piercing riveted joints must be established for durability considerations. As the use of self-piercing rivets gradually became more widespread, researchers then began to focus their attention on process optimisation and subsequently investigated other means to enhance the fatigue life. The necessity to simulate the fatigue behaviour of SPR numerically led to studies of the fatigue failure mechanisms. The research studies that have been conducted, mainly during the last two decades, have significantly advanced our knowledge of the mechanical behaviour of SPR. However, there are still areas where knowledge needs to be extended in order to permit more accurate numerical simulation.

This chapter will focus initially on a comparison of the fatigue behaviour between SPR and spot-welding, followed by a discussion of the factors that influence the fatigue behaviour of self-piercing rivet joints. Finally there is reference to fretting wear and fretting fatigue. The fatigue behaviour of self-piercing riveted joints has been the subject of several investigations. These studies have concentrated on joints between alloys that are used by the automotive industry. According to the results of these investigations, self-piercing riveted

joints do not exhibit a fatigue limit. For this reason, in this chapter, their fatigue behaviour is described in terms of fatigue strength.

3.2 Comparison between self-piercing riveted and resistance spot-welded joints

The initial research on the fatigue behaviour of self-piercing riveted joints focused on a comparison with resistance spot-welded joints. All these studies (Booth *et al.* 2000; Fu and Mallick 2001, 2003; Hahn *et al.* 1999; Krause and Cherenkoff 1995; Li and Fatemi 2006; Mizukoshi and Okada 1997; Ramjoo and Westgate 1999) are in agreement that self-piercing riveted joints exhibit superior fatigue strength in comparison to spot-welded joints. In general, self-piercing riveted joints display fatigue strength that is twice as high as that for resistance spot-welds. Mizukoshi and Okada (Mizukoshi and Okada 1997) compared the fatigue behaviour of self-piercing riveted joints, clinch joints and spot-welded joints for the automotive body panel aluminium alloys GC45-O (Al-4.6%Mg), GC55-O (Al-5.5%Mg) and SG112-T4 (Al-0.5%Mg-1.1%Si). The authors compared the behaviour of joints using a parameter that they described as the 'fatigue ratio', which was the ratio between fatigue strength and lap shear strength. The self-piercing riveted joints were observed to have superior fatigue strength compared with the other two joint types. The 'fatigue ratio' for self-piercing riveted joints was around 0.4, which was twice as high as that for spot-welded joints.

Booth *et al.* (2000) conducted a set of comparative fatigue tests between SPR and spot-welded joints for 5754 aluminium alloy sheet. The fatigue life of 1.2 mm SPR joints after 1×10^6 cycles was observed to be twice as high as those of spot-welded joints. For 3 mm 5754 sheet, the fatigue strength was about 50% higher. The same study showed similar findings for SPR joints between mild steel sheet of 0.8 mm thickness, which is around the value of the conventional thickness for automotive steels. In this case the fatigue strength for mild steel was about 25% superior to that of spot-welded joints. Comparison can also show that 1.2 mm 5754 SPR joints have about twice the fatigue strength of 0.8 mm mild steel spot-welds after 1×10^6 cycles.

The reasons for the superiority of self-piercing riveted joints over spot-welded aluminium alloy joints have been discussed by a number of researchers. Some (He *et al.* 2007) have attributed this behaviour to the fact that the metal around the spot-weld is likely to be in a softer state due to the welding heat, whereas in the SPR joints the areas adjacent to the rivet undergo work-hardening. According to Booth *et al.* (Booth *et al.* 2000), the probable reason for this behaviour is that self-piercing riveting is likely to provide a significantly lower stress concentration. According to the same authors, the geometric change with SPR is likely to be lower in comparison to resistance spot-welded nuggets.

3.3 Factors that affect the fatigue behaviour of self-piercing riveted joints

The self-piercing riveting process involves piercing of the top sheet by the rivet followed by flaring and locking into the bottom sheet. Both the rivet and the sheets to be joined undergo a significant amount of deformation, creating a buttonhole at the bottom of the lower sheet. From the point of view of fatigue behaviour, it is very important that this fast and complex joining process avoids formation of defects and stress concentrations. Current knowledge of the fatigue behaviour of self-piercing riveted joints is based on the results of several research investigations. In order to determine the fatigue behaviour of such joints, numerous fatigue tests must be carried out from a statistical point of view. Unfortunately fatigue tests are time-consuming and costly and for this reason most studies have conducted only a limited number of tests. Nevertheless, these studies have identified the important parameters that affect the fatigue behaviour of self-piercing riveted joints as:

1. the cyclic load;
2. the sheet thickness;
3. the piercing direction (in the case of joints between dissimilar metals);
4. the frictional force between the joined sheets.

Fu and Mallick (Fu and Mallick 2001) were the first to conduct a detailed investigation of the effect of the process variables on the behaviour of self-piercing riveted joints. The parameters that were considered in their study were:

- sheet thickness (1 mm and 2 mm);
- rivet diameter (3 mm and 5 mm);
- rivet length (4 mm and 5 mm for joining 1 mm thick sheets and 6 mm and 6.5 mm for 2 mm thick sheets);
- rivet hardness ($410 H_V$ and $480 H_V$);
- two different rivet coatings;
- die tip height (0 mm, 0.025 mm and 0.050 mm).

The pre-clamping pressure was set at 60 bar, while the rivet setting pressure depended on the rivet diameter; a rivet setting pressure of 150 bar was used for the 5 mm diameter rivets and 110 bar for the 3 mm rivets. The sheet material was 5754-O aluminium alloy, while the rivets were made from 0.35%C steel. Analysis of variance was applied to determine the contribution of each parameter to the fatigue behaviour by performing statistical analysis using SAS software (SAS/BASE and SAS/STAT). The relative contribution of each design parameter was calculated using analysis of variance (ANOVA). According to the results the sheet thickness was the most influential parameter at around 40%. The second most influential factor (28.39%) was the level of the cyclic load, but it must be noted that around 27% of the variance was due to experimental error. Out of the other processing parameters, the rivet diameter was the most influential at 3.17%, while

each of the remaining parameters contributed less than 1% influence. It must be noted that these results were very different compared with the analysis of variance for static lap shear results, where the die tip height was the most influential factor (56.61%), followed by the rivet length (8.87%), sheet thickness (6.35%), rivet hardness, rivet coating and rivet diameter. For static lap shear testing, only about 19% variance was due to experimental error.

In a later study, Fu and Mallick (2003) investigated the effect of the rivet setting pressure on the static and cyclic behaviour of self-piercing riveted 6111-T4 joints. As the rivet setting pressure increased from 50 bar to 120 bar, the lap shear static strength was observed to increase. Samples that were produced within the same range of setting pressure values also underwent fatigue testing using maximum loads from about 1 kN to 2 kN. It was observed that at a maximum load of 1.07 kN the fatigue life increased only slightly with the rivet setting pressure. At maximum loads of 1.33 kN, 1.60 kN and 2.00 kN, the rivet setting pressure had no influence on the fatigue life.

Iyer *et al.* (Iyer *et al.* 2005) conducted fatigue testing for single-rivet joints for aluminium alloy 5754-O of 1 mm, 2 mm and 3 mm thickness. All the samples were manufactured at a setting speed of 96 mm s^{-1} and a setting force of 80 kN. The authors confirmed that the higher the sheet thickness, the higher the maximum fatigue load for a given fatigue life. In other words, the fatigue strength increased with sheet thickness.

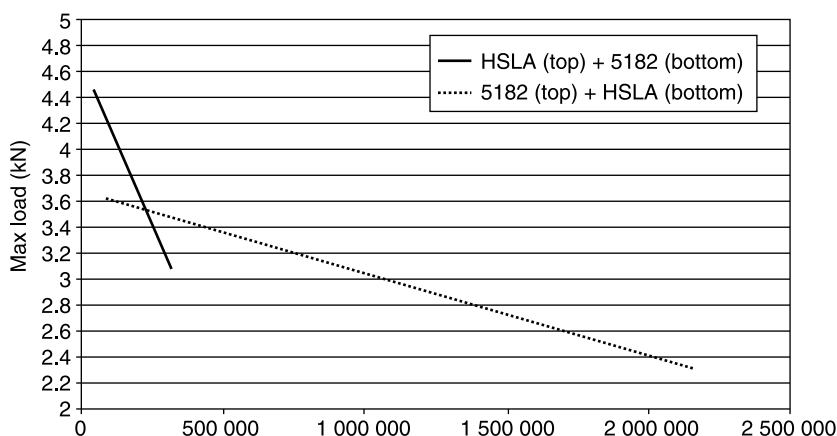
Sun *et al.* (2007) compared the fatigue behaviour of different joint populations of 5182-O aluminium alloy where the thickness of the pierced sheet was varied, while the thickness of the locked sheet remained constant (2 mm). It was observed that, when the thickness of the pierced sheet was 1 mm, the fatigue strength was significantly lower compared with results with a 2 mm pierced sheet. Within the life cycle range of 10^5 to 10^6 the fatigue strength was twice as high for the joint with the 2 mm pierced sheet.

When using SPR to join two different sheet materials, the piercing direction can influence the fatigue behaviour. This was demonstrated by Sun *et al.* (2007) who investigated the behaviour of SPR joints between 1 mm HSLA350 and 2 mm 5182-O. The SPR joint where the HSLA350 acted as the pierced sheet had a higher fatigue strength by about 30%. Both types of self-piercing riveted joints failed by a similar fatigue failure mode; this was in the form of eyebrow cracking of the pierced sheet. However, the position of the crack initiation point was slightly different due to the head side geometry that resulted from different rivet head/surrounding material flush levels. For the samples where the 1 mm HSLA sheet acted as the locked sheet, the crack initiation point was at the contact area between the rivet and the pierced (the 2 mm 5182-O) sheet. For the samples where the HSLA was the pierced sheet, the crack initiated on the surface of the HSLA, a short distance away from the rivet head. The fatigue behaviour was further studied by Sun *et al.* (Sun *et al.* 2007) by testing joints using a stronger steel (DP600 of 1.6 mm thickness) in combination with 5182-O. The fatigue life data were virtually

similar to those for the HSLA-5182-O combination. When using the DP600 as the locked sheet, the fatigue failure mechanism was by eyebrow cracking in the 5182-O sheet. On the other hand, when the DP600 steel was the pierced sheet, fatigue failure was observed to occur by either rivet fracture or tail side cracking.

The observation of different fatigue failure modes indicates the presence of different stress concentration areas. Since the self-piercing riveting process is essentially a cold-working process, piercing through a strong head side material may potentially cause rivet damage during the process. The selection of riveting parameters and the riveting direction must therefore take into account the specific combination of materials to be joined.

Much of the published research on the self-piercing riveting of dissimilar materials suggests that using the softer metal as the tail side is advantageous to both the static strength and fatigue strength due to the higher interlock distance into the bottom sheet. However, work conducted by the author of this chapter has shown that, in some specific materials combinations and over a range of fatigue load values, the configuration with the stronger material as the tail side may exhibit better fatigue resistance. Specifically when joining a 1.2 mm HSLA steel (yield stress=250 MPa and UTS=400 MPa) and 1.5 mm 5182 aluminium alloy (yield stress=140 MPa and UTS=290 MPa), the samples having the HSLA as the pierced sheet (with average interlock distance of 0.85 mm) failed at an average lap shear load of 6.24 kN in comparison with 4.85 kN for samples pierced in the reverse direction (with average interlock distance of 0.49 mm). The results of fatigue testing for the two different types of joints are shown in Fig. 3.1. While the fatigue strength of the samples with the HSLA steel as the pierced sheet is superior at the higher fatigue loads, this is not so at lower fatigue loads. As Sun *et al.* (Sun *et al.* 2007) have quite rightly pointed out, any general



3.1 Fatigue behaviour of self-piercing riveted joints between HSLA steel and aluminium 5182 with different piercing directions.

recommendations such as using the softer metal as the tail side must be exercised with some degree of caution for a particular material combination. Thus any decisions on the piercing direction must be verified by experimental data.

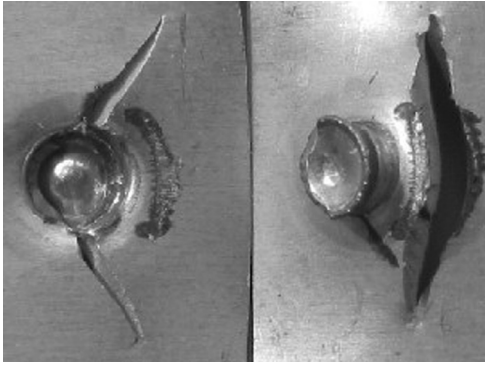
During the self-piercing riveting process, a high enough upset force must be applied in order to lead to yielding and deformation of the rivet. Upon removal of the upset force, the component parts are left in compressive contact with each other, while the rivet is left in tension perpendicular to the joint. When loaded, the joint configuration will experience frictional forces that distribute the load over a greater area so that the lap shear strength and the fatigue strength are improved. In a lap shear joint, part of the applied load is transferred by friction between the contact surfaces, while the rest is transferred by bearing between the rivet and the sheet adjacent to the rivet. The importance of the frictional forces at the interface between the sheets that are riveted together was demonstrated by Han *et al.* (Han *et al.* 2006a). The fatigue behaviour was examined for self-piercing riveted joints between three different combinations of 5754 aluminium alloy sheets. The first of the three sets of samples was produced using uncoated 5754 sheets, the second had a wax coating, while the third used PTFE tape inserted between the two 5754 sheets. Direct shear apparatus was used to measure the coefficient of friction of the three types of samples. The wax-coated and the uncoated sheets had a coefficient of friction of 0.26 and 0.24 respectively, while the use of a PTFE insert gave a value of 0.03. It was observed that the fatigue strength decreased as the coefficient of friction decreased.

Fatigue failure for the uncoated and the wax-coated samples was observed to take place by means of eyebrow failure of the pierced sheet close to the rivet head. In contrast to this, the sample with the PTFE insert failed by rivet fracture. The much lower coefficient of friction resulted in a lower frictional force at the interface between the two sheets and this altered the load transfer mechanism of the joint. This increased the bearing load acting on the rivet, which as a consequence suffered fatigue failure.

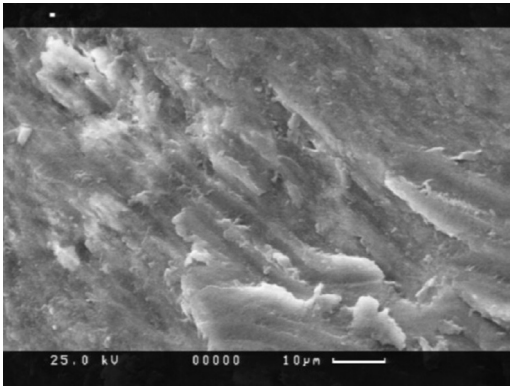
3.4 Fretting fatigue

When a self-piercing riveted joint experiences a load, part of the load will be transferred by friction between the contacting surfaces. The presence of such a frictional force is essential for the proper function of the joint; without this frictional force the joint will be weaker. At the same time the presence of friction at the contacting surfaces leads to fretting fatigue. The failure of self-piercing riveted joints by fretting fatigue was investigated by Iyer *et al.* (Iyer *et al.* 2002) and by Han and co-workers (Han *et al.* 2006b).

During cyclic loading of self-piercing riveted joints, fretting scars develop at the contact area between the two sheets adjacent to the rivet. Typical fretting scars and their position are demonstrated in Fig. 3.2. Iyer *et al.* (Iyer *et al.* 2002) observed that fatigue crack initiation in self-piercing riveted joints involved



3.2 Typical fretting scars as a result of fatigue for a self-piercing riveted joint between two 5754 aluminium alloy sheets.



3.3 Scanning electron micrograph of fretting scars on the surface of aluminium alloy 5182.

fretting wear at the interface between (i) the rivet and the joined sheets and (ii) the interface between the two sheets. They also reported that fretting wear became more severe as the sheet thickness increased.

Upon the application of a cyclic load, fretting wear at the interface between the two contacting sheets will initiate. During the initial stages of fretting, the fretting scars may not be visible to the naked eye; however, examination of the contacting surfaces by using SEM reveals scarring and wear, as shown in Fig. 3.3. The contacting sheets are aluminium 5754 and analysis of the fretting scars reveals the presence of mainly aluminium oxide with traces of magnesium oxide (magnesium being the main alloying element in alloy 5754). The scars at this stage are not deep and seem like 'laminates' coming off the surface. If the alloy is coated with a solid lubricant, early fretting will involve wear of the solid lubricant layer. As the number of cycles increases, black scars that are typical of fretting wear gradually

appear. As fretting damage progresses, stress concentration can build up at these areas leading to the nucleation of a fatigue crack, which propagates obliquely to the sliding direction. The crack further grows in the same direction into the subsurface and then changes direction and continues to propagate perpendicular to the sliding direction until fracture. Han *et al.* (Han *et al.* 2006b) have also shown that the fretting action led to work-hardening of the metal subsurface. Even though the effects of the work-hardening have not been studied extensively, it is possible that they may provide some additional resistance to crack propagation.

3.5 References

- Booth G, Olivier C, Westgate S, Liebrecht F and Braunling G (2000), 'Self-piercing riveted joints and resistance spot-welded joints in steel and aluminium', SAE Technical paper 2000-01-2681.
- Fu M and Mallick P K (2001), 'Effect of process variables on the static and fatigue properties of self-piercing riveted joints in aluminium alloy 5754', SAE Technical paper 0825, 117–129.
- Fu M and Mallick P K (2003), 'Fatigue of self-piercing riveted joints in aluminium alloy 6111', *Int. J. Fatigue*, **25**, 183–189.
- Hahn O, Mescut G and Peetz A (1999), 'Mechanical properties of punch-riveted and adhesively-bonded aluminium sheets', *Weld. Cutting*, **51**, E130–E134.
- Han L, Chrysanthou A and O'Sullivan J M (2006a), 'Fretting behaviour of self-piercing riveted aluminium alloy joints under different interfacial conditions', *Mater. Des.*, **27**, 200–208.
- Han L, Chrysanthou A, Young K W and O'Sullivan J M (2006b), 'Characterisation of fretting fatigue in self-piercing riveted aluminium alloy sheets', *Fatigue Fract. Engng. Mater.*, **29**, 646–654.
- He X, Pearson I and Young K W (2007), 'Finite element analysis of self-pierce riveted joints', *Key Eng. Mater.*, **344**, 647–654.
- Iyer K, Brittman F L, Hu S J, Wang P C, Hayden D B and Marin S P (2002), 'Fatigue and fretting of self-piercing riveted joints' In: *Proceedings of the ASME International Mechanical Engineering Congress and Exposition IMECE 2002*, November, 17–22 2002, New Orleans, LA, pp. 401–415.
- Iyer K, Hu S J, Brittman F L, Wang P C, Hayden D B and Marin S P (2005), 'Fatigue of single- and double-rivet self-piercing riveted lap joints' *Fatigue Fracture Eng. Mater. Struct.*, **28**, 997–1007.
- Krause A R and Cherenkoff R A (1995), 'A comparative study of the fatigue behaviour of spot-welded and mechanically fastened aluminium joints', SAE Technical paper 950710.
- Li B and Fatemi A (2006), 'An experimental investigation of deformation and fatigue behaviour of coach peel riveted joints', *Int. J. Fatigue*, **28**, 9–18.
- Mizukoshi H and Okada H (1997), 'Fatigue properties of mechanical fastening joints', *Mater. Sci. Forum*, **242**, 231–238.
- Ramjoo G R and Westgate S (1999), 'Fatigue properties of clinched, self-piercing riveted and spot-welded joints in steel and aluminium alloy sheets', TWI Report 680/1999.
- Sun X, Stephens E V and Khaleel M A (2007), 'Fatigue behaviour of self-piercing rivets joining similar and dissimilar sheet metals', *Int. J. Fatigue*, **29**, 370–386.

Corrosion behaviour of self-piercing riveted joints

A. CHRYSANTHOU, University of Hertfordshire, UK

DOI: 10.1533/9780857098849.1.41

Abstract: This chapter describes the corrosion mechanisms that are encountered when a self-piercing riveted assembly is subjected to a corrosive environment. The chapter begins with a short introduction and a description of the fundamental theory of the likely corrosion mechanisms for self-piercing riveted joints. This is followed by a description of relevant methods of studying the corrosion behaviour and the results of a study of the corrosion of self-piercing riveted joints between interstitial-free steel and aluminium 5182 as conducted by the author. The chapter ends with a description of the means that are used to minimise or eliminate the corrosion of self-piercing riveted joints.

Key words: self-piercing riveting (SPR), corrosion mechanisms, self-piercing riveted joints.

4.1 Introduction

Corrosion is defined as the chemical degradation of metals and can lead to metal loss as well as metal and component failure. For this reason, the cost of corrosion is very high. In 1971, a UK Government Committee on Corrosion and Protection (Hoar 1971) concluded that the total cost of corrosion to the national economy accounted for 3.5% of the country's gross national product (GNP), while in the United States in 1975 the figure was 4.2% (Editorial 1980, *Corrosion Prevention and Control*). It is generally estimated that the cost of corrosion in the developed economies is of the order of about 3% of GNP, which is a significantly high figure.

The corrosion of automotive vehicles has been the subject of several previous studies and reports. There is probably no other consumer product that attracts so much attention and concern, owing to what vehicles suffer from exposure to the atmosphere (at ambient temperatures, in rain, in humid conditions, in increasing reactive concentrations, etc.). The main reasons for scrapping cars have been documented to be accidents, obsolescence and corrosion (McArthur 1981). As the level of corrosion may determine the ability to repair a car following an accident, the role of corrosion and corrosion protection cannot be overestimated.

In addition, the strength of the car body is likely to be affected by the amount of corrosion that it suffers. In the event of impact, the ability of the car body to absorb energy and provide safety to the passengers is likely to be influenced by the amount of corrosion the body has suffered. Arguably, corrosion is the main

factor that determines the lifetime of a vehicle and the ability to repair it following an accident. It is therefore no surprise that, from the 1980s onwards, car manufacturers have paid significant attention to reducing corrosion. These developments have led to improved corrosion resistance to such an extent that new vehicles are sold with a warranty against cosmetic, perforation and structural corrosion. This has been achieved largely through the use of better design against differential aeration corrosion, through the use of improved coating systems and, in the case of steel, by the increasing use of galvanised products (Atwood 1995). Some of these methods were discussed by Ostermiller *et al.* (Ostermiller *et al.* 1996).

The use of alternative materials, such as aluminium for car body applications, has led to the introduction of new joining processes, including self-piercing riveting. The ability to maintain corrosion protection in car bodies that are constructed with new materials and processes is still paramount. This chapter will address the corrosion of self-piercing riveted joints. Following a short summary of the background to the mechanisms of corrosion of lap joints, the chapter will examine the corrosion mechanisms for self-piercing riveted joints and outline some of the corrosion protection methods.

4.2 Background theory of corrosion

The most common class of corrosion is wet corrosion and this occurs as an electrochemical reaction. This class of corrosion takes place in an aqueous environment and is also referred to as aqueous corrosion. In the process of electrochemical corrosion, metal atoms lose electrons to become ions and in the process they go into solution. During the corrosion reaction, an electric circuit is formed and the system is called an electrochemical cell. A typical example of an electrochemical cell is presented in Fig. 4.1. The cell consists of three components:

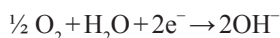
1. The anode that gives up electrons to the electric circuit and corrodes. The anode loses electrons and oxidises by forming ions, which enter the electrolytic solution. The electrons leave the anode and travel to the cathode through the electrical connection. The anode is the positively charged side of the circuit. The anodic reaction is

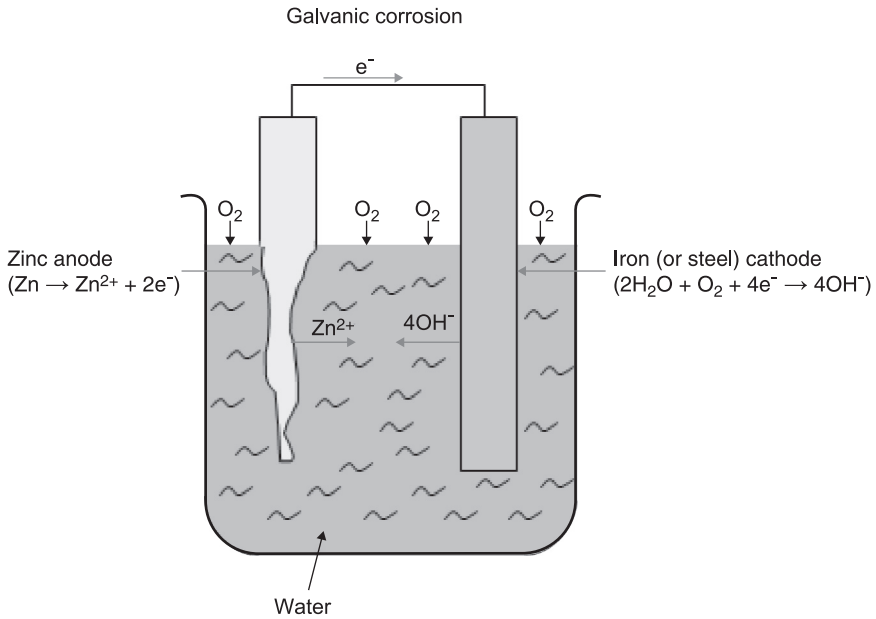


or



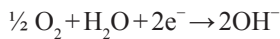
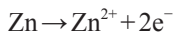
2. The cathode receives electrons from the circuit. In aerated water, oxygen reacts at the cathode to form hydroxide ions:



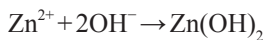


4.1 Diagram of an electrochemical cell.

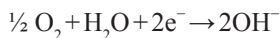
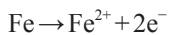
The hydroxide ions react with the positively charged metal ions to produce a solid product or rust. In the case of zinc as presented in Fig. 4.1,



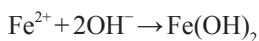
and



The most commonly used alloy globally is steel. When steel corrodes the reactions that take place are:



and



and eventually



The corrosion process leads to the formation of haematite (Fe_2O_3), which is commonly referred to as 'rust'.

3. An electrolyte must be in contact with both the anode and the cathode. The electrolyte is conductive and provides the route for the metal ions to leave the anode and travel to the cathode. Water is the most common electrolyte. It must be stressed that for wet corrosion to take place both oxygen and an electrolyte must be present.

When a metal is placed in a corrosive (i.e. electrolytic) solution, it develops an electrode potential, which is a measure of the tendency of the metal to lose its valence electrons. The driving force for the oxidation reaction must be offset by an equal and opposite driving force for the reduction reaction. Therefore it is not possible to measure the electrode potential of an individual material; for this another electrode is required. Values of the electrode potential are thus measured in a half-cell by connecting a metal in a molar solution of its ions to a standard electrode in a molar solution of its own ions. The hydrogen electrode is used as the standard reference electrode and, by definition, its electrode potential is set equal to zero volts.

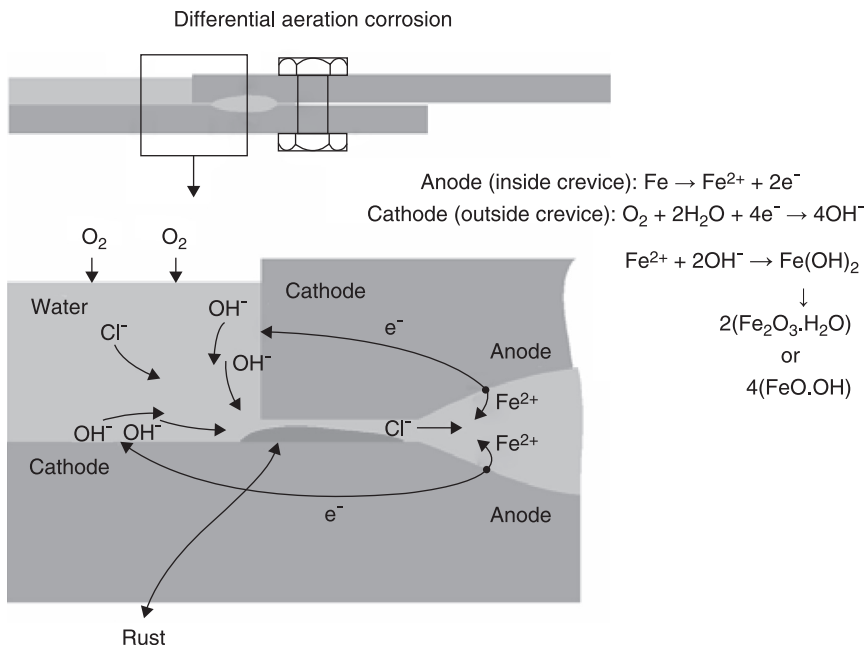
Before looking at the corrosion of self-piercing rivets in more detail, the fundamental theory behind the possible corrosion mechanisms will be addressed. These are galvanic or bi-metallic corrosion, differential aeration corrosion and stress cells. Galvanic corrosion takes place when two metals are in contact with each other in the presence of an electrolyte, leading to the formation of an electrochemical cell. The more reactive of the two connected metals will undergo preferential corrosion (i.e. it will act as the anode), while the more noble metal will be protected (i.e. it will act as the cathode) as in Fig. 4.1. The tendency of a metal to act as the anode or the cathode is determined by its position in the galvanic series. Table 4.1 presents the galvanic series for selected metals. The anodic

Table 4.1 The electrochemical series for selected metals

Metal	Standard electrode potential (V)
$\text{Mg} \rightarrow \text{Mg}^+ + \text{e}^-$	-2.37
$\text{Al} \rightarrow \text{Al}^{3+} + 3\text{e}^-$	-1.66
$\text{Zn} \rightarrow \text{Zn}^{2+} + 2\text{e}^-$	-0.76
$\text{Fe} \rightarrow \text{Fe}^{2+} + 2\text{e}^-$	-0.44
$\text{Ni} \rightarrow \text{Ni}^{2+} + 2\text{e}^-$	-0.25
$\text{Sn} \rightarrow \text{Sn}^{2+} + 2\text{e}^-$	-0.14
$\text{H} \rightarrow \text{H}^+ + \text{e}^-$	0.00
$\text{Cu} \rightarrow \text{Cu}^{2+} + 2\text{e}^-$	+0.34
$\text{Ag} \rightarrow \text{Ag}^+ + \text{e}^-$	+0.80
$\text{Pt} \rightarrow \text{Pt}^{4+} + 4\text{e}^-$	+1.20
$\text{Au} \rightarrow \text{Au}^{3+} + 3\text{e}^-$	+1.50

metals are placed at the top of the series and the cathodic metals at the bottom (note that American sources arrange the galvanic sources in the reverse order). According to the series, if aluminium and mild steel are electrically coupled together in the presence of water, aluminium, which is higher up the series, will suffer preferential corrosion and steel will be protected. Since self-piercing riveting of aluminium is carried out using steel rivets, galvanic corrosion would be possible.

Differential aeration corrosion takes place due to the presence of differences in the composition of an electrolyte. This corrosion mechanism is typically observed when there are areas of contact between the metal and the electrolyte where starvation of oxygen is present. Electrons will flow from the low-oxygen region, which acts as the anode (and corrodes), to the high-oxygen area that serves as the cathode. Areas where this type of corrosion is likely to take place include the joint interface between the riveted sheets and the gap between the rivet and the sheet metals where the oxygen concentration is likely to be low. An example illustrating the corrosion in the overlap of a mechanically fastened assembly is presented in Fig. 4.2. Another possible corrosion problem in self-piercing riveted joints



4.2 Schematic diagram portraying the mechanism of differential aeration corrosion within the overlap of a mechanically fastened assembly.

involves crevice corrosion within cracks that might arise if the rivet were to break through during the riveting or other stage.

Stress cells are developed when a metal contains areas with variations of local stresses. These stresses could be in the form of applied or residual stresses. In the case of a self-piercing riveted joint, the process leads to deformation of the metallic sheets and the rivet. The most highly stressed areas will behave as anodic regions and corrode, while the parts with lower stress will be cathodic. The highly stressed areas of a self-piercing riveted joint like the buttonhole, the regions around the pierced hole and the rivet itself are areas which are likely to suffer from this type of corrosion.

4.3 Methodology of corrosion studies

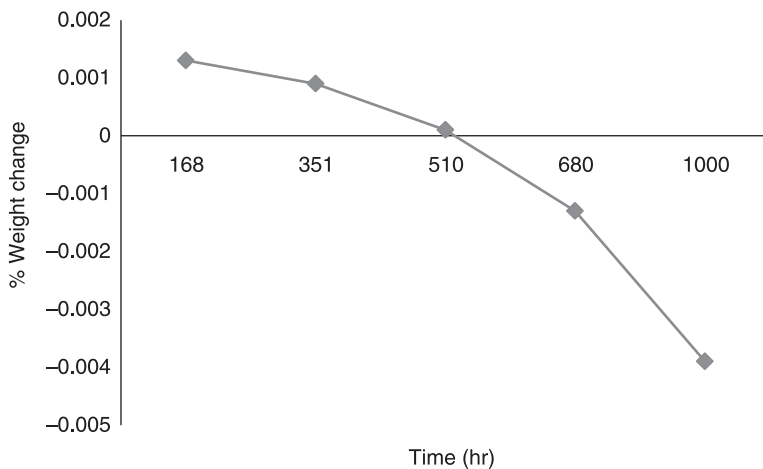
The corrosion of self-piercing riveted joints is described in the next section from studies that were conducted using the ASTM-B117-97 corrosion standard, which describes the standard practice for operating salt-spray (fog) apparatus. To date there are no specific standards for the corrosion of self-piercing riveted joints, but there are some standards that are relevant to the corrosion of lap joints. These are the European Coil Coating Association (ECCA) test method T19 for atmospheric corrosion and the German specification VDA 621-415 on the accelerated ageing of anti-corrosion coatings in automotive applications.

The procedure based on the ASTM-B117-97 standard that was used to obtain the corrosion results presented in this chapter is described below.

The samples that were used during the corrosion study that is reported in the next section involved interstitial-free (I.F.) steel that was joined to aluminium 5182 using a semi-tubular rivet made of steel that could be hardened to 500H_V. Both the I.F. steel and the rivet were covered with a Sn-Zn protective coating. The I.F. steel acted as the pierced (top) sheet and aluminium 5182 was the locked (bottom) sheet. The samples were cleaned using a soft nail brush, followed by treatment in an ultrasonic bath filled with acetone to remove any grease. The samples were then thoroughly dried by blowing hot air at them for 5 minutes. They were subsequently left to dry for 48 hours in an oven at 70°C before being weighed to an accuracy of four decimal places. Corrosion was performed at 35°C (±1.5°C) in a salt-spray chamber using a 5% NaCl solution in de-ionised water. The total time of exposure was 1000 hours. This treatment was carried out in hourly cycles. This involved the samples being subjected to a fog spray (salt spray) for 10 minutes at a flow rate of 0.8 litres/hour followed by 50 minutes of hot air (drying). The sequence was repeated every hour. Samples were removed at various intervals for weight measurement and examination. The test was stopped after 1000 hours for weight measurement and analysis after they were cleaned in an ultrasonic bath using de-ionised water to remove NaCl deposits then washed with propan-2-ol and dried at 70°C in an oven.

4.4 Corrosion of self-piercing riveted joints

The weight change with time for interstitial-free (I.F.) steel riveted to aluminium 5182 is presented in Fig. 4.3. During the initial stages of corrosion, a small weight gain was recorded and this was followed by a gradual weight loss. The weight loss was due to the loss of iron as 'rust' (Fe_2O_3), which occurred in the later stages of corrosion after the zinc-based coating had undergone sufficient corrosion to expose the underlying I.F. steel. The first signs of corrosion led to a small weight gain and started to be visibly evident in the form of white specks on the surface of the rivet and on the surface of the I.F. steel after about 48 hours. This was due to corrosion of zinc from the protective two-phase Sn-Zn coating on the surface of the rivet and the I.F. steel. In the presence of a very aggressive environment, as in the accelerated salt-spray test according to the ASTM B117-97 standard, protective zinc coatings can suffer corrosion at a fast rate. The corrosion mechanism on the surface of the rivet and the I.F. steel involved galvanic corrosion since zinc is higher up in the galvanic series than tin. In the case of the coating on the surface of the I.F. steel, corrosion was further accelerated by galvanic corrosion, since at the overlap the coating was in direct contact with the aluminium alloy, with the latter undergoing corrosion since it is higher up the galvanic series. The use of X-ray diffraction identified the main corrosion products on the surface of the rivet and the steel to be zinc hydroxide and hydrocarbonate and zinc hydroxychloride (or simonkolleite) with the formula $\text{Zn}_5\text{Cl}_2(\text{OH})_8 \cdot 2\text{H}_2\text{O}$. Two zinc hydrocarbonates are possible: hydrozincite $[\text{Zn}_5(\text{CO}_3)_2(\text{OH})_6]$, which is the most common, and $\text{Zn}_4\text{CO}_3(\text{OH})_6 \cdot \text{H}_2\text{O}$, whose formation is limited to marine environments or conditions with high levels of sodium chloride.

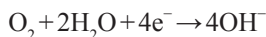


4.3 Plot of percentage weight change with time for the corrosion of a self-piercing riveted assembly of I.F. steel with aluminium 5182.

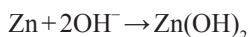
During the initial stages, there is also evidence of the beginning of corrosion within the outside ends of the overlap. The mechanism of corrosion within the overlap is differential aeration corrosion and is due to a differential in the oxygen concentration as the electrolyte gradually moves into the overlap. The electrolyte in the inner parts of the overlap normally contains a lower amount of oxygen; these parts act as the anode, while the parts on the extreme outside of the overlap contain higher levels of oxygen and act as the cathode. The anodic reaction in the early stages involved the corrosion of zinc by



while the cathodic reaction formed hydroxide ions



The overall corrosion reaction is

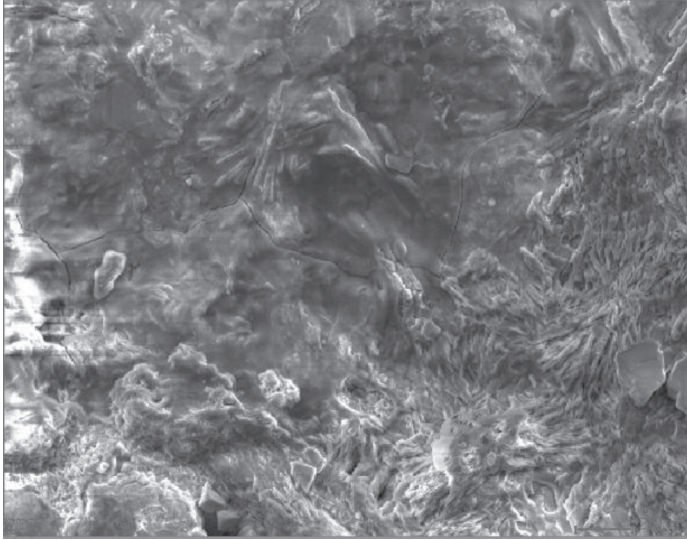


The combination of the two reactions led to a build up of zinc hydroxide, while the consumption of oxygen by the cathodic reaction maintained the oxygen differential that drove the corrosion reaction. The lower mobility of the hydroxide ions led to an increase in the chloride ion concentration and, as a result, to an increase in corrosion close to the corrosion front. With time, at the entrance to the overlap joint, the aerated (higher oxygen concentration) electrolyte led to the formation of a thick layer of a metallic corrosion product that was richer in zinc hydroxide and zinc hydrocarbonate. Elemental analysis using energy dispersive X-ray microanalysis (EDAX) shows evidence of mainly zinc and oxygen and traces of chlorine at the entrance to the overlap joint, as presented in Fig. 4.4. This confirmed that the corrosion product at the entrance of the overlap was mainly zinc hydroxide. The microstructural morphology was significantly different in the inner areas of the overlap where the chloride concentration was higher. In these areas, a plate-like morphology was evident. Based on the EDAX analysis in Fig. 4.5 the plates were identified as $\text{Zn}_5\text{Cl}_2(\text{OH})_8 \cdot 2\text{H}_2\text{O}$. The likely reaction was



The access of the electrolyte into the overlap regions was gradual; as a result the corrosion reactions within the overlap progressed gradually inwards. As the corrosion product continued to build up within the overlap, aluminium began to corrode as well; presumably by then the direct contact between the two sheets was virtually lost and no galvanic corrosion could be maintained. Thus corrosion of the aluminium alloy commenced during the later stages of the test.

The interfacial area between the top of the rivet and the I.F. steel was another area where differential aeration corrosion was observed. The progression of corrosion in this region is presented in Figs 4.6(a), 4.6(b) and 4.6(c). During the initial stages, corrosion of zinc was observed to take place. When this became

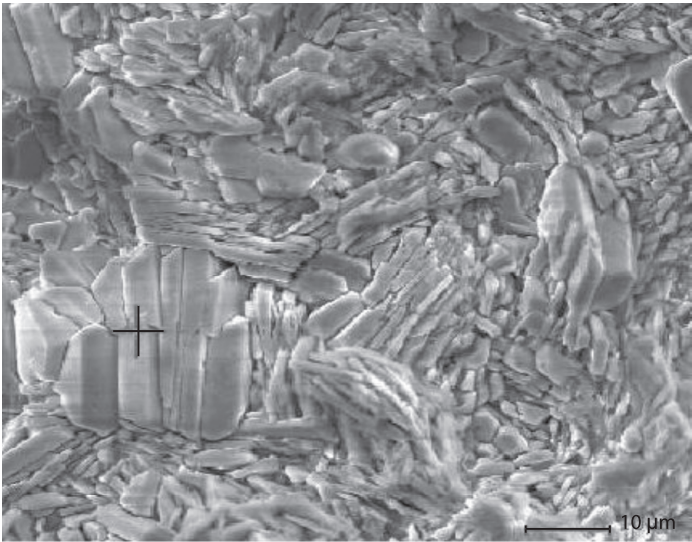


Element	Wt%	At%
OK	36.20	69.35
ClK	01.85	01.60
ZnK	61.96	29.05
Matrix	Correction	ZAF

4.4 EDAX analysis at the entrance to the overlap joint showing the presence of mainly zinc hydroxide.

severe enough for the I.F. steel to be exposed, the formation of Fe_2O_3 around the entire rivet hole took place. Another corrosion mechanism that is likely to be active around the rivet hole is due to stress cells, which develop when a metal/alloy contains areas of different local stresses. The piercing process will create deformation around the rivet hole and this region will be more highly stressed than the areas further away from the rivet hole. The regions that are more highly cold-worked will act as the anode in comparison with the surrounding areas that experience low deformation stresses and act as cathodic sites.

The effect of corrosion within the overlap on the lap shear strength of the self-piercing riveted joint is shown in Fig. 4.7. During the initial stages of corrosion the lap shear strength increased. Earlier work by Howard and Sunday (Howard and Sunday 1983) had reported that, after a 90-day alternate immersion test, there was no significant deterioration in the lap shear strength of self-piercing riveted aluminium alloy joints. This type of behaviour is likely to be due to an increase in

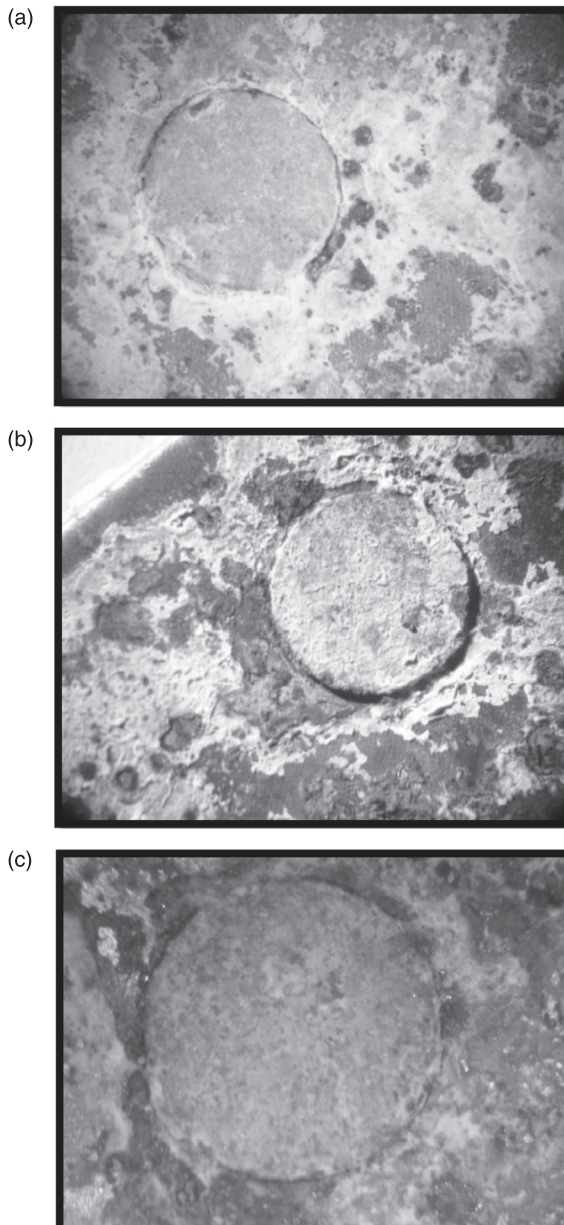


Element	Wt%	At%
OK	14.27	37.42
ClK	13.95	16.51
ZnK	71.78	46.07
Matrix	Correction	ZAF

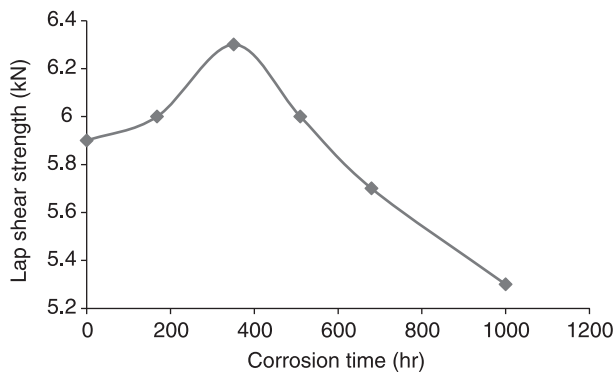
4.5 EDAX analysis revealing the presence of plates of $\text{Zn}_5\text{Cl}_2(\text{OH})_8 \cdot 2\text{H}_2\text{O}$ deep within the overlap areas.

the coefficient of friction (and hence of frictional force) at the interface between the mating sheets as the corrosion product builds up. However, during the later stages of the salt-spray corrosion test, the excessive build up of the corrosion products led to an increase in the amount of stress acting on the rivet. As a consequence, failure of some of the self-piercing rivets occurred even in the unloaded condition, effectively opening up the overlap as shown in Figs 4.8(a) and 4.8(b). Crevice corrosion of the steel rivet due to the presence of a differential in the oxygen concentration within the gaps between the rivet and the alloys can also contribute to this observation. The rivets in their initial condition are covered with the zinc-based coating, but parts of the coating are normally damaged during the piercing and locking stages of the self-piercing riveting process. This exposes significant parts of the steel, which starts to corrode even during the early stages of the corrosion test. The gradual loss of iron from the exposed rivet surface can create stress concentrations that may lead to eventual failure of the rivet.

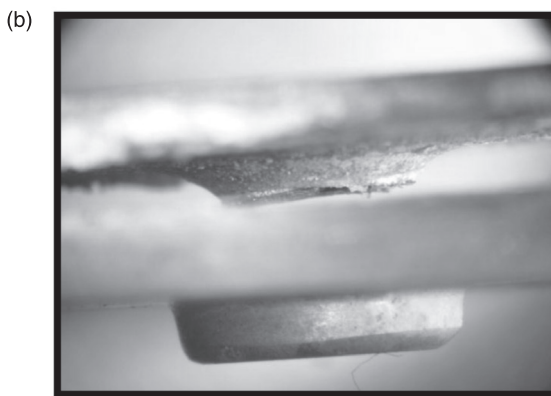
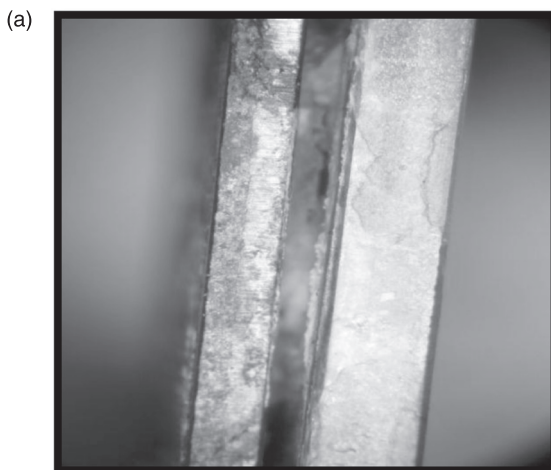
Sunday, February 02, 2014 3:06:28 AM



4.6 The progression of corrosion in the interfacial area between the rivet and I.F. steel: (a) after 351 hours; (b) after 510 hours; (c) after 850 hours.



4.7 The effect of corrosion on the lap shear strength of a self-piercing riveted joint between I.F. steel and aluminium 5182.



4.8 (a) Build up of corrosion products within the overlap of a self-piercing riveted joint between I.F. steel and aluminium 5182. (b) Failure as a result of build up of corrosion products within the overlap.

The rivet buttonhole was the other area where corrosion took place. There are a number of potential reasons for corrosion in this region. These are summarised below.

1. Stress cells are likely to develop at the buttonhole areas that have been deformed and are therefore highly stressed compared with the surrounding areas. As above, the deformed areas are going to act anodically to the less stressed cathodic regions.
2. The buttonhole, depending on its shape and amount of deformation as well as its orientation during the corrosion test, may act as a water (electrolyte) trap giving rise to differential aeration corrosion.
3. In cases where zinc-coated steel is the bottom sheet, the zinc coating may be damaged as the material is deformed. Depending on the amount of deformation, the damage may be such that the zinc coating cannot 'heal' itself. As a consequence localised damaged areas will expose the steel to the electrolyte and will suffer from corrosion.

4.5 Corrosion protection of self-piercing rivets and joints

There are a number of corrosion protection measures that can be applied to self-piercing riveted joints in the automotive industry. As discussed above, one of the corrosion mechanisms involves galvanic corrosion due to the use of steel rivets to join aluminium alloys and future effort is likely to focus on the use of aluminium alloy rivets. In the development of suitable aluminium alloy rivets, it is clear that the rivet material must be stronger than the sheets to be joined. For this reason, the rivet and sheet materials are unlikely to be of the same composition and will exhibit slightly different chemical properties and different values of electrode potential. As a consequence, the problem of galvanic corrosion in self-piercing riveted assemblies cannot be totally eliminated. Recently Hoang *et al.* (Hoang *et al.* 2009) joined sheets of AA6060 alloy in different conditions using rivets made of 6082-T6, 7108-T5 and 7278-T6 rivets. Their study showed that these rivets can successfully join sheets of AA6060 alloy. Mechanical tests showed that the aluminium alloy rivets gave joints that were lower in strength than joints with steel rivets. The best performing rivet was the 7278-T6 rivet, which resulted in joints of strength of about 10% lower than the strength of joints with rivets made of steel.

Self-piercing rivets are coated primarily for protection against corrosion and sometimes for decorative purposes. A variety of coatings are available and these include zinc and a combination of tin–zinc of composition ranging from 50% to 90% tin. The main technique that is used for coating self-piercing rivets is mechanical plating. This is based on a cold-welding concept that is carried out in tumbling rubber-lined barrels and applies mechanical energy at room

temperature. Zinc, tin and aluminium can be applied by this means either singly or in combination. The rivets along with the metallic coating powders, glass beads (which act as the impact medium) and surface conditioners are placed in the barrels, which are then rotated. The coating powder is impacted by the glass beads onto the rivet surface through the rotation of the barrels. A mechanical bond is thus created between the rivet and the metal coating. Zinc coatings ranging from about 5 μm to 15 μm are possible with good protection against corrosion. The other major process that can be used to coat self-piercing rivets is electroplating.

Zinc coatings have been used for many decades in order to provide corrosion protection to steel. In recent years, tin–zinc coatings have been introduced. Since there is no mutual solubility between tin and zinc at room temperature, the coating consists of a two-phase mixture of virtually pure grains of tin and zinc. The coating is impermeable to water and, under corrosive conditions, zinc will corrode first and thus maintain its sacrificial property. Sn–Zn coatings were originally developed in order to replace the toxic cadmium coatings, but they are now also competing with zinc coatings, owing to their superior corrosion resistance. They are generally thought to be about five times more corrosion resistant than zinc coatings. They also possess other advantageous properties including good frictional properties and good wear resistance. Of particular interest to the automotive industry is the fact that the Sn–Zn coating can maintain its strength at higher temperatures, which is important for retaining the joint strength during the finishing operations. In addition, the coating can retain high electrical conductivity and can therefore be used as an electrical grounding member. Its good ductility also helps it prevent coating damage when bent or stamped.

Sn–Zn coatings have been used for the corrosion protection of self-piercing rivets in the Jaguar XJ as well as the Audi TT. In the case of the latter, corrosion concerns are even more serious because steel sheet rear-part members have been joined to the aluminium body assembly. In automotive body applications, self-piercing rivets are used in combination with adhesive bonding, which forms the basis of insulating the mating sheets and sealing the overlaps. In the case of the Jaguar XJ, about 3200 self-piercing rivet joints are set over about 90 metres of aerospace-industry sourced epoxy adhesive. In the Audi TT a further measure has had to be taken by sealing the overlaps between steel and aluminium with polyvinyl chloride (PVC) or with wax following the cathaphoretic coating process.

4.6 References

- Attwood B (1995), 'Development of coated flat-rolled products for automotive end use', *Steel Times International*, **19**, 36–38.
 Editorial, 1980, *Corrosion Prevention and Control*, **27**(3), 1.

- Hoang N-H, Porcaro R, Langseth M and Hanssen A-G, 2009, 'Self-piercing riveting connections using aluminium rivets', *International Journal of Solids and Structures*, **47**, 427–439.
- Hoar T P (1971), 'Report of the committee on corrosion and protection', HMSO, London.
- Howard R M and Sunday S P, (1983), 'The corrosion performance of steel self-pierce rivets when used with aluminium components', SAE Technical Paper Series 831816.
- McArthur H, (1981), 'Motor vehicle corrosion – safe at any age?', *Corrosion Prevention and Control*, **28**(3), 5–8.
- Ostermiller M R, Piepho L L and Singer L (1996), 'Advances in automotive corrosion resistance', Technical Paper, Society of Manufacturing Engineers FC, 96 (270), X1–11.

Dynamic strength evaluation/crashworthiness of self-piercing riveted joints

X. SUN, Pacific Northwest National Laboratory, USA

DOI: 10.1533/9780857098849.1.56

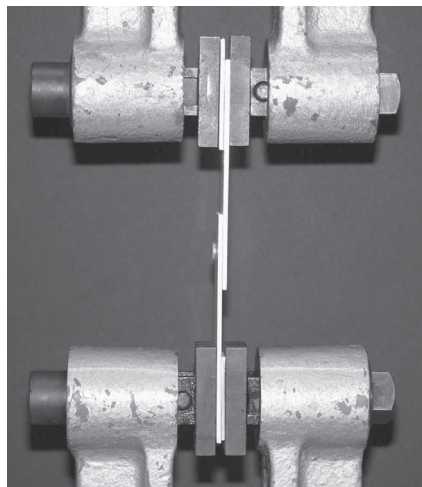
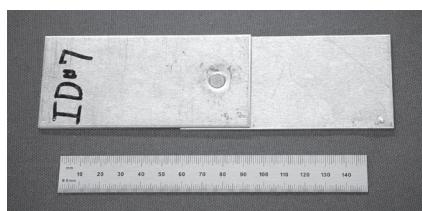
Abstract: This chapter discusses the dynamic SPR strength evaluation procedures and the measured dynamic strength data for various joint populations of self-piercing rivets (SPR) joining similar and dissimilar metals. A state-of-the-art review of the current practice for conducting dynamic tensile/compressive strength tests in different strain rate regimes is presented, and the generic issues associated with dynamic strength testing are addressed. The joint strength testing procedures and fixture designs used in the current study are then described, and the typical load versus displacement curves under different loading configurations are presented. Detailed static and dynamic strength data and the associated energy absorption levels for all the samples in the joint populations are also included.

Key words: dynamic strength, high rate, strain rate, fixture design, energy absorption.

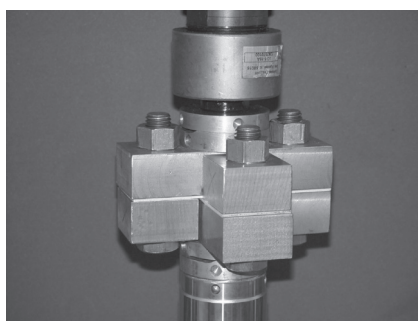
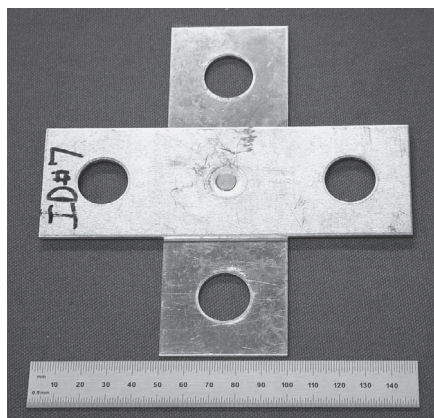
5.1 Introduction

In order to ensure passenger safety and to comply with various impact safety regulations, vehicle design engineers must have sufficient information and knowledge about joint strength and other mechanical properties when new materials and joining processes are introduced to a specific vehicle design. In addition to the static material and joint properties, the dynamic strengths of these joints under different loading modes subject to dynamic loading are also critical in evaluating the crashworthiness of the joint structures.^{1–10,19–22}

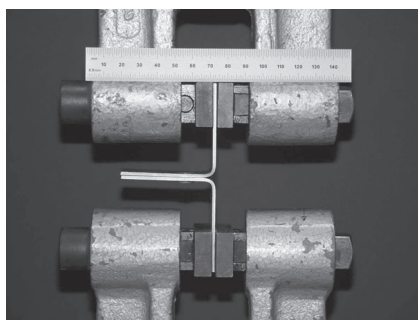
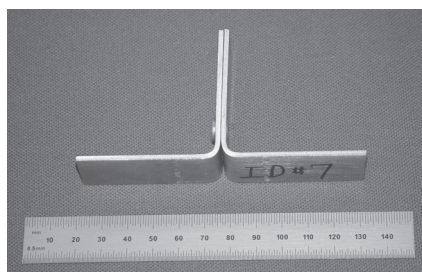
The mechanical performance evaluations of an SPR by laboratory tests can be very complex because joint strength often depends on coupon size and configuration, loading mode, loading rate and loading environment. In addition, different processing parameters used in the fabrication process usually render SPR with different strengths. The mechanical strength of an SPR under quasi-static loading has been discussed in Chapter 5 under different loading conditions. Comparisons have been made for samples with and without breakthrough and with various failure mechanisms. See Fig. 5.1(a)–(c) for typical fixture designs for static SPR joint strength evaluations. Chapter 6 discusses the fatigue tests and fatigue behaviors of SPR under different loading conditions with various coupon configurations and associated fixture designs.



(a)



(b)



(c)

5.1 Coupon configuration and fixture design for static tests: (a) lap shear loading condition, (b) cross tension loading condition, and (c) coach peel loading condition.

These coupon configurations and the associated fixture designs are for static/fatigue loading only and they cannot be applied directly under dynamic loading conditions because of a variety of issues, such as reliability of the gripping systems under high rate loading, heavy fixtures' inertia effects, individual hydraulic

systems' loading rate capacity, as well as the differences in data acquisition systems needed. In general, special fixtures are needed for dynamic tests.

In this chapter, we first review the state-of-the-art dynamic testing methodologies in different strain rate regimes. The generic issues related to high rate strength testing are then discussed. Since the strain rate of relevance to the automotive safety community is less than 1000/s, we propose to use a servo-hydraulic system with specific fixture designs to characterize the dynamic joint strength. The testing procedures and the associated fixture designs for the dynamic tests are presented next.

Typical dynamic load and displacement versus time curves are presented in raw form, without any numerical filtering. The uniqueness of the current testing procedure is established by comparing the joint strength data obtained in this study with results in the open literature. Dynamic joint strength and energy absorption results for various SPR joint populations are provided in tabulated format. The effects of loading rates on joints' ductility and peak strength are then discussed for different loading configurations. The dynamic joint strength can be used by automotive safety engineers in evaluating the crashworthiness of a specific vehicle design made from these specific material combinations.

5.2 State-of-the-art review of dynamic tensile tests

Materials' mechanical properties under dynamic loading are usually very important for impact and explosive resistant structural design.¹¹ This section reviews the dynamic factors and typical experimental methods for high strain rate base material tests.

There is no very clear definition distinguishing static and impact loading. If the load is applied slowly enough, the test can be considered as quasi-static or static. ASTM E8 requires strain rate not to exceed $5 \times 10^{-5} \text{ s}^{-1}$ for steel or $15 \times 10^{-5} \text{ s}^{-1}$ for aluminum for quasi-static tests.¹² Mechanical behaviors of metals at high strain rates usually differ considerably from those observed at quasi-static strain rates. The difference can be attributed to the activation of different slip systems, differences in dislocation mobility, pile up and accommodation processes under different strain rates. In practice, an important difference between static and impact resistant design is also that statically loaded parts must be designed to carry loads, whereas parts subjected to dynamic impact must also be designed to absorb energy.

Material strength properties usually vary with the speed of load application. For steels in general, both the yield and ultimate tensile strengths increase with the speed of loading.¹²⁻¹⁴ Studies indicate that a linear relationship exists between flow stress and the logarithm of plastic strain rate in the range from quasi-static rates to about 10^3 s^{-1} for low carbon steels.¹³⁻¹⁴ Above this range, the flow stress generally rises far more rapidly with strain rate. At strain rates in excess of 10^4 s^{-1} , the lower yield stress is often found to be directly proportional to strain rate, rather

than to the logarithm of strain rate. On the other hand, aluminum alloys show less sensitivity to loading rate. For example, a nearly constant level of yield strength has been observed for 2xxx series of aluminum alloys for the strain rate range from quasi-static rates to about 10^2 s^{-1} .¹⁴ Table 5.1 summarizes the experimental methods for high strain rate base material test at different strain rate ranges as recommended by the American Welding Society.¹⁵

Typical quasi-static mechanical tests are performed at the strain rate of around 10^{-4} s^{-1} in a hydraulic test frame. In these tests, regular strain-gage load cells can be used to record the load response, and the displacement is usually measured by linear variable differential transformer (LVDT) or by direct hydraulic ram displacement provided that the stiffness of the machine is much higher than the stiffness of the connection and that the fixtures are very strong and that no slippage occurs at the gripping surfaces. Typically, very bulky fixtures, such as wedge grips, are used to satisfy these requirements. Similar equipment and technique can generally be extended to strain rates as high as 0.1 s^{-1} without much difficulty. For tests at strain rates above 0.1 s^{-1} , grip slipping, inertia effects, wave propagation effects, shock wave effects, thermal effects, as well as the difficulty with load and strain measurements are likely to appear. These dynamic effects become more significant at higher strain rates.^{12,15–18}

5.2.1 Inertia and wave propagation effects

A fundamental difference between a high strain rate test and a quasi-static test is that inertia and wave propagation effects become more pronounced at higher strain rates. When the strain rate is increased through the medium strain rate regime, the measurement of load is the first to be affected by natural frequencies

Table 5.1 Experimental methods for base material property test at different strain rate ranges

Mode	Applicable strain rate, s^{-1}	Testing techniques
Compression	<0.1	Conventional load frames
	0.1–100	Special servo-hydraulic frames
	0.1–500	Cam plastometer ¹⁹ and drop test
	200– 10^4	Hopkinson pressure bar in compression
	10^4 – 10^5	Taylor impact test and flyer plate test
Tension	<0.1	Conventional load frames
	0.1–500	Special servo-hydraulic frames ²³
	100– 10^4	Hopkinson pressure bar in tension
	10^4	Expanding ring and flyer plate in spallation mode
	> 10^5	Flyer plate

of the loading apparatus and stress wave propagation. As the strain rate increases even further, uniform deformation within the specimen becomes more critical. Inertia initially opposes uniform deformation, and a stress wave is transmitted and reflected within the test piece. The velocity of waves and the size of the test piece determine the upper limit of strain rate for accurate measurement of stress–strain curves. At very high strain rate (beginning at about 10^4 or 10^5 s^{-1}), shock wave propagation becomes critical. Since we focus on intermediate strain rate tests in this study, the extremely high strain rate tests will not be discussed in detail.

5.2.2 Conventional load frames at intermediate strain rates

In automotive accident studies, strain rates between 100 s^{-1} and 200 s^{-1} are most often observed. This is in the range of intermediate strain rate and the joint strength under this loading rate range can be determined by conventional load frames with high rate actuators.

Conventional test machines can be pneumatic or hydraulic, with high rate actuators to deliver increasing ram velocities. The crosshead speed of hydraulic machines is limited to the capacity of the hydraulic pump to deliver a steady pressure on the piston of the actuator or crosshead. Servo-hydraulic test machines often offer a wider range of crosshead speeds. For dynamic testing of automotive components, specially designed servo-hydraulic systems can reach as high as 30 m/s (67 mph).¹⁵

Many other factors also influence the loading speed the specimen experiences. For example, the speed may be influenced by the load that the ram is attempting to apply, and the no-load, empty-frame speed may be much higher than the full-load speed. Second, a long stroke machine may attain a given speed only after a significant amount of travel. Third, the specimen length could influence test results because considerable specimen strain could occur before final maximum velocity is obtained in a tension test. Finally, the ability to control speed is a function of the response capability of a servo-controlled machine working in a closed-loop mode. Open-loop machines provide speeds that can be influenced by specimen strength and cannot easily reproduce predetermined velocities or strain rates on materials with different yield strengths or strain hardening behaviors.

5.2.3 Load cell ringing and response time

In typical quasi-static and low speed tests, strain-gage load cells and pressure transducers are often used to measure load. For strain-gage load cells, strain gages are mounted on precision-machined alloy-steel elements, sealed in a case with the necessary electrical outlets, and arranged for tensile and/or compressive loading. The load cell can be mounted so that the specimen is in direct contact, or the cell can be indirectly loaded through the machine crosshead, table, or columns of the load frame. The load cells are calibrated to provide a specific voltage as an output

signal when a certain force is detected. In pressure transducers, which are variations of strain-gage load cells, the strain-gage member is activated by the hydraulic pressure of the system.

These strain-gage load cells often have natural frequencies ranging from 500 to 5000 Hz. The natural frequency of a specific load cell is an intrinsic design parameter that is determined by geometry and physical properties, such as density and elastic modulus. For tests at low strain rates, a typical strain-gage load cell can provide sufficient frequency response. However, problems often arise at intermediate to high strain rate due to ringing in the load cells.

When a constant high rate test is performed, deformation must be initiated by an impact due to the acceleration time required by the ram. If the test response frequency is close to the natural frequency of the load cell, the impact can excite the natural vibrational mode of the load cell, which will produce oscillations in the output signal that can mask the actual load measurements. This effect is called load cell ringing.¹² For tests with strain rate ranging from 100 to 500 s⁻¹, a standard strain-gage load cell either may not possess the necessary frequency response or it may ring excessively. These characteristics render it inadequate for load measurement under intermediate strain rate. Ringing of the load cell can be minimized by selecting a load cell with a high vibration frequency. If the natural frequency is sufficiently high, the vibrational mode may not be excited by the impact; or, even if excited, it may be possible to remove it from the signal with a low pass filter. Generally, the load cell response time must be short enough compared with the total duration of the test. For example, if a load cell has a natural frequency of 1 kHz, its period of vibration is 10⁻³ s. This load cell could then be used only for experiments that last over 10 times that amount, e.g. 10⁻² s.

Since the typical duration of a dynamic strength test for automotive joints is within milliseconds, regular strain-gage load cells do not have sufficiently high natural frequencies. Under these loading rates, a quartz piezoelectric device is usually used. A quartz piezoelectric load cell is feasible because of its excellent intrinsic frequency response and high fundamental vibrational frequency. Piezoelectric transducers usually have natural frequency between 10 kHz and 300 kHz, though, as with any other force transducers, the system's natural frequency will be lower because of the unavoidable mass of necessary attached/fixture components.

Another method to reduce ringing is to dampen the impact that initiates deformation within the specimen. Often, a thin layer of soft, deformable material placed between the impacting surfaces is sufficient to remove the higher frequencies generated by the impact that can excite the natural frequency of the load cell. This is a general practice when performing high rate tests on plastics. Such layers, however, may complicate measurements of displacement within the specimen. In addition, the desired strain rate level may also be compromised by the use of this type of mechanical dampening mechanism.

5.2.4 Fixture and load train design

The distance from the load cell to the deforming portion of the specimen must satisfy certain conditions to ensure true load measurements. If the distance is too long, the finite elastic wave travel time may result in load data that is not timely coincident with strain data. To prevent phase lags from obscuring the experimental data, the wave transit time from the specimen to the load cell should be negligibly small compared with the test duration. Test specific fixtures should be designed to achieve this.

In addition to the load cell natural frequency, the natural frequency of the entire load train (including test fixtures) should also be checked out to make sure that its response time is much faster than the specimen failure duration. A simple, empty load frame natural frequency test can be performed by a hammer test in which an impulse load from a hammer can be used to excite the load frame with load cell and attached test fixtures. The free vibration responses can be recorded by the load cell. If the natural frequency of the load train is too low in comparison with the expected test duration, improvements need to be performed prior to tests. This can usually be achieved by reducing the compliances of the load frame, increasing the fixture stiffness, and reducing the fixture weight.

5.2.5 Lack of international and/or industry-wide standards

In addition to the above-discussed intrinsic issues related to dynamic base material strength tests, it should be mentioned that currently there is no international or industry-wide standard for determining the impact strength and performance of welded or mechanically fastened joints. Owing to the lack of standards and recommended practices, there is usually a large scatter of reported dynamic strength for similar joints, and therefore some reluctance in using the reported data. Major issues that prevent the wider use of dynamic joint strength data in vehicle crashworthiness simulations include:

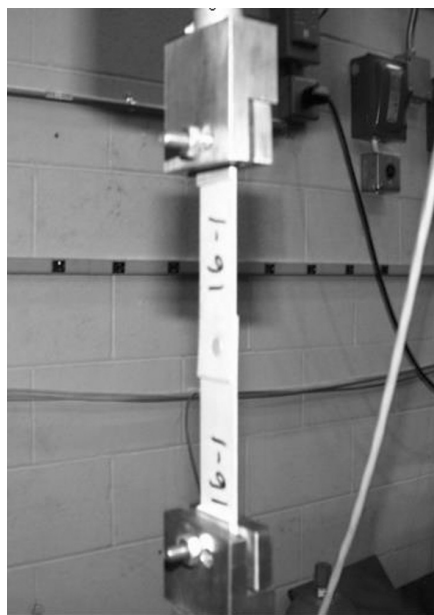
- no industry-wide calibration standards and practices;
- no standard on sample design;
- each user must define application-specific test requirements;
- machine requirements for dynamic high rate testing are undefined;
- different machines and test-setup produce different results using similar samples;
- data comparisons among different tests are risky and not generally recommended.

Because of these issues, there is a lack of confidence in consolidating dynamic strength data reported by different sources, and many resources could be saved by providing the automotive manufacturers and suppliers with an industry-wide joint dynamic strength testing procedure.

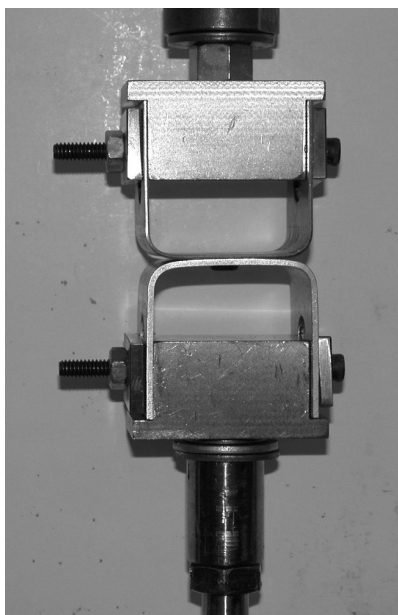
5.3 Recommended joint dynamic strength testing procedures

Since the most relevant strain rate to an automotive impact event lies in the intermediate strain rate regime, servo-hydraulic test frames with high rate actuators are used in the current experimental study. In order to evaluate the dynamic joint strength of different joint populations under loading modes similar to those examined earlier under quasi-static loading, two different fixture and gripping systems were designed and machined for the dynamic tests; see Fig. 5.2(a) and (b). These fixtures were designed such that they screw directly into the load cell and thereon to the rest of the test frame. It also minimizes the distance from the load cell to the joint such that accurate, in-phase joint force versus displacement relationship can be captured for the test duration. The fixtures were machined from titanium alloy to ensure light weight, high stiffness and therefore high resonant frequency in the loading direction.

The load train's free vibration natural frequency was checked prior to actual tests using the hammer test. Since the typical response time of the samples is 1–2 milliseconds, the compliance of the load frame was adjusted prior to the tests such that a sufficiently high natural frequency, with minimum value around 10kHz,



(a)



(b)

5.2 Fixture designs for dynamic tests: (a) lap shear and coach peel and (b) cross tension.

was achieved. This ensures less ‘masking’ of the dynamic load measurement by system ringing.

A piezoelectric load washer with 100kHz un-mounted natural frequency was used for load measurement. The data acquisition frequency used was 300kHz. Displacement of the hydraulic ram was used as the displacement measurement of the sample. Using the above-described fixtures, all the dynamic tests were performed using a servo-controlled hydraulic testing frame under two ram velocities: 4.47m/s (10mph) and 8.94m/s (20mph). All dynamic load versus displacement data presented in this chapter are raw, un-filtered results.

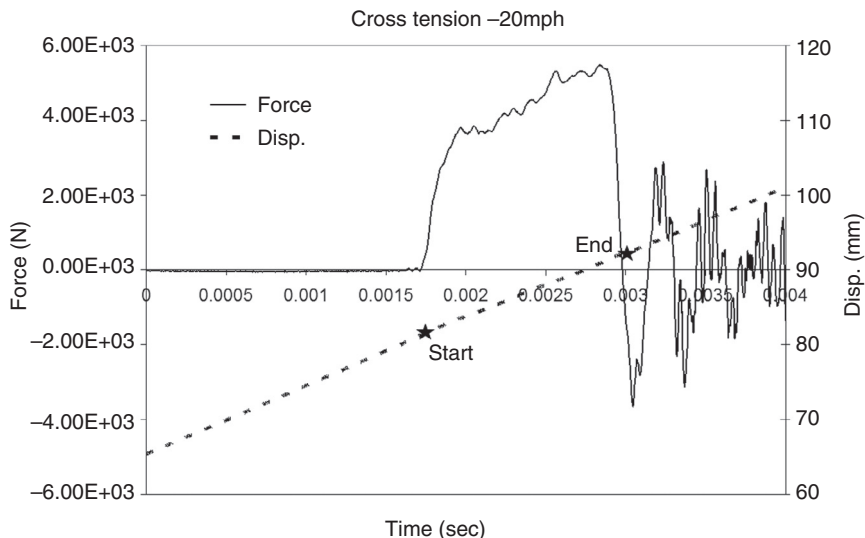
The SPR joint populations examined in this study are summarized in Table 5.2. Materials ranging from AA5182-O to DP600 were joined with a common rivet head with a diameter of 7.5mm in all the SPR populations. For the bonded populations, the adhesive covered the entire overlap area of the joint samples; see Fig. 5.1(a)–(c). The thickness of the adhesive layer was controlled by the glass beads (0.25mm diameter) in the adhesive material.

In order to allow the ram velocity build-up and to test the specimen at constant velocity as specified, a slack adaptor was designed and machined to allow the ram to travel freely for the first 12.7mm (0.5 inch) without loading the specimen. Once the ram achieved the desired velocity level after the initial 12.7mm (0.5 inch) of load-free travel, the slack adaptor engaged and loaded the specimen with a step-function in velocity.²³ The monitored displacement versus time curve for the ram was used to ensure the constant loading rate. No mechanical dampening mechanism was used such that the tests can be considered as step-loading with constant velocity.

Figure 5.3 shows the typical load and displacement versus time curves for a cross tension joint in ID 7 under 8.94m/s (20mph) impact loading. The constant slope of the displacement versus time curve from point ‘start’ to point ‘end’ in Fig. 5.3 indicates that the actual ram velocity was constant at around 8.5m/s (19mph) during the entire joint sample failure process. This is a unique feature of the current joint strength testing procedure compared with other dynamic joint strength measurements reported in the open literature. For example, the displacement versus time curve depicted in Fig. 5 of Lin *et al.*² indicates that, in the opening mode test (equivalent to cross tension here), the specimen was initially loaded with very low initial velocity. The loading velocity gradually built up to the desired level of 6.7m/s (15mph), but then dropped significantly when load exceeded 4000N. At peak load, the loading rate was only about 2.68m/s (6mph). This type of loading rate fluctuation could be the source of variations in measured dynamic strength under different ‘desired’ loading rates. In addition, Fig. 5.3 indicates that much higher ringing frequency was achieved prior to peak load; therefore no numerical filtering was necessary to obtain the true joint strength under 8.94m/s (20mph) impact loading.

Table 5.2 Summary of the joint populations studied

Joint ID	Joining method	Top material	Top thickness (mm)	Middle material	Bottom material	Bottom thickness (mm)	Stack thickness (mm)	Rivet head diameter for SPR or weld fusion zone size for RSW (mm)
7	self-piercing rivet (SPR)	5182-O	2.0	–	5182-O	2.0	4.0	7.5
8	SPR	5182-O	1.0	–	5182-O	2.0	3.0	7.5
9	SPR	1008	1.4	–	5182-O	2.0	3.4	7.5
10	SPR	5182-O	2.0	–	HSLA 350	1.0	3.0	7.5
10A	SPR	5182-O	2.0	Dow Betamate 4601	HSLA 350	1.0	3.0	7.5
11	SPR	HSLA 350	1.0	–	5182-O	2.0	3.0	7.5
11A	SPR	HSLA 350	1.0	Dow Betamate 4601	5182-O	2.0	3.0	7.5
12L	SPR	5182-O	2.0	–	DP 600	1.6	3.6	7.5
12A	SPR	5182-O	2.0	Dow Betamate 4601	DP 600	1.6	3.6	7.5
13	SPR	DP 600	1.6	–	5182-O	2.0	3.6	7.5



5.3 Typical force and displacement versus time curves for ID 7 at 8.94 m/s (20 mph) under cross tension loading.

It should be noted that with higher sample strength, a larger decrease from empty-frame velocity to loaded ram velocity is possible. This decrease can be compensated by carefully overshooting the initial empty-frame ram velocity. In the test results presented in this study, the maximum allowed deviation from the specified impact velocity to the actual loaded frame velocity is 5%. The results of the dynamic strength tests for all the joints are obtained in the form of load versus displacement curves using un-filtered load versus time and displacement versus time data. In addition to the peak load and displacement at peak load for all the joints, total energy absorption was also calculated by numerical integration.

5.4 Results and discussion

For each joint population, five replicate dynamic strength tests were conducted under 4.47 m/s (10 mph) and 8.94 m/s (20 mph) ram velocity for each loading configuration. The static and fatigue strength of the same joint populations have been studied and reported elsewhere.⁹⁻¹⁰ Table 5.3(a)–(c) list the mean and standard deviation of joint strength (peak load) and energy absorption for quasi-static (30 samples), 4.47 m/s (10 mph) and 8.94 m/s (20 mph) dynamic tests under three test configurations for all the joint populations. In all the dynamic results presented here, the actual loaded frame velocities during deformation were measured and ensured to be within 5% deviation from the specified impact velocity.

Table 5.3(a) Lap-shear strength and energy absorption comparison

Joint ID	Static strength (KN) Mean(standard deviation)	4.47m/s (10mph) Strength (KN) Mean(standard deviation)	8.94m/s (20mph) Strength (KN) Mean(standard deviation)	Static energy absorption (mm-KN) Mean(standard deviation)	4.47m/s (10mph) Energy absorption (mm-KN) Mean(standard deviation)	8.94m/s (20mph) Energy absorption (mm-KN) Mean(standard deviation)
7	7.44 (0.36)	9.855 (0.76)	11.01 (0.48)	39.9 (3.3)	42.17 (1.33)	30.2 (1.1)
8	2.74 (0.04)	4.55 (0.014)	5.01 (0.21)	13.6 (0.75)	8.2 (0.71)	9.3 (0.42)
9	5.84 (0.11)	9.6 (1.27)	10.62 (0.31)	44.3 (1.58)	47.2 (4.2)	39.7 (2.1)
10	5.43 (0.11)	7.5 (0.62)	8.74 (1.4)	11.9 (1.48)	11.1 (0.36)	15.52 (1.46)
10A	19.96 (0.59)	21.11 (2.03)	23.7 (0.2)	121.1 (17.99)	167.7 (29.5)	287.0 (39.2)
11	5.68 (0.09)	8 (1.2)	7.58 (0.58)	42.9 (1.17)	40.2 (3.2)	30.6 (0.8)
11A	20.47 (0.59)	18.24 (0.19)	19.42 (0.49)	168.8 (20.64)	162.222 (6.2)	161.1 (11.86)
12L	6.37 (0.23)	6.90 (0.55)	7.6 (0.34)	25.2 (1.86)	24.1 (1.1)	20.5 (0.84)
12A	20.45 (0.63)	22.56 (0.60)	23.35 (1.03)	114.9 (18.5)	147.2 (19.63)	130.7 (41.13)
13	8.8 (0.11)	7.38 (0.16)	7.59 (0.33)	44.8 (1.75)	38.92 (1.83)	34.99 (2.44)

Table 5.3(b) Cross tension strength and energy absorption comparison

Joint ID	Static strength (KN) Mean(standard deviation)	4.47 m/s (10 mph) Strength (KN) Mean(standard deviation)	8.94 m/s (20 mph) Strength (KN) Mean(standard deviation)	Static energy absorption (mm-KN) Mean(standard deviation)	4.47 m/s (10 mph) Energy absorption (mm-KN) Mean(standard deviation)	8.94 m/s (20 mph) Energy absorption (mm-KN) Mean(standard deviation)
7	5.1 (0.32)	5.115 (0.05)	5.33 (0.2)	46 (3.8)	50.8 (9.05)	41.85 (2.33)
8	2.23 (0.057)	3.22 (0.12)	3.315 (0.08)	12.26 (0.59)	17.15 (0.89)	16 (1.19)
9	4.95 (0.11)	6.1 (0.12)	6.02 (0.21)	44.9 (2.88)	91.0 (1.35)	70.4 (6.12)
10	2.9 (0.19)	3.23 (0.074)	3.28 (0.17)	16 (2.8)	13.87 (1.2)	13.25 (0.18)
10A	5.73 (0.48)	3.62 (0.20)	3.66 (0.25)	48.8 (5.04)	38.56 (3.11)	25.6 (3.15)
11	4.92 (0.12)	4.89 (0.10)	4.9 (0.11)	54.94 (2.85)	77.10 (2.6)	56.9 (5.9)
11A	7.01 (0.50)	3.68 (0.06)	3.72 (0.13)	80.24 (7.51)	58.26 (1.4)	42.03 (1.9)
12L	5.18 (0.13)	5.53 (0.23)	5.78 (0.08)	51.84 (4.4)	66.29 (6.2)	51.8 (5.5)
12A	6 (0.51)	5.26 (0.12)	5.45 (0.24)	59.8 (5.1)	61.64 (2.3)	43.5 (3.99)
13	4.14 (0.08)	3.35 (0.15)	3.42 (0.06)	32.4 (1.93)	34.17 (2.13)	22.5 (2.21)

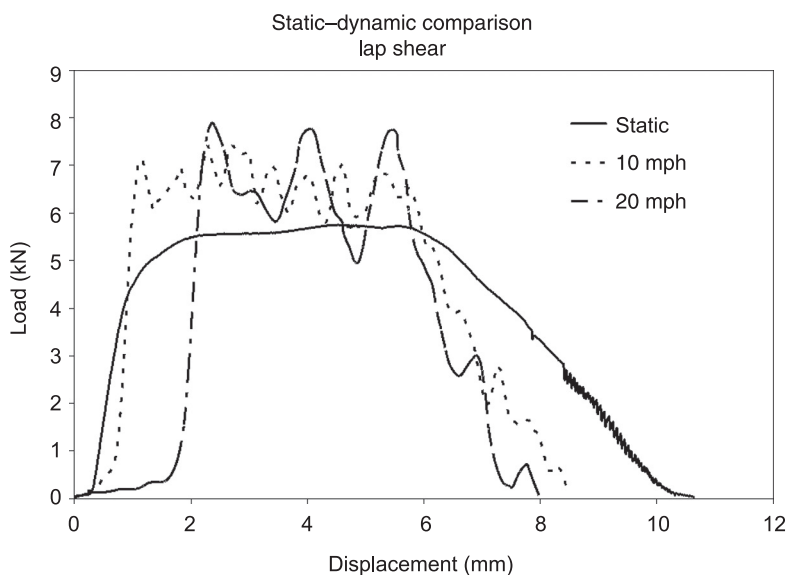
Table 5.3(c) Coach peel strength and energy absorption comparison

Joint ID	Static strength (KN) Mean(standard deviation)	4.47 m/s (10 mph) Strength (KN) Mean(standard deviation)	8.94 m/s (20 mph) Strength (KN) Mean(standard deviation)	Static energy absorption (mm-KN) Mean(standard deviation)	4.47 m/s (10 mph) Energy absorption (mm-KN) Mean(standard deviation)	8.94m/s (20 mph) Energy absorption (mm-KN) Mean(standard deviation)
7	1.96 (0.046)	2.44 (0.233)	2.46 (0.14)	36 (1.4)	35.585 (8.6)	26.99 (0.78)
8	0.81 (0.055)	1.12 (0.04)	1.11 (0.04)	9.4 (1.3)	8.63 (0.38)	8.2 (0.33)
9	2.2 (0.28)	2.75 (0.44)	2.54 (0.01)	33.2 (3.07)	46.97 (3.44)	27.86 (0.03)
10	1.38 (0.19)	1.7 (0.12)	1.69 (0.22)	12.4 (3.5)	9.535 (0.35)	8.3 (1.85)
10A	1.67 (0.25)	2.45 (0.26)	2.27 (0.07)	18 (5.24)	28.97 (10.0)	15.34 (0.47)
11	2.19 (0.31)	2.6 (0.29)	2.4 (0.44)	29 (3.6)	35.6 (3.4)	22.6 (4.4)
11A	2.35 (0.39)	3.19 (0.08)	3.14 (0.44)	31.42 (1.2)	30.395 (0.85)	20.3 (1.69)
12L	2.04 (0.084)	2.25 (0.04)	2.13 (0.065)	25.7 (1.4)	27.45 (1.00)	18.2 (0.74)
12A	1.95 (0.047)	2.76 (0.62)	2.5175 (0.10)	23.6 (0.93)	30.12 (1.68)	21.1 (0.75)
13	2.23 (0.13)	1.73 (0.04)	1.66 (0.05)	21.7 (1.4)	16.55 (1.35)	9.3 (0.67)

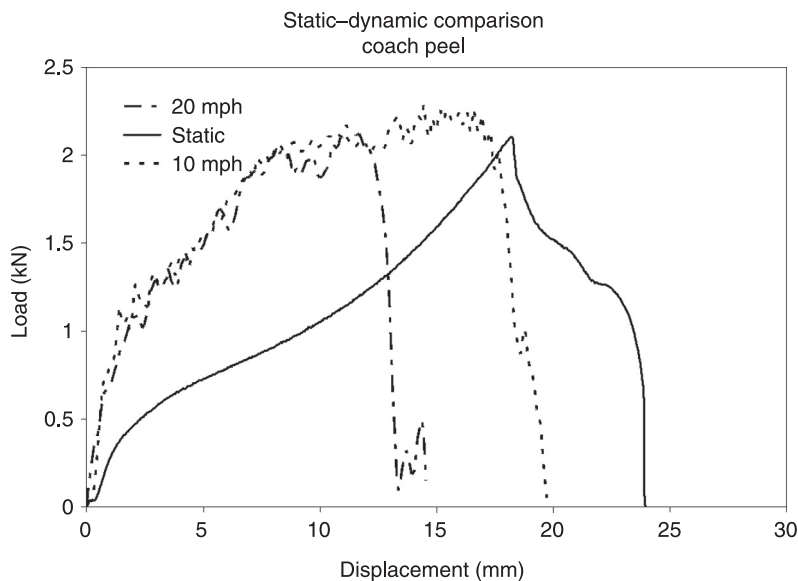
Note that no data filtering was performed on the dynamic load vs. displacement curves, and peak load is used as joint strength in this study. This is based on the ‘clean’, low-ringing quality of most dynamic data as shown in Figs 5.3, 5.5 and 5.6. It should be mentioned, though, that slightly higher magnitude of ringing was observed for some dynamic lap shear samples under 8.94 m/s (20 mph) impact. This is due to the shorter response time of these samples (~ 0.5 msec) compared with those for the cross tension and coach peel samples (~ 1 – 2 msec) under dynamic loading. Since the load train has a ringing frequency at around 10 kHz (limitation of the test frame used), more ringing induced oscillations were recorded for the lap shear samples, particularly under the higher impact velocity of 8.94 m/s (20 mph). For these samples, the oscillation magnitudes are within 15% of the peak loads.

Under dynamic loading, the strengths of most joint populations are higher than their static counterparts, the only exceptions being the populations with adhesive, i.e. 10 A, 11 A and 12 A under cross tension loading, and ID 13 under all three loading conditions. Reasons for some of these inconsistencies will be addressed below.

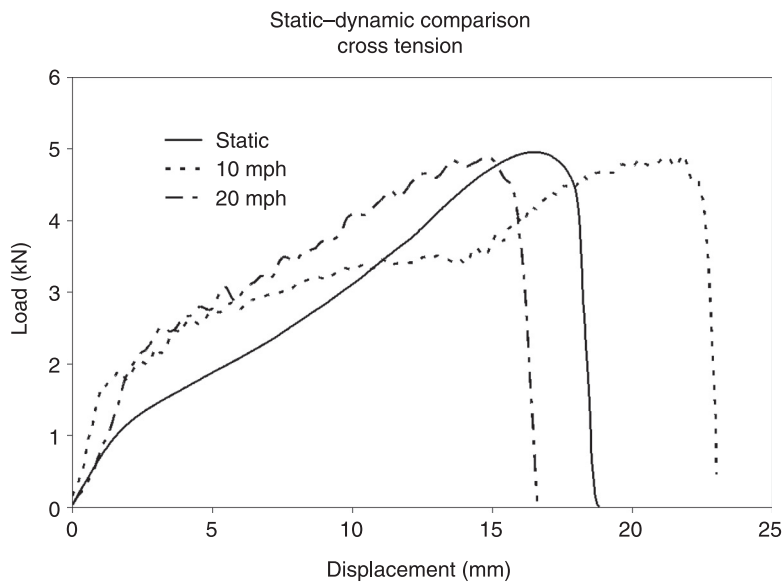
Moreover, the strength increase from quasi-static to 4.47 m/s (10 mph) is much more significant than the strength increase from 4.47 m/s (10 mph) to 8.94 m/s (20 mph). This is particularly true for the populations with steel as top or bottom material, i.e. ID 9, ID 10 and ID 11, and it can be attributed to the higher strain rate sensitivity of steel than AA5182-O. For example, the typical load versus displacement curves for ID 11 (HSLA350/5182) are shown in Figs 5.4–5.6 for lap



5.4 Lap shear load versus displacement curves for ID 11 under three testing velocities.



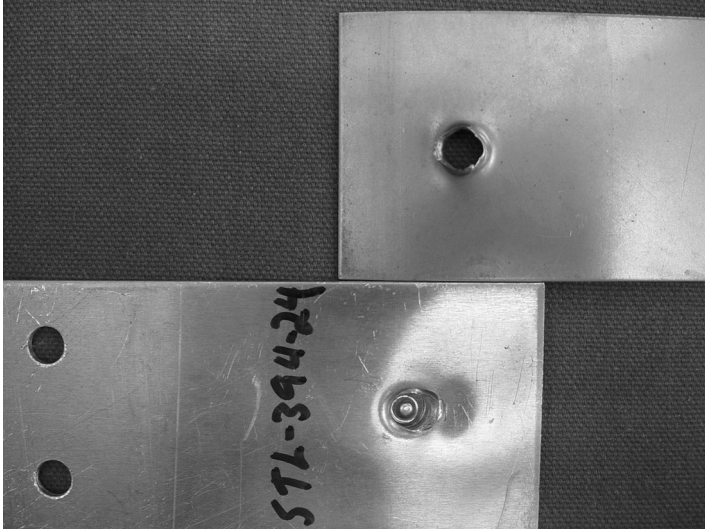
5.5 Coach peel load versus displacement curves for ID 11 under three testing velocities.



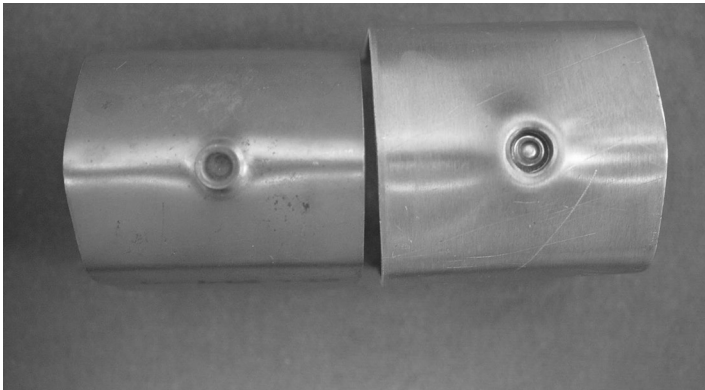
5.6 Cross tension load versus displacement curves for ID 11 under three testing velocities.

Sunday, February 02, 2014 3:06:34 AM

shear, coach peel and cross tension loading conditions respectively. Under lap shear loading, the riveted coupons' failure mode is consistently complete rivet head pull-out; see Fig. 5.7. Under cross tension loading, tail pull-out was consistently observed in which the flared portion of the steel rivet tail pulled out from the clinched portion of the tail side aluminum material; see Fig. 5.8. The consistency of the lap shear and cross tension results can also be observed from the standard deviations tabulated in Tables 5.3 (a) and (b). Since the strength of



5.7 Failure mode for ID 11 lap shear sample under 8.94 m/s (20 mph) impact loading.



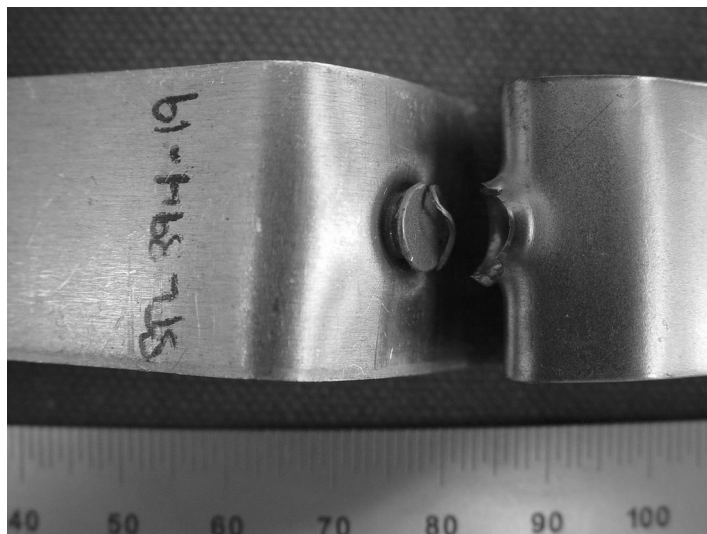
5.8 Failure mode for ID 11 coach peel sample under 8.94 m/s (20 mph) impact loading.

tail side aluminum alloy does not exhibit strong rate dependency, the measured joint strength does not vary significantly from static to dynamic tests for the cases with tail pull out modes; see Fig. 5.6. Under lap shear dynamic tests, however, the rivet head also partially pulled out from the head side of the HSLA 350 material. The observed dynamic rivet strength is slightly higher than the static one because of the strain rate sensitivity of the head side steel material.

Under 8.94 m/s (20 mph) coach peel loading, the majority of the samples failed in rivet head pull-out (see Fig. 5.9) and one failed in rivet tail pull-out mode. The sample failed in tail pull-out had a much higher displacement to failure, leading to the high standard deviation of energy absorption for ID11 under coach peel.

In addition to the influence on joint strength, higher loading rates also influence the deformation modes of the joint samples, therefore rendering different energy absorption levels. Figures 5.4 and 5.6 show that for joint ID 11, samples' displacements to failure decrease with increasing loading rates. This conclusion is generally true for most samples under lap shear and coach peel loading, and it is also true for the comparisons of 8.94 m/s (20 mph) test with 4.47 m/s (10 mph) test under cross tension loading. Similar reduction of failure displacement with increasing loading rate has been reported in Fig. 6 of Lin *et al.*² for opening mode loading.

The static cross tension samples experience more membrane stiffening effects than the dynamic samples due to the differences in fixture designs (see Figs 5.1(b) and 5.2(b)). The dynamic samples tend to deform slightly at the bent corners prior



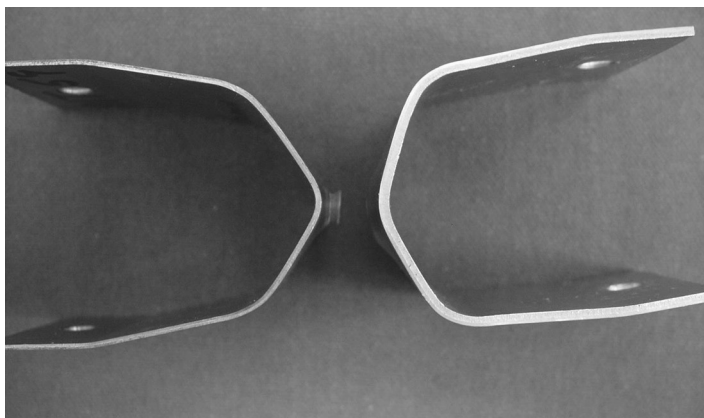
5.9 Failure mode for ID 11 cross tension sample under 8.94 m/s (20 mph) impact loading.

to final joint failure (see Fig. 5.10) therefore yielding slightly higher displacement compared with the static one. Even so, the observations on loading rate effect still hold true for the 4.47 m/s (10 mph) and 8.94 m/s (20 mph) data comparison in Fig. 5.6.

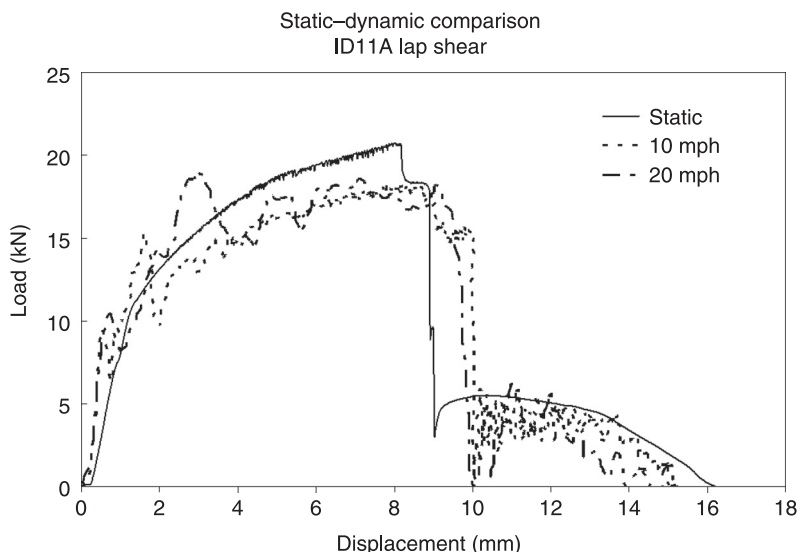
The energy absorption levels under different loading rates depend on the area under the load versus displacement curves. For joint ID 11 under lap shear, even though higher loading rates offer higher joint strength, higher displacement to failure for the lower loading rates still offers higher levels of total energy absorption. For most of the populations studied, 8.94 m/s (20 mph) tests provide lower energy absorption than 4.47 m/s (10 mph) tests since the decreases in displacements are much more significant than the increases in joint strength.

The apparent increase of joint samples' 'brittleness' with increasing loading rate is not generally observed in base metal behaviors under intermediate strain rate tests for metallic materials.¹³ Here, increased brittleness of the joint samples can be attributed to the inertia effects of the joint sample geometry: slower tests allow more time for the joint samples to deform before final failure occurs at the joint region. The ductility of the joint samples, and therefore their corresponding energy absorption levels under different loading rates, are primarily determined by their global material behaviors rather than the joints themselves. Therefore, caution should be exercised when utilizing results such as those listed in Table 5.3 in deriving any displacement, strain or energy-based failure criteria for vehicle crash simulations.

For joint samples with adhesives, two distinct load peaks were obtained during static and dynamic tests; see Fig. 5.11 for example. The first peak is the strength of the adhesive and the second peak is the strength of the mechanical fastener. Comparison of Figs 5.3 and 5.11 reveals that the secondary peak of the SPR strength in ID 11A is very similar to the SPR strength without the adhesive layer



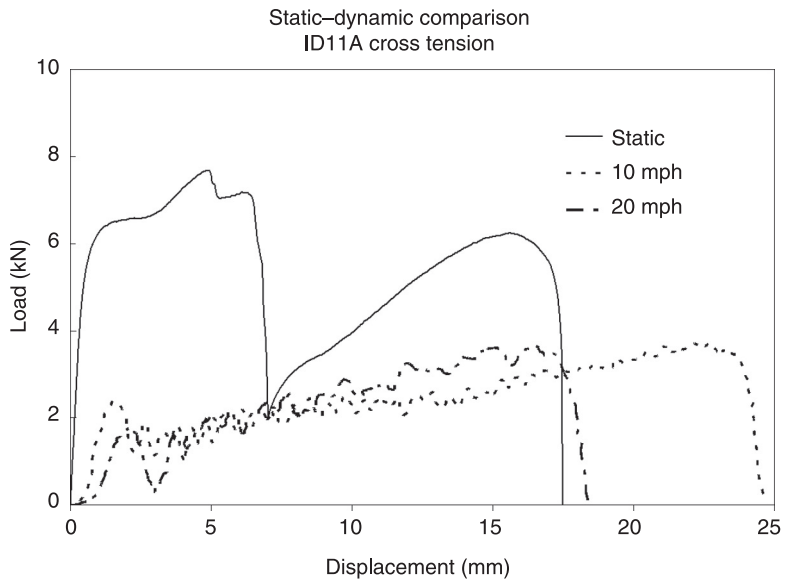
5.10 Sheet deformation for ID 11 cross tension sample under 8.94 m/s (20 mph) impact loading



5.11 Lap shear load versus displacement curves for ID 11A under three testing velocities.

in ID 11; this is particularly true under static loading. This observation suggests the de-coupling nature of the adhesively-bonded rivet samples. Moreover, the initial peak load and energy absorption offered by the adhesive layer are much higher than those offered by SPR only under lap shear loading. This is true for both static and dynamic loading conditions. These results indicate that for joints primarily designed to carry shear loading, the existence of SPR is not critical in its strength and energy absorption capacity. In addition, the data in Table 5.3 suggest that strain rate sensitivity for the adhesive layer under lap shear impact test is less significant than those under cross tension and coach peel test. However, it is also important to point out the high standard deviations on energy absorption for the lap shear samples with adhesive. This is due to the large variation of displacement to failure for the adhesively-bonded rivet samples under lap shear loading, and it is true for both static and dynamic loading. These results suggest the need for quality control of adhesive bonds to ensure their consistent energy absorption capability.

It should also be mentioned that the cross tension strength comparison for ID 11A indicates a huge drop of dynamic adhesive strength compared with the static one; see Fig. 5.12. This is due to the coupon preparation process for the dynamic samples. The U-shape dynamic cross tension samples were made by bending up the free flanges of the pre-made, flat adhesively-bonded rivet samples. Inadvertently, the bending operation caused some initial de-bonding at the periphery of the adhesive layers. These results therefore indicate the high sensitivity of bond strength to its edge conditions.



5.12 Cross tension load versus displacement curves for ID 11A under three testing velocities.

5.5 Conclusions

In this chapter, the dynamic impact strength of various SPR joints for similar and dissimilar metals is discussed. First, current dynamic testing practices in different strain rate regimes are discussed and the generic issues with dynamic test such as inertia effect, wave propagation effect and load cell ringing effects are discussed. Ways to mitigate and minimize these effects are discussed. Then, the testing procedures for carrying out the 4.47 m/s (10 mph) and 8.94 m/s (20 mph) dynamic impact tests are presented. Using the described testing procedures, ‘clean’, un-filtered dynamic load versus displacement curves were obtained for the sample populations. The comparison between static and dynamic strength for the 13 joint populations are then presented in terms of peak joint strength and energy absorption levels. Major findings regarding the dynamic joint performance are as follows.

1. In general, joint strength increases with increasing loading rate. The percentage of increase from quasi-static to 4.47 m/s (10 mph) is much higher than that from 4.47 m/s (10 mph) to 8.94 m/s (20 mph).
2. The joint samples’ displacements to failure decrease with increasing loading rates. This is true for lap shear and cross tension loadings where the same sample designs were used for static and dynamic tests. For cross tension tests, lower displacement to failure was observed for the quasi-static samples

because of the membrane stiffening effects caused by the differences in sample design.

3. Displacement, strain or energy-based joint failure criteria derived with dynamic test data similar to the ones obtained in this study should be used with caution in vehicle safety simulations unless total joint coupon deformation is considered.
4. Application of structural adhesive dramatically increases the strength and energy absorption levels of riveted joints under lap shear loading. Under cross tension and coach peel loading, the percentages of strength and energy increase are modest. However, more bond quality control is needed to ensure consistent bond layer energy absorption.

5.6 References

1. Lin S H, Pan J, Wu S R, Tyan T and Wung P (2002), 'Failure loads of spot welds under combined opening and shear static loading conditions', *International Journal of Solids and Structures*, 39, 19–39.
2. Lin S H, Pan J, Wu S and Tyan T (2004), 'Failure loads of spot welds specimens under impact opening and shear loading conditions', *Experimental Mechanics*, 44(2), 147–157.
3. Chao Y J (2003), 'Ultimate strength and failure mechanism of resistance spot weld subjected to tensile, shear or combined tensile/shear loads', *Journal of Engineering Materials and Technology*, 125, 125–132.
4. Lin S H, Pan J, Tyan T and Prasad P (2003), 'A general failure criterion for spot welds under combined loading conditions', *International Journal of Solids and Structures*, 40, 5539–5564.
5. Stephens E V, Sun X, Khaleel M A and Davies R W (2003), *Performance Comparisons through Weibull Analyses of Self-Piercing Rivets and Resistance Spot Welds Joining Dissimilar Metals*, PNNL-14296, Pacific Northwest National Laboratory, Richland, Washington.
6. Vela E and Sun X (2002), *Lap Shear Coupon Design Sensitivity Study for Self-Piercing Rivets and Resistance Spot Welds*, PNNL-13943, Pacific Northwest National Laboratory, Richland, Washington.
7. Peterson W and Borchelt J (2000), 'Maximizing cross tension impact properties of spot welds in 1.5 mm low carbon, dual-phase, and martensitic steels', SAE Paper No. 2000-01-2680.
8. *Weld Quality Test Method Manual* (October 1997), Auto/Steel Partnership, Standardized Welding Test Method Task Force.
9. Sun X and Khaleel M A (2005), 'Performance optimization of self-piercing rivets through analytical rivet strength estimation', *Journal of Manufacturing Processes*, 7(1), 83–93.
10. Sun X, Stephens E V and Khaleel M A (2007), 'Fatigue behaviors of self-piercing rivets joining similar and dissimilar sheet metals', *International Journal of Fatigue*, 29, 370–386.
11. Orphal D and Anderson C E (2001), 'Target damage from highly oblique hypervelocity impacts of steel spheres against thin laminated targets', *International Journal of Impact Engineering*, 26, 567–578.

12. *American Society of Metals (ASM) Handbook*, 9th edn, Volume 8, Mechanical Testing, 79–92.
13. Yan B (2003), ‘High strain rate behavior of advanced high strength steels for automotive applications’, *Great Design in Steel Seminar*, American Iron and Steel Institute, 19 February 2003.
14. Moon D P and Campbell J E (1961), *Effects of Moderately High Strain Rates on the Tensile Properties of Metals*, Defense Metals Information Center, Battelle Memorial Institute.
15. American Welding Society (AWS), *Standard Methods for Mechanical Testing of Welds*, ANSI/AWS B4.0-98.
16. American Society of Testing and Materials (ASTM), *Standard Test Methods for Tension Testing of Metallic Materials*, ASTM E8-04.
17. American Society of Testing and Materials (ASTM), *Standard Test Methods for Notched Bar Impact Testing of Metallic Materials*, ASTM E23.
18. American Society of Testing and Materials (ASTM), *Standard Test Method of Sharp-Notch Tension Testing of High-Strength Sheet Materials*, ASTM E338.
19. Hockett J E and N A Lindsay (1971), ‘Cam plastometer data acquisition system’, *Journal of Physics E: Scientific Instruments*, 4, 520–522.
20. Sun X, Stephens E V and Khaleel M A (2004), ‘Effects of fusion zone size on failure modes and static strength of aluminum resistance spot welds’, *Welding Journal*, November, 188-s–195-s.
21. Porcaro R, Hanssen A G, Langseth M and Aalberg A (2006), ‘The behaviour of a self-piercing riveted connection under quasi-static loading conditions’, *International Journal of Solids and Structures*, 43, 5110–5131.
22. Langrand B, Markiewicz E, Deletombe E and Draz P (2000), ‘Identification of nonlinear dynamic behavior and failure for riveted joint assemblies’, *Shock and Vibration*, 7(3), 121–138.
23. *Recommendations for Dynamic Tensile Testing of Sheet Steels* (2005), International Iron and Steel Institute.

Modelling the strength of self-piercing riveted joints

S. FAYOLLE, EDF R&D, France, P.-O. BOUCHARD
and K. MOCELLIN, Centre for Material
Forming (CEMEF), Mines ParisTech, France

DOI: 10.1533/9780857098849.1.79

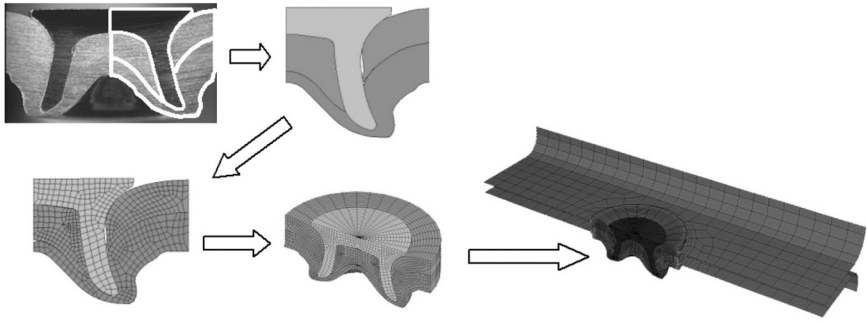
Abstract: Predicting the mechanical strength of self-piercing riveted structures is of prime importance in industry. This chapter describes how numerical simulation can be used to obtain accurate predictive results. First, it is important to account for the mechanical history of the material resulting from the SPR process as input data for the mechanical strength simulation. The use of a coupled damage approach to account for the progressive mechanical degradation of the materials' properties is recommended. The materials' properties and damage parameters have to be carefully identified. Inverse analysis is an efficient methodology to obtain the materials' parameters. Finally, some finite element simulations are presented and validated with respect to mechanical tests. The numerical approach presented here also enables the equivalent elements that can be used at the structure scale to be defined.

Key words: self-piercing riveting, continuum damage mechanics, finite element, fracture modes, equivalent element.

6.1 Introduction

Self-piercing riveting (SPR) is used extensively to join sheets of different types. Numerical modelling of the mechanical strength of SPR joints is extremely important from an industrial point of view in order to improve the design and to lighten the weight of structures joined in this way. Despite the success of this joining technique, improvements in the structural strength of SPR connections are still mainly due to trial and error tests or procedures based on previous experience.

The application of finite element analysis to self-piercing riveting is relatively new. The first simulations dealing with the mechanical strength of SPR connections were proposed in 2002 by Westerberg (Westerberg 2002). These simulations dealt with the dynamic behaviour of riveted connections using Abaqus-explicit. Chengui (Chergui 2004) modelled the fatigue and static behaviour of riveted structures. The main drawback of these studies was that the mechanical history of the materials during the SPR process was not used as input data. Geometries used for simulations were obtained from SPR specimens as shown in Fig. 6.1.



6.1 Geometrical definition of the SPR connection based on an experimental cut.

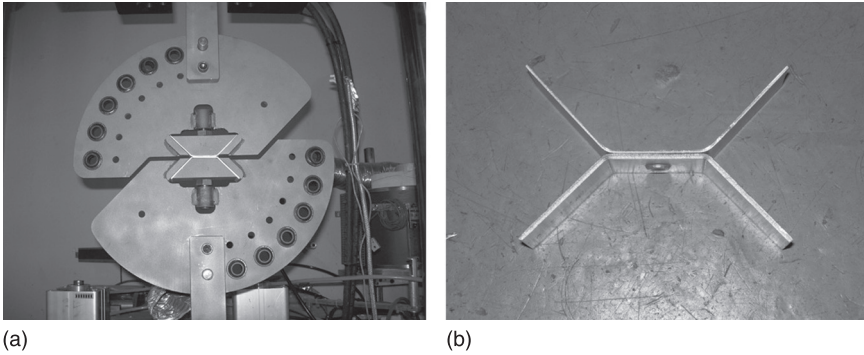
Between 2005 and 2008, numerical simulations of the SPR mechanical strength that accounted for the materials' mechanical history were published by many authors (Bouchard and Lasne 2004; Gårdstam 2006; Porcaro *et al.* 2006; Bouchard *et al.* 2008; Fayolle 2008). These studies show that it is essential to account for this mechanical history in order to obtain predictive computations of quasi-static mechanical tests on SPR connections. Plastic strain, residual stresses and damage are the main parameters influencing SPR mechanical strength. They have to be computed during an SPR process simulation and need to be used as inputs for SPR strength simulations.

In this chapter the methodology to perform accurate computations of SPR mechanical tests is presented. First a specific mechanical test device that can deal with complex quasi-static loadings on an SPR specimen is presented. This test can be used to load the connection from pure shearing to pure tension. Special attention is then paid to identifying the material behaviour. The study of the mechanical strength of an SPR connection means that both sheets and rivets can undergo high plastic deformation as well as damage growth and fracture. Finally, numerical simulations of the mechanical strength of SPR connections are presented. The final results are compared and validated with experimental data.

6.2 Mechanical strength of a self-piercing riveting (SPR) structure

6.2.1 The ARCAN test device

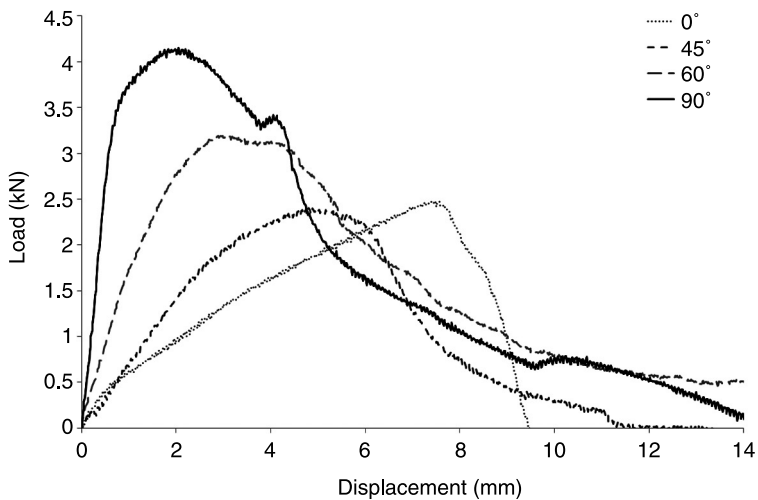
Depending on the application, SPR connections can be subjected to quasi-static, dynamic or cyclic loadings. We focus here on quasi-static loading. The study of the quasi-static mechanical strength of an SPR connection requires the use of a mechanical test that enables the loading of the connection from pure shearing to pure tension. The ARCAN test device (Fig. 6.2(a)) is particularly suitable for



6.2 (a) ARCAN test and (b) cross-shaped specimen.

mixing and controlling tensile and shear loadings on a riveted cross-shaped specimen. This mechanical device, which was originally designed for fibre-composite materials (Arcan *et al.* 1978; Banks-Sills *et al.* 1984), was then used for many other applications, such as mixed mode fracture mechanics (Sutton *et al.* 2000) or mechanical testing of joined materials (Langrand and Combescure 2004). The use of a cross-shaped specimen (Fig. 6.2(b)) facilitates the positioning and loading of the SPR connection in the ARCAN test.

Figure 6.3 shows the classical behaviour of an SPR connection submitted to pure shearing (0°), pure tension (90°) or mixed mode loading (45° and 60°). The mechanical strength of such a joined connection is much better for pure shear than



6.3 Load-displacement curves obtained from pure shearing (0°), pure tension (90°) and mixed loading (45° , 60°) mechanical tests.

for pure tension. This is the reason why such mechanical connections are used in shear-loaded areas in the automotive and aeronautic industry.

6.2.2 Equivalent element

From experimental curves, it is possible to define a simple failure criterion of the joint. Indeed, the angle θ between the axis of revolution of the rivet and the line of load application of the cross-piece defines the ratio between the normal force N and the shearing force S (Fig. 6.4). The total effort applied during the mechanical test (noted F) is split into two terms:

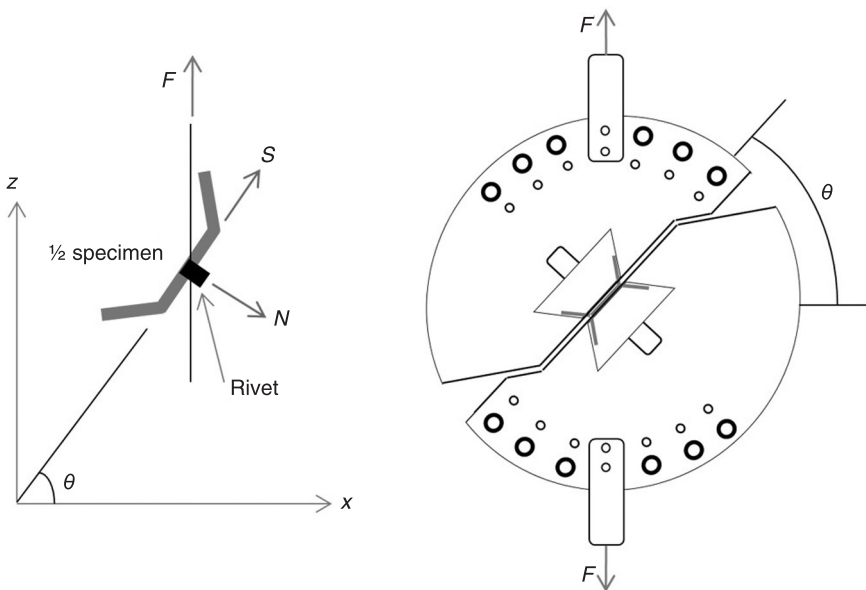
$$N(\theta) = F \cos(\theta) \quad [6.1]$$

$$S(\theta) = F \sin(\theta) \quad [6.2]$$

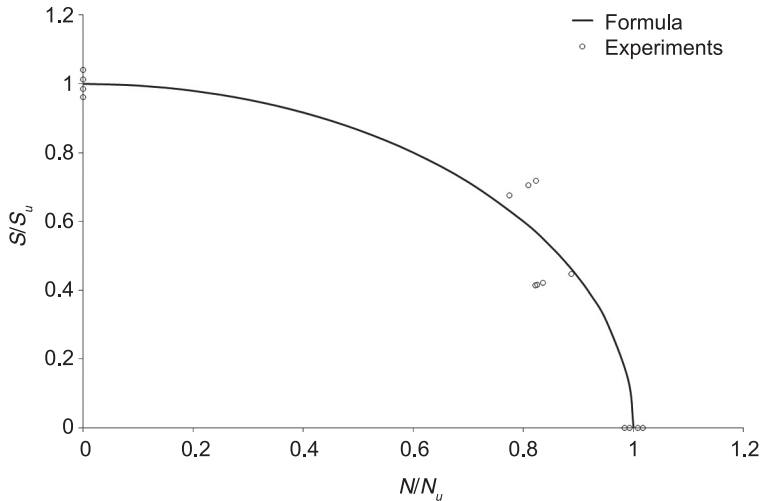
The expression of the failure criterion of the connection can be expressed by:

$$\left(\frac{N}{N_u} \right)^a + \left(\frac{S}{S_u} \right)^b = 1 \quad [6.3]$$

The shearing and tensile forces are respectively normalized with respect to the maximum normal force N_u (measured at 0°) and the maximum shearing force S_u (measured at 90°). Such a failure criterion is extremely important within the



6.4 Decomposition of forces on the joint in a normal and a tangential component.



6.5 Experimental failure criterion of a SPR joint.

framework of the definition of an equivalent element that can be used at a structure scale (Langrand *et al.* 2003). Figure 6.5 shows an example of a failure criterion obtained for a riveted joint.

6.2.3 Failure modes

Depending on the loading conditions, different failure modes are obtained. Three different failure modes were obtained for pure shear loading:

- Failure mode s1: rotation of the rivet and top sheet failure. The rivet rotates, generating a high level of deformations and damage in the top sheet. Finally, the top sheet breaks and leaves a part of its material wedged between the rivet and the lower sheet (Fig. 6.6).
- Failure mode s2: rotation and pull-out of the rivet from the bottom sheet. The rivet starts to rotate in the lower sheet. The rivet generates high deformations and damage in the top sheet. However, the rivet pulls out of the bottom sheet before the complete rupture of the top sheet (Fig. 6.7).
- Failure mode s3: shearing of the lower sheet. This mode of rupture appears when the stiffness of the top sheet is higher than that of the lower sheet. The rivet remains stuck in the top sheet and shearing appears in the bottom sheet, generating a rupture of the joint (Fig. 6.8).

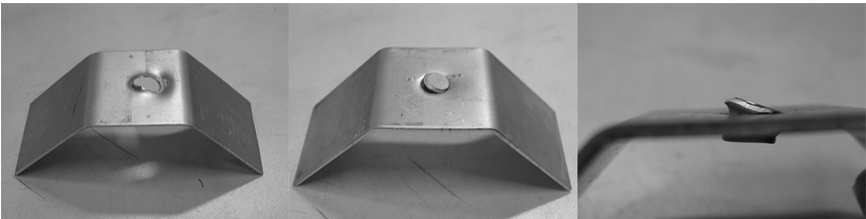
Under tensile loading, two main failure modes can be observed:

- Failure mode t1: rupture of the top sheet. The hole in the top sheet generated during the riveting process expands under the head of the rivet when the load is

applied. Cracks appear following the direction of loading. Once the hole is sufficiently wide the top sheet is no longer connected to the bottom one (Fig. 6.9).

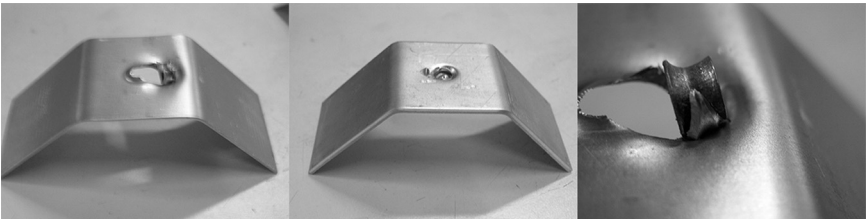
- Failure mode t2: pull-out of the rivet from the bottom sheet. This failure mode appears when the top sheet is more rigid than the lower sheet or when the rivet has not expanded enough during its set up (the thickness of the sheets to be joined is more important than the length of the rivet). The rivet is then pulled out by the top sheet from the bottom sheet (Fig. 6.10).

The failure modes of the riveted samples under mixed loading conditions are a combination of the previous failure modes. Figures 6.11 and 6.12 show some examples.



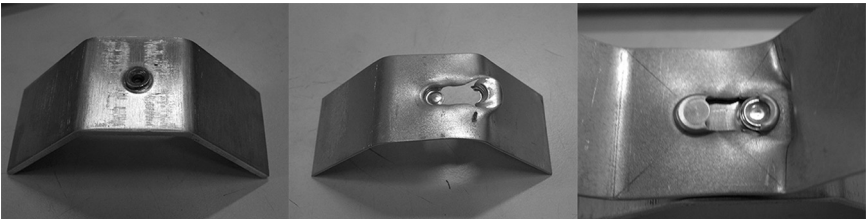
Top sheet Lower sheet Failure zone

6.6 Failure mode s1 for shear loading.



Top sheet Lower sheet Failure zone

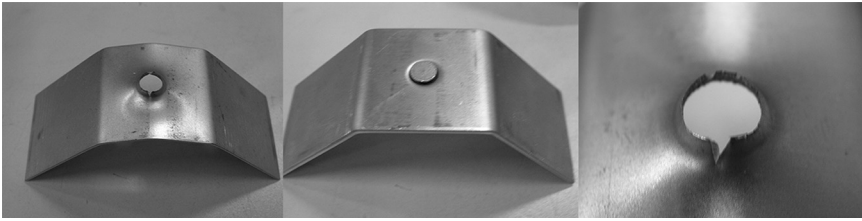
6.7 Failure mode s2 for shear loading.



Top sheet Lower sheet Failure zone

6.8 Failure mode s3 for shear loading.

Sunday, February 02, 2014 3:06:45 AM



Top sheet

Lower sheet

Failure zone

6.9 Failure mode t1 for tensile loading.

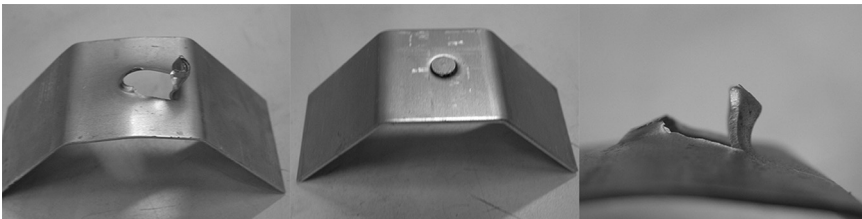


Top sheet

Lower sheet

Failure zone

6.10 Failure mode t2 for tensile loading.



Top sheet

Lower sheet

Failure zone

6.11 Combination of failure modes s1 and t1 for mixed loading conditions.



Top sheet

Lower sheet

Failure zone

6.12 Combination of failure modes s3 and t2 for mixed loading conditions.

In some cases, in particular for cyclic loadings, the rivet can break, inducing a fracture of the connection (Sun *et al.* 2007).

6.3 Mechanical behaviour and damage analysis

The accuracy of the numerical simulation relies on the accuracy of the mechanical behaviour of the sheets and the rivet. Usually, materials used for such applications (steel or aluminium sheets, rivets) present elastic–plastic behaviour. The strain rate has a minor influence on the mechanical behaviour and can be neglected. In order to model the progressive failure of the SPR connection, a continuum damage mechanics approach can be used. An improved Lemaitre damage model is used here to account for the progressive damage growth during the simulation. Damage is coupled with the elastic–plastic behaviour law so that the progressive softening of the mechanical behaviour is taken into account. Finally, the identification of the materials' parameters is also an important issue. An inverse analysis methodology is presented here to identify these mechanical and damage parameters.

6.3.1 Elastic–plastic behaviour

Materials joined using self-piercing riveting are usually steels (sheets and rivets) and aluminium alloys. Under limited plastic deformation, these materials exhibit an elastic–plastic behaviour that can be represented using the set of equations presented below.

The strain rate tensor is split into an elastic part $\dot{\epsilon}^e$ and a plastic part $\dot{\epsilon}^p$:

$$\dot{\epsilon} = \dot{\epsilon}^e + \dot{\epsilon}^p = \frac{1}{2} \left(\vec{\nabla} \vec{v} + (\vec{\nabla} \vec{v})' \right) \quad [6.4]$$

where \vec{v} is the velocity vector.

The elastic behaviour is given by Hooke's law:

$$\sigma = 2\mu\epsilon^e + \lambda \operatorname{tr}(\epsilon^e) \mathbf{I} \quad [6.5]$$

where μ and λ are the Lamé constants and \mathbf{I} is the unit second order tensor.

The yield function is given by the von Mises criterion:

$$f(\sigma; r) = J_2(\sigma) - \sigma_0(r) \leq 0 \quad [6.6]$$

where $J_2(\sigma)$ is the second deviatoric stress invariant, $J_2(\sigma) = \sqrt{3s:s}/2$ in which s is the deviatoric stress tensor and $\sigma_0(r)$ is the isotropic hardening law given by the Swift law:

$$\sigma_0(r) = K(r + r_0)^n \quad [6.7]$$

where K is the consistency of the material, n is the isotropic hardening exponent, r the hardening variable related to the equivalent plastic strain and r_0 is a regularization parameter, which can also be used to define the initial yield stress.

The plastic strain rate is given by the associated flow rule:

$$\dot{\epsilon}^p = \dot{\lambda} \frac{\partial f}{\partial \sigma} = \dot{\lambda} \frac{3}{2} \frac{\mathbf{s}}{J_2(\sigma)} \quad [6.8]$$

where $\dot{\lambda}$ is the plastic multiplier. The loading/unloading criterion is defined through the usual Kuhn–Tucker conditions:

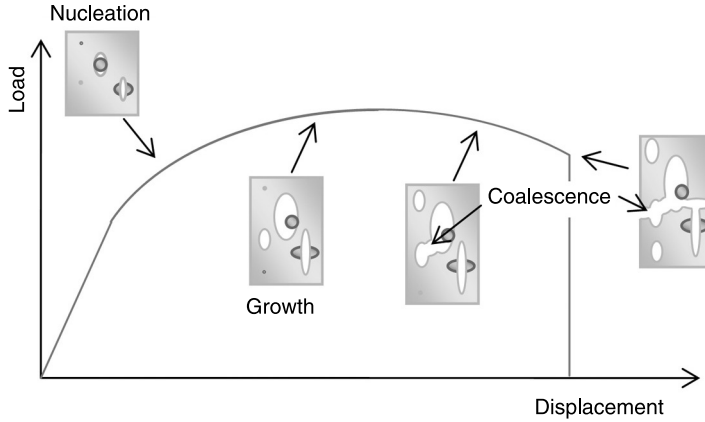
$$\dot{\lambda} \geq 0, f \leq 0, \dot{\lambda} f = 0 \quad [6.9]$$

Remark: Isotropic behaviour with a linear hardening law is usually considered for reasons of simplicity. However, as a result of the sheet manufacturing processes (rolling) and the anisotropic behaviour, the use of a kinematic hardening law would be more appropriate.

6.3.2 Damage model

When large plastic deformation occurs, it is necessary to use a damage approach to model the progressive mechanical degradation of the material properties. Several damage models have been proposed in the literature. Some of these models compute the damage parameter as the integral of a function over the plastic strain history. This function depends on mechanical parameters such as the maximum principal stress or the stress triaxiality ratio (Cockcroft and Latham 1968; McClintock 1968; Rice and Tracey 1969; Oyane *et al.* 1980). As there is no coupling between the damage variable and the behaviour law, the damage analysis is limited to simple mechanical loadings, and the progressive softening of the materials cannot be modelled. More recently, new ductile failure criteria were introduced by Wierzbicki and co-workers (Wierzbicki *et al.* 2005; Bai and Wierzbicki 2008). These criteria consist in defining a plastic strain at fracture, which is a function of the stress state. This stress state is defined using both the stress triaxiality ratio and the Lode angle parameter.

Coupled damage models are more suitable for complex loadings since damage and mechanical properties are directly coupled, so the material fracture process is modelled by a progressive decrease of the global response of the structure. The damage model of Tvergaard and Needleman (Tvergaard and Needleman 1984), based on the initial model introduced by Gurson (Gurson 1977), accounts for micromechanical damage mechanisms such as nucleation, growth and coalescence of micro-voids (Fig. 6.13). The continuum damage approach (Kachanov 1958; Chaboche 1989; Lemaitre 1996) defines the notion of effective stress, which represents the actual stress transmitted by the bulk material between the microdefects. Unlike uncoupled approaches, coupled damage models are more difficult to implement in numerical software. However, these models are closer to the physical damage phenomenon and give a better representation of the progressive damage evolution within the material progressively leading to fracture.



6.13 Load–displacement curve and microstructural damage mechanisms.

In order to deal with damage, a coupled Lemaitre damage model is used here (Lemaitre 1996; Lemaitre and Desmorat 2005). The damage variable, based on the strain equivalence hypothesis, represents the average material degradation. Damage and hardening are assumed to be isotropic, with a single mechanism governed by the increase in the accumulated plastic strain. The Lemaitre model is based on the concept of the effective stress tensor $\tilde{\sigma}$ given by:

$$\tilde{\sigma} = \frac{\sigma}{1-D} \quad [6.10]$$

in which D is the internal isotropic damage variable ($D=0$ in the undamaged material and $D=1$ corresponds to fracture). The constitutive relations of the damaged material are derived from those of the undamaged material. The stress, yield function and plastic strain are then expressed as:

$$\sigma = (1-D) \left(2\mu \varepsilon^e + \lambda \operatorname{tr}(\varepsilon^e) \mathbf{I} \right) \quad [6.11]$$

$$f(\sigma, r, D) = \frac{J_2(\sigma)}{1-D} - \sigma_0(r) \leq 0 \quad [6.12]$$

$$\dot{\varepsilon}^p = \dot{\lambda} \frac{\partial f}{\partial \sigma} = \frac{\dot{\lambda}}{1-D} \frac{3}{2} \frac{s}{J_2(\sigma)} \quad [6.13]$$

The damage evolution law is given by:

$$\dot{D} = \frac{\dot{\lambda}}{1-D} \left(\frac{Y}{S_0} \right)^b \quad [6.14]$$

where S_0 , b are materials damage parameters and Y is the damage strain energy release rate given by:

$$Y = \frac{J_2(\sigma)}{2E(1-D)^2} \left(\frac{2}{3}(1+\nu) + 3(1-2\nu) \left(-\frac{p}{J_2(\sigma)} \right)^2 \right) \quad [6.15]$$

where p is the hydrostatic pressure, $p = -tr(\sigma/3)$, E is Young's modulus and ν is the Poisson ratio. The ratio $-p/J_2(\sigma)$ is the triaxiality of the stress tensor. The triaxiality characterizes the local state of stress (tensile, shearing or compressive state) and is one of the most important parameters in the study of damage growth. Two other parameters are used here: $\bar{\epsilon}_D$, which is the equivalent plastic strain at which damage initiation takes place, and D_c , which is the critical damage value leading to fracture.

The model presented above is able to predict damage growth with reasonable accuracy. However, one important aspect of damage growth is not considered in Eqs 6.14 and 6.15. In fact, there is no distinction between damage growth for tensile and compressive states. Such a distinction is necessary since voids and micro-cracks that initiate during the tensile stages tend to partially close during the compressive stages. This partial closure induces an increase in the local stiffness of the material. Furthermore, the damage rate under compressive mechanical states is also lower than for tensile states.

This phenomenon is called the crack closure effect. One way to account for crack closure effects is to split the stress tensor into a tensile part and a compressive part. Moreover, a regularization parameter h is used to minimize damage evolution for compressive mechanical states. For more details, the reader is referred to previous work by Ladevèze (Ladevèze 1983; Ladevèze and Lemaitre 1984). Some extensions of this model that are dedicated to manufacturing processes can also be found in (Bouchard *et al.* 2011).

6.3.3 Parameters identification

The identification of the behaviour and damage parameters is a critical stage in obtaining predictive results. For the modelling of the strength of SPR, elastic, hardening and damage parameters have to be identified. A first approach consists in identifying these parameters with classical mechanical tests. The elastic and plastic parameters can be obtained through a classical uniaxial tensile test. However, damage parameters are harder to identify. A wide range of direct and indirect damage measurement techniques can be found in (Lemaitre and Desmorat 2005).

Another well-known method consists of identifying rheological parameters using an inverse analysis technique. The identification procedure is based on the comparison between experimental and numerical data (or observables) and a minimization algorithm. The observables used can all be data recorded during a mechanical test such as a load–displacement curve, strain field, etc. The cost

function is defined as the difference between the experimental and the numerical observables. The minimization algorithm modifies the materials' numerical parameters in order to minimize the cost function.

Two common classes of optimization algorithms can be found in the literature:

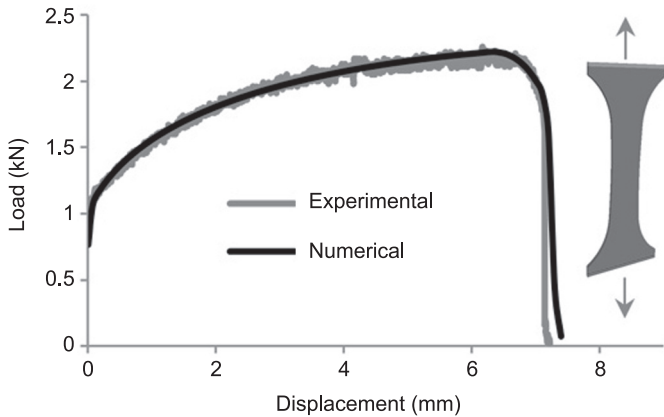
1. gradient-based methods in which the gradient of the cost function is used to minimize the cost function and define a new set of material parameters;
2. genetic or evolution strategy algorithms: these algorithms are based on the creation of a population of individuals that correspond to the set of parameters that have to be identified. The evolution of this population towards the final result is based on the natural evolution phenomenon, through selection, recombination and mutation rules. An application of such algorithms to identify materials parameters can be found in (Peyrot *et al.* 2009).

In (Fayolle *et al.* 2007), an automatic inverse analysis procedure enables the identification of materials' parameters based on experimental load–displacement curves. This identification software runs the finite element software automatically, and iteratively modifies the materials' parameters in order to match experimental results. The minimization technique is based on an evolutionary strategy algorithm (Bäck *et al.* 1997).

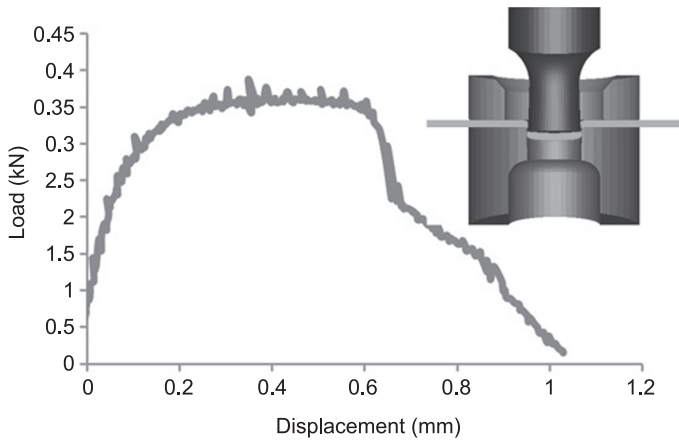
Owing to the large number of unknown parameters, the identification is made in two steps. First the isotropic hardening law is identified on the first part of the load displacement curve, i.e. before softening occurs. Then the damage parameters are determined on the rest of the curve.

The experimental data can be provided using different mechanical tests. For metal sheets, tensile tests on plate specimens are generally used because damage has a direct effect on the tensile load–displacement curve. However, the stress state in the damaged area of a tensile specimen (high positive stress triaxiality ratio) does not really correspond to the stress state of the damaged area that develops during the SPR process. Blanking tests give a closer stress state within the sheet (shearing), but load–displacement curves are more sensitive to the experimental conditions (punch wear, friction, clearance between the punch and the tools). This sensitivity is problematic since inverse analysis is based on these experimental curves. Figure 6.14 shows the load–displacement curves obtained using a tensile test (Fig. 6.14(a)) or an indentation test (Fig. 6.14(b)) for a 5754-O aluminium alloy.

The rivet used here is made of boron high-strength steel. Prediction of the behaviour of the rivet material is trickier. This difficulty is a result of a combination of several factors. First, the rivet has a complex geometry and a simple test, such as the uniaxial tensile test for sheets, is not possible. Moreover, the size of the rivets is very small. Finally, the rivets are manufactured in several cold forging steps that generate internal residual stresses and strains. The manufacturing process may also involve various heat-treatments. For more accuracy, it would therefore be necessary to take into account the thermomechanical history of the rivet-forming process. This would enable one to get a correct initial stress and strain state for the rivet.



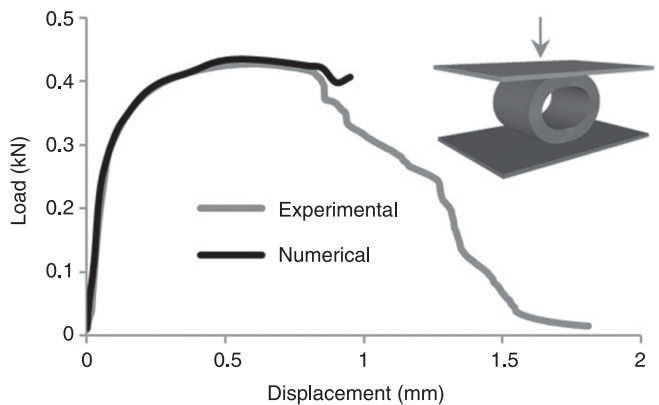
(a)



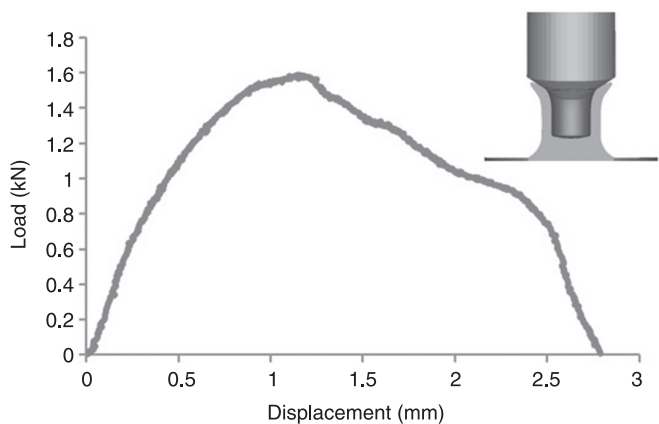
(b)

6.14 Aluminium 5754-O load–displacement curves for materials parameters identification: (a) tensile test, (b) indentation test.

In order to overcome these difficulties, two specific mechanical tests can be used. The first test is a flare test as shown in Fig. 6.15(b). This test has the advantage of reproducing the strain path undergone by the rivet during the SPR process. However, this promising test may lead to non-reproducible results and is hardly usable for inverse analysis. The second test is a compression test of a cylinder cut in the shank of the rivet (Fig. 6.15(a)). This test was proposed by Porcaro and co-workers (Porcaro *et al.* 2006). The main advantage of this test is the simplicity of the experimental procedure and the straightforward numerical simulation. Tables 6.1 and 6.2 summarize the identified parameters of the hardening law and damage model for the materials used here.



(a)



(b)

6.15 Identification of rivets' mechanical properties: (a) compression test, (b) flare test.

Table 6.1 Identified elastic–plastic parameters

	E (GPa)	K (MPa)	n	r_0 (%)
Aluminum alloy	64	477.02	0.327	0.84
Steel sheet	210	650.63	0.302	1.69
Rivet	190	2400	0.197	5.69

Table 6.2 Identified damage parameters

	$\bar{\epsilon}_D$	S_0 (MPa)	b	D_c
Aluminum alloy	0.195	3.9	1	0.44
Steel sheet	0.202	3.1	2	0.6

6.4 Numerical modelling

The modelling of the mechanical strength of SPR joints is performed using a 3D finite element model. The software accounts for 3D contact, large plastic deformation, damage and fracture.

6.4.1 The mechanical problem

In order to describe the kinematics, an updated Lagrangian formulation is used. Between incremental time steps, the assumption of small strain and rotation is made.

For a solid, $\Omega \in \mathbb{R}^3$, the strong form of the mechanical problem to be solved is defined by the set of the following local balance equations and its associated boundary conditions:

$$\begin{cases} \vec{\nabla} \cdot \boldsymbol{\sigma} = \vec{0} \\ \vec{\nabla} \cdot \vec{v} = - \left(\frac{\dot{p}}{\kappa(1-D)} + \frac{\dot{D}}{\kappa(1-D)^2} p \right) \\ \vec{v} = \vec{v}_0 \quad \text{on} \quad \partial\Omega_v \\ \vec{t} = \vec{t}_0 \quad \text{on} \quad \partial\Omega_t \end{cases} \quad [6.16]$$

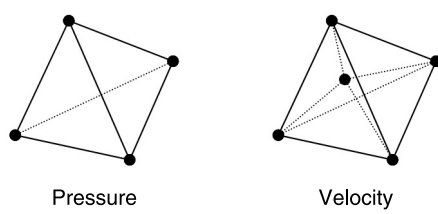
where κ is the hydrostatic modulus. The terms \vec{v}_0 and \vec{t}_0 represent the boundary conditions in terms of velocity and normal stresses, and are applied respectively to $\partial\Omega_v$ and $\partial\Omega_t$ ($\partial\Omega = \partial\Omega_v \cup \partial\Omega_t$).

For simplification, the boundary conditions related to free surfaces or related to contact and friction conditions are not taken into account in this formulation. The volumetric forces are also neglected. The weak form of the problem is written here in a mixed velocity/pressure formulation.

$$\begin{cases} \int_{\Omega} s(\vec{v}) : \dot{\boldsymbol{\varepsilon}}(\vec{v}^*) d\Omega - \int_{\Omega} p \vec{\nabla} \cdot \vec{v}^* d\Omega - \int_{\partial\Omega_t} \vec{t}_0 \cdot \vec{v}^* d\Gamma = 0 \\ \int_{\Omega} p^* \left(-\vec{\nabla} \cdot \vec{v} - \frac{\dot{p}}{\kappa(1-D)} - \frac{\dot{D}}{\kappa(1-D)^2} p \right) d\Omega = 0 \\ \mathbf{V}(\vec{v}^*, p^*) \in V^0 \times P \end{cases} \quad [6.17]$$

in which \vec{v}^* and p^* are respectively a kinematically acceptable velocity vector and a pressure field defined in the spaces V^0 and P . A unique solution exists for this problem and it is obtained under the conditions of Brezzi's theorem, which raises the inf-sup condition for stability. For the quasi-compressible equation, the demonstration of this condition is given by Brezzi and Fortin (Brezzi and Fortin 1991).

This system of equations is solved using the finite element method. Mixed velocity/pressure P1 + /P1 tetrahedral finite elements are used here. The



6.16 Degrees of freedom for P1 + /P1 tetrahedral elements.

particularity of this type of element is the addition of an additional velocity degree of freedom at the centre of the element (called bubble) in order to satisfy the stability condition (Fig. 6.16).

Contact conditions are based on a penalty formulation together with a master–slave approach. The friction law is introduced in the formulation [6.16] through a new boundary condition (Chenot *et al.* 2002). The friction behaviour is described here using a limited Coulomb friction law. A friction coefficient μ defines the relation between the shear stress vector and the sliding vector. Table 6.3 shows the values of the friction coefficient between the different parts of the connection. These coefficients are the same as those used in SPR process simulations.

Once damage reaches the critical value, the fracture behaviour has to be modelled. This may be done using either a crack propagation modelling (Bouchard *et al.* 2000; Bouchard *et al.* 2003) or the so-called ‘kill-element’ technique. When the damage parameter reaches a critical value inside an element of the mesh, the mechanical contribution of the element to the stiffness matrix is first set to zero in the current resolution and the element is then deleted from the mesh in the following time iteration.

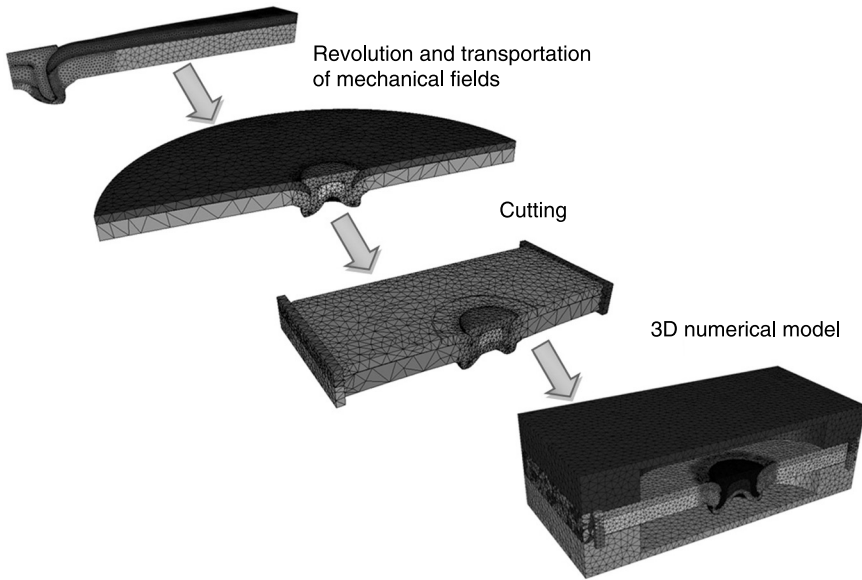
6.4.2 Transfer of the SPR process solution as an input for the 3D numerical modelling of the structural analysis

Owing to their geometries and tools kinematics, numerical simulations of the self-piercing riveting process are often conducted using a 2D axi-symmetric numerical model. However a 3D geometry is required to perform structural analysis tests.

Table 6.3 Friction coefficients between the different parts

Part 1	Part 2	Friction coefficient
Rivet	Upper sheet	0.2
Rivet	Lower sheet	0.12
Upper sheet	Lower sheet	0.12

Sunday, February 02, 2014 3:06:45 AM



6.17 Creation of the 3D numerical model from the 2D axis-symmetrical results of the SPR process simulation.

The creation of the 3D numerical model is performed in three steps using the final geometries and the mechanical state obtained from the SPR process simulation (Fig. 6.17).

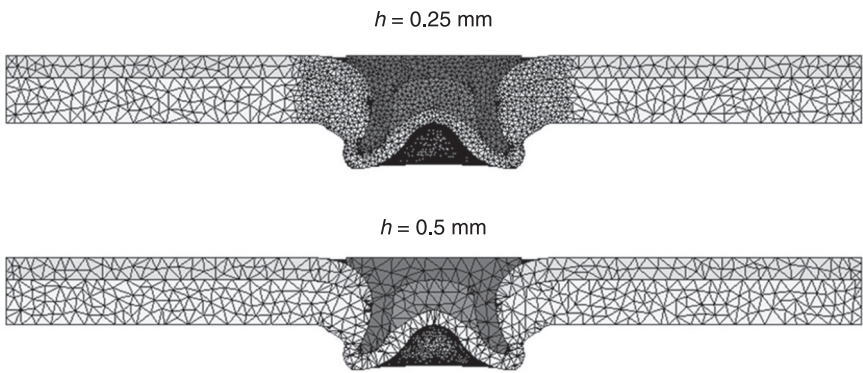
First, a 3D geometry is extrapolated from the 2D geometry using a simple revolution. Then a new mesh is generated and the mechanical fields (residual strains, residual stresses, damage, etc.) are transported using an interpolation technique. To finish, 3D circular meshes are cut to obtain a rectangular numerical specimen closest to the experimental geometry. Only the contact area between the two sheets is represented here and the Arcan type device is modelled as a rigid body.

6.4.3 Study of the numerical model

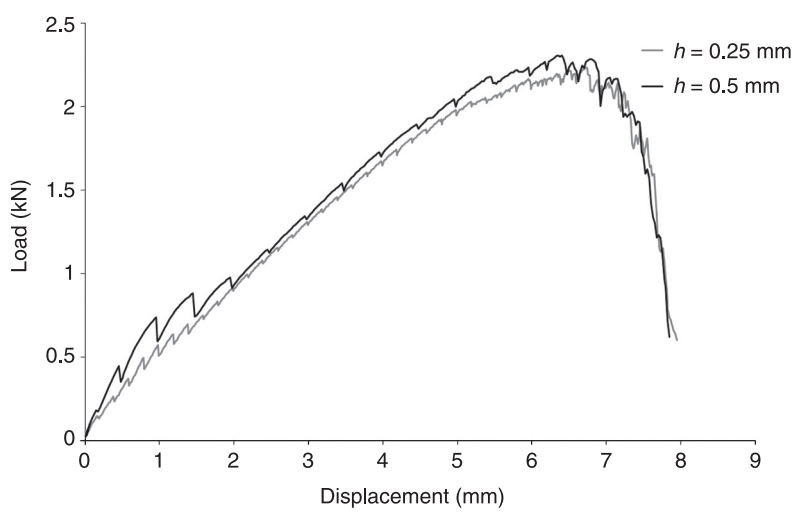
Influence of mesh size

In order to study the influence of the spatial discretization on the results, two different configurations were tested. The first configuration uses a mesh with an average size of 0.25 mm in the area close to the rivet. The second mesh has an average mesh size of 0.5 mm in the same zones (Fig. 6.18).

The results are presented in terms of load–displacement curves from a tensile mechanical test (Fig. 6.19). They show that the mesh size has a small influence on



6.18 Two different spatial discretizations.



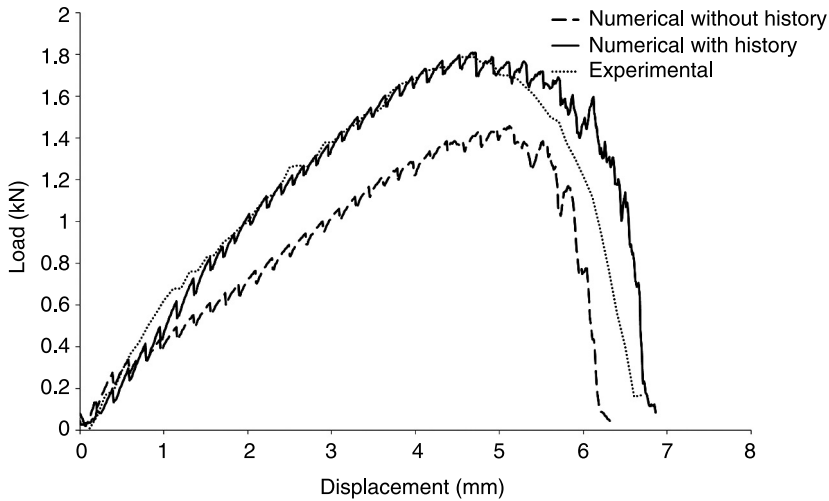
6.19 Mesh size influence on the load–displacement curve for a tensile test.

the results for the two studied meshes. Indeed, the size of the mesh plays a role only on the oscillation sizes, which appear on the load–displacement response curve. These oscillations were identified as being due to the remeshing steps, which occur during the simulation.

Influence of SPR process history

As mentioned above, it is extremely important to account for the mechanical history of the sheets in order to improve the accuracy of the mechanical strength computation. In order to characterize the influence of the mechanical history on

Sunday, February 02, 2014 3:06:45 AM

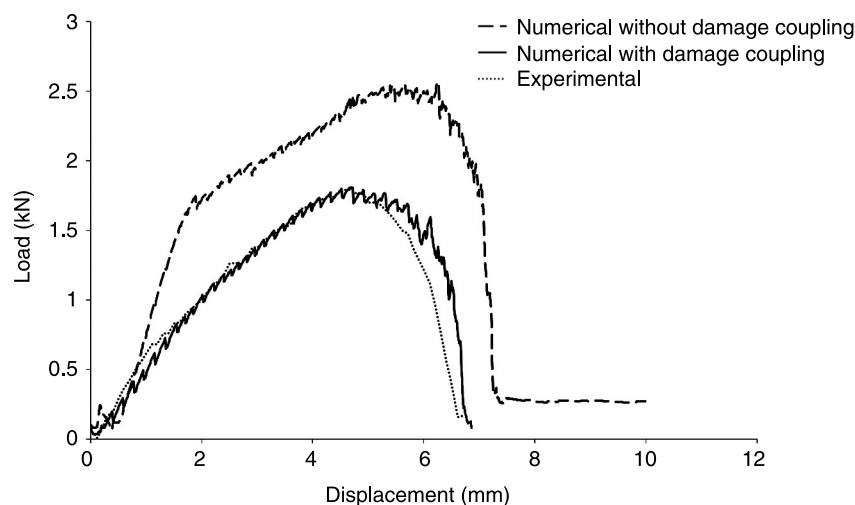


6.20 Influence of the mechanical history on the mechanical strength simulations.

the mechanical strength of a joining point, a comparison is carried out using the load–displacement curves obtained considering the residual stress, plastic deformation and damage. Two simulations of pure traction (0°) are prepared with the following configuration: a 1 mm thick steel sheet riveted with a 2 mm thick aluminium alloy sheet by using a 5 mm diameter steel rivet. Comparisons are made taking into consideration one simulation with the transfer of all the mechanical fields and the other one without transfer. Figure 6.20 shows the load–displacement curves calculated for these two simulations. As can be observed, the mechanical transfer of the fields has a significant effect. Indeed, without accounting for the mechanical history, the joined structure has a less stiff behaviour. This is in agreement with what is presented in the literature. It is thus important to be able to model the stage of the riveting process correctly in order to be able to predict the mechanical strength of the joining point correctly.

Influence of damage

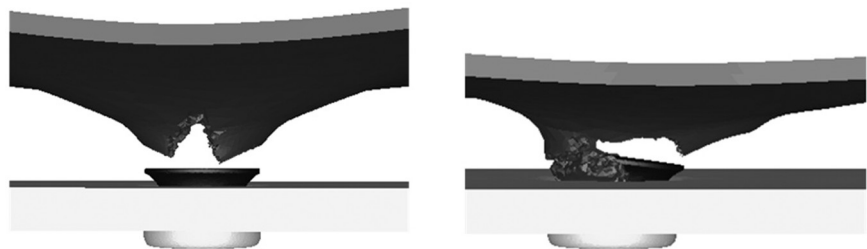
In addition to residual stresses, the computation of damage growth during the SPR process has a clear impact on the computation of the mechanical strength. Two simulations are compared here in order to underline the importance of damage computation. Both simulations include the SPR process simulation and the mechanical strength simulation. In the first simulation, damage is not taken into account whereas, in the second simulation, damage is coupled with the



6.21 Influence of damage on the load–displacement curve of a tensile test.

elastic–plastic mechanical behaviour of the materials. Figure 6.21 shows a comparison of the two calculated load–displacement curves with respect to the experimental one. It clearly shows that it is important to take into account the behaviour–damage coupling in order to predict correctly the connection strength. Indeed, the damage softens the behaviour of the materials and consequently decreases the force necessary for the final failure of the SPR connection.

With regard to the failure mode, the use of this coupled damage model with the ‘kill-element’ technique allows the simulation of the fracture process of the sheets during the mechanical strength tests (Fig. 6.22). It is obvious that, without a damage model, it is more difficult to model the failure mode of the riveted joint correctly.



6.22 Examples of calculated failure modes.

6.4.4 Numerical results and validation

The validation of the numerical model is based on the load–displacement curves and the failure mode analysis.

Load–displacement curves

Figure 6.23 represents the superimposition of the load–displacement curves obtained from experiments and those obtained by numerical calculations. Whatever the loading conditions – 0° (pure traction), 45° (mixed mode) or 90° (pure shearing) – the numerical model gives excellent results with a good correlation between the numerical and the experimental curves.

The most important difference is observed for the mixed loading. This difference may have several origins including the following.

1. The rigidity of the mechanical facility has to be considered.
2. The high level of stress may lead to a deflection of the machine that is not taken into account in the numerical model.
3. The cross-shaped specimen may slide in the Arcan device.
4. The failure mode is complex and the kill-element method is not precise enough to represent it.

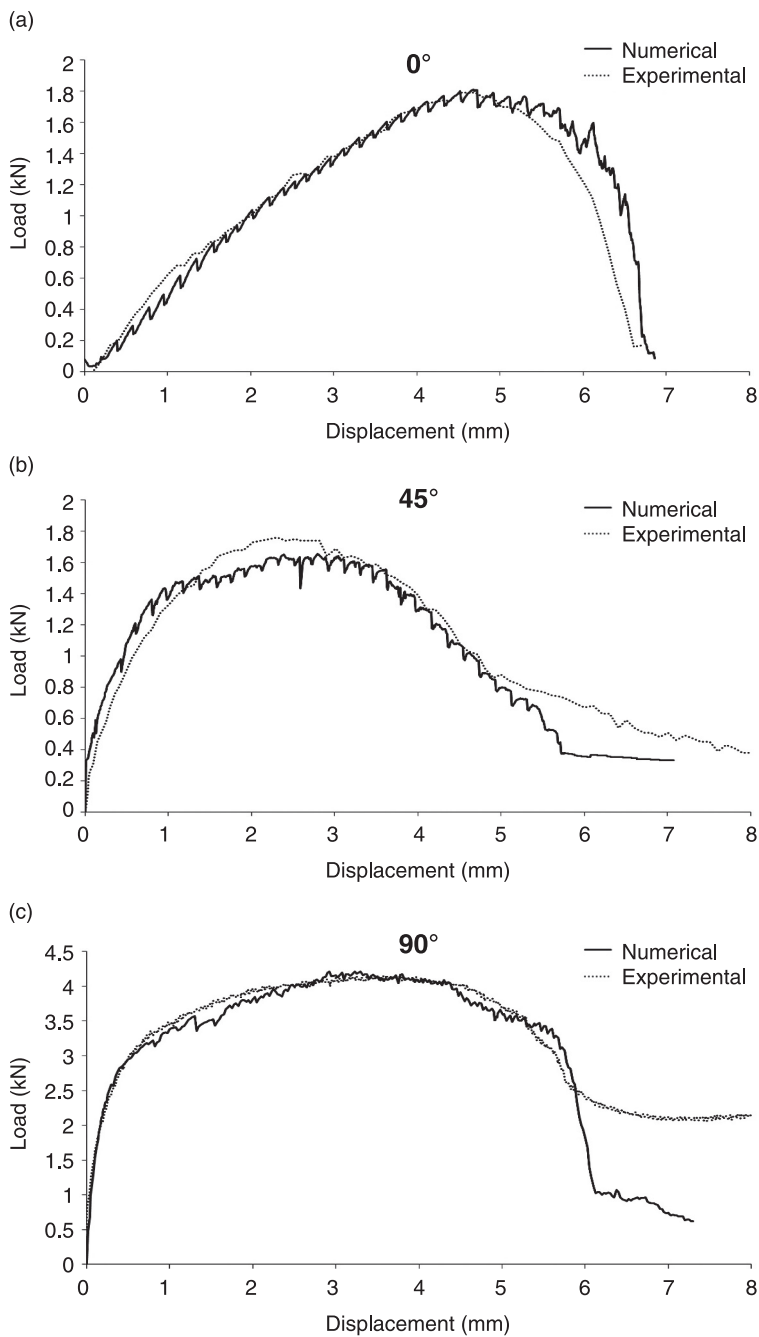
The comparisons of the experimental and calculated ultimate efforts show that the numerical model gives excellent results (Table 6.4). Indeed, the maximum variation noted for the mixed loading is below 7%.

Failure modes

The second observable used to validate the results of numerical simulations is the failure mode of the riveted points. Figure 6.24 recapitulates the calculated and observed failure modes for the tensile loading (0°). There is a good correlation between the numerical prediction and the experimental observation. Indeed, the failure mode is characterized by the fact that the rivet remains in the lower sheet, and that cracks initiate and propagate around the hole in the upper sheet.

Figure 6.25 illustrates the fracture mode for a mixed load (45°) configuration. This failure mode is close to that observed in traction, except that there is a rotation of the rivet before failure. The rivet remains in the lower sheet and the higher sheet is torn without breaking completely. We can see that the numerical model reproduces the rupture of the upper sheet with extreme accuracy.

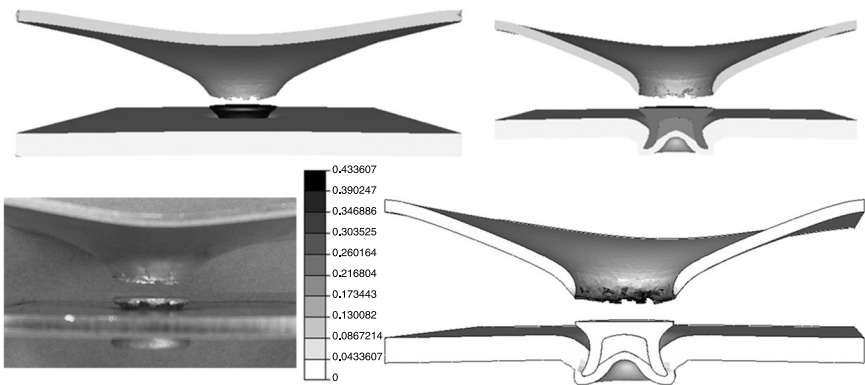
Finally, Fig. 6.26 illustrates the comparison of the mode of rupture, calculated and observed, in experiments for a pure shear loading (90°). The rivet remains in the lower sheet and the higher sheet fractures, while leaving matter under the head of the rivet. As for the load–displacement curves, an excellent correlation on the modes of rupture is obtained. The numerical model is thus predictive of the fracture topography.



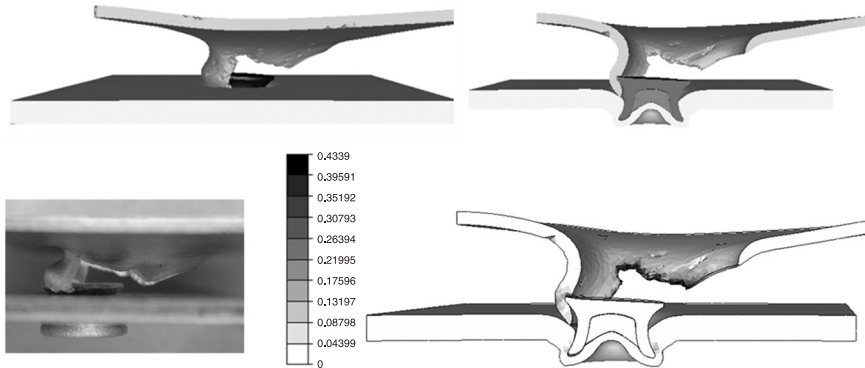
6.23 Comparisons of experimental and numerical load–displacement curves for different loading directions.

Table 6.4 Measured and calculated ultimate forces

Loading	Measured ultimate load kN	Calculated ultimate force kN	Variation (%)
0°	1.79	1.81	1.1
45°	2.36	2.21	6.4
90°	4.16	4.21	1.2

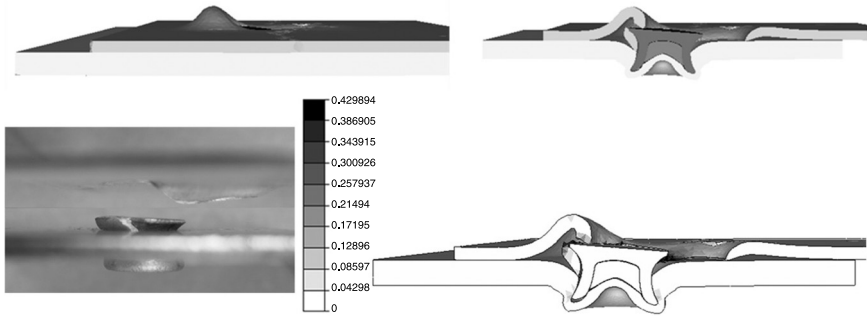


6.24 Calculated and observed failure modes and damage field for tensile loading (0°).



6.25 Calculated and observed failure modes and damage field for mixed loading (45°).

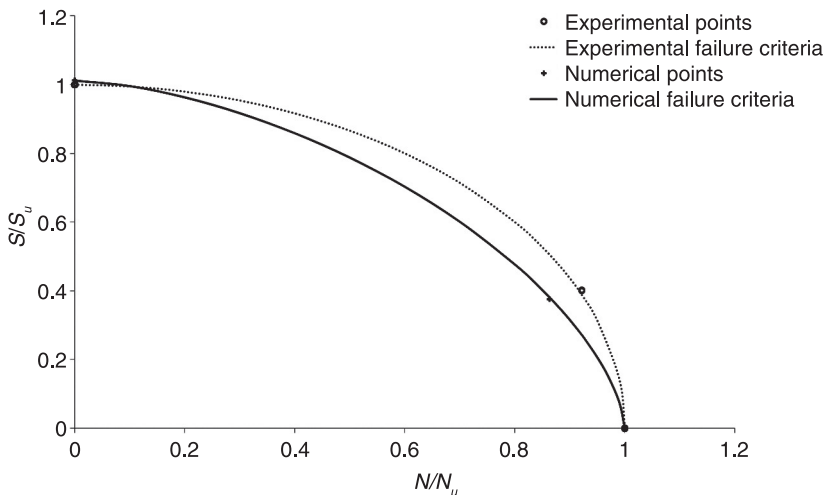
Sunday, February 02, 2014 3:06:45 AM



6.26 Calculated and observed failure modes and damage field for shear loading (90°).

The fracture criterion

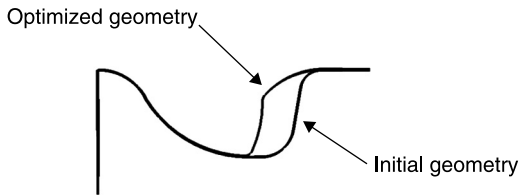
One of the goals of such a 3D numerical approach is often to define a fracture criterion of the assembly. This information could be integrated at the level of an equivalent element. This element is an approximate, simple and cheap element that replaces the exact modelling of a joined connection. The experimental and numerical rupture criteria (Fig. 6.27) were superimposed. As can be observed, the two criteria are extremely close. Moreover, the value of the numerical criterion is below that of the experimental one. Consequently, the numerical criterion is more restrictive than the experimental criterion. This is interesting from a dimensioning point of view in structural analysis.



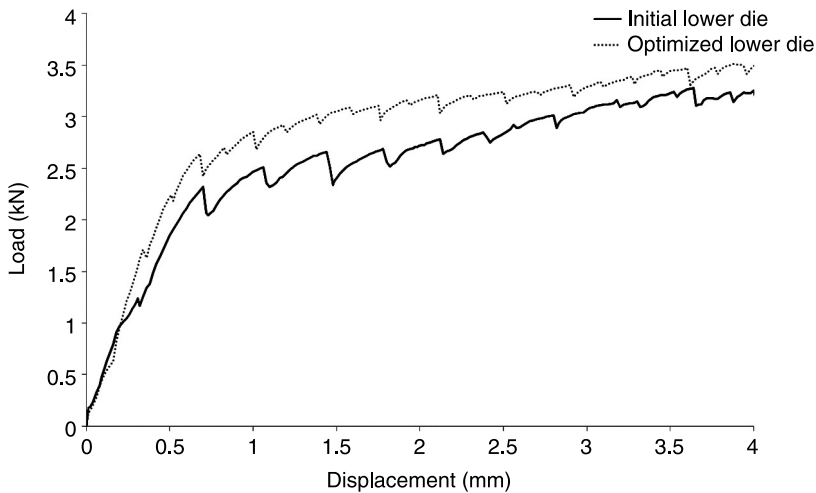
6.27 Comparisons of numerical and experimental failure criteria.

Optimization of the lower die geometry

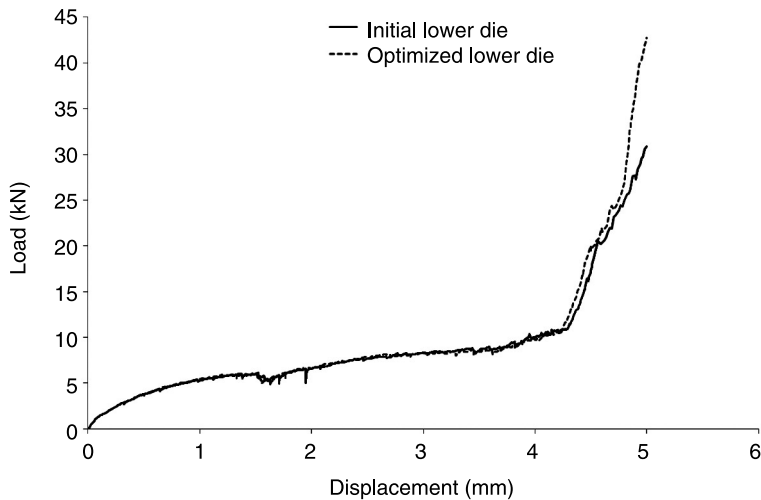
The performance of the mechanical strength of a self-piercing riveted joint depends on a great number of parameters. These parameters can be geometrical (lower die, rivet, etc.) or related to the riveting process (blank holder load, velocity and load of the punch, etc.) (Fu and Mallik 2001; Han *et al.* 2005). In order to test the ability of the numerical model, an optimization of the geometry of the lower die is presented. For a certain number of riveting configurations, the lower tool is not entirely filled fully by the material of the lower sheet at the end of the riveting process. The optimization proposed here consists of modifying the geometry of the lower die to improve the mechanical strength of the SPR connection. The assumption made here is that complete filling of the lower die would increase the compressive residual stresses and consequently the final mechanical strength. After several optimization iterations, the lower die is entirely filled by the bottom sheet during the riveting process. Figure 6.28 illustrates the initial and optimized geometries of the lower die. The comparison of the mechanical strength of the two assemblies is carried out using a shear test. Figure 6.29 shows that the riveted



6.28 Initial and optimized geometries of the lower die.



6.29 Load-displacement curves on a shearing test for the initial and optimized lower dies.



6.30 Load-displacement curves of the riveting process for the initial and optimized lower dies.

joint with the optimized lower tool geometry has an improved shearing behaviour compared with riveting with the standard die. However, it must be noted that this modification also induces a significant increase in terms of the load required to form the SPR connection (Fig. 6.30). This load increase can influence not only the lifetime of the tools, but also the life of the press.

This simple example shows that it is possible to optimize the geometry of the lower tool to increase the mechanical strength of a riveted assembly. However, this modification of the geometry led to an increase in the load necessary to form the self-piercing rivet. Users thus have to make a compromise between the loading process (and thus the lifetime of the tools and the press) and the performance of the joint. In this particular case, this optimization was carried out manually and it was necessary, between each simulation, to sketch a new geometry for the lower die. Such optimization methodologies should be performed automatically, based on automatic optimization algorithms (Peyrot *et al.* 2009). Such an automatic optimization strategy was used successfully in (Roux and Bouchard 2013) to optimize the final strength of a clinched structure by modifying the clinching process tools geometry.

Optimization of other riveting parameters is not presented here. However, the developed numerical tool can be used to study the influence of: the blank holder load, the press kinematics, rivets geometry, etc.

6.5 Conclusions and future trends

One of the most important aspects of the numerical modelling of the mechanical strength of an SPR point is the need to use the results of the self-piercing riveting

process as an input for the numerical modelling of the structural analysis. It is shown here that if the mechanical history is not taken into account, there can be more than 50% error in the calculated strength of riveted structures.

The second main aspect to model the mechanical strength of an SPR joint efficiently is the use of a coupled elastic–plastic damageable behaviour. Indeed, if damage–behaviour coupling is not used in the numerical model, it is not possible to reproduce the progressive softening of the material due to damage. This leads to an overestimation of the mechanical strength. Moreover, the correct prediction of the failure modes of the joint is directly related to the robustness of the damage model.

Based on this virtual chain of numerical simulations (joining process and structural analysis), it is shown that one can optimize the strength of the SPR structure by modifying the geometry of the tools used during the joining process. From an industrial point of view, the automatic optimization of the whole chain of simulations represents a real gain of time, together with SPR increased mechanical properties.

During the design stage of a whole structure, it is not realistic to model each 3D SPR connection. The results obtained on the mechanical strength of the SPR joints for different directions can be used to define a structural equivalent element. An SPR connector can be created so that the degrees of freedom of the connector would represent the mechanical strength of the SPR joint for each direction.

6.6 References

- Arcan M, Hashinz Z and Voloshin A (1978), 'A method to produce uniform planestress states with applications to fibre-reinforced materials', *Experimental Mechanics*, 18(2), 141–146.
- Banks-Sills L, Arcan M, Bortman Y (1984), 'A mixed mode fracture specimen for mode II dominant deformation', *Engineering Fracture Mechanics*, 20 (1), 145–157.
- Bäck T, Fogel D and Michalewicz Z (1997), *Handbook of Evolutionary Computation*, Oxford University Press, Oxford, UK.
- Bai Y and Wierzbicki T (2008), 'A new model of metal plasticity and fracture with pressure and Lode dependence', *Int. J. Plast.*, 24(6), 1071–1096.
- Bouchard P-O, Bay F, Chastel Y, Tovina I (2000), 'Crack propagation modelling using an advanced remeshing technique', *Computer Methods in Applied Mechanics and Engineering*, 189, 723–742.
- Bouchard P-O, Bay F and Chastel Y (2003), 'Numerical modelling of crack propagation: automatic remeshing and comparison of different criteria', *Computer Methods in Applied Mechanics and Engineering*, 192, 3887–3908.
- Bouchard P-O and Lasne P (2004), 'Numerical modeling of riveted joint structures – From riveting process modeling down to structural analysis', 7th ESAFORM Conference, Trondheim (Norway), April 27–30.
- Bouchard P-O, Laurent T and Tollier L (2008), 'Numerical modeling of self-pierce riveting – From riveting process modeling down to structural analysis', *J. Mat. Proc. Tech.*, 202, 290–300.
- Bouchard P-O, Bourgeon L, Fayolle S and Mocellin K (2011), 'An enhanced Lemaitre model formulation for materials processing damage computation', *Int. J. Mater. Form.*, 4(3), 299–315.

- Brezzi F and Fortin M (1991), *Mixed and Hybrid Finite Elements Methods*, Springer-Verlag, New York.
- Chaboche J L (1989), 'Constitutive equations for cyclic plasticity and cyclic viscoplasticity', *Int. J. Plast.*, 5, 247–302.
- Chenot J-L, Fourment L and Mocellin K (2002), 'Numerical treatment of contact and friction in FE simulation of forming processes', *J. Mat. Proc. Tech.*, 125–126 (9), 45–52.
- Chergui A (2004), 'Beitrag zur ermüdungsgerechten auslegung stanzengeteuer aluminium-leichtbaukonstruktionen', Ph.D. thesis, University of Paderborn.
- Cockcroft M G and Latham D J (1968), 'Ductility and the workability of metals', *J. Inst. Met.*, 96, 33–39.
- Fayolle S, Bouchard P-O and Mocellin K (2007), 'Joining and mechanical strength of self-piercing riveted structure – numerical modelling and experimental validation', ICEM13, Greece.
- Fayolle S (2008), 'Etude de la modélisation de la pose et de la tenue mécanique des assemblages par déformation plastique – Application au rivetage auto-poinçonneur', Ph.D. thesis, Mines ParisTech.
- Fu M and Mallik P K (2001), 'Effect of process variables on the static and fatigue properties of self-piercing riveted joints in aluminium alloy 5754', *Society of Automotive Engineers*, Paper No. 2001-01-0825, doi:10.1016/S0142-1123(02)00115-9.
- Gårdstam J (2006), 'Simulation of mechanical joining for automotive applications', Stockholm, Licentiate Ph.D. thesis, Royal Institute of Technology.
- Gurson A L (1977), 'Continuum theory of ductile rupture by void nucleation and growth: Part I – Yield criteria and flow rules for porous ductile media', *Journal of Engineering Materials and Technology-Transactions of the ASME*, 99(1), 2–15.
- Han L, Young K W, Hewitt R, Chrysanthou A and O'Sullivan J M (2005), 'The effect of pre-straining on the mechanical behaviour of self-piercing riveted aluminium alloy sheets', *Advanced Materials Research*, 6–8, 157–162.
- Kachanov L M (1958), 'Time of the rupture process under creep condition', *Izv. Akad. Nauk. SSSR, Otd. Tekhn. Nauk*, 8, 26–31.
- Ladevèze P (1983), 'On an anisotropic damage theory', *Proceedings of CNRS International Colloquium 351– Failure criteria of structured media*, Vilars-de-Lans, Boehler J P (ed.), France, 355–363.
- Ladevèze P and Lemaitre J (1984), 'Damage effective stress in quasi unilateral conditions', *16th Int. Congress Theor. Appl. Mech.*, Lyngby, Denmark.
- Langrand B, Fabis J, Deubon A and Mortier J M (2003), 'Détermination expérimentale du comportement mécanique et de critère de rupture d'assemblages sous chargements mixtes. Application aux rivets et points soudés', *Mécaniques & Industries*, 4, 273–283.
- Langrand B and Combescure A (2004) 'Non-linear and failure behaviour of spotwelds: a "global" finite element and experiments in pure and mixed modes I/II', *Int. J. Solids Struc.*, 41, 6631–6646.
- Lemaitre J A (1996), *A Course on Damage Mechanics*, Springer-Verlag.
- Lemaitre J and Desmorat R (2005), *Engineering Damage Mechanics*, Springer-Verlag.
- Oyane M, Sato T, Okimoto K and Shima S (1980) 'Criteria for ductile fracture and their applications', *J. Mech. Working Tech.*, 4, 65–81.
- McClintock F A (1968), 'A criterion for ductile fracture by growth of holes', *J. Appl. Mech.*, 35, 363–371.
- Peyrot I, Bouchard P-O, Ghisleni R and Michler J (2009), 'Determination of plastic properties of metals by instrumented indentation using a stochastic optimization', *J. Mat. Res.*, 24(3), 936–947.

- Porcaro R, Hanssen A G, Langseth M and Aalberg A (2006), 'Self-piercing riveting process: an experimental and numerical investigation', *J. Mat. Proc. Tech.*, 171, 10–20.
- Rice J R and Tracey D M (1969), 'On the ductile enlargement of voids in triaxial stress fields', *J. Mech. Phys. Solids*, 17, 201–217.
- Roux E and Bouchard P-O (2013), 'Kriging metamodel global optimization of clinching joining processes accounting for ductile damage', *J. Mat. Proc. Tech.*, 213(7), 1038–1047.
- Sun X, Stephens E V and Khaleel M A (2007), 'Fatigue behaviors of self-piercing rivets joining similar and dissimilar sheet metals', *Int. J. Fatigue*, 29, 370–386.
- Sutton M A, Boone M L, Ma F and Helm J D (2000), 'A combined modeling–experimental study of the crack opening displacement fracture criterion for characterization of stable crack growth under mixed mode I/II loading in thin sheet materials', *Engineering Fracture Mechanics*, 66(2), 171–185.
- Tvergaard V and Needleman A (1984), 'Analysis of the cup–cone fracture in a round tensile bar', *Acta Metall. Mater.*, 32, 157–169.
- Westerberg C. (2002), 'Finite element simulation of crash testing of self-piercing rivet joints, peel specimen', Master's dissertation, Lund University.
- Wierzbicki T, Bao Y, Lee Y-W and Bai Y (2005), 'Calibration and evaluation of seven fracture models', *Int. J. Mech. Sci.*, 47(4–5), 719–743.

Assessing the suitability of materials for self-piercing riveting (SPR)

K. MORI, Toyohashi University of Technology, Japan

DOI: 10.1533/9780857098849.2.111

Abstract: High strength steel and aluminium alloy sheets were joined by self-piercing riveting. Die geometry was optimised to attain proper joints and the joining range for the high strength steel and the aluminium alloy sheets was shown. In addition, the finite element simulation of self-piercing riveting was effective in designing the process. Finally, future trends of self-piercing riveting were given.

Key words: self-piercing riveting, high strength steel sheets, aluminium alloy sheet, interlock, die geometry.

7.1 Introduction

Reducing the weight of automobile parts is a common method of improving automobile fuel consumption. High strength steel and aluminium alloy sheets with high specific strengths are attractive materials for weight reduction (Lai and Brun 2007). It is not easy to weld aluminium alloy sheets because of their high thermal conductivity, low melting point, natural surface oxide layer, etc. To solve these problems, self-piercing riveting has been developed as a cold joining process for sheet metals. In this joining process, the sheets are mechanically interlocked without metallurgical bonding by controlling plastic deformation. Because this is a cold process, the thermal properties of aluminium alloy sheet are not a problem.

Self-piercing riveting without heating has the following advantages in comparison with techniques such as resistance spot welding:

- Highly dissimilar materials may be joined
- Improved environmental safety
- Short joining times
- High reliability of joints
- Long tool life
- Simple equipment requirements.

In addition, self-piercing riveting produces a higher strength joint and is cheaper than conventional riveting that requires pre-drilling. The disadvantages of the two processes are as follows:

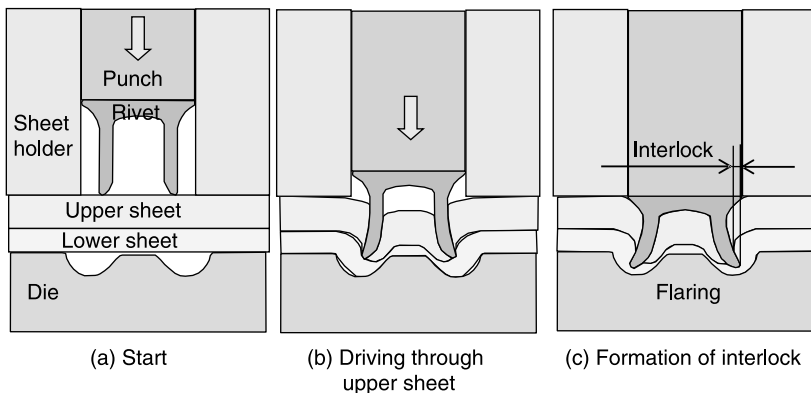
- There is a need for access from both sides of the joint with a punch and die.
- An appropriate ductility of the sheets is required.
- Bulges and indents in the joint can occur.
- A relatively large joining force is required.

7.2 How self-piercing riveting (SPR) joins materials

Self-piercing riveting is a cold process for joining two or more sheets by directly piercing the sheets with a tubular rivet without a pre-drilled hole, as shown in Fig. 7.1. In this riveting, the sheets are joined by driving the rivet through the upper sheet and flaring the skirt of the rivet in the lower sheet. The upper and lower sheets are joined by the interlock between the lower sheet and the flared skirt of the rivet, hooking the lower sheet on the flared skirt. Successful joining of sheets in self-piercing riveting requires:

- driving the rivet skirt through the upper sheet;
- achieving an interlock formation by flaring the rivet skirt into the lower sheet;
- no fracture of the lower sheet.

When the rivet skirt is not driven through the upper sheet, the sheets do not join, as the rivet skirt does not penetrate into the lower sheet. Sheet fracture leads to corrosion. To avoid this, plastic deformation of the sheets and rivet is controlled. The shapes of the rivet and die are changed according to the thickness, strength, ductility, combination, etc. of the sheets. The rivet must be strong enough to pierce the sheets, and ductile enough for the skirt to flare into the lower sheet. The rivets are mostly made of boron steel for high strength, with a measured hardness ranging between 400 and 530 HV. The rivet strength needs to be



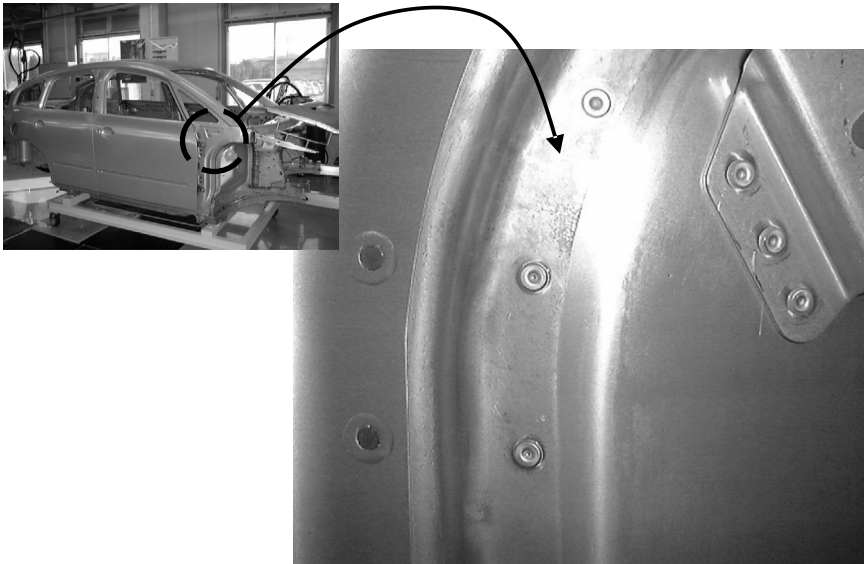
7.1 Joining of sheets by self-piercing riveting, (a) start, (b) driving through upper sheet and (c) formation of interlock.

appropriate for the materials to be joined: if the sheet strength is too high, the rivet skirt will not penetrate into the sheets, whereas if the thickness and ductility of the lower sheet are too low, the lower sheet will fracture, leading to the interlock failing to form.

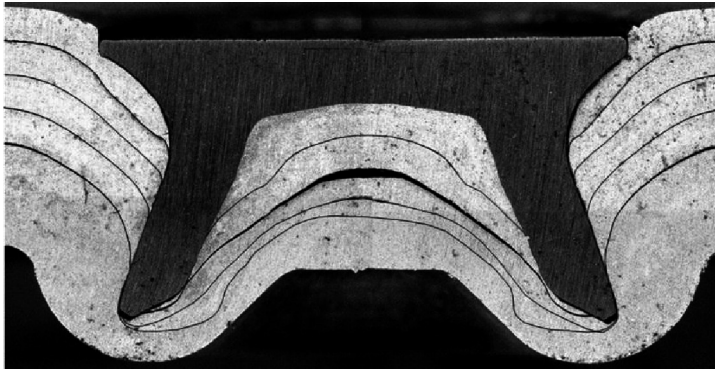
7.3 Joining of similar metals

Self-piercing riveting is mainly applied to the joining of aluminium alloy sheets, as resistance welding of aluminium sheets is not easy. Particularly in car manufacture, the spot welding that is generally used for steel sheets tends to be replaced by self-piercing riveting for joining of aluminium bodies (see Fig. 7.2). Since rivets made of boron steel are much stronger than the aluminium alloy sheets that they join, self-piercing riveting is relatively straightforward. The joining range of aluminium alloy sheets by self-piercing riveting varies, between a total thickness of the upper and lower sheets of 8 mm and a thickness of the lower sheet of 0.5 mm. Steel, copper and polymer sheets with sufficient ductility may also be joined by self-piercing riveting.

Self-piercing riveting can be used for joining more than three sheets, as shown in Fig. 7.3. In designing the joining process for more than three sheets, the sheets, except for the lowest sheet, are treated as one sheet, because the rivet skirt is driven through these sheets (Kato *et al.* 2007).



7.2 Self-piercing riveting of automobile body panels.



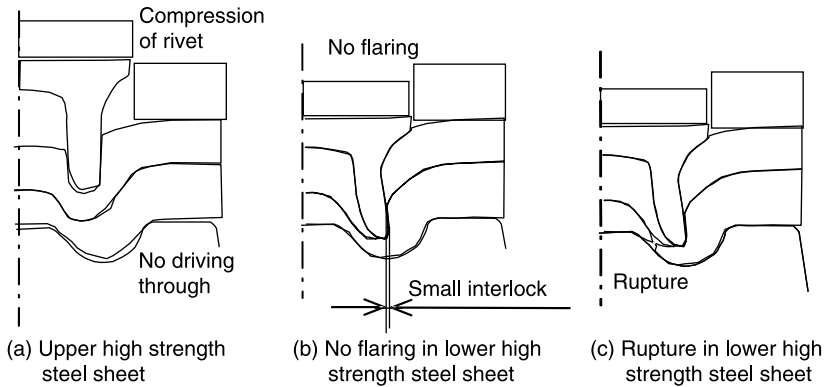
7.3 Self-piercing riveting of five aluminium alloy sheets.

7.4 Joining of dissimilar metals

High strength steel and aluminium alloy sheets are increasingly used in automobile body panels in order to reduce weight. Since high strength steel and aluminium alloy sheets are often used together, reliable joining methods for these two dissimilar materials are required. As steel and aluminium have very different melting temperatures, conventional fusion welding and resistance spot welding are unsuitable for joining sheets made of these materials.

In joining these dissimilar sheets, self-piercing riveting gives great advantages. It is particularly desirable in the automobile industry to join steel and aluminium alloy sheets for lightweight automobiles. In the joining of dissimilar sheets, defects tend to occur due to the differences in flow stress and ductility between the sheets, necessitating controlling plastic deformation of the sheets. It is comparatively easy to join mild steel and aluminium alloy sheets with self-piercing riveting because the flow stresses of the sheets are similar and the sheets have enough ductility (Abe *et al.* 2006). The effect of the differences of flow stress between steel and aluminium alloy sheets on the joinability of the self-piercing riveting has been examined using a finite element simulation (Cacko *et al.* 2004).

In the self-piercing riveting of high strength steel and aluminium alloy sheets, the strength of the high strength steel sheet approaches that of the rivet, introducing a level of difficulty for the rivet to pierce, as shown in Fig. 7.4. In the upper high strength steel sheet, a scenario where the rivet skirt is not driven through the hard upper sheet due to the compression of the rivet skirt is shown in Fig. 7.4(a). The flaring of the rivet skirt in the hard lower sheet becomes difficult, as shown in Fig. 7.4(b), and the risk of the rupture of the lower sheet becomes high due to the low ductility of the high strength steel sheet, as shown in Fig. 7.4(c). Thus, the joinability is greatly influenced by differences in strength between the upper and lower sheets that are to be riveted together.



7.4 Defects for self-piercing riveting of high strength steel and aluminium alloy sheets: (a) upper high strength steel sheet; (b) no flaring in lower high strength steel sheet; and (c) rupture in lower strength steel sheet.

The cross-sectional shapes of the rivet and sheets for the upper high strength steel sheet and the lower aluminium alloy sheet are shown in Fig. 7.5, where t_u and t_l are the thicknesses of the upper and lower sheets, respectively (Abe *et al.* 2009b). The high strength steel sheets with nominal tensile strengths of 440 and 590 MPa are successfully joined with the low aluminium sheet without defects, because the differences in flow stress are not very large.

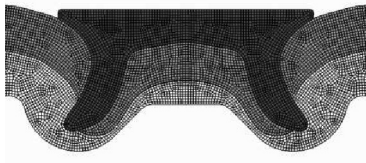
The cross-sectional shapes of the rivet and sheets for an upper ultra-high strength steel sheet with a nominal tensile strength of 980 MPa, paired with a lower aluminium alloy sheet, are shown in Fig. 7.6 (Mori *et al.* 2006). With a conventional die that is used in joining aluminium alloy sheets, the rivet could not drive through the hard upper sheet due to the compression of the rivet skirt (Fig. 7.6(a)). By optimising the die geometry, the 980 MPa steel and aluminium alloy sheets were successfully joined; see Fig. 7.6(b).

The joining ranges for the high strength steel and the aluminium alloy sheets using a conventional rivet and die used for aluminium alloy sheets obtained from the experiment are shown in Fig. 7.7 (Abe *et al.* 2009b). The ratios of the thickness of the lower sheet R_l and the rivet length ratio R_{rl} are defined as

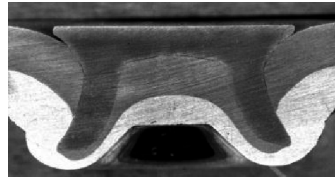
$$R_l = t_l / (t_u + t_l) \quad [7.1]$$

$$R_{rl} = l_r / (t_u + t_l), \quad [7.2]$$

where l_r is the length of the rivet. When the ratio of the thickness of the lower sheet is small, no flaring of the rivet skirt in the lower sheet or rupture of the lower sheet occurs, making joining difficult. Although the range of the upper SPFC590 is comparatively small, it was found that the joining range is reasonably wide for high strength steel sheets below 590 MPa, even with the conventional rivet and die used for aluminium alloy sheets.

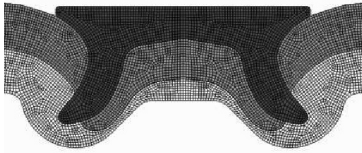


Calculated

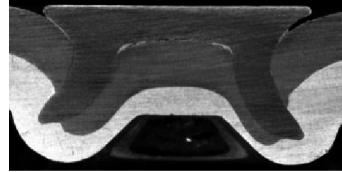


Experimental

(a) SPFC440

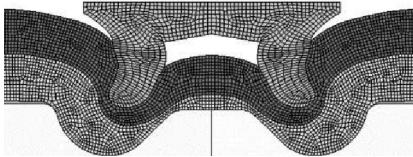


Calculated

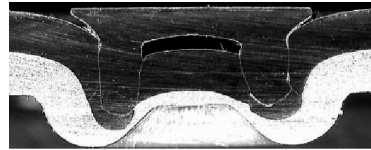


Experimental

(b) SPFC590



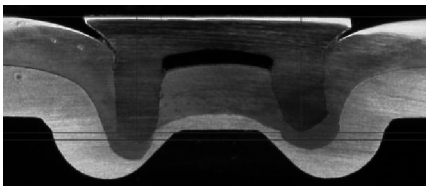
Calculated



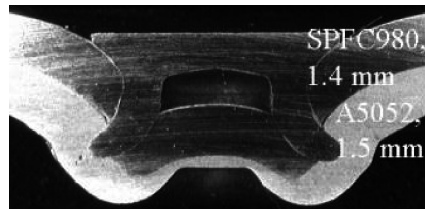
Experimental

(c) SPFC980

7.5 Cross-sectional shapes of rivet and sheets for upper high strength steel sheet of $t_u = 1.4$ mm and lower aluminium alloy sheets of $t_l = 1.5$ mm: (a) SPFC440, (b) SPFC590, (c) SPFC980.

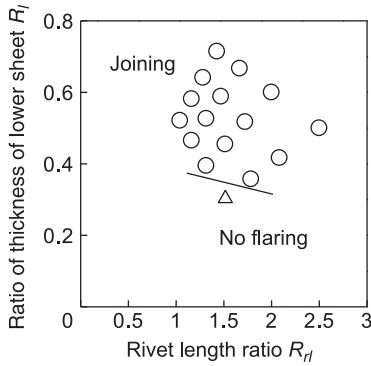


(a) Conventional die

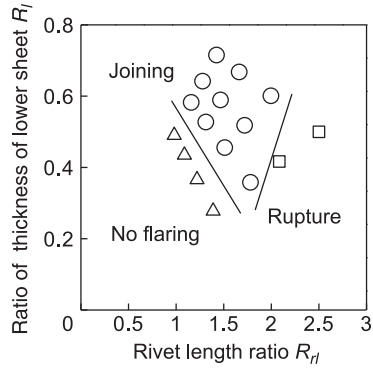


(b) Optimised die

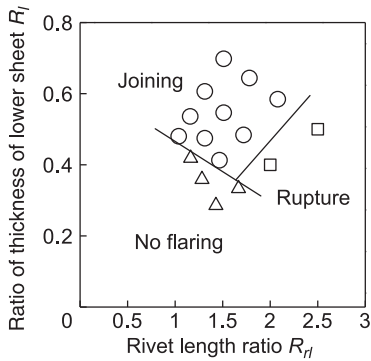
7.6 Cross-sectional shapes of rivet and sheets for upper ultra-high strength steel sheet of $t_u = 1.4$ mm and lower aluminium alloy sheets of $t_l = 1.5$ mm, (a) conventional die and (b) optimised die.



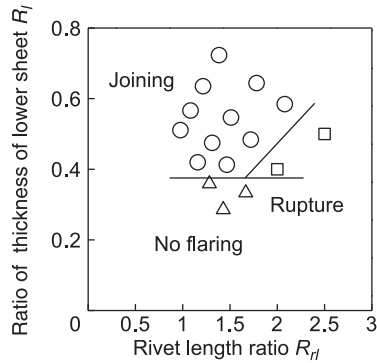
(a) Upper SPFC440 and lower aluminium alloy



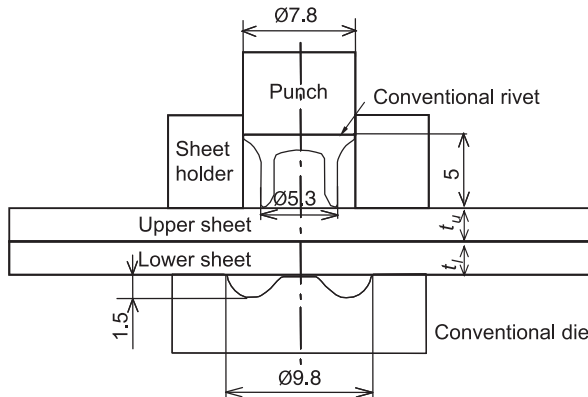
(b) Upper SPFC590 and lower aluminium alloy



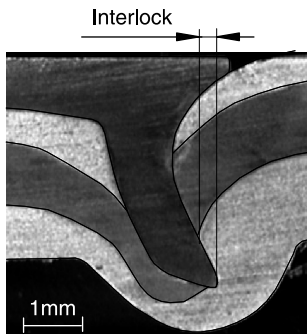
(c) Upper aluminium alloy and lower SPFC440



(d) Upper aluminium alloy and lower SPFC590



7.7 Joining range for high strength steel and aluminium alloy sheets with conventional rivet and die used for aluminium alloy sheets obtained from experiment: (a) upper SPFC440 and lower aluminium alloy; (b) upper SPFC590 and lower aluminium alloy; (c) upper aluminium alloy and lower SPFC440; (d) upper aluminium alloy and lower SPFC590.



7.8 Cross-sectional shapes of rivet and sheets obtained from experiment of riveting of upper and lower aluminium and middle steel sheets for $t_u = 0.5$ mm, $t_m = 1.2$ mm and $t_l = 1.5$ mm

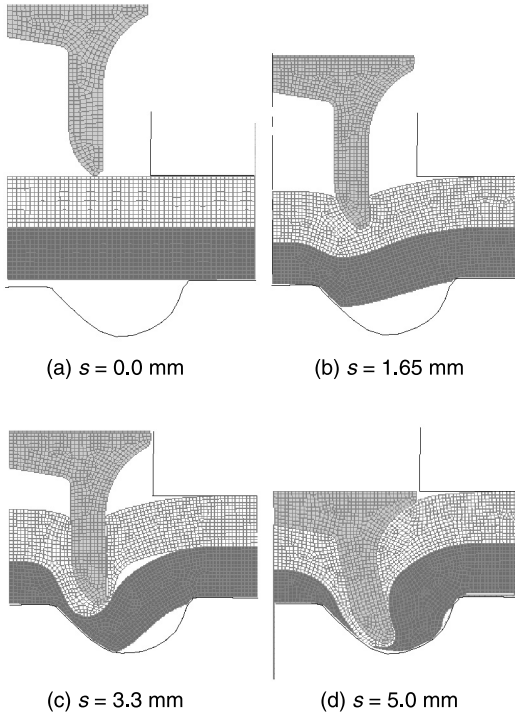
Figure 7.8 shows an example of self-piercing riveting of three sheets: the upper and lower sheets are made of aluminium alloy, and the middle sheet is made of steel (Abe *et al.* 2008; Mori *et al.* 2010). Polymer and aluminium alloy sheets (Settinieri *et al.* 2010) and fibreglass composite and aluminium alloy sheets (Fratini and Ruisi 2009) may also be joined by self-piercing riveting.

7.5 Finite element simulations of the riveting process

Finite element simulation is effective in optimising joining conditions for the self-piercing riveting process. Since the large plastic deformation of the sheet is concentrated around the rivet skirt tip, the accuracy of calculated results deteriorates, and the analyses may even terminate prematurely due to convergence issues for excessive deformation. Adaptive remeshing has been employed to avoid the severe distortion in the self-piercing riveting (Porcaro *et al.* 2006).

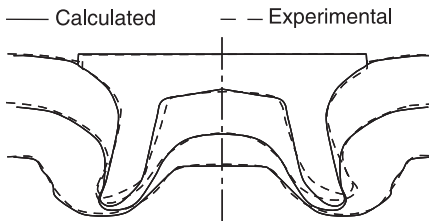
The deforming shapes of the sheets and rivet obtained from the calculation for the two aluminium sheets are shown in Fig. 7.9, where s is the punch stroke (Mori *et al.* 2007). The commercial dynamic explicit finite element code LS-DYNA was used in the simulation. Since axi-symmetric deformation is assumed by limiting the calculation to the vicinity undergoing plastic deformation, the cross-sections of the sheets and rivet are meshed with quadrilateral elements. Both sheets and rivet undergo plastic deformation during the joining process, and the die, punch and holder are assumed to be rigid. Automatic remeshing is performed in the simulation to avoid severe distortion of the element mesh. A self-piercing riveting process of aluminium alloy and steel sheets has been simulated by the finite element method (Abe *et al.* 2005).

In a finite element simulation of self-piercing riveting, the piercing process of the rivet skirt through the upper sheet needs to be properly simulated. This fracture and separation process was modelled with the normalised Latham and Cockroft



7.9 Deforming shapes of sheets and rivet obtained from calculation for two aluminium sheets: (a) $s = 0.0$ mm, (b) $s = 1.65$ mm, (c) $s = 3.3$ mm and (d) $s = 5.0$ mm.

damage law (Chenot and Massoni 2006), the Gurson–Tvergaard damage model (Atzeni *et al.* 2007) and the Lemaitre coupled damage model (Bouchard *et al.* 2008). In addition, the driving of the rivet through the sheets was treated by removing elements when the local thickness decreases to a very small value, e.g. below 0.1 mm. As shown in Fig. 7.10, the calculated result is in good agreement with the experimental one, and thus this simple treatment is acceptable. The point-connector



7.10 Comparison between cross-sectional shapes of sheets and rivet obtained from calculation and experiment for two aluminium sheets.

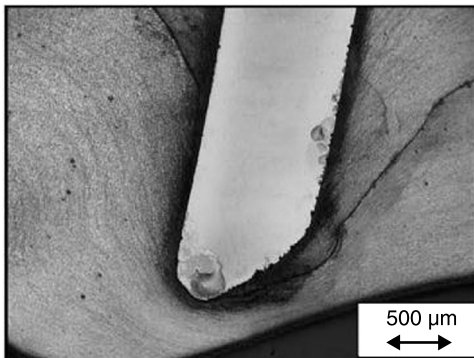
model has been employed to evaluate the static strength of the joint by the self-pierce riveting in the shell element approximation (Hanssen *et al.* 2010).

7.6 Future trends

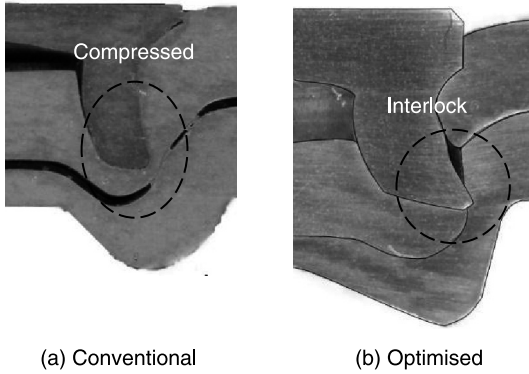
Self-piercing riveting is mainly employed for joining aluminium alloy sheets, and the applicable range also extends to steel, copper and composite sheets, etc. It is not easy to join sheets with low ductility, due to the tendency of lower sheets to fracture. Since the ductility of magnesium alloy sheets is low at room temperature, the sheet is heated with a laser beam in self-piercing riveting (Durandet *et al.* 2010) to avoid fracture of the lower sheet (see Fig. 7.11). It is also desirable to join carbon fibre reinforced plastic sheets, due to the rapidly increasing applications of these sheets in aeroplanes and automobiles in improving fuel consumption. The optimisation of the shapes of the dies and rivets, as well as the heating approach, is required for the joining.

Although hard steel rivets are conventionally used for the self-piercing riveting of aluminium alloy sheets, rivets made of aluminium alloys have been developed to improve recyclability (Abe *et al.* 2007, 2009a; Hoang *et al.* 2010). Since the strength of aluminium alloy rivets is less than that of steel rivets, if the aluminium alloy rivet is made in the shape conventionally used for steel rivets, the rivet will fail to form a mechanical interlock (see Fig. 7.12(a)). The shapes of the rivet and die have been optimised to decrease the compressive deformation of the rivet and to form the interlock as shown in Fig. 7.12(b).

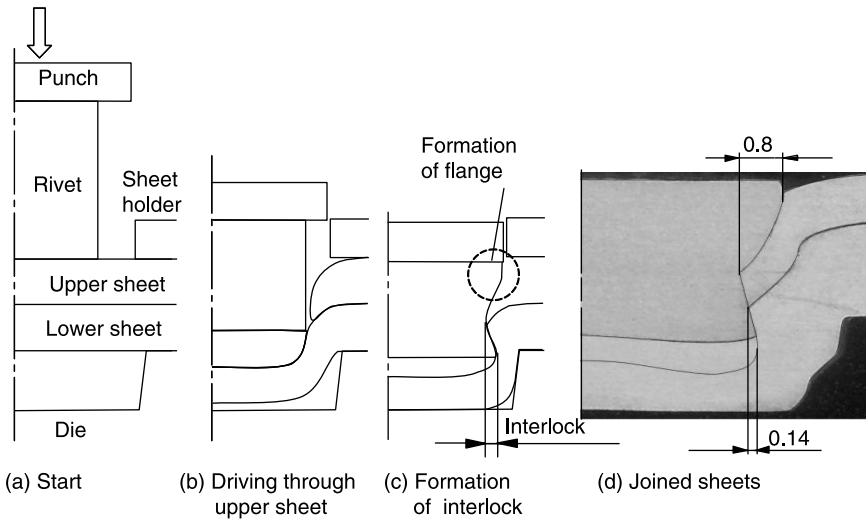
A cylindrical aluminium alloy rivet without a skirt has been developed to improve recyclability (Kato *et al.* 2010). For the cylindrical rivets, the shape of the die was optimised to form an interlock, as shown in Fig. 7.13. The cylindrical rivets have the advantages of a simpler manufacturing process, and of decreased distortion during riveting (Neugebauer *et al.* 2011). A pipe rivet has also recently been developed by Huang *et al.* (2011).



7.11 Laser assisted self-piercing riveting of magnesium alloy sheets.



7.12 Self-piercing riveting with aluminium alloy rivets:
(a) conventional and (b) optimised.



7.13 Self-piercing riveting with cylindrical aluminium alloy rivets:
(a) start, (b) driving through upper sheet, (c) formation of interlock
and (d) joined sheets.

7.7 References

- Abe Y, Kato T, Mori K and Wu X (2005), 'Finite element simulation of joining process of aluminium alloy and steel sheets using self piercing rivet', in Bariani P F *et al.* (eds), *Advanced Technology of Plasticity*, CD-ROM.
- Abe Y, Kato T and Mori K (2006), 'Joinability of aluminium alloy and mild steel sheets by self piercing rivet', *Journal of Materials Processing Technology*, 177(1–3), 417–421.

- Abe Y, Kato T and Mori K (2007), 'Joining of aluminium alloy sheets by aluminium alloy self-piercing rivet', in F. Vollertsen *et al.* (eds), *Proc. 2nd International Conference on New Forming Technology*, 451–460.
- Abe Y, Kato T and Mori K (2008), 'Self-pierce riveting of three high strength steel and aluminium alloy sheets', *International Journal of Material Forming*, Supplement 1, 1, 1271–1274.
- Abe Y, Kato T and Mori K (2009a), 'Aluminium alloy self-pierce riveting for joining of aluminium alloy sheets', *Key Engineering Materials*, 410–411, 79–86.
- Abe Y, Kato T and Mori K (2009b), 'Self-piercing riveting of high tensile strength steel and aluminium alloy sheets using conventional rivet and die', *Journal of Materials Processing Technology*, 209(8), 3914–3922.
- Atzeni E, Ippolito R and Settineri L (2007), 'FEM modeling of self piercing riveted joint', *Key Engineering Materials*, 344, 655–662.
- Bouchard P O, Laurent T and Tollier L (2008), 'Numerical modeling of self-pierce riveting – From riveting process modeling down to structural analysis', *Journal of Materials Processing Technology*, 202(1–3), 290–300.
- Cacko R, Czyzewski P and Kocanda A (2004), 'Initial optimization of self-piercing riveting process by means of FEM', *Steel-Grips*, 2, 307–310.
- Chenot J-L and Massoni E (2006), 'Finite element modelling and control of new metal forming processes', *International Journal of Machine Tools and Manufacture*, 46(11), 1194–1200.
- Durandet Y, Deam R, Beer A, Song W and Blacket S (2010), 'Laser assisted self-pierce riveting of AZ31 magnesium alloy strips', *Materials & Design*, Supplement 1, 31, S13–S16.
- Fratini L and Ruisi V F (2009), 'Self-piercing riveting for aluminium alloys–composites hybrid joints', *International Journal of Advanced Manufacturing Technology*, 43, 61–66.
- Hansson A G, Olovsson L, Porcaro R and Langseth M (2010), 'A large-scale finite element point-connector model for self-piercing rivet connections', *European Journal of Mechanics – A/Solids*, 29(4), 484–495.
- Hoang N-H, Porcaro R, Langseth M and Hanssen A-G (2010), 'Self-piercing riveting connections using aluminium rivets', *International Journal of Solids and Structures*, 47(3–4), 427–439.
- Huang Z C, Fan K C and Lai J M (2011), 'The mechanical behaviour of self-piercing riveting with pipe rivet', *Proc. the 10th International Conference on Technology of Plasticity*, 742–745.
- Kato T, Abe Y and Mori K (2007), 'Finite element simulation of self-piercing riveting of three aluminium alloy sheets', *Key Engineering Materials*, 340–341, 1461–1466.
- Kato T, Abe Y and Mori K (2010), 'Plastic joining of aluminium alloy sheets by aluminium alloy cylinder', *Steel Research International, Supplement Metal Forming*, 81(9), 1136–1139.
- Lai M and Brun R (2007), 'Latest developments in sheet metal forming technology and materials for automotive application: the use of ultra high strength steels at Fiat to reach weight reduction at sustainable costs', *Key Engineering Materials*, 344, 1–8.
- Mori K, Kato T, Abe Y, Ravshanbek Y (2006), 'Plastic joining of ultra high strength steel and aluminium alloy sheets by self piercing rivet', *CIRP Annals – Manufacturing Technology*, 55(1), 283–286.

- Mori K, Abe Y and Kato T (2007), 'Finite element simulation of plastic joining processes of steel and aluminum alloy sheets', in Cesar de Sa J M A *et al.* (eds), *Materials Processing and Design: Modeling, Simulation and Application*, AIP Conf. Proc., 1, 197–202.
- Mori K, Abe Y, Kato T and Sakai S (2010), 'Self-pierce riveting of three aluminium alloy and mild steel sheets', in Barlat F *et al.* (eds), *Proc. 10th Int. Conf. Numerical Methods in Industrial Forming Processes*, AIP Conf. Proc., 1252(2), 673–680.
- Neugebauer R, Rössinger M, Wahl M, Schulz F, Eckert A and Schützle W (2011), 'Predicting dimensional accuracy of mechanically joined car body assemblies', *Key Engineering Materials*, 473, 973–980.
- Porcaro R, Hanssen A G, Langseth M and Aalberg A (2006), 'Self-piercing riveting process: An experimental and numerical investigation', *Journal of Materials Processing Technology*, 171(1–3), 10–20.
- Settinieri L, Atzeni E and Ippolito R (2010), 'Self piercing riveting for metal–polymer joints', *International Journal of Material Forming*, 3, Supplement 1, 3, 995–998.

Quality control and non-destructive testing of self-piercing riveted joints

P. JOHNSON, SBC, University of Shanghai for Science and Technology, People's Republic of China

DOI: 10.1533/9780857098849.2.124

Abstract: Quality control and the non-destructive testing of self-piercing riveting have become increasingly important with the introduction of aluminium as a light weight joining material. Computer vision and ultrasonic testing can be used at various points in the self-piercing riveting process to provide real-time non-destructive testing of aluminium joining materials and can therefore save time, money and material waste.

Key words: self-piercing riveting, SPR, rivets, non-destructive testing, NDT, computer vision, image processing, ultrasound, narrowband, ultrasonic testing, NBUS.

8.1 Introduction

This study discusses the need for non-destructive testing (NDT) for self-piercing riveting (SPR)¹, as well as monitoring systems and sensors that can be used to provide this type of testing. The automotive industry has for many decades been using resistance spot-welding (RSW) as the standard method of assembling steel cars. While there are approximately 4000 welds per car, only around 0.625% of these are checked to examine whether they are of an acceptable quality. In a production line environment approximately 150 welds are checked every 60 cars – with six different sets of 25 welds, and one set is checked every ten cars. The only way these checks can be performed without destroying the joint is by manual ultrasonic testing with a handheld probe, which is tedious and time-consuming.

The impact of vehicle emissions on the environment is an ever-increasing concern worldwide. A reduction in emissions can be achieved by making lightweight vehicles, which in turn, requires smaller engines to move the reduced mass. With this in mind, the European Union introduced directive 70/220/EEC, which dictates the maximum emissions for passenger vehicles of eight seats or fewer (category M₁). This information is summarised in Table 8.1. As expected, many automotive manufacturers and in particular low- and medium-volume car producers have attempted to reduce vehicle weight by switching from steel to aluminium bodies. With the introduction of aluminium car assembly,

Table 8.1 Directive 70/220/EEC for M₁ vehicles, detailing the required reduction of vehicle emissions over time

Tier	Date	CO	HC	HC+NOx	NOx	PM
Diesel						
Euro 1 †	1992/07	2.72 (3.16)	–	0.97 (1.13)	–	0.14 (0.18)
Euro 2, IDI	1996/01	1.0	–	0.7	–	0.08
Euro 2, DI	1996/01 ^a	1.0	–	0.9	–	0.10
Euro 3	2000/01	0.64	–	0.56	0.50	0.05
Euro 4	2005/01	0.50	–	0.30	0.25	0.025
Euro 5	2009/09 ^b	0.50	–	0.23	0.18	0.005 ^e
Euro 6	2014/09	0.50	–	0.17	0.08	0.005 ^e
Petrol						
Euro 1 †	1992/07	2.72 (3.16)	–	0.97 (1.13)	–	–
Euro 2	1996/01	2.2	–	0.5	–	–
Euro 3	2000/01	2.30	0.20	–	0.15	–
Euro 4	2005/01	1.0	0.10	–	0.08	–
Euro 5	2009/09 ^b	1.0	0.10 ^c	–	0.06	0.005 ^{d,e}
Euro 6	2014/09	1.0	0.10 ^c	–	0.06	0.005 ^{d,e}

† – the values in the brackets are the conformity of production limits.

a – until 1999/09/30, after which DI engines must meet IDI limits.

b – 2011/01 for all models.

c – and NMHC=0.068 g/km.

d – only applies to vehicles with DI engines.

e – proposed to change to 0.003 g/km using the PMP measurement procedure.

SPR is currently used to apply several thousand rivets per car. Unfortunately, SPR also suffers from similar inadequate quality control techniques to those of RSW.

Since Ford began assembling lightweight aluminium cars, such as the Jaguar X350 and X600, they have used self-piercing riveting rather than spot-welding because the electrical and thermal conductivity requirements of aluminium are 2.5 to 3 times the current and only 33% the weld time of steel. As a result of the lower resistance and increased current for aluminium in comparison to steel, superior spot-welding machinery is required. This machinery generates more heat in the electrode arms, which requires greater cooling to help limit tool wear. While spot-welding of aluminium is possible, it is difficult and is not cost-effective².

It is difficult if not impossible to provide direct conclusive NDT of SPR joints from a single sensor. However, by introducing a fusion of sensors and careful analysis of the data, it is possible to monitor the process, machinery health and tool wear to ensure a greater accuracy in the prediction of the mechanical interlock quality. This saves time and money by avoiding destructive testing methods and by improving on existing monitoring techniques. Ideally it should be possible to

incorporate these additional sensors into existing NDT systems and production line environments to improve current quality control and minimise costs.

8.2 Current technologies

Joining techniques in the automotive industry are predominantly driven by advances in materials, working with dissimilar materials and the call for increased automation as a result of a decline in the skilled labour force³.

Riveting machines apply rivets to materials in a wide variety of configurations, from manually operated handheld riveting guns to multi-head automated riveting tools that are electrically, pneumatically, or hydraulically actuated. There are three main types of riveting machinery: compression riveting, non-impact riveting (also known as orbital riveting), and impact riveting. Compression riveting forms the head of the rivet by squeezing or pulling the rivet shank, while non-impact riveting forms the head by performing a spinning or rolling action to the end of the top of the shank. Impact riveting – as used in SPR – forms the head by impacting the top of the shank, using riveting hammers/punches.

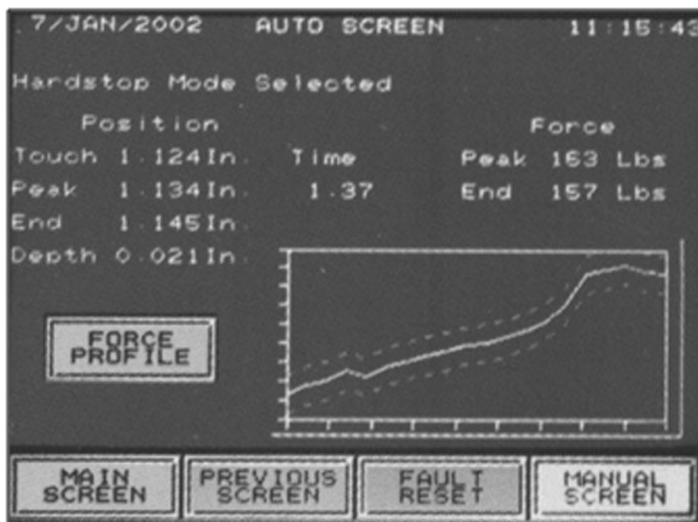
Henrob Ltd is an industry leader in SPR joining and monitoring systems. Their client list includes eight leading automotive manufacturers: BMW, Audi, Jaguar, Volvo, Chrysler, Mercedes, Freightliner and Hyundai. In 1994 Audi used Henrob's pre-clamping SPR system for the majority of the A8's single point joints⁴. In 1999 the same SPR system was used for various parts of the Audi A2, which featured a lightweight all aluminium body⁵. Jaguar also used self-piercing rivets in 2001 for their X350⁶. The engineers decided to use SPR because significant parts of the X350 body shell were made from aluminium. Jaguar implemented a SPR system developed by Henrob, and used Kawasaki robots to apply the rivets. Some four years later, in 2005, Jaguar re-evaluated their manufacturing processes and concluded that SPR still presented the best solution for joining aluminium⁷.

Henrob along with Bollhoff – another prominent supplier of SPR machinery – offer monitoring systems to accompany their joining machinery. Like Henrob, Bollhoff operates in volume manufacturing plants in the automotive industry⁸. These companies offer a variety of hydraulic and electric servo-joining solutions tailored to the joining specification of the customer. The monitoring system may be purchased at an additional cost. Henrob's monitoring system is called RivMon and can be purchased at an additional cost for its hydraulic and electric servo systems, while Bollhoff's monitoring system is an optional extra on its RIVSET systems^{9–12}. The main feature of these monitoring systems is their dedicated sensors that monitor the setting force and punch movement throughout the riveting process, resulting in a force–displacement curve. This curve is compared with a trained reference curve. If the process curve fits within a pre-defined tolerance of the reference curve, the joint is passed; otherwise the joint may be flagged for attention or the process may even be halted. The sensors employed depend on the

variant of the SPR system. Hydraulic systems have a positional sensor to locate the punch and up to two pressure sensors to monitor the clamp and punch pressures. Electric servo-systems monitor the punch location, punch velocity and torque (motor current).

Orbitform offers a process monitoring system called Watchdawg, shown in Fig. 8.1. Although this system is designed for non-impact (orbital) riveting, it works on the same force–displacement technology. The force and displacement data are plotted against each other on a graph and create what is known as a ‘force–displacement curve’. Force–displacement curves often have tolerances extending around them to add greater flexibility to the technique – shown as a dashed line around the graph plot in Fig. 8.1. These tolerances vary depending on the types of joint and materials, as well as the forces applied and material thickness.

The most prominent alternative NDT techniques for SPR not based on the force–displacement curve technology are real-time visual inspection and ultrasonic testing. The engineering department at SBC, The University of Shanghai for Science and Technology¹⁴, is currently researching real-time visual inspection for various aspects of the SPR process. Ultrasonic testing appears to be another promising method of NDT and is under evaluation by Warwick Manufacturing Group at the University of Warwickshire¹⁵ and Uppsala University¹⁶.



8.1 ‘Watchdawg’ process monitoring system from Orbitform¹³.

8.3 Non-destructive testing (NDT) techniques: computer vision

8.3.1 Rivet status

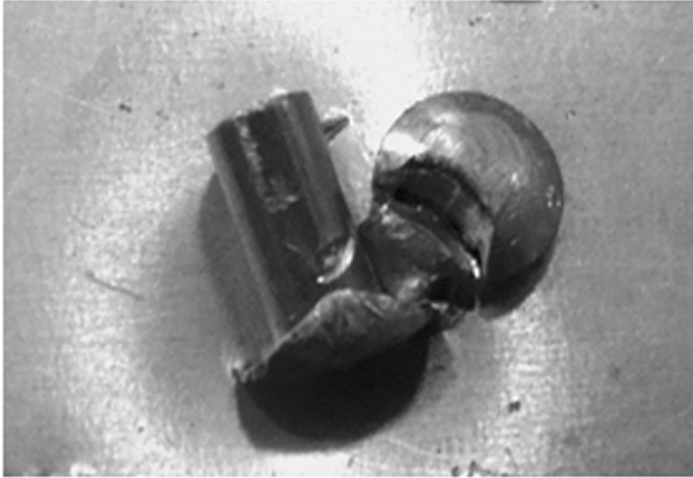
The machine jaws are an ideal location to begin pre-process monitoring as this is where the rivets rest prior to setting. It is also possible to detect the status and orientation of a loaded rivet by visual inspection of the machine jaws. It is possible to prevent a number of incidents from occurring, such as a punch imprint on the joining material or a multiple rivet piercing by identifying the rivet status pre-process. A punch imprint is caused when a rivet has failed to load into the machine jaws and the SPR process triggers regardless. Without a rivet present the punch makes direct contact with the joining materials, causing an indentation, shown in Fig. 8.2. If multiple rivets are loaded into the rivet jaws it is also possible for the SPR process to trigger. These rivets may still pierce the joining materials, but the resulting joint will be unacceptable, as shown in Fig. 8.3.

These incorrect rivet settings not only compromise joint strength and aesthetics, but often require replacement of the joining materials. If these materials are on a car panel on an automotive production line, any stoppage means spiralling costs due to decreased production and redundant staff.

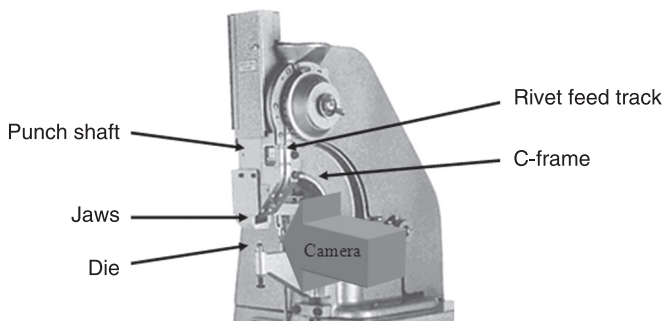
The problem of incorrect rivet settings may be prevented by monitoring the image amplitude across the machine jaws. To do this a camera must be positioned with a clear view of the jaws, which on the riveting machine (Doidge 120¹⁷) used in G.E.R.I is only accessible at 90° anticlockwise from the front of the machine, as shown in Fig. 8.4.



8.2 A punch imprint in aluminium joining materials.



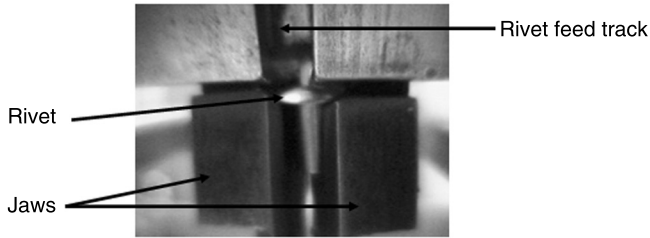
8.3 Two rivets set into aluminium joining materials.



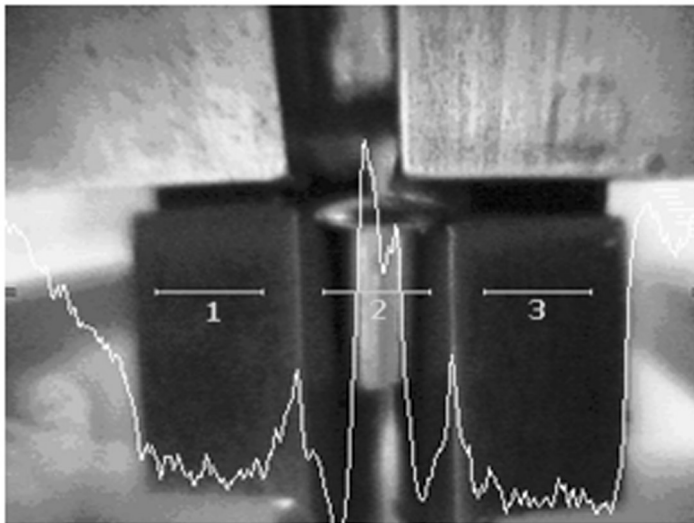
8.4 The camera position for checking the rivet status.

This view allows the rivet jaws and feed track to be monitored, as shown in Fig. 8.5. The rivets travel down the feed track and sit in the jaws until they are set. If multiple rivets are present they will cause a backlog, starting at the rivet in the jaws and regressing up the rivet feed track.

The G.E.R.I. algorithm works by finding and comparing the amplitude of x values on the y axis, shown in Fig. 8.6. The white line plots the amplitude where $y=120$, while the three labelled regions highlight the three points of interest (50 pixel each) on the x -axis where $x=70-100$ (labelled as 1), $x=150-200$ (labelled as 2) and $x=230-280$ (labelled as 3).

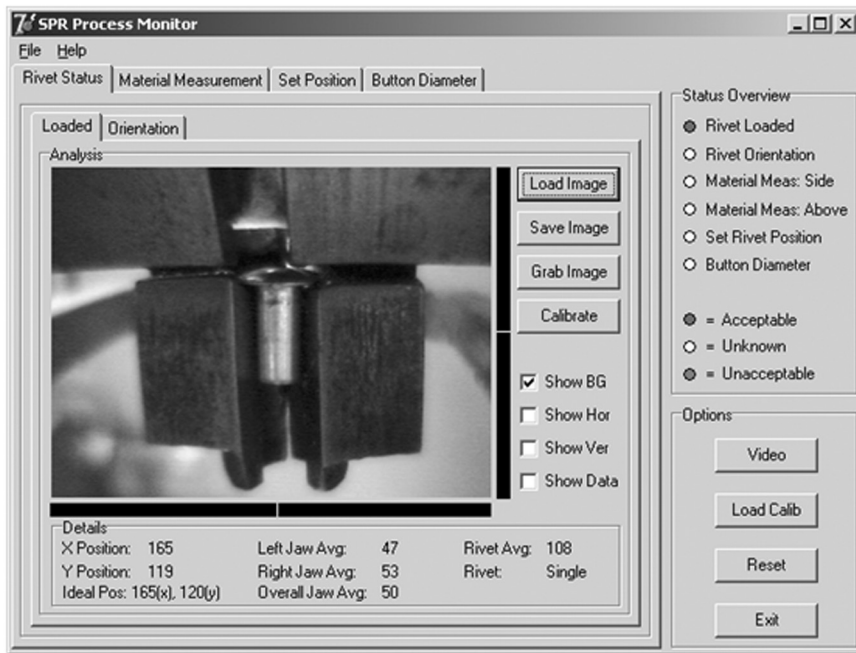


8.5 The camera view of the jaws from the position shown in Fig. 8.4.



8.6 Amplitude values of a single rivet plotted across the x-axis.

The amplitudes of point 1 and 3 are used as a brightness control and are compared with that of point 2. The difference in amplitude is used to identify whether a rivet is missing, is present or if multiple rivets are present. The difference in amplitude varies depending on the ambient lighting, which is why the bespoke software includes a calibration feature. Once the software has been calibrated for a particular joint, the algorithm will determine the status of the loaded rivet as shown in Fig. 8.7. A single rivet will give the highest amplitude value, with multiple or missing rivets achieving a much lower intensity. Multiple rivets are identified as having an intensity below the lower tolerance of a single rivet but above zero, while the amplitude of a missing rivet will be below zero when subtracted from the amplitude of the machine jaws.

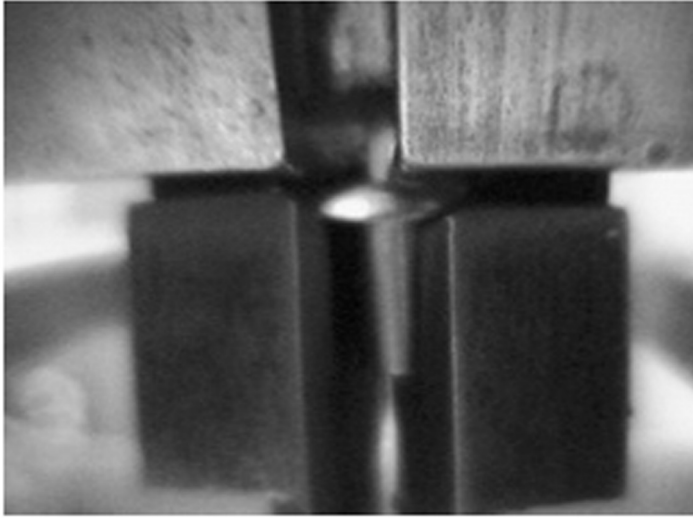


8.7 The bespoke process monitoring software showing the details of the loaded rivet status tab.

The software displays values for each of the individual amplitude measurements as well as a final decision on the rivet status. The 'Rivet' label will provide an indicator of 'missing', 'single' or 'multiple', depending on the outcome of the algorithm. A simplified colour indicator in the 'Status Overview' produces a red or green light to let the operator know if the rivet was set correctly or not. The indicator will appear red for missing a rivet or for applying multiple rivets and green for a single rivet. For users requiring further analysis there are checkboxes to display horizontal and vertical amplitude overlays as well as numerical data for both axes.

8.3.2 Rivet orientation

When a rivet is loaded into the machine jaws the shaft should run parallel to the jaws (which is vertical on the camera view) to ensure the punch hits the rivet head in the centre. If the rivet is not vertical before setting, as shown in Fig. 8.8, the punch can cause the rivet to rotate (or tumble), creating a poor joint that is unlikely to completely pierce the top material, as shown in Fig. 8.9. The camera is situated in the same location as the 'rivet status' technique discussed previously in Fig. 8.4.



8.8 Non-vertical rivet orientation.



8.9 Tumbled rivet set into aluminium.

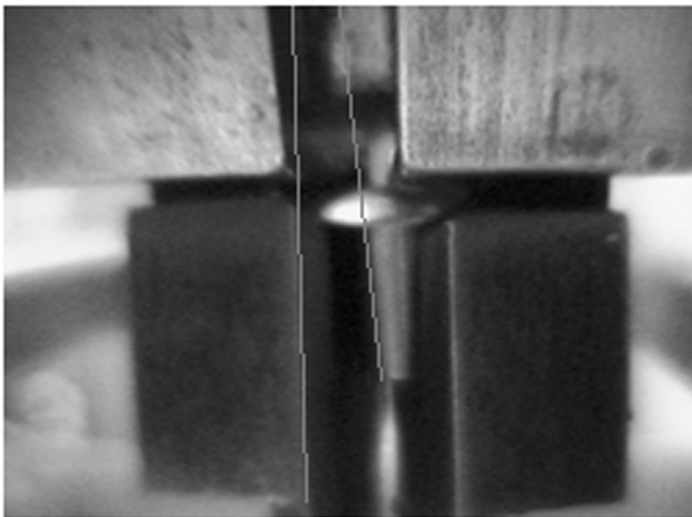
The rivet in Fig. 8.8 is orientated only a few degrees from vertical, but this misalignment often causes the rivet to tumble when it is impacted by the punch. The rivet in Fig. 8.9 has tumbled approximately 110° clockwise, resulting in the rivet head piercing the joining materials rather than the rivet shaft and setting

incorrectly. The rivet head is neither designed nor long enough to pierce the joining materials and this results in a substandard joint that damages the top sheet and needs to be repaired or replaced before being re-set.

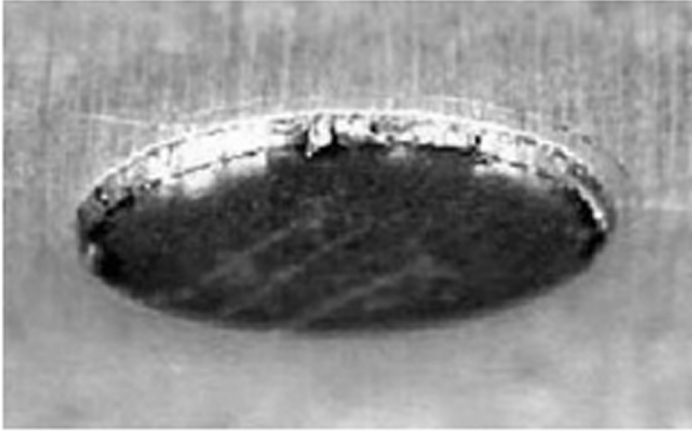
The G.E.R.I. algorithm created to detect the angular orientation of the rivet works by first identifying the rivet and machine jaws using edge detection and threshold techniques. Since the rivet jaws are intended to hold the rivet in the correct orientation prior to setting, the jaws can be used as the control. If the rivet is seated correctly the jaws and rivet should appear parallel, otherwise they will appear misaligned as shown in Fig. 8.10. The lines highlight the disorientation of the rivet in comparison with the machine jaws, by showing that they will converge at some point and are therefore not parallel. This eventual convergence allows an extrapolation of the angular deviation. Any angular deviation can be checked against specified system tolerances to determine if a rivet is in an acceptable orientation.

8.3.3 Material measurement

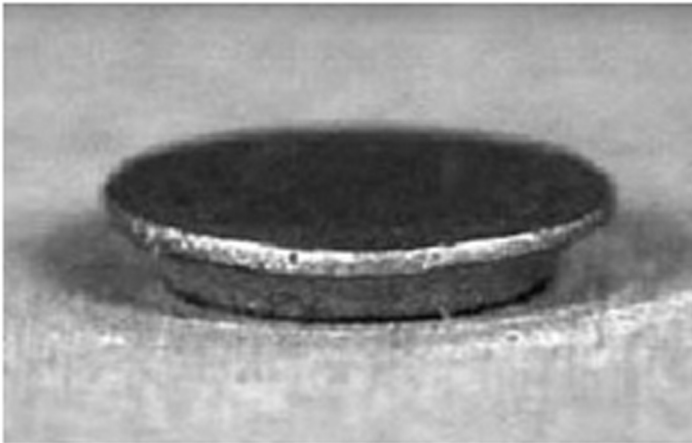
The ability to measure the depth of the aluminium materials (BS170:1987) presented to the SPR machinery can help solve a number of problems associated with incorrectly configured machinery. Incorrect triggering can cause damage to the materials to be joined and/or to the riveting machinery. The vision system is used to compare the presented materials against the expected materials, which is determined by the machine's setting force. For example, if a rivet head is set too deep it could mean that the materials were too thin or the setting force was too



8.10 Extrapolated angular deviation of a rivet.



8.11 Deep set rivet head.



8.12 High set rivet head.

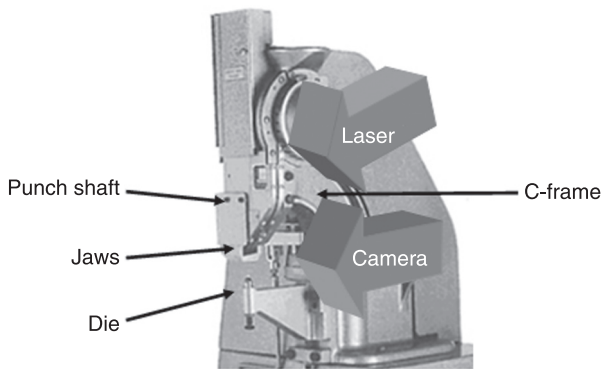
great. Similarly, a high set rivet head could mean that the materials were too thick or the setting force was too small; see Figs 8.11 and 8.12.

Such instances will compromise the joint strength and aesthetics. Monitoring the presented materials and comparing them against the expected materials can therefore facilitate a change in setting force or halt the joining process if necessary. Two measurement techniques have been developed, each of which will be discussed in turn.

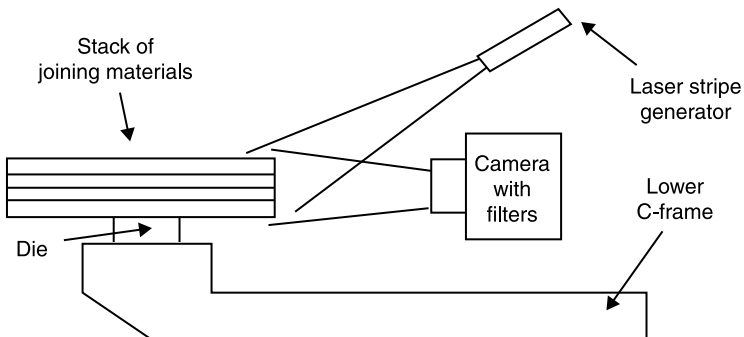
8.3.4 Side material measurement

The measurement technique uses a laser line and optical filters in conjunction with the camera to provide a laser-based measurement system. The laser and camera are fixed to the back of the C-frame at 180° to the front of the machinery as shown in Fig. 8.13. These locations on the rear of the C-frame provide the greatest joint clearance. This is of paramount importance as the system is designed to operate on a robot arm where joint access is the single most limiting factor for SPR joining applications.

The camera is situated perpendicular to the side of the materials to be joined. The laser can be positioned at any point on the C-frame that enables a clear line of sight to the material to be joined as the laser stripe must fall vertically on the stacked materials as presented in Fig. 8.14.

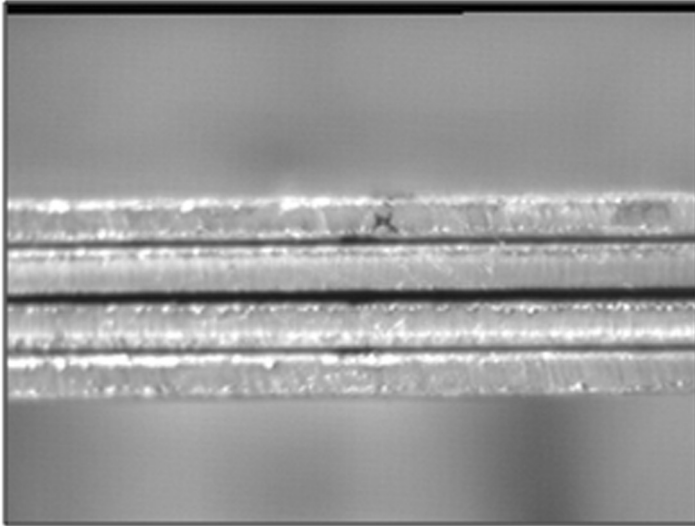


8.13 The camera and laser position for material measurement from the side.

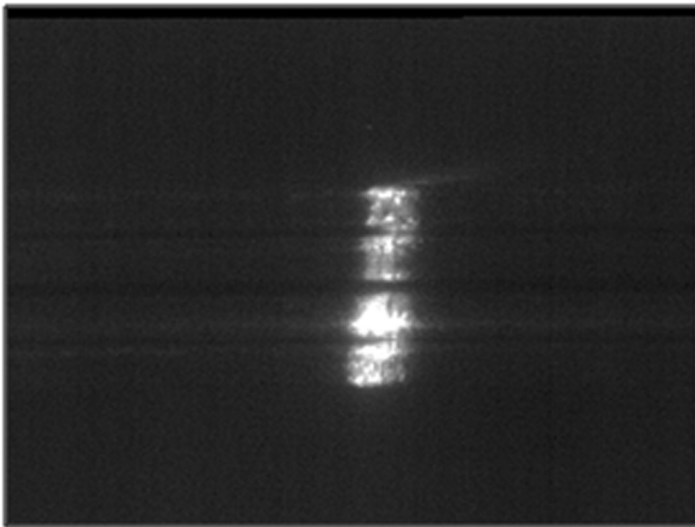


8.14 Diagram of the side laser measurement setup.

Neutral density and red filters are placed directly in front of the camera lens. The neutral density filters reduce the overall brightness and the red filter ensures that only red light that matches the wavelengths generated by the laser (~670 nm) reaches the camera; compare Figs 8.15 and 8.16. The filters help ensure that light



8.15 Stacked aluminium without optical filtering.



8.16 Stacked aluminium with neutral density and red filters.

reflected from the metallic measuring materials is presented to the camera in a way that minimises corrective image pre-processing.

Figure 8.15 shows a stack of four sheets of 1.5mm aluminium without any optical filtering. As can be observed, there are many bright areas; this would require substantial pre-processing before feature extraction could begin. Figure 8.16, on the other hand, shows the same stack of aluminium with the laser line using the optical filters. The filters provide a crude segmentation and minimise further pre-processing. The next step is to perform a threshold, generating a black and white image, which highlights the laser stripe in white as it appears on the side of the measurement materials. The mid-point of the white pixels on each of the y -axes is highlighted as shown in Fig. 8.17.

It is important to notice that the threshold and the red mid-point pixels do not create a continuous line; this is due to gaps between the stacked materials. These gaps have no noticeable effect when joining soft metals such as aluminium, but it is important that the measurement technique is able to distinguish between the overall width, which includes the air gaps, and the joined width, which excludes the air gaps. The most useful measurement is exclusive of air gaps as this enables the material thickness to be checked against the current setting force for suitability.

In order to obtain a real-life measurement from the digital image, the number of red pixels are counted up and calculated according to the distance of the camera from the measurement materials.

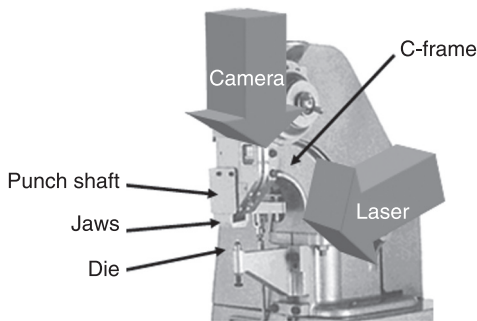


8.17 The measurement materials with a laser line threshold and threshold midpoint.

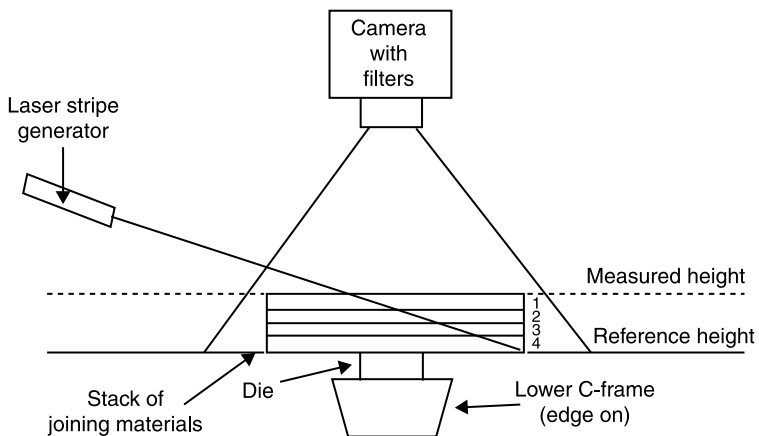
8.3.5 Top material measurement

The top measurement technique also uses a laser line and optical filters in conjunction with the camera for the laser-based measurement system. The camera is directed parallel to the rivet shaft and the laser is positioned at 45° clockwise on the C-frame, as shown in Fig. 8.18.

When the measuring materials are stacked prior to joining, the position of the bottom material is known because it rests on the die. This is known as the reference height and it can be used to derive a thickness measurement for the stacked materials. In order to achieve this, the camera observes the joining materials from above, while the laser stripe is directed into the field of view (FOV) of the camera from the back of the C-frame at an angle of 45°, as shown in Fig. 8.19.

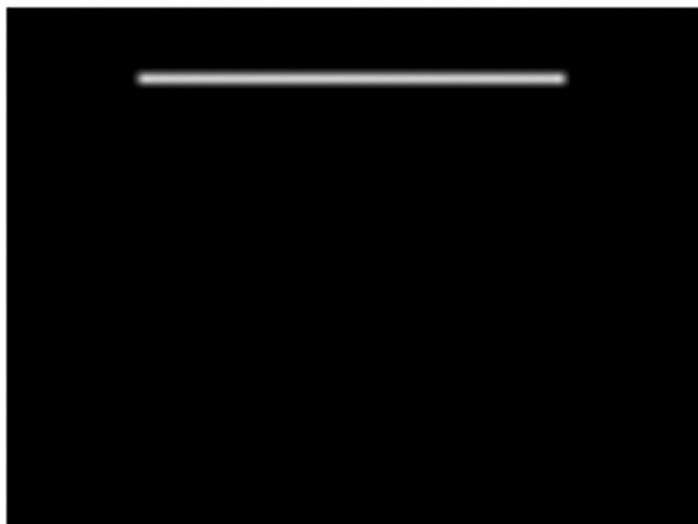


8.18 The camera and laser position for material measurement from the top.



8.19 Diagram of the top laser measurement setup.

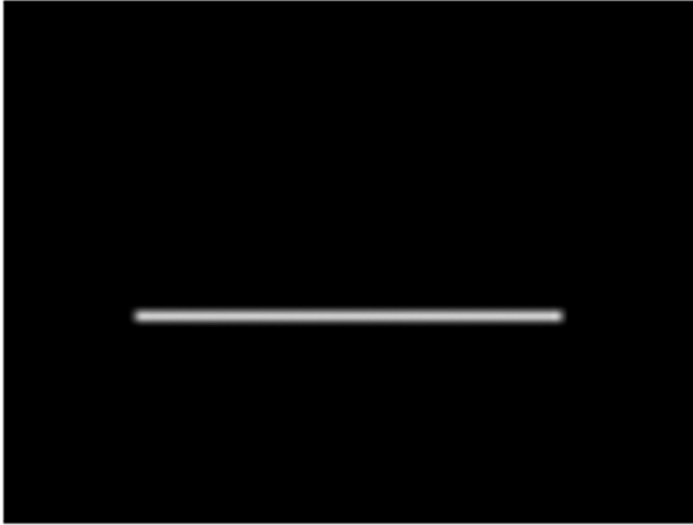
The bottom of the stacked materials is known as the reference height, while the top is known as the measured height. Owing to the laser stripe angle of emission, the position where the stripe intersects the material stack is dependent on the stack height and can be used to measure the depth of the stack. Several examples of what would be observed by the camera in the previous diagram are shown in Figs 8.20–8.23.



8.20 Bottom sheet material (4).



8.21 Third sheet material (3).



8.22 Second sheet material (2).



8.23 Top sheet material (1).

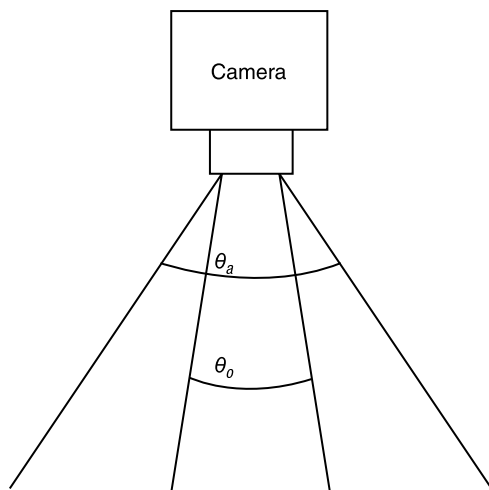
Figure 8.20 shows how the bottom sheet (labelled as 4 in Fig. 8.19) would be observed by the camera. As the thickness of the stack increases the laser stripe will be observed moving further down in the captured images. Figure 8.23 shows how the top sheet (labelled as 1 in Fig. 8.19) would be observed by the camera. The location of the laser stripe as observed by the camera is converted into a pixel

Sunday, February 02, 2014 3:07:02 AM

measurement. However, the variation in measurement height introduces errors to the calculations for scaling pixels to real-life measurements of length (e.g. mm). Therefore the measurements are only accurate at a set distance. This effect can be minimised by changing the camera lens and therefore changing the field of view of the camera [1–3] shown in Fig. 8.24, where θ_a is a wide field of view and θ_o is a narrow field of view. Each of the lenses available for the camera was tested for pixel to millimetre-scaling accuracy in order to determine which lens is best suited to a particular range.

The lenses and the corresponding FOV angles are shown in Table 8.2. Figures 8.25 and 8.26 show an identical scene viewed through 16 mm and 3.6 mm lenses, respectively. Although these figures show the stacked materials being measured from the side, the same is true of any top down measurement.

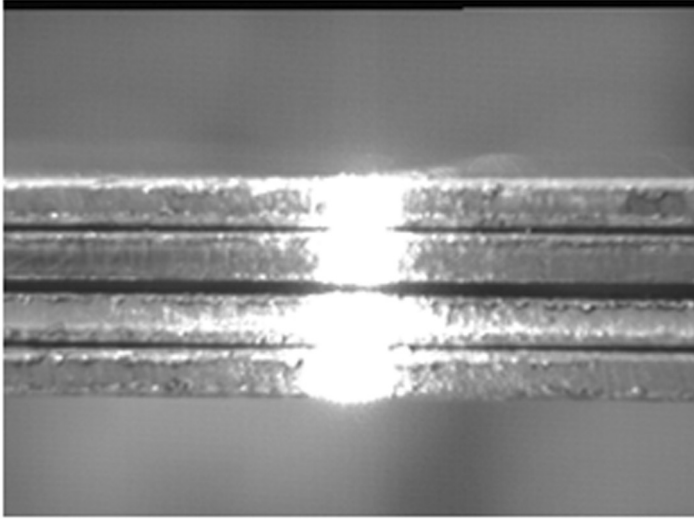
The section of stacked joining materials visible through the 16 mm lens is highlighted in the image captured through the 3.6 mm lens. The 3.6 mm lens offers



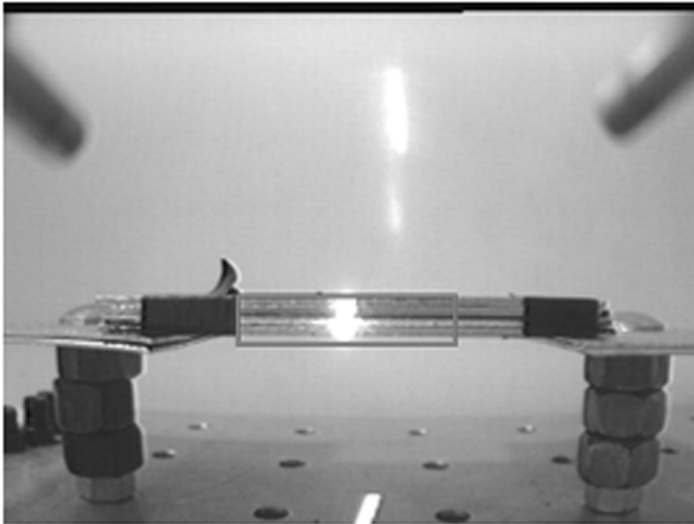
8.24 Camera FOV.

Table 8.2 The lenses available for this experiment

Lens	Field of view
3.6 mm	92°
6 mm	53°
8 mm	40°
12 mm	28°
16 mm	19°



8.25 Stacked measuring materials using the 16mm lens.



8.26 Stacked measuring materials using the 3.6mm lens.

such a wide field of view that the part of the camera housing that holds optical filters in place is visible.

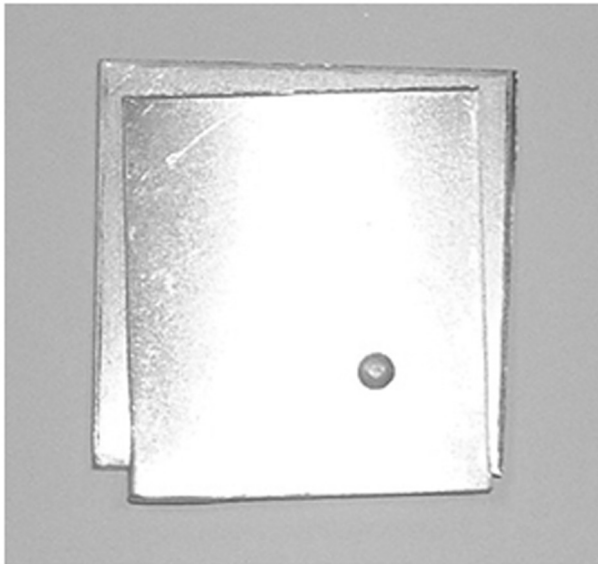
As the FOV of the 16 mm lens is much smaller than the 3.6 mm lens, the camera has to be moved back further from the materials in order to gain focus. Increasing the distance between the camera and measuring materials allows the angular error to be reduced to closer to the ideal of finite distance and 0° FOV, where the trace

lines of the points of interest enter the camera in a parallel beam, no matter from where they originate in the image. In an ideal case, an object of known size would measure the same number of pixels, no matter what distance it was from the camera. By decreasing the FOV and increasing the distance, this assumption still approximately holds, albeit over a short range of distance values.

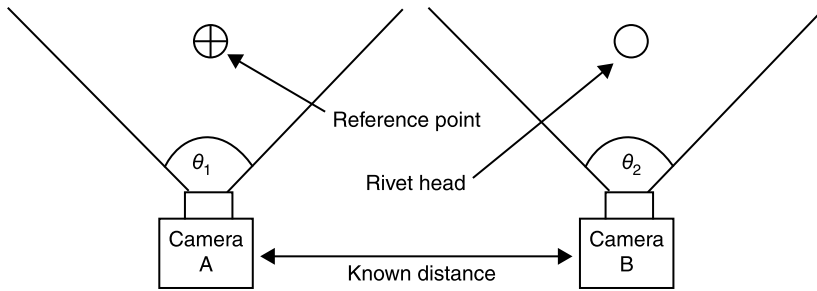
8.3.6 Rivet head position

One of the problems highlighted through discussions with companies involved in the automotive SPR sector was the need to measure the head of a set rivet visually, shown in Fig. 8.27, relative to a defined point.

In order for the rivet head position to be of maximum use, the defined point should be a feature of a known location, which can be used as a reference point. Through careful camera positioning and image processing as shown in Fig. 8.28, one can then calculate the position of the rivet head relative to the feature. Assuming that this feature is a known location, the calculation provides an absolute measurement of the rivet head position. Figure 8.28 shows two cameras: Camera A observes the reference point and Camera B observes the rivet head position. Although the points of interest should appear roughly central to the field of view of the camera, their positions may move slightly over time as a result of machine wear and vibrations. The field of view of cameras A (θ_1) and B (θ_2) depend on the lens used, which depends upon the size of the objects being



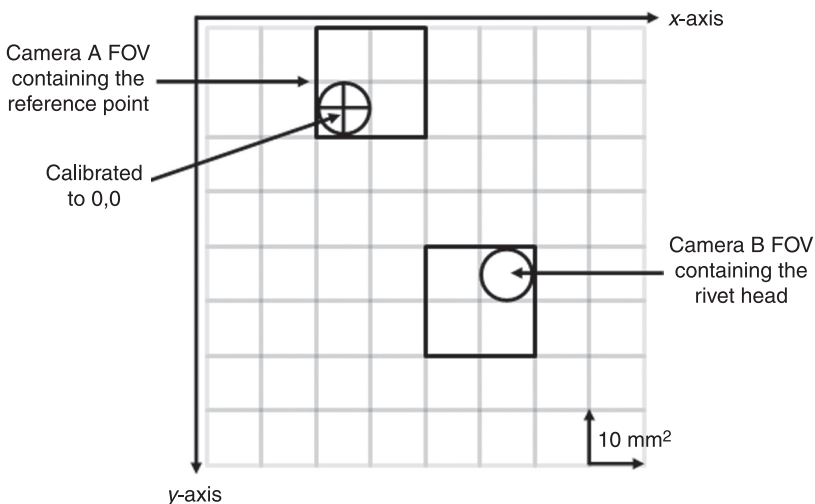
8.27 The head of a rivet after setting into aluminium sheets.



8.28 Rivet head position measurement diagram.

observed. A 16 mm lens with a narrow 19° FOV is used for this technique as the points of interest are relatively small. The narrow lens also reduces any distortions caused by the ‘fish eye’ effect, which can interfere with scaling pixels to real-life measurements.

The algorithm uses a 2D array (x, y) to calculate an absolute measurement of the rivet head position. For example, if the reference point is expected to be observed at 160×120 pixels (the centre of a 320×240 image) in the captured image, but after image processing it is found to be observed at 152×122 pixels, it means that the centre of the reference point is eight pixels to the left and two pixels higher than originally expected. The difference between the expected and actual pixel location must be included in the algorithm and used to fine tune the reference point location. After these adjustments have been made, the reference point location is designated as 0,0 on the 2D array as shown in Fig. 8.29. As the



8.29 Simplified rivet head position array.

distance between Cameras A and B is known, this only leaves fine tuning adjustments of the rivet head location in order to gain an absolute measurement for the rivet head. The same adjustment procedure is applied to Camera B, by comparing the expected pixel values for the location and the actual values.

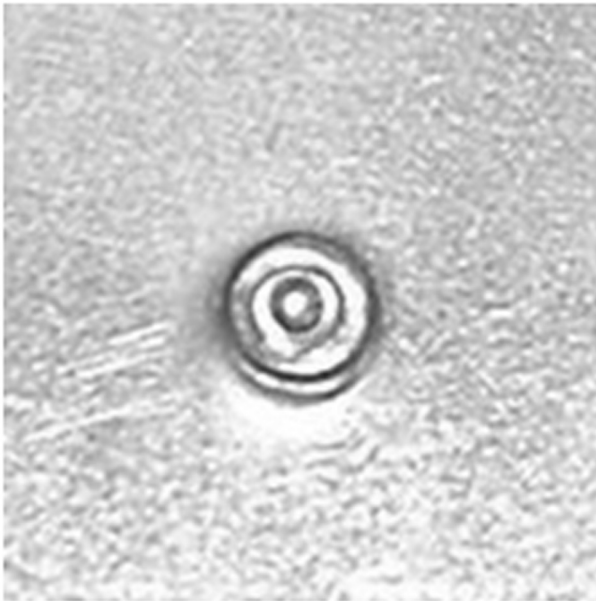
If the above array is used as an example, with the upper left corner of the reference point calibrated as 0,0, the rivet head would be 3,3. The rivet head is therefore 30 mm below and 30 mm to the right of the reference point before any fine tuning adjustments are made. Using Pythagoras' theorem for this simplified example, the distance between the two locations is 4.24 mm to two significant figures. Any pixel adjustments can then be scaled to real-life measurements to give an absolute rivet head location. The complete calculation is as shown below where *RP* is the reference point and *RH* is the rivet head location:

$$RP + RP_{\text{Adjustment}} = 0,0$$

$$\text{absolute measurement} = (RP + RP_{\text{Adjustment}}) - (RH + RH_{\text{Adjustment}})$$

8.3.7 Rivet button diameter

According to work by the Welding Institute, a visual indication of SPR joint quality can be determined by performing dimensional checks of the rivet button formation¹⁸ as shown in Fig. 8.30. The button formation is created as a consequence of the rivet pushing through and displacing the materials that are being joined.



8.30 Button formation pre-processing.



8.31 Button formation post-processing.

Computer vision can perform dimensional checks on this formation using the edge detection and thresholding techniques. This segmentation, in conjunction with other simple image processing techniques that remove non-circular features and random noise, identifies the button formation as shown in Fig. 8.31.

The easiest way to do this is to measure the diameter of the button in pixels across an axis. As the button formation is spherical, it has an infinite number of axes, any of which can be chosen for measurement. It is important that the camera is situated central and perpendicular to the button formation as this removes the need for corrective depth perception processing and reduces the complexity of the algorithm. Once the diameter has been calculated across the axis, it must be scaled to real-life measurements (in units of length) and compared with known good dimensions for that joint. Scaling is depending on how far the camera is from the button formation, in addition to the camera field of view, which is determined by the lens.

8.4 NDT techniques: ultrasonic testing

Evaluation of ultrasonic testing as a means of NDT for the SPR process provided some interesting results. Experimental procedures have focused on the quality of the self-piercing rivet¹⁹, as well as the completed SPR joint²⁰. These locations are inspected using an ultrasonic continuous wave passed through a differential piezoelectric transducer operated at a predetermined frequency. The quality is evaluated by monitoring the variations in the electrical impedance of the transducer presented by both the phase and the amplitude displayed in the complex impedance plane. To test the quality of a self-piercing rivet a spring loaded transducer is built into a probe that can easily be centred on the rivet head. Transducer design is key to the success of this procedure. The tip of the probe is matched to the diameter of the rivet head.

The experimental assessment of self-piercing rivets using ultrasound presented a new technique known as narrowband ultrasound spectroscopy (NBUS)²¹. The difference between the impedance corresponding to the inspected rivet and the

predetermined scatter values that correspond to a sound rivet is monitored. The technique has confirmed that the specially designed spring loaded probe is capable of detecting defects encountered in self-piercing rivets.

During the NDT of a completed SPR joint, the probe is positioned above the rivet head. The SPR transducer excites elastic waves that propagate in different directions and are refracted by the interfaces in the joint [20]. The mechanical load of the joint is transformed into electrical impedance and is measured as the output of the transducer.

The experimental work, as measured by the transducer output, identified differences between various aluminium joints. However, the success of the technique was dependent on operator skill and therefore this raises concerns regarding the robustness of the system. Furthermore, the sensitivity of the transducer means that the technique is unsuitable when working with very thin aluminium as, under these conditions, differences in joints were undetectable.

8.5 Conclusions

It is clear from that computer vision is a potentially valuable addition to existing methods when determining the quality of the mechanical interlock for SPR joints. Employing the aforementioned techniques alongside traditional SPR monitoring techniques can prevent the occurrence of a number of common failures that may compromise the mechanical interlock in terms of both joint strength and product aesthetics. Future work will focus on the development of a computer vision algorithm to identify the relative location of rivet heads using a modified version of the circular Hough transform.

8.6 References

1. Sprovieri, J (April 2007), 'The spectrum of riveting', *Assembly*, 50(4), 46–55. ISSN: 1050-8171.
2. He X, Pearson I and Young K (2008), 'Self-pierce riveting for sheet materials: state of the art', *Journal of Materials Processing Technology*, 199(1–3), 27–36.
3. Messler, Jr. R W (1997), 'Joining technologies for the next century: drivers and directions', *Assembly Automation*, 17(1), 55–65.
4. Henrob Brochure: 'Automotive Applications'. Accessed 09/07/2008. <http://www.henrob.co.uk/GB/downloads.php>
5. Kochan A (2000), 'Audi moves forward with all-aluminium cars', *Assembly Automation*, 20(2), 132–135.
6. Mortimer J (2001), 'Jaguar uses X350 car to pioneer use of self-piercing rivets', *Industrial Robot*, 28(3), 192–198.
7. Mortimer J (2005), 'Jaguar "Roadmap" rethinks self-piercing technology', *Industrial Robot*, 32(3), 209–213.
8. Bollhoff, (2007), Self Pierce Riveting Systems for Automatic Processing. Flexible, economic and safe, ABF/MBF/MTF Product Catalogue, Bollhoff Fastenings Ltd, Midacre, Willenhall, West Midlands, WV13 2JW, UK.

9. Henrob Brochure: 'Introduction to SPR'. Accessed 09/07/2008. <http://www.henrob.co.uk/GB/downloads.php>
10. Henrob Brochure, 'General Industry Applications'. Accessed 09/07/2008. <http://www.henrob.co.uk/GB/downloads.php>
11. Mortimer (2003), 'Mix of robots used for Jaguar's aluminium-bodied XJ luxury car', *Industrial Robot*, 30(2), 145–151.
12. Orbitform Product Catalogue (2006), 1600 Executive Drive, Jackson, MI 49203, USA.
13. Johnson P. (2013), SBC, University of Shanghai for Science and Technology, 1195 Fuxing Zhong Road, Shanghai 200031, People's Republic of China.
14. Han L (2007), Warwick Manufacturing Group, University of Warwick, Coventry, CV4 7AL, UK.
15. Stepinski T (2006), Uppsala University, Uppsala, Sweden.
16. Doidge Fastenings Ltd. Type 120 Machine, accessed 16/07/2008, <http://doidge.com/original/english/machine120.html>.
17. TWI World Centre for Materials Joining Technology, *High Speed Sheet Joining – by Mechanical Fastening*, January/February 1996 Bulletin.
18. Stepinski T (2006), 'Assessing quality of self-piercing rivets using ultrasound', *Proc. of the 9th European Conference on NDT*, Berlin, 25–29 Sept. 2006.
19. Han L, Hewitt R, Shergold M, Chrysanthou A. *et al.*, (2007), 'An evaluation of NDT for self-pierce riveting', SAE Technical Paper 2007-01-1364; doi:10.4271/2007-01-1364.
20. Stepinski T and Engholm M (2006), 'Narrowband ultrasonic spectroscopy for inspecting multilayered aerospace structures', *9th European Conference on NDT*, Berlin, September 2006.

Optimization of the strength of self-piercing rivets (SPRs)

X. SUN, Pacific Northwest National Laboratory, USA

DOI: 10.1533/9780857098849.2.149

Abstract: This chapter discusses strength optimization and failure mode prediction of self-piercing rivets (SPRs) for automotive applications. The limit load-based strength estimator is used to estimate the static strength of an SPR under a cross tension loading configuration. Failure modes associated with the estimated failure strength are also predicted. Experimental strength and failure mode observations are used to validate the model. It is shown that the strength of an SPR joint depends on the material and gauge combinations, rivet design, die design and riveting direction. The rivet strength estimator is then used to optimize the rivet strength by comparing the measured rivet strength and failure mode with the predicted ones. Two illustrative examples are used in which rivet strength is optimized by changing rivet design and riveting direction from the original manufacturing parameters.

Key words: self-piercing rivets, rivet strength, analytical rivet strength estimation, rivet strength optimization, dissimilar materials joints.

9.1 Introduction

The increasing use of dissimilar lightweight, high-strength and coated materials has led the automotive industry to re-examine traditional methods of components assembly, as direct welding of these materials is difficult or impossible. Alternative joining techniques encompass a broad range of methods ranging from threaded fasteners (nuts, bolts and screws), to different forms of rivet and mechanical interlocking methods¹⁻². In the previous chapters of this book, an introduction to the self-piercing riveting process (SPR) has been made and joint properties in terms of static and dynamic strength have been discussed.

This chapter will introduce a limit load-based approach to estimate and further optimize SPR strength³. As previously discussed, the difference between SPR and conventional riveting is that SPR does not require a pre-drilled hole. This brings great benefits in terms of reducing production costs and ease of automation compared with conventional riveting. An SPR joint is produced by placing the sheets to be joined between a punch and a die in a press tool and driving a tubular rivet into the sheets. The rivet pierces the top sheet and then expands (flares) into the lower sheet, normally without piercing through it, and forms a mechanical interlock. The strength of the riveted joint is primarily determined by the strength

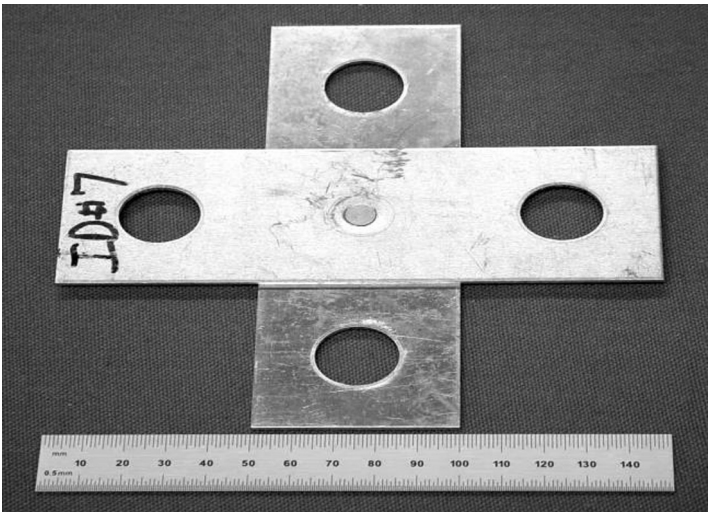
of the mechanical interlock mechanism between the expanded rivet shank and the base metal that has been cold worked.

Although the SPR technology has been used in selected platforms in the automotive industry in recent years, there are still a number of barriers to the wider application of this joining method. Among them are the lack of performance targets and limited performance data available for joints made of dissimilar metals. In order to predict rivet strength, various researchers have recently used finite element analysis to evaluate the static and dynamic strength of SPR under different loading conditions. For example, Strömstedt simulated the crash testing of self-piercing rivet lap shear joint specimens under three different velocities ⁴, while Westerberg simulated the crash testing of self-piercing rivet joints under coach peel loading condition ⁵. Both of these authors studied DDQ steel and DP600 steel as the head and tail side materials, and a common rivet configuration was assumed for these two material combinations. For the actual riveting process, the mechanical properties of the materials have a significant influence on the clinching mechanism of the riveted area and hence on the resulting strength of the rivet joints. As will be shown in this chapter, the rivet clinching mechanism cannot be simply assumed to be the same for combinations of different materials. Moreover, simulations like these are time-consuming and cannot be routinely performed by manufacturing engineers.

In this chapter, a simple limit load-based analytical model is first introduced to estimate the static cross tension strength of an SPR using the characteristics of the rivet cross sections. The model is first validated by comparing the predicted strength and failure modes with experimental observations from various joint populations. The estimator is next used to optimize the static cross tension strength of an SPR for different material and gauge combinations by optimizing rivet designs and riveting directions. The objectives of this chapter are to: (i) provide automotive design engineers with a quick estimate of the rivet strength for certain material and gauge combinations such that the total number of rivets needed and their optimized locations can be determined during the early design stage and (ii) provide manufacturing engineers with some performance target estimations before actual joints are fabricated and tested. If the tested rivet strength for a certain materials combination is much lower than the analytically estimated strength, it may be necessary to improve the riveting process further, such that the targeted joint performance can be achieved.

9.2 Rivet strength estimation

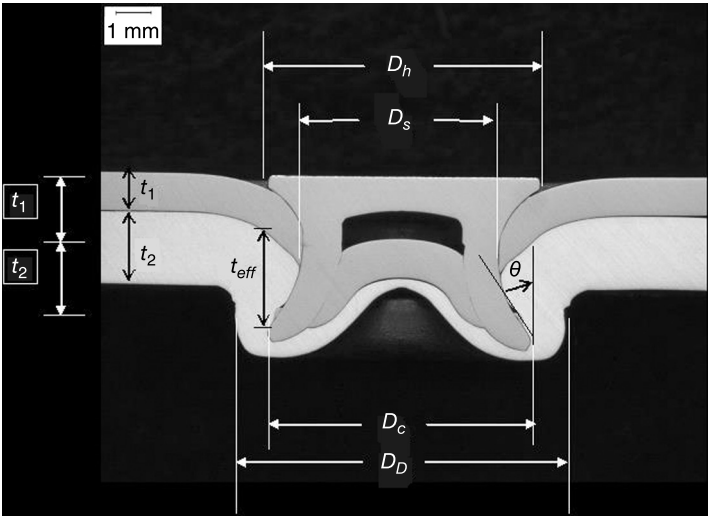
The strength evaluation of a single joint sample typically consists of joint coupon tests with three configurations: cross tension, tensile shear (also known as lapshear) and coach peel ^{3,6,7}. Among these three loading conditions, we will focus on cross tension since it is a nearly symmetrical loading condition around the rivet joint and therefore the easiest to analyze (see Fig. 9.1). Moreover, previous studies



9.1 SPR joint coupon for cross tension loading condition.

have shown that the joint strength under lapshear and coach peel loading conditions can be related to its cross tension strength⁷.

As an illustrative example, Fig. 9.2 shows a typical cross section of a rivet joint of a 1 mm steel to a 2 mm aluminum sheet. Under cross tension loading, the base metal surrounding the rivet head is pulled against the rivet head and the base



9.2 Cross section through a Henrob rivet, joining 1 mm steel to 2 mm aluminium.

metal on the tail side surrounding the rivet tail is pulled against the flared portion of the rivet tail. The resulting rivet strength and the corresponding failure mode are therefore determined by the relative strength of the head side and the tail side of the rivet joint. It should be mentioned that the rivet shank is also an important load transfer link for the joint. Theoretically, failure in the rivet shank itself should also be considered as a possible failure mode for the rivet joint under tension loading. However, the rivets are made of a stronger material (typically a martensitic boron steel with very high yield strength of about 1500 MPa⁵) and rivet shank failure rarely occurs in actual static overloading tests. Extensive experimental observations confirm that the failure mode of an SPR under static cross tension loading is either by the rivet tail being pulled out from the base material or by the rivet head being pulled out of the base material⁷. Attention will thus focus on these two main failure modes: head pullout or tail pullout.

As indicated in some earlier studies⁸, the strength of the rivet depends on the material thickness, rivet material and design, and the die design. In order to estimate the tensile strength of the rivet, the material strengths on each sides of the rivet need to be estimated and the lower value will represent the final joint strength³.

9.2.1 Strength estimation for head pullout

Under uniaxial tension loading, assuming that the rivet joint and the loading condition are perfectly axi-symmetric, the whole circumference of the head sheet of radius D_h and the whole circumference of the tail sheet of radius D_c should carry the applied load. In order for the rivet joint to fail by the head pullout mode, the rivet head would have to plastically deform through the entire thickness of the head sheet at radius D_h , such that the base metal along the entire circumference of radius D_h would fail due to extensive plastic deformation. For most metals, the load carrying sheet thickness should be close to the head side sheet thickness t_1 . Therefore, the head pullout strength can be estimated as:

$$F_h^T \approx \eta_h \beta_h t_1 \pi D_h \sigma_h \quad [9.1]$$

where

F_h^T – rivet strength for head pullout failure;

σ_h – yield strength of the head side material;

t_1 – material thickness on the head side;

β_h – empirical coefficient for head side sheet bending induced thickness reduction,

$\beta_h = 1$ for $t_1 > 1.0$ mm, $\beta_h \approx 0.7$ for $t_1 \leq 10$ mm;

η_h – empirical coefficient for parent material degradation due to the piercing process on the head side.

Similar lower bound limit load analysis was used in^{9,10} to estimate spot-weld strength under tension-loading. The yield strength is used here instead of the

ultimate tensile strength because the effects of necking and work hardening are not taken into account. In addition, rivet head failure is not considered and it is assumed that the rivet is made of a much stronger material than the base metal.

It should also be mentioned that β_h and η_h in Eq. 9.1 are empirical parameters to account for thin sheet bending and material degradation during the riveting process. When the sheet for the head side is very thin, typically less than 1 mm, severe head side sheet bending would occur prior to the final head pullout failure. The bending induced sheet rotation would reduce the effective thickness under tension loading and a correction coefficient, β_h , should be introduced for thin sheets on the head side. This is particularly true for weaker material, i.e. aluminum alloys, on the head side. Typically, $\beta_h=1$ should be used for $t_1>1.0$ mm, and $\beta_h\approx 0.7$ should be used for $t_1\leq 1.0$ mm.

For materials with good ductility, such as low carbon steel, AA5754 and AA5182-O with elongation values greater than 15%, material degradation around the rivet head due to the piercing process is not significant. Therefore, the coefficient η_h should be set to 1.0. For materials with limited ductility, such as aluminum extrusions and castings, the coefficient η_h should be greater than 0, but less than 1. The exact value of η_h depends upon the degree of material degradation caused by the piercing process. For aluminum extrusions and castings, past experience suggests that the coefficient η_h can be chosen to be around 0.5, to account for the base material degradation around the riveted area.

9.2.2 Strength estimation for tail pullout

If the rivet fails by tail pullout, the flared portion of the rivet tail needs to shear through an effective thickness of the sheet material on the tail side, denoted by t_{eff} in Fig. 9.2.

The rivet strength under tail pullout mode can again be estimated as:

$$F_t^T \approx \beta_t \eta_t t_{eff} \pi D_c \sigma_{t-s} \quad [9.2]$$

where

- F_t^T – rivet strength for tail pullout failure;
- σ_{t-s} – yield strength in shear for the virgin material on the tail side;
- t_{eff} – effective material thickness on the tail side, see Fig. 9.2;
- D_c – diameter of the clinched portion of the rivet tail, see Fig. 9.2;
- β_t – empirical coefficient for tail side sheet bending induced thickness reduction,

$$\beta_t = 1 \text{ for } t_2 > 1 \text{ mm, } \beta_t \approx 0.7 \text{ for } t_2 \leq 1.0 \text{ mm}$$

η_t – empirical coefficient to take into account the degradation of the parent material yield strength due to the riveting process on the tail side.

Again, the coefficient η_t should be 1.0 for materials with elongation greater than 15% and η_t can be chosen to be 0.5 for extrusions or castings on the tail end. This

will be illustrated in the validation examples. A correction factor β_p , similar to β_h , is introduced to account for the tail side sheet thickness reduction due to bending when thin sheet is used on the tail side. Again, standard values of β_t should be used; for $t_2 > 1$ mm, $\beta_t = 1$ and if $t_2 \leq 1.0$ mm, $\beta_t \approx 0.7$ should be used. Since it is very difficult to obtain an accurate value of the shear strength of materials that exhibit some ductility, obtaining σ_{t-s} data for all the materials of interest may not be possible. It is generally agreed that the shear yield strength of ductile cast iron is about 0.6 to 0.7 times its tensile yield strength¹¹. Taking a similar approach, it can be assumed that the shear yield strength of the material on the tail side is about 70% of its tensile yield strength. Therefore Eq. 9.2 takes the form:

$$F_t^T = 0.7\beta_t\eta_{t\text{eff}}\pi D_c\sigma_t \quad [9.2a]$$

in which σ_t represents the yield strength of the virgin material on the tail side.

It is important to note that the tail pullout strength estimation presented above is based on the assumption that sufficient rivet tail flare is achieved during the riveting process such that a good material interlocking mechanism has been created at the rivet tail. The degree of rivet tail 'flaring' can be quantified with the flaring angle θ as shown in Fig. 9.2. A large flaring angle θ usually suggests a good interlocking mechanism. On the other hand, a near zero flaring angle θ suggests that the rivet tail was simply inserted into the tail side material without sufficient interlocking, and therefore it would be very easy to slip out upon tensile loading.

9.2.3 Strength estimation and validation

The static rivet tensile strength can now be determined as the lower value of the head and tail pullout strength:

$$F^T = \min(F_h^T, F_t^T) \quad [9.3]$$

As indicated by Eqs 9.1 and 9.2a, the rivet strength in tension directly depends on the sheet thickness, the sheet material properties and the configuration of the riveted area. In most cases, when the two sheets being riveted are made of the same material of equal thickness, rivet tail pullout appears to be the primary failure mode because the shear yield strength of the material is lower than its tensile yield strength provided that the values of D_c and D_h are close to each other.

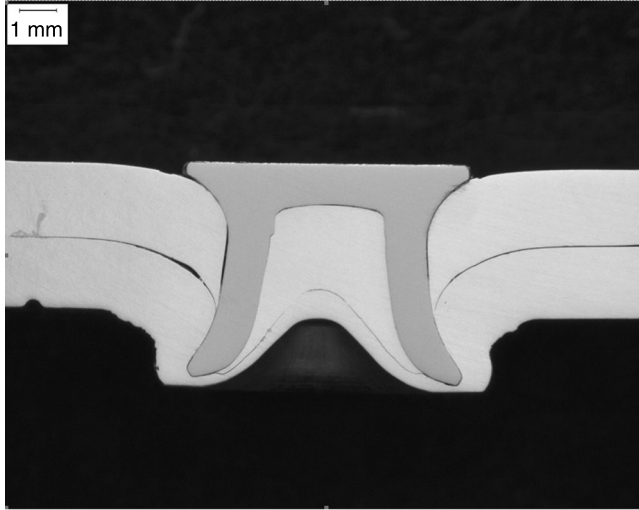
Next, some experimental cases will be used to validate the above strength estimator for SPR of different materials combinations. First, the tensile yield strengths for the materials used in the validation cases are listed below¹¹⁻¹⁴:

SAE1008: 170 MPa
 SAE1010: 180 MPa
 HSLA350: 350 MPa
 DP600: 360 MPa
 AA5754-O: 110 MPa

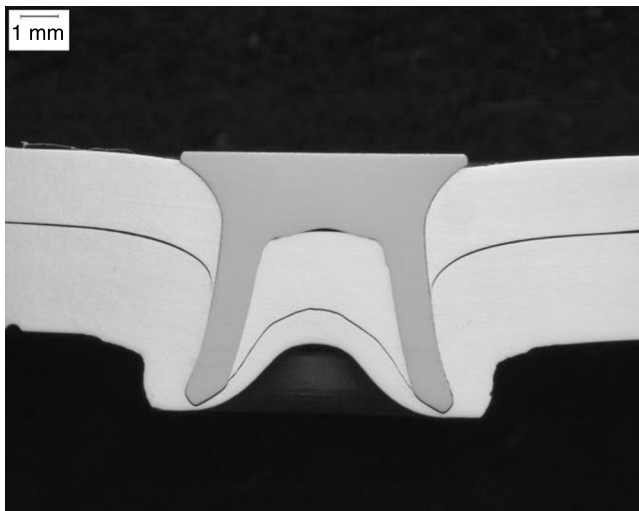
AA5182-O: 130 MPa

AA6063-T6: 214 MPa

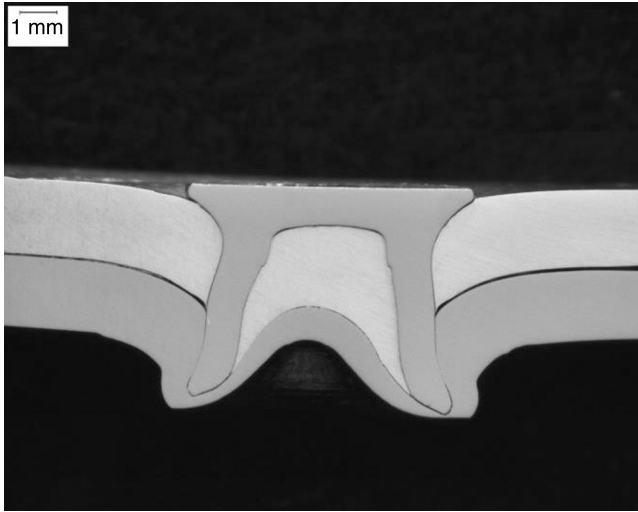
The rivet pins used in the validation cases have a common shank diameter of 5 mm and head diameter of 7.5 mm. The rivet length and the shape of the die used can vary from case to case. Figs. 9.3–9.11 illustrate the metallurgical cross



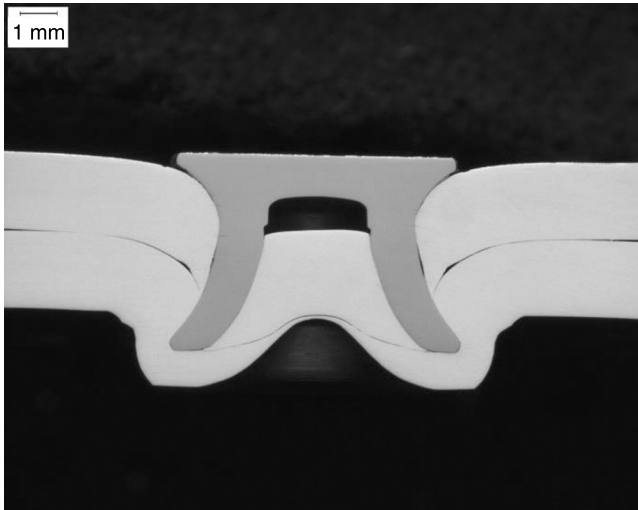
9.3 Cross section for SPR of 2 mm AA5754-O (head side)/2 mm AA6063-T6 (tail side).



9.4 Cross section for SPR of 2 mm AA5754-O (head side)/3 mm AA6063-T6 (tail side).

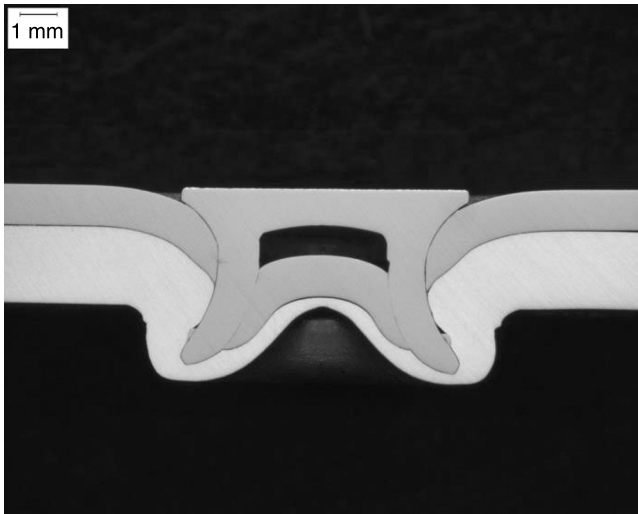


9.5 Cross section for SPR of 2 mm AA5754-O (head side)/1.9 mm HSLA350 (tail side).

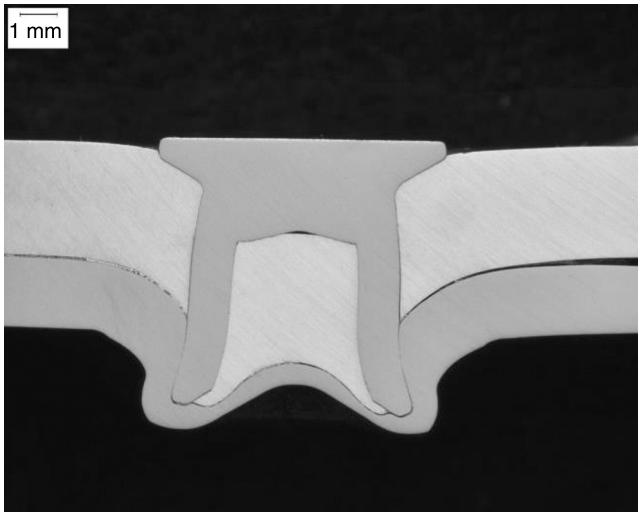


9.6 Cross section for SPR of 2 mm AA5182-O (head side)/2 mm AA5182-O (tail side).

sections of the SPR joints for various material combinations. Table 9.1 shows the detailed comparisons of predicted strength versus measured strength and predicted failure modes versus experimentally observed failure modes, as well as the various parameters used in Eqs 9.1 and 9.2a for the different SPR material

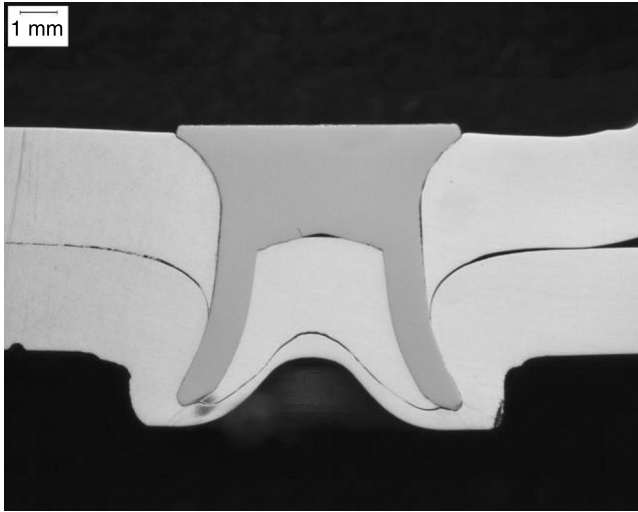


9.7 Cross section for SPR of 1 mm HSLA350 (head side)/2 mm AA5182-O (tail side).

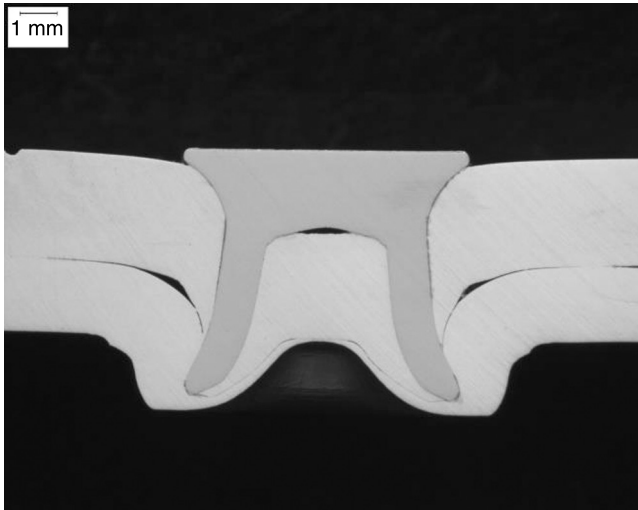


9.8 Cross section for SPR of 3 mm AA5754-O (head side)/1.9 mm SAE1010 (tail side).

combinations. Fig. 9.12 compares the predicted and measured rivet strength for the above nine SPR populations. Considering the simple nature of the analysis procedure, reasonably good strength estimation has been obtained. In addition, the failure mode for each case is also correctly predicted by the analysis procedure.

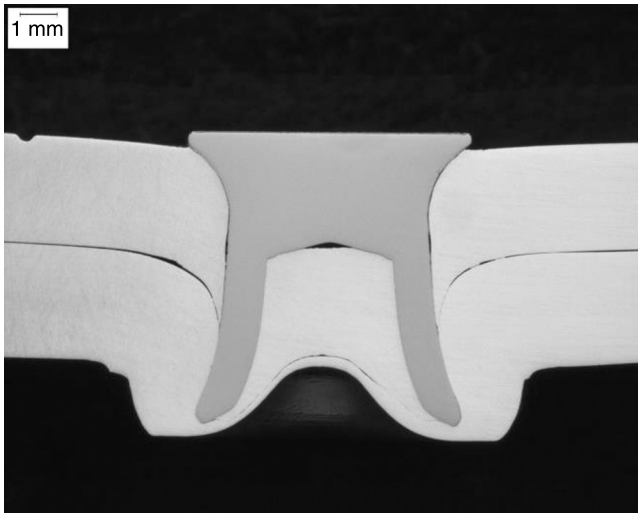


9.9 Cross section for SPR of 3 mm AA5754-O (head side)/3 mm AA6063-T6 (tail side).



9.10 Cross section for SPR of 3 mm AA5754-O (head side)/2 mm AA6063-T6 (tail side).

It should be mentioned that even though this estimator has been developed using joints of two layers of materials, it can be directly applied to joints made up of three or more layers of material stack-ups. In addition, the failure load predicted by tail pullout is usually higher than the experimentally measured strength



9.11 Cross section for SPR of 3 mm AA6063-T6 (head side)/3 mm AA5754-O (tail side).

data because the effects of lubrication on the sheet metal are not considered in this study.

9.3 Rivet strength optimization

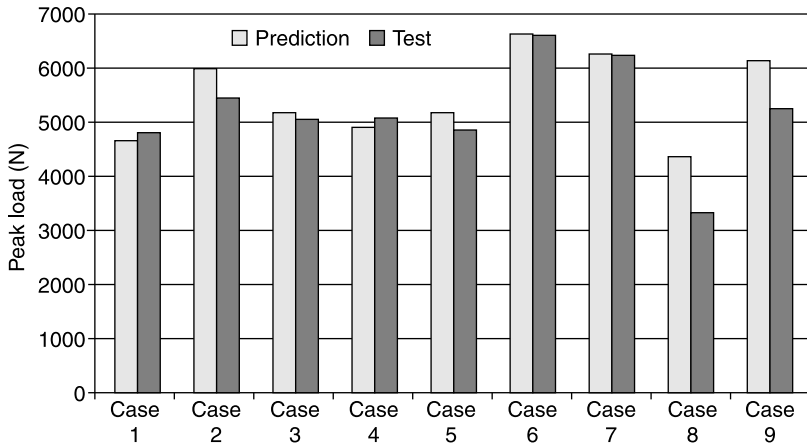
The above rivet strength estimation procedure can be used to optimize further the static rivet strength. If the experimentally measured joint strength is much lower than the predicted rivet strength, or if the observed failure mode does not correspond to prediction, improvements in the material interlocking mechanism need to be made by optimizing the riveting parameters, i.e. rivet design and/or riveting direction, to increase t_{eff} and D_c in Eq. 2a. Two illustrative examples will be used to demonstrate this process.

9.3.1 Strength optimization with rivet length

An SPR joint between 5182-O (2 mm) and DP 600 (1.6 mm) will be used as the example. During the first round of the riveting trials, a rivet pin with a 5 mm shank diameter, 7.5 mm head diameter and 6 mm rivet length was used. The riveting parameters and die used are summarized in Table 9.2. Using the softer aluminum as the head side material, the resulting rivet cross section is shown in Fig. 9.13. This joint population is labeled as ID 12.

Table 9.1 Comparisons of estimated rivet strength and failure mode with experimental observations

Case No.	Material combination (head/tail)	t_i (mm)	η_h	β_h	D_h (mm)	σ_h (MPa)	F_h^T (N)	t_{eff} (mm)	η_t	β_t	D_c (mm)	σ_t (MPa)	F_t^T (N)	Estimated strength (N)	Predicted failure side	Tested strength (N)	Tested failure side
1	AA5754-O/AA6063-T6 extrusion	2	1	1	7.5	110	5181	2.7	0.5	1	7.4	214	4699	4699	Tail	4826	Tail
2	AA5754-O/AA6063-T6 extrusion	2	1	1	7.5	110	5181	3.57	0.5	1	7.14	214	5995	5181	Head	5471	Head
3	AA5754-O/HSLA350	2	1	1	7.5	110	5181	2.7	1	1	7.1	350	14747	5181	Head	5026	Head
4	AA5182-O/AA5182-O	2	1	1	7.5	130	6123	2.3	1	1	7.5	130	4931	4931	Tail	5130	Tail
5	HSLA350/AA5182-O	1	1	0.7	7.5	350	5773	2.5	1	1	7.3	130	5215	5215	Tail	4920	Tail
6	AA5754-O/SAE1010	3	1	1	7.5	110	7772	2.64	1	1	6.4	180	6685	6685	Tail	6606	Tail
7	AA5754-O/AA6063-T6 extrusion	3	1	1	7.5	110	7772	3.57	0.5	1	7.5	214	6297	6297	Tail	6272	Tail
8	AA6063-T6 extrusion/AA5754-O	3	0.5	1	7.5	214	7560	2.5	1	1	7.3	110	4412	4412	Tail	3336	Tail
9	AA6063-T6 extrusion/AA5754-O	3	0.5	1	7.5	214	7560	3.6	1	1	7.1	110	6180	6180	Tail	5294	Tail



9.12 Comparisons of predicted and measured rivet strength for nine rivet populations

Based on Eq. 9.1, an initial estimation of the rivet head pullout strength should be:

$$F_h^T = \eta_h \beta_h t_1 \pi D_h \sigma_h = 1.0 * 1.0 * 2 * 3.14 * 7.5 * 130 = 6100 \text{ N}$$

The rivet cross section in Fig. 9.13 indicates that a very small flaring angle θ was obtained for this joint. Assuming that rivet tail slip-out will not occur under cross tension, the rivet strength for tail pullout can be estimated as:

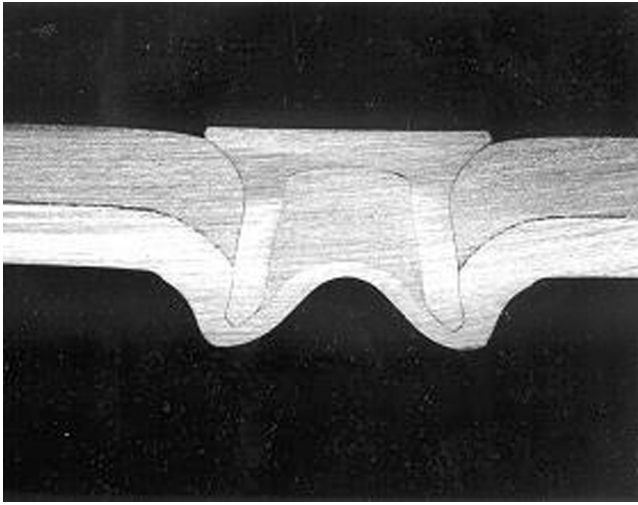
$$F_t^T = 0.7 \eta_t \beta_t t_2 \pi D_c \sigma_t = 0.7 * 1 * 1 * 1.4 * 3.14 * 6.1 * 370 = 6948 \text{ N}$$

Therefore under this assumption, the predicted failure mode should be rivet head pullout. However, the experimentally measured cross tension load was only 3700 N and the failure mode observed was tail pullout; see Fig. 9.15(a). Further examination of the failed samples indicates that the rivet pin was simply pulled out of the tail side material without shearing through it. The joint tensile strength was primarily generated through friction force between the rivet pin tail and the tail side material.

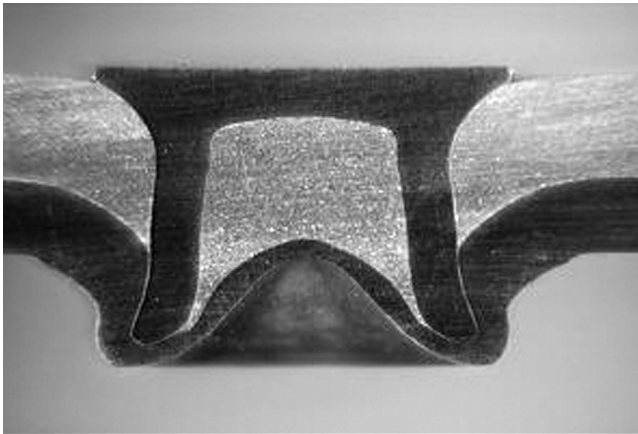
The discrepancies of failure mode and rivet strength between observation and prediction suggest that the rivet tail clinching mechanism needs to be improved. Noticing that the rivet tail has a much smaller diameter ($\sim 7 \text{ mm}$) than the die diameter (9 mm), a slightly longer rivet with length 6.5 mm was used in the second riveting trial while keeping all the other riveting parameters unchanged (see Table 9.2). This joint population is labeled as ID 12L and its cross section is shown in Fig. 9.14. With less than 8% increase in rivet length, ID 12L has much better clinching mechanism than ID 12 in terms of t_{eff} , D_c and θ . Under cross tension loading conditions, ID 12L failed by the head pullout mode

Table 9.2 Riveting parameters for ID12 and ID12L

Joint ID	Top material	Top thickness (mm)	Bottom material	Bottom thickness (mm)	Joint stack	Henrob Rivet P/N	Henrob Die P/N	Pre-Clamp pressure	Setting pressure
12	5182-O	2.0	DP 600	1.6	3.6	C50644AY04	DZ09-000	123	230
12L	5182-O	2.0	DP 600	1.6	3.6	C50D44AY04	DZ09-000	120	240



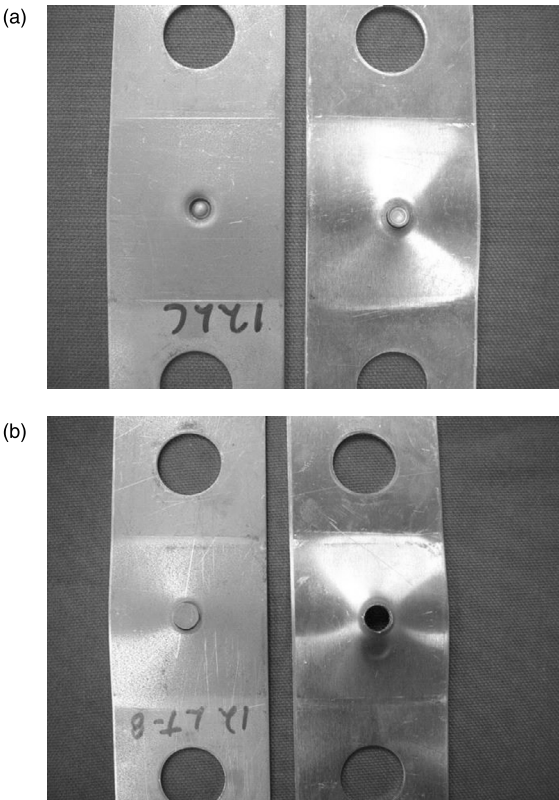
9.13 ID 12: SPR of 2 mm AA5182-O (head)/1.6 mm DP 600 (tail) with 6 mm rivet length.



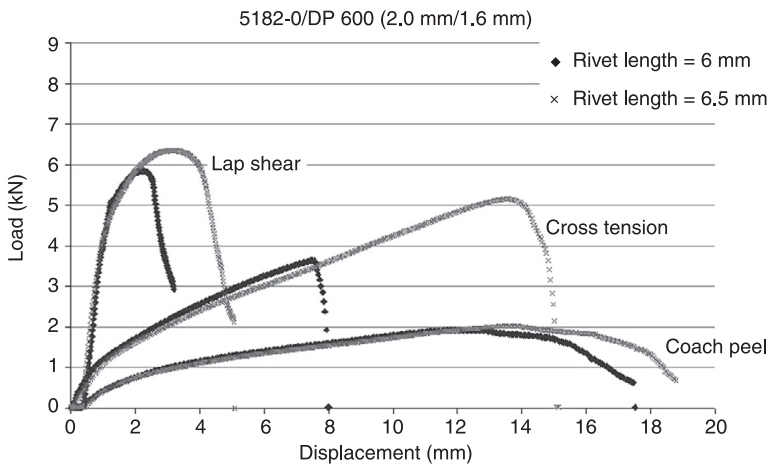
9.14 ID 12L: SPR of 2 mm AA5182-O (head)/1.6 mm DP 600 (tail) with 6.5 mm rivet length.

and the measured rivet strength increased to 5300 N (averaged over 30 samples). Fig. 9.15(b) illustrates the typical failure mode of ID 12L in cross tension.

A static rivet strength test was also performed under lapshear and coach peel loading conditions. Fig. 9.16 compares the static load versus displacement behavior of the two rivet populations. It is interesting to note that an 8% increase in rivet length resulted in about 45% increase in its cross tension strength, while keeping all the other riveting parameters unchanged. Moreover, the better interlock



9.15 Cross tension failure mode comparison of ID 12 and ID 12L:(a) ID 12 tail pullout, (b) ID 12L head pullout.



9.16 Load versus displacement comparison of ID 12 and ID 12L.

mechanism achieved by the longer rivet also provides larger displacement to failure, therefore significantly improving the joint's energy absorption levels.

It is worth noting that the rivet tail clinching mechanism could potentially be further improved with optimized rivet pin length and die design. However, the SPR static cross tension strength for this materials combination cannot be further increased for this pin design because the desired failure mode has already been achieved.

9.3.2 Strength optimization with piercing direction

Next, SPR between 5182-O (2 mm) and HSLA350 (1 mm) is used as another joint optimization example. For this materials combination, a rivet pin that has 5 mm shank diameter, 7.5 mm head diameter and 6 mm rivet length was used. The riveting parameters and die used are summarized in Table 9.3. Following the industry rule of thumb by putting the softer aluminum at the head side, the resulting rivet cross section is shown in Fig. 9.17. This joint population is labeled as ID 10.

Based on Eq. 9.1, an initial estimation of the rivet strength by head pullout should be:

$$F_h^T = \eta_h \beta_h t_1 \pi D_h \sigma_h = 1.0 * 1.0 * 2. * 3.14 * 7.5 * 130. = 6100 \text{ N}$$

Assuming sufficient interlocking mechanism, the rivet strength by tail pullout should be:

$$F_t^T = 0.7 \eta_t \beta_t t_{eff} \pi D_c \sigma_t = 0.7 * 1. * 0.7 * 1. * 3.14 * 7.1 * 350. = 3823 \text{ N}$$

Therefore the predicted rivet strength is 3823 N and the failure mode should be by rivet tail pullout from the steel side. In this case, the experimentally observed failure mode was indeed by tail pullout as predicted, but the measured rivet strength was 2900 N. The reason that the measured strength was considerably lower than the predicted strength could again be some degrees of rivet pin slip-out. In this case, because the tail side material is so thin, the tail side sheet rotation further aggregates the rivet tail slip-out even though an acceptable material interlock had been achieved by the riveting process.

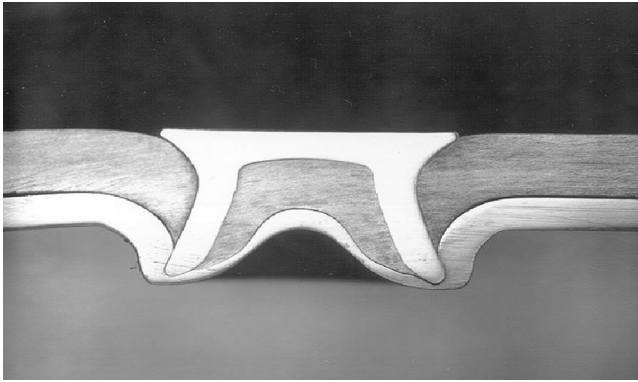
To maximize the joint strength, failure should occur on the softer material side, that is, the aluminum side. In order to achieve this, the piercing direction was changed and HSLA350 was used as the head side material. Using the same riveting parameters as shown in Table 9.3, the resulting rivet cross section is shown in Fig. 9.18. This joint population is labeled as ID 11. By using the strength estimation routine in Eqs 1–3 and Fig. 9.18, the estimated strength for this rivet joint is:

$$F^T = \min \left\{ \begin{array}{l} F_h^T = \eta_h \beta_h t_1 \pi D_h \sigma_h = 0.7 * 1 * 1. * 3.14 * 7.5 * 350. \approx 5770 \text{ N} \\ F_t^T = 0.7 \eta_t \beta_t t_{eff} \pi D_c \sigma_t = 0.7 * 1. * 1. * 2.5 * 3.14 * 7.3 * 130. \approx 5217 \text{ N} \end{array} \right\}$$

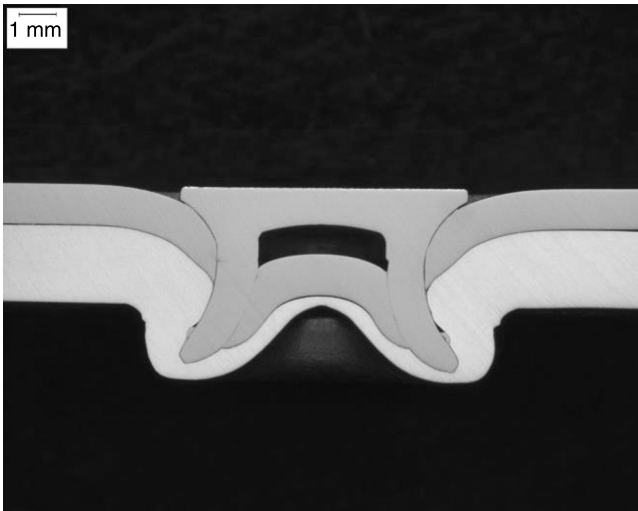
= 5217 N (tail pullout)

Table 9.3 Riveting parameters for ID10 and ID11

Joint ID	Top material	Top thickness (mm)	Bottom material	Bottom thickness (mm)	Joint stack	Henrob rivet P/N	Henrob die P/N	Pre-Clamp pressure	Setting pressure
10	5182-O	2.0	HSLA350	1.0	3.0	C50644AY04	DZ09-000	120	230
11	HSLA350	1.0	5182-O	2.0	3.0	C50644AY04	DZ09-000	120	230

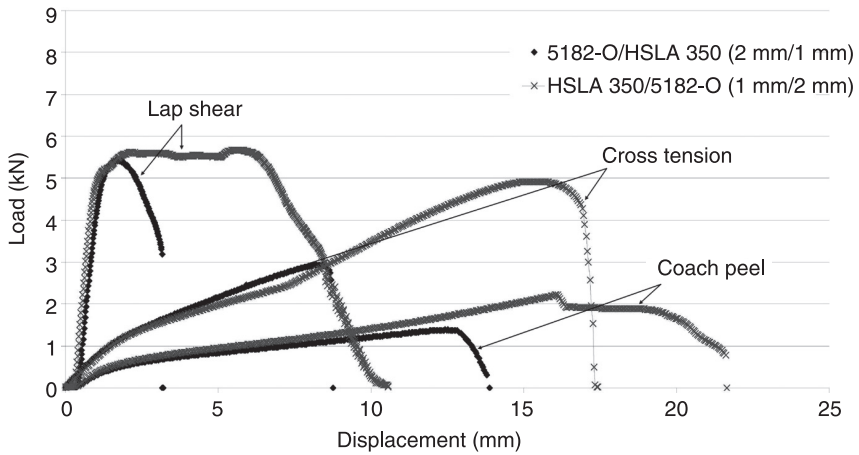


9.17 ID 10: SPR of 2 mm AA5182-O (head)/1 mm HSLA 350 (tail).



9.18 ID 11: SPR of 1 mm HSLA 350 (head)/ 2 mm AA5182-O (tail).

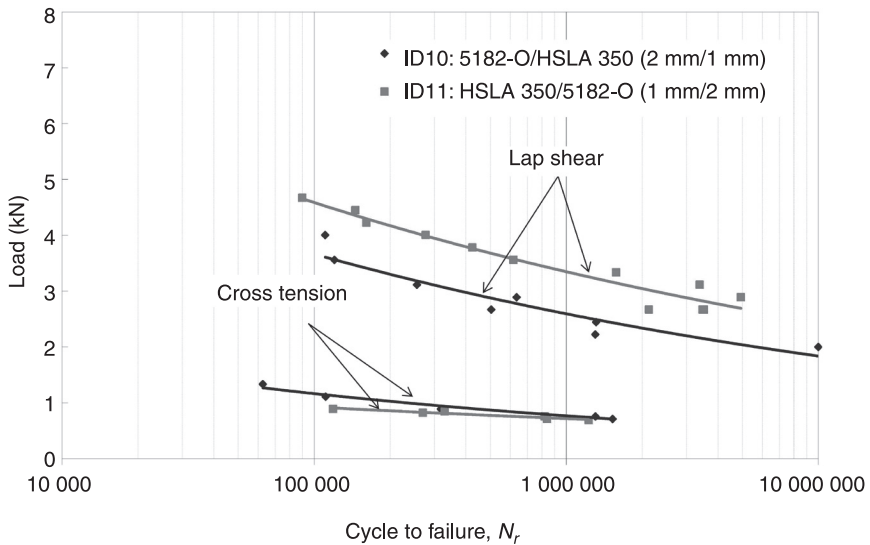
A static cross tension test of this improved joint population yielded an averaged static strength level of 4920 N and the observed failure mode was consistently by means of tail pullout. Figure 9.19 shows the experimentally measured load versus displacement comparisons under three loading conditions between the two riveting directions. By altering the piercing direction, a much better clinching mechanism was achieved and the cross tension strength was almost doubled. In addition, because of the better material interlock at the tail end, a much higher displacement to failure was achieved, which dramatically improved the energy absorption capacity of the rivet joints (see Fig. 9.19). Moreover, longer die life



9.19 Experimental load versus displacement comparison of ID 10 and ID 11.

should be expected since the softer material is in contact with the die surface, therefore reducing die wear.

It is also interesting to point out that noticeable fatigue strength improvement is also achieved by placing the softer material at the tail side of the rivet as shown in Fig. 9.20. This is particularly true for life cycles in the range 10^5 – 10^6 , which is of



9.20 Fatigue strength comparison of ID 10 and ID 11.

significant relevance to the automotive durability community. The improved lap shear fatigue strength of ID 11 can be attributed to the better clinched, more snugly fit rivet tail end as illustrated in Fig. 9.18¹⁵.

9.4 Conclusions

In this chapter, we discussed the analytical and experimental studies on the strength estimation and optimization of self-piercing rivets for automotive applications. Based on lower bound limit load analysis, the static cross tension strength of an SPR joint can be estimated and the corresponding failure mode can be predicted. Experimental strength measurements and failure mode observations from nine SPR joint populations were used as validations of the rivet strength estimator. Reasonably good correlations on strength and failure mode were achieved. The results presented in this chapter also demonstrated that the rivet strength depends strongly on the rivet design and the material interlocking mechanisms of the rivet tail.

The rivet strength estimation procedure was then used to optimize the SPR strength for a given material and thickness combinations. Two examples were provided to demonstrate that the optimization procedure and the rivet strength and energy absorption were significantly increased by improved manufacturing parameters. In general, attention should be paid when thicker (>3 mm) or stronger material (i.e., high-strength steel) is used as the tail side, due to the difficulties associated with creating a sufficient material interlocking mechanism.

Theoretically, improvement for rivets of higher gauge and stronger materials can be achieved by using larger rivet and larger die size with a higher riveting force. However, the practical issues of the assembly plant may prohibit the change of specific manufacturing parameters. Therefore, the rivet strength optimization is a constraint-optimization process. The question that design engineers need to ask is whether the current rivet strength is sufficient for structural rigidity, strength and other safety and vehicle performance related requirements.

9.5 References

1. Bokhari N and LaPensee M (1995), *Self-Piercing Riveting in Automotive Applications*, Henrob Corporation.
2. Bokhari N (1995), 'Self-piercing riveting- process and equipment', *Welding and Metal Fabrication*, May.
3. Sun X and Khaleel M A (2005), 'Strength estimation of self-piercing rivets using lower bound limit load analysis', *Science and Technology and Welding and Joining*, 10(5), 624–635.
4. Strömstedt E (2002), 'Finite element simulation of crash testing of self-piercing rivet lap shear joint specimens', Report No. IM-2002-021, Institute for Metals Research, Sweden.
5. Westerberg C (2002), 'Finite element simulation of crash testing of self-piercing rivet joints, peel specimen', Report No. IM-2002-020, Institute for Metals Research, Sweden.

6. *Weld Quality Test Method Manual* (October 1997), Auto/Steel Partnership, Southfield, MI.
7. Sun X, Vela E and Khaleel M A (2002), 'Analytical strength estimator for self-piercing rivets', PNNL Technical Report, August 28.
8. Westgate S, Riches S, Nicholas D and Powell H (1995), 'Alternative joining technologies for lightweight vehicle manufacture', *Advanced Technologies & Processes, Proceedings of the International Body Engineering Conference (IBEC)*, 127–134.
9. Lin S-H, Pan J, Wu S-R, Tyan T and Wung P (2002), 'Failure loads of spot welds under combined opening and shear static loading conditions', *International Journal of Solids and Structures*, 39, 19–39.
10. Sun X, Stephens E V, Davies R W, Khaleel M A, and Spinella D J (2004), *Welding Journal*, 83(11), 308-s–318-s.
11. *Metal's Handbook, Ninth Edition, Volume 1, Properties and Selection: Irons and Steels* (1978), American Society for Metals, Metals Park, OH.
12. *ASM Specialty Handbook: Aluminum and Aluminum Alloys* (1993), ASM International, Metals Park, OH.
13. Cornille, Jr H J, Danyo M W and Young C S (2003), 'The P2000S unitized sport utility vehicle body structure', SAE paper No. 2003-01-0573.
14. Rathbun R W, Matlock D K and Speer J G (2003), 'Fatigue behavior of spot welded high-strength sheet steels', *Welding Journal*, 82(8), 207-s–218-s.
15. Sun X, Stephens E V and Khaleel M A (2007), 'Fatigue behaviors of self-piercing rivets joining similar and dissimilar sheet metals', *International Journal of Fatigue*, 29, 370–386.

Self-piercing riveting (SPR) in the automotive industry: an overview

M. W. DANYO, Ford Motor Company, USA

DOI: 10.1533/9780857098849.2.171

Abstract: The automobile industry is one of a growing number of industries to use SPR. One of the main reasons is that alternative lightweight materials are being used in place of steel. The reason for using lightweight materials for vehicles is the need to reduce fuel consumption, reduce CO₂ and minimize the footprint that the automobile leaves on the environment. There are two main types of self-piercing rivets that have unique product and manufacturing considerations.

Key words: self-piercing riveting (SPR), automobile industry, lightweight materials.

10.1 Introduction

The auto industry uses several methods to join the body sheet metal together. These include:

- resistance spot-welding (RSW);
- MIG/TIG welding;
- laser welding;
- self-piercing rivets (SPRs);
- clinches;
- adhesives.

This chapter will discuss the use of SPRs in the automobile industry. Self-piercing rivets were actually used over 100 years ago. Their main application was in the transportation industry: they were used to assemble horse harnesses.

Over the last 30 years the automobile industry has been significantly changing towards building more fuel efficient vehicles. The main factors driving this are the cost of fuel, fuel economy/CO₂ emissions and the public awareness of the environment. An improvement in fuel economy has been achieved in four main ways:

1. fuel efficient powertrains,
2. vehicles with a smaller carbon footprint,
3. lightweight materials,
4. a combination of any of the first three listed.

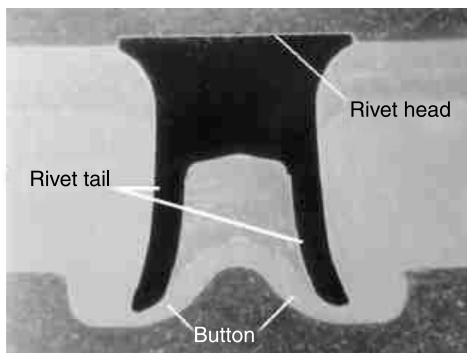
The use of lightweight materials is a favorite option. This allows a vehicle to maintain its size and function, yet be significantly lighter. Depending on the application of the lightweight materials, secondary weight saving may also be implemented. If a vehicle were to lose significant mass in the structure and/or interior, this could allow one to decrease the size of the powertrain and downsize the suspension and brakes, and it may also enable the vehicle to use less fuel to cover the same distance, thus allowing the vehicle to carry less fuel, and therefore have less mass.

To make use of lightweight materials, particularly in an automaker's bodyshop, new joining techniques (at least new to the high volume production of automobiles) need to be employed. SPRs are one of these techniques being employed by many of the automakers. SPRs can be used with a number of different materials. These include: steel, aluminum, magnesium and some plastics. Self-piercing riveting can also be used to join any combination of these materials. Since it is a mechanical process, material mixing is not required. We will discuss this in more detail later in the chapter.

The ability to use different lightweight materials allows the manufacturers to achieve the optimum strength, weight, cost and stiffness.

Figure 10.1 shows a cross-section of a semi-tubular SPR. Some common terms that will be used are:

- Head side: Side of the joint where the rivet insertion begins. This is where the head of the rivet rests.
- Button or Die side: This is the bottom layer of material. This is the side of the joint where the upset rivet lies and where the parent material of the joint is displaced into the die.
- Barrel or Shank: The straight portion of the rivet.
- Tail: The end of the rivet that is flared to create interlock.
- Interlock: The interference between the flare of the rivet and the bottom-most layer in the joint.



10.1 Rivet description.

10.2 Types of self-piercing rivet (SPR)

There are two main types of self-piercing rivet:

1. semi-tubular, and
2. solid.

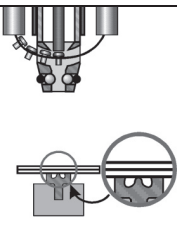
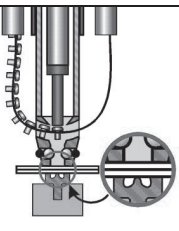
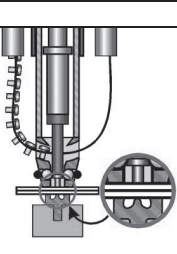
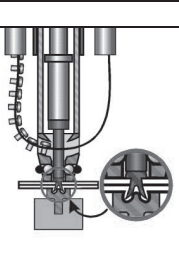
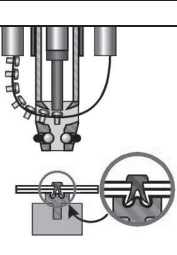
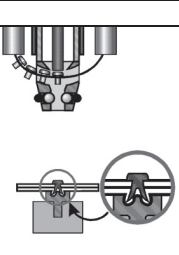
Both types require two-sided access and both can be used to join similar and dissimilar materials. The first type, and probably most common, is the semi-tubular (see Fig. 10.2). The semi-tubular rivet is commonly used throughout many industries. As stated above, the automotive industry is increasingly using self-piercing rivets, and the semi-tubular rivet is the most common for mixed metal and light metal constructions.

Basically, the self-piercing rivet is installed using a rivet setter. The rivet is fed into the nose of the gun, a punch is displaced and the rivet is pushed into the stack-up. As it is being pushed, the volume of the rivet displaces the parent materials. The parent materials are then displaced to the backside of the joint, also known as the die or button side. As the displaced material has stopped flowing into the button, the tail of the rivet flares open, causing the rivet and material to interlock, one of the factors that lead to joint strength (see Fig. 10.3). The rivet does not break through, keeping a sealed button (or die) side of the joint.

Typically the semi-tubular SPRs are made of a martensitic steel and are heat treated to varying levels of hardness. Harder rivets are used for harder, higher yield materials. The rivet hardness needs to be matched with the materials being joined: too soft a rivet will buckle during installation, too hard a rivet will break



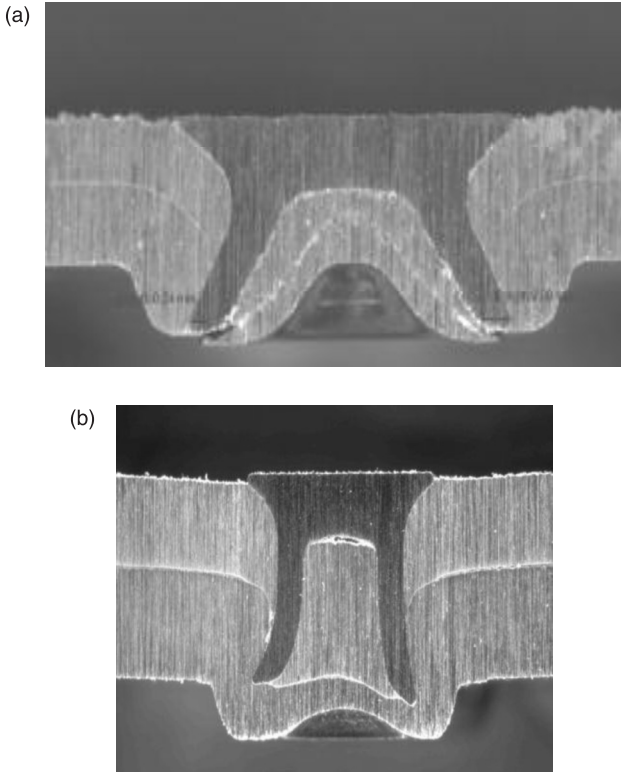
10.2 Examples of semi-tubular rivets (courtesy of Henrob Corp.).

	
1. Material in position on the upsetting die, ready to rivet.	2. Rivet setter nose advances to clamp the material against the die.
	
3. Riveting punch advances, pushing the rivet through the nose of the rivet setter.	4. Rivet is inserted into the material, flaring out into the upsetting die.
	
5. Rivet setter retracts and the next rivet is fed into the tool.	6. Cycle is complete.

10.3 Rivet setting process for semi-tubular rivets (courtesy of Henrob Corp.).

through the button (see Fig. 10.4(a), (b)). SPR hardness is just one factor in determining the rivet/die/setting parameters. The steel SPRs are usually used in body panels. The parent materials for the joint are typically aluminum to aluminum or aluminum to steel. To prevent galvanic corrosion, the rivets are coated with a mechanical tin–zinc plating (to avoid hydrogen embrittlement) or Almac. Both coatings have been successfully used in the auto industry.

The installation of the solid SPR is similar to that of the semi-tubular. The main difference is on the die side of the rivet. The solid rivet (see Fig. 10.5) acts as a punch. The rivet installation actually produces a slug and the slug is ejected through the die. The die then coins metal into the riveted joint to lock the rivet and the parent metal together (see Fig. 10.6).



10.4 (a) Breakthrough; (b) collapsed rivet.



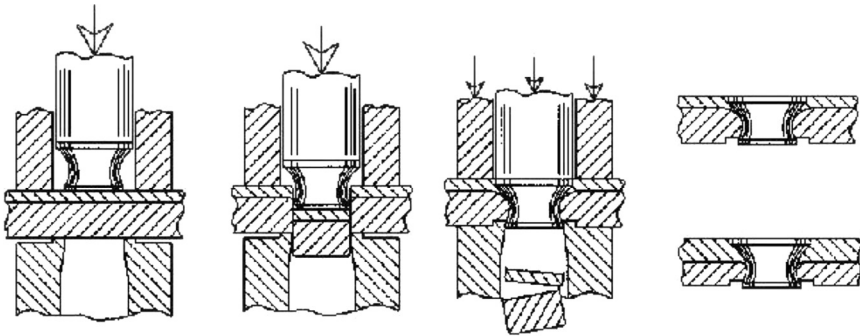
10.5 Examples of solid rivets (courtesy of AKH Fas-Ner System).

The other type of SPR is the solid rivet (see Fig. 10.5). The solid SPR is not as widely used as the semi-tubular SPR. The main benefits of the solid rivet are:

- It is relatively flush on both sides (no button on the back side).
- Installation into harder materials is easier (column stability).

The main shortcomings are:

- Slugs have to be managed.
- Installing through adhesive may contaminate the tooling with adhesive build-up.



10.6 Solid rivet installation process (courtesy of AKH Fas-Ner System).

10.3 Uses for SPRs

The main use for SPRs in the automotive industry is for joining aluminum to aluminum or aluminum to steel. Most applications are in body-in-white (BIW) applications. The SPRs are used to replace resistance spot welds (RSW), the traditional two-sided method of joining used on all steel structures. Typical applications include, but are not limited to,

- hoods,
- fenders,
- doors,
- decklids,
- liftgates,
- body-in-white.

There are other uses in motor vehicles, such as seat structures, door modules, moonroof structures and other hardware.

There are several reasons for using SPRs in all the above applications. The first is the absence of heat. When resistance spot-welding or MIG welding aluminum, the amount of energy that is put into the work pieces is higher than that for steel. The reason for this is that, even though aluminum has a lower melting point, it has a higher thermal conductivity. So to get the material to melt, more energy is dumped into it than into steel. The high energy density dumped into the work piece makes the assembly more prone to thermal distortion. The SPR typically does not require thermal energy to be introduced and so does not cause thermal distortion.

The second advantage is that surface cleanliness is not a major factor in the installation of the rivet. The rivet can pierce through pretreatments, oxides, lubes and other contaminants. Welding and adhesive processes in aluminum are more

sensitive to these factors. Since the surface condition is key in welding light metals, SPRs remove this variable.

The third advantage is the ease with which dissimilar metals or dissimilar alloys can be joined. There are times when the strength of certain types of steels is required (in local areas). The SPR enables one to join dissimilar metals with joint peak loads of durability similar to RSWs. This advantage gives the engineer more freedom to design with more material combinations.

The fourth advantage is the ease of riveting through adhesives and sealers. The SPR can go through the adhesives with the mechanical insertion forces. The most important requirement for using SPRs to go through adhesive is to apply a pre-clamp. The pre-clamp is needed to push the adhesive out of the riveted area. This allows a more consistent geometry in the riveted joint.

There are several disadvantages to using semi-tubular rivets. The first is the cost of the rivet. The rivet has a hard cost; a discussion is still going on about the cost of installing a rivet versus other methods, such as RSW. The fact is that the individual parts have an associated cost. The next disadvantage is with the button that is formed on the backside of the joint. The presence of a button requires engineers to make sure that there are clearances around the button for mating parts. The third disadvantage is the material properties that are required for the parent materials in the assembly. There is a balance between hardness, yield strength, elongation and forming characteristics. It is up to the engineer to figure out which joining method works best for the application. For aluminum and mixed metal, the benchmarking shows that SPRs are the predominant joining method.

10.4 Product considerations

Now, when considering whether to use SPRs, one must take into consideration the following factors:

1. Geometry
 - a. material thickness/stack-up
 - b. flange length
 - c. rivet size
 - d. rivet diameter
 - e. rivet placement
2. Materials
3. Application

The design and manufacturing engineers must continuously collaborate to achieve the design intent, the quality, robustness and a cost effective design.

Typically, an engineer can replace SPR with RSW. The most important fact to remember is that the rivet is directional, based on the tooling and metal thickness stack-up, while RSW is non-directional and the welding parameters are based on

the governing metal thickness (GMT). This means that the rivet prefers to go from thin material to thicker. However, the rivet can go from thick to thin as long as the bottom layer of the joint stack-up is about 1/3 of the total stack-up, while the GMT (typically the thinnest metal layer in the joint) does not have to be in a certain sequence in the joint stack-up.

When looking at the geometry, one parameter that drives the design engineer is the flange length. This depends on a number of factors. First is the choice between using a 3 mm diameter rivet and a 5 mm diameter rivet (this is determined by peak load requirements, materials and joint stack-up). The setting nose and die diameters for a 5 mm rivet are larger than the 3 mm setting nose and die diameters. This will drive the flange size. The second factor is the dimension of the trim edge to the center of the rivet. The closer to the edge the rivet is, the lower the peak load. The last factors are the manufacturing requirements for trim line tolerances, robot tolerances and part placement.

As stated in the previous section, the material properties are another factor for the design engineer. While the option of using dissimilar materials can give the engineer more latitude, there are limits to the materials that can be used in SPR joints. Material hardness is one of these. If the material in the joint is as hard as or harder than the rivet, it will be virtually impossible to create a joint. Elongation is another important factor. If the material elongation is too low, then proper formation of the button will not occur. The material yield strength is also critical. Material with too high a yield strength may cause the rivet to deform during installation. Lastly, the forming characteristics of the metal in the joint need to be taken into account: how formability factors limit the ability to form a button.

10.5 Manufacturing considerations

Like any joining process, the manufacturing inputs are critical to the creation of a joint. As stated in the previous section, the design engineer must work with the manufacturing team to achieve the joint performance required for the product. The four main considerations that overlap Product Design and Manufacturing are:

1. flange length,
2. rivet spacing,
3. rivet size,
4. materials (alloy and gauge).

First, flange length is a very important consideration. This is the effective amount of flat in the stack-up needed to achieve a satisfactory joint (see Fig. 10.7). The design engineer will want to shorten the flanges as much as possible. This will allow for a larger section (a larger moment of inertia) with a better weight and cost efficiency. The manufacturing engineer, in an ideal world, supports this. The manufacturing engineer ensures that the product has enough flat for the tool to be seated. Inputs that affect the amount of flat include:

- part to part variations,
- variation induced by upstream processes,
- variations in the setting tool,
- variations introduced by the robot or operator.

These increase the flange length requirements.

The second critical agreement is rivet spacing (Table 10.8). In areas where increased stiffness and strength are required, rivet spacing needs to be tighter. In reality, rivet spacing is dictated by the size of the rivet setter and die button and manufacturing tolerances. Basically, the rivet spacing (S) is equal to the fillet of the first button (R_{bfl}), plus the radius of the die (R_{d}), plus the manufacturing tolerances (to_1), plus the radius of the button (R_{but}) minus the fillet of the die face (R_{D2}) (see Fig. 10.8):

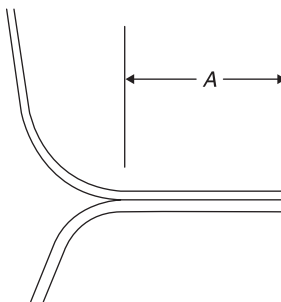
$$S = R_{\text{bfl}} + R_{\text{d}} + to_1 + R_{\text{but}} - R_{\text{D2}}$$

$$\text{rivet spacing} = R_{\text{bfl}} + to_1 + R_{\text{D2}}$$

Making use of a calculation like this will prevent the die from crashing into an already formed button.

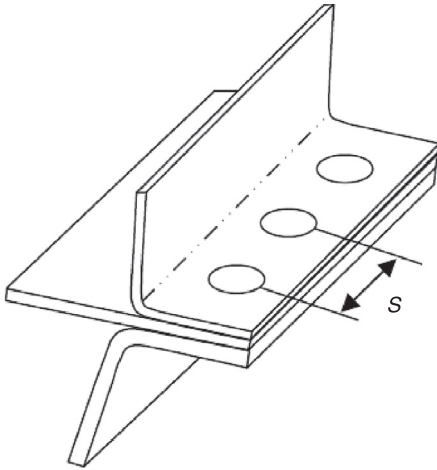
Items 3 and 4 in the list of considerations, above, are very interrelated. Rivet size (diameter, length, hardness and head type) are related to the materials and gauges chosen for the product. The main goal that Product Design and Manufacturing engineers have is to simplify the number of rivet/die combinations, in other words, to reduce the in plant complexity. To reduce complexity, Product Design can reduce the number of gauges and alloys chosen to build a certain product. In addition, rivet/die combinations may be optimized in order to handle several different joints.

The reason that this is important is twofold. First, the more rivet/die combinations that are required, the more under-utilized robots will be required, driving up investment. This may also increase the length of the line and reduce cycle time. The second reason is the sheer complexity of the number of rivets and dies that



$A = \text{tool} + \text{part tolerances} +$
 $\text{robot tolerances} + \text{positioning tolerances}$

10.7 Flange length.



10.8 Rivet spacing, S , based on center of rivet to center of rivet distance.

must be handled by the plant. This helps poke-yoke the lines so there is less chance of errors.

10.6 Future trends

SPR is one of the top options for joining the aluminum vehicles that are currently on the market and it can be used in conjunction with adhesives, making a very reliable joint. The lack of heat put into the system during joining allows a much more dimensionally stable joining process. As the benefits are realized, more innovations will be introduced.

Self-piercing rivet usage will continue increasing with the increasing use of light metals and light metals in combination with steel. In particular, with the increased emphasis on fuel economy and CO₂ emissions, light metals will be increasingly used. Rivets of different materials, coatings and geometries will continue to be developed and tested as the desire to join less elastic metals increases. The tools will also develop and mature to optimize the insertion process and allow optimum performance. Materials such as boron and carbon fiber have limitations in joining. However, these are the next real frontiers for self-piercing rivets. They are the materials, besides the light metals, that require joining.

Self-piercing riveting (SPR) in automated vehicle construction

R. HEWITT, Bentley Motors Ltd, UK

DOI: 10.1533/9780857098849.2.181

Abstract: This chapter initially looks at the drivers impacting upon the automotive sector at the moment, specifically reduced emissions and the introduction of lightweight materials. There are many joining options available and there are many factors to consider when choosing a specific process. A cost model is discussed for evaluating comparable processes. It is noted that specific strengths and weaknesses of each joining process may be the deciding factor when the final selection has to be made. The benefits of a specific process may be driven by cost or may equally be driven by the joint parameters, process flexibility, speed of production and other joint specific issues. The chapter gives an evaluation, providing a robust process selection for the specific application required and an understanding of the perceived benefits against other joining processes, as well as the reasoning from which to make this assessment.

Key words: self-piercing riveting (SPR), process stability, robust, capable, cost comparison, process selection, process evaluation, lightweight, aluminium joining, joint performance.

11.1 Introduction

The application of any joining process within an automated vehicle construction facility has to be evaluated in a number of ways to ensure that the required cost, performance and application targets are met. This chapter will demonstrate this process, while trying to meet the challenges now facing the automotive industry, including the requirement to meet the stringent emission reduction targets being legislated for and anticipated by the customer base around the world, leading to the use of lighter materials and high strength materials (Barnes and Pashby 1998).

This target is being resolved by developing a number of key avenues:

1. Basic driveline technology
2. Aerodynamics
3. Rolling resistance
4. Electrification and hybridisation
5. Heat management
6. Energy carriers
7. Lightweight design.

Improvements are being made in all the above areas, leading to significant improvements in recent years. This chapter will address the requirement to use the self-piercing riveting process in the drive towards lightweight materials, in the last avenue mentioned above.

In an effort to meet this demand, as well to achieve the structural, crash and corrosion performances, many new or improved materials have been proposed for incorporation into the vehicle structure. So far the product design approach has been as follows: (i) all-steel BIW structures have been created for the A and B segments, (ii) steel and aluminium BIW have been provided in the B, C and D segments with aluminium mainly being included within the bolt-on assemblies and (iii) some all-aluminium solutions have been provided within the E & F luxury segment. This has not been consistent across the industry but it can be used as a rule of thumb. Wheeler (1998) has demonstrated that aluminium structured vehicles can be designed to be crashworthy and to provide at least the same level of occupant protection as equivalent steel structured vehicles, but at about half the vehicle structure weight. For the breakdown of the car market, the segment classification has been used as identified within the EEC Regulations (EEC 1999) where the following classifications are used:

- A – mini cars
- B – small cars
- C – medium cars
- D – large cars
- E – executive cars
- F – luxury cars
- S – sport coupés
- M – multi purpose cars
- J – sport utility cars (including off-road vehicles).

The application of new materials is increasing with the development of electric and zero emission vehicles, driving the use of more exotic materials such as carbon fibre, magnesium, etc., but these have not yet transferred to main stream usage. This chapter will therefore primarily review the application of rivets to structures incorporating aluminium and aluminium and steel. From a manufacturing point of view the key areas to establish when integrating these new materials are:

- the handling, forming and cutting of advanced materials;
- the joining of these materials both to themselves and also to the existing materials within the vehicle structure, which may cause specific corrosion concerns;
- the end of life recyclability of the materials used, with legislative targets driving the reduction of waste to landfill and increasing the reuse of materials at either the same or reduced performance expectations within the vehicle structure;

- the use of simulation tools is a key requirement with any new material and/or joining process; the ability to predict performance will reduce material and component trials, as well as provide a basis for capability and quality control plans within the production environment;
- the energy efficiency of the manufacturing process itself; so far there is no legislation demanding the limit of CO₂ emissions throughout the production process, but the original equipment manufacturers (OEMs) are evaluating any new process to ensure the overall product totals are constrained, especially with the volatile energy market.

11.2 Material requirements

The distribution of weight within the vehicle structure is also important for a number of key factors, which can be demonstrated with a number of rough guidelines:

- 10% mass reduction \approx 6% improvement in fuel economy.
- Ride and handling favours 50/50 weight distribution front-to-rear and a reduction in the un-sprung mass. The body weight reduction therefore needs to be concentrated in the front end to offset the engine mass.
- Handling also benefits from a lower centre of gravity, leading to a concentration of effort on parts above the required centre of gravity. Target components have therefore been closure assemblies such as bonnets, doors, tailgates and trunk lids.

Recent BMW cars have been developed with an aluminium front end, reducing weight and overall body mass, whilst retaining a balance of weight front-to-rear. Jaguar vehicles have aggressively pursued the all-aluminium structure for the complete model range. However, even these vehicles still retain a number of steel panels to meet structural requirements and thus still require a dissimilar material joining process.

The combination of materials, gauges and processes varies greatly, especially in the aluminium structure. Designers have a choice of sheet, casting or extrusion and, depending on the volume strategy, chosen design solutions can be tabled with a varying mix of the materials above. This can range from a sheet-intensive structure, as chosen for the Jaguar XJ, through to modular construction made of extrusions and castings as demonstrated by Lotus. Audi have also manufactured aluminium intensive vehicles utilising a wide range of materials and joining processes, notably for the A8 and the TT models. From these examples and the market sectors that they occupy, it is noted that at this time there is a cost penalty for incorporating these materials. This cost penalty can only be carried by the Premium Vehicle Sector. However, the steel sector is keen to point out that considerable weight savings can be made within traditional steel structures if

Table 11.1 Material usage within BIW

	Mild steel	HSS	Aluminium	UHSS	AHSS	Composites
2006 Data	46%	29%	10%	8%	5%	2%
2015 Forecast	15%	30%	30%	14%	8%	3%
Vehicle specific:						
	Steel sheet	Al sheet	Al extrusions	Al castings		
Audi A8	8%	35%	22%	35%		
Audi TT	31%	31%	16%	22%		
	Mild steel	HSS	Aluminium	UHSS	AHSS	Composites
Audi Q7	36%	26%	6%	32%		

advances in design, materials grades and processing are embraced and utilised (Auto Steel Partnership – A/SP).

Balancing weight reduction opportunities against structural requirements and cost targets has therefore driven the predictions outlined in Table 11.1. Aluminium has seen significant uptake within the premium vehicle sector, whilst High Strength (HSS), Advanced High Strength (AHSS) and Ultra High Strength Steels (UHSS) have been utilised within the structures on mainstream vehicles, utilising high volumes to optimise the piece cost of the incorporation of these new materials and driving process optimisation.

11.3 Joining techniques

The joining techniques used in automobile manufacturing can be divided simply into thermal or mechanical joining processes. Table 11.2 provides a non-exhaustive selection of the processes commonly used.

Table 11.2 Joining techniques used in automotive manufacturing

Mechanical	Thermal
Self pierce riveting	MIG welding
Flow drill screwing	MAG welding
Clinching	Laser welding
Bonding	Resistance spot welding
Hemming	Stud welding
Blind riveting	Projection welding
Punch elements: Bolts, nuts and inserts	TIG welding
Spot and linear friction welding	Drawn Arc welding
	Brazing (Arc and laser)

The choices then have to be made as to which process best suits the materials used and the volumes at which the vehicle is to be manufactured. There are a number of key factors associated with the basic parameters of application:

1. The capability to join dissimilar materials, e.g. aluminium to steel.
2. Single or double sided access – greater design freedom is provided when only one side of the joint has to be accessed, but the ability to clamp the joint to achieve the required control will then become an issue.
3. The joint speed – either spot joint rate or metres per minute in the case of linear joining processes.
4. The ability to combine with bonding, allowing increased joint performance.
5. Levels of distortion through either heat or mechanical force.
6. The consumable requirements / joint materials including rivets, weld or braze wire, weld tips, etc.
7. The energy consumption.
8. The power delivery, primarily electric, pneumatic or hydraulic.
9. The flexibility – the ability of a single application head to apply the process to different material stacks, in terms of type of material, gauge of material, number of layers and access requirements. This can be of utmost importance, as the greater the flexibility, the fewer the number of application heads required.
10. The cost of the application head.
11. The quality of the joint surface.
12. The structural performance, like quasi-static and fatigue performance.
13. The corrosion performance.
14. The robustness to anticipated variation in production.
15. The simulation tools available to support process development and parameter selection.
16. Non-destructive testing / destructive testing of the joint.
17. The anticipated volume application – the ratio of capital versus variable cost will vary depending upon the specific volume requirements and drive the selection to optimise the resultant cost per vehicle.

When comparing processes the key factors have to be taken into account, to ensure that the optimum process solution is chosen. Initial trials will take place using material test coupons, moving on to production samples, and efforts should be made to understand the design opportunities provided by specific processes, allowing the optimisation of the production rather than just a straight swap of process to the same base design. For example, as laser welding requires a minimal flange width, designs utilising this process are able to reduce flange lengths, so improving the viewing angle around door pillars or window apertures.

11.4 Evaluation of processes

The development of a joining process for application within a production facility requires evaluation in order to ensure that the capability of the weld is understood and the key parameters of the joint are identified, enabling confirmation of joint success to be established. Examples of the parameters that require evaluation when applying a laser-welded joint are:

- interface width
- penetration
- porosity
- weld strength
- surface concavity
- top bead width
- top surface cut through
- spatter
- burn through.

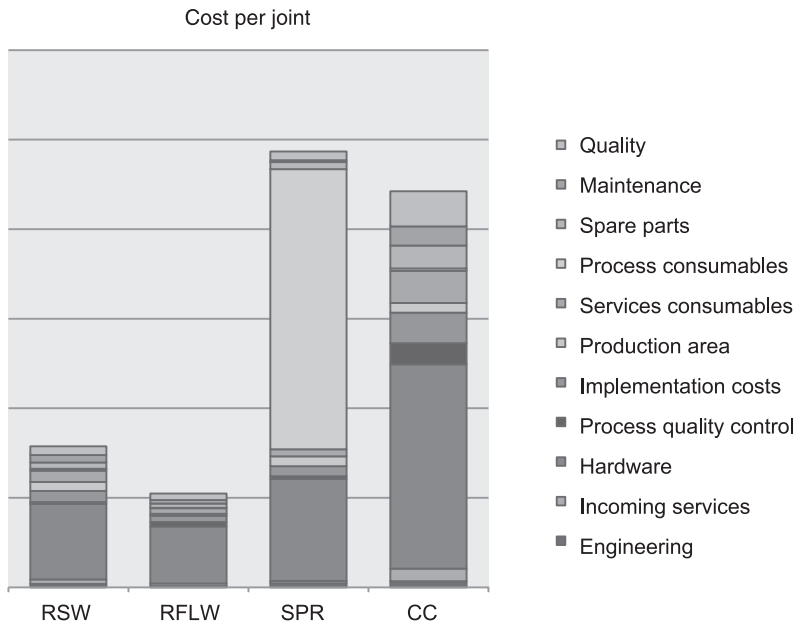
These can be compared with the acceptance criteria for a self-pierced rivet joint:

- head height
- remaining material thickness
- rivet interlock
- no cracking, collapse or buckling of rivet
- no cracking of the rivet button
- no gaps around the rivet shank.

Initial evaluation will create joints at the nominal design condition, setting application parameters for the particular process. The system performance will also be evaluated to ensure that the application will perform throughout its envelope of operation to the required dimensional accuracy and repeatability. The range of material combinations will be extended to the anticipated extent of gauge, material or combination anticipated within the chosen application, including any contamination of lubricants, corrosion inhibitors, coatings, adhesives, etc. The final stage is then to understand the process variations, for example, joint gaps, flange condition, local press hardening, etc. Each joining process will require a review of the design against the process requirements to ensure that suitable trials are carried out to identify critical quality control concerns and ensure that control plans are generated that will mitigate them. It is important to understand the ease of control for each process being compared and the level of technical expertise required to maintain the operating parameters within an acceptable limit.

11.5 Cost comparisons

For a valid comparison, technologies have to be evaluated by creating a sound base from which to compare the specific processes to be adopted.

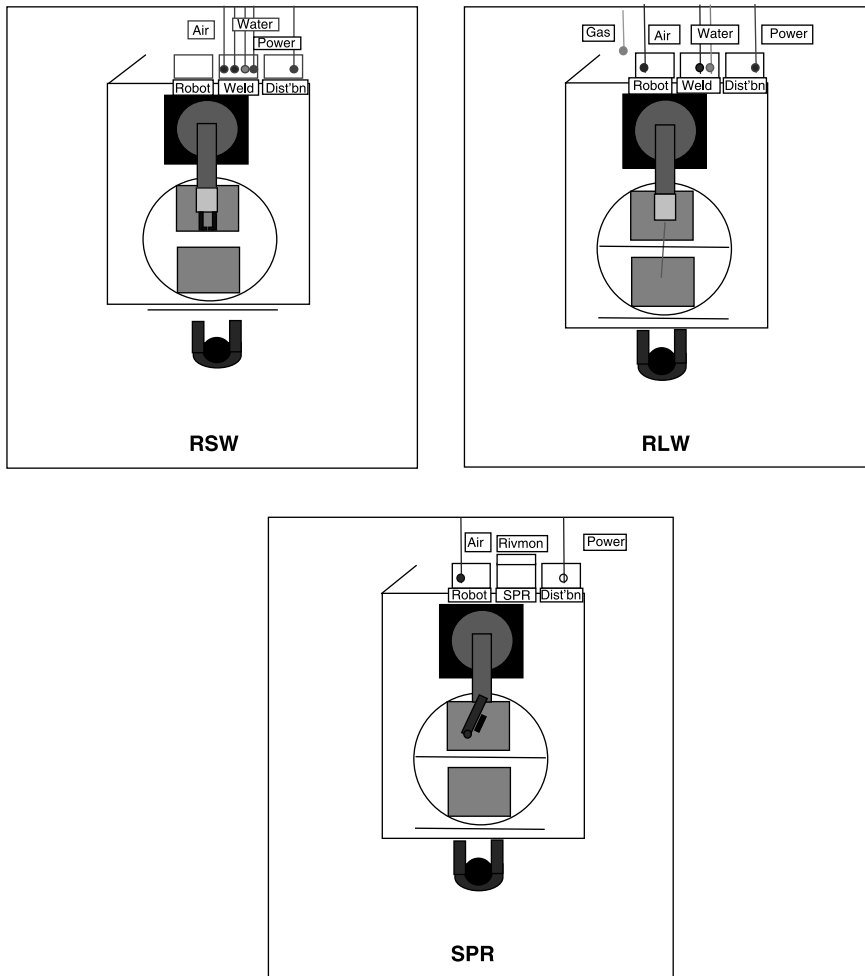


11.1 Comparative cost analysis.

A key evaluation between processes is to understand the comparative cost of application. This evaluation has to include all the key cost contributors, including both fixed and variable costs. The investigation can be hampered through concerns over the specific application, but the initial assessment in Fig. 11.1 is based on the full utilisation of the specific joining method when mounted on a robot within a single robot cell. It can be assumed that each application could operate at the optimum process speed with overall equipment effectiveness (OEE) of 85%. Each cell would then have to be facilitated to ensure optimum performance.

This has been demonstrated by the welding cell configuration shown in Fig. 11.2; the single cell robot configurations identified are used to model the comparative requirements for each application. The following items would therefore need to be included:

- Power / utility supply infrastructure
- Capital equipment required
- Revenue expenditure
- Power requirements (CO₂ emissions)
- Consumables
- Manpower
- Preparation / rework requirements.



11.2 Welding cell configurations.

The business case model compares self-piercing riveting applied within a robotic spot-welding cell with resistance spot-welding, remote laser welding and close-coupled laser welding applied within a robotic cell. This model can then be expanded to compare most joining processes. The evaluation needs not only to include all the fixed and variable costs of the process, but also to understand the specific limitations or benefits within the specified application.

The investment costs associated with this equipment and resource content have been estimated for plant facilities and services and then the costs have been suitably apportioned down to a cellular level for the specific process equipment,

providing a realistic cost at plant level. The operating costs covering the cell production area, all power consumption elements within the cell, production consumables, spares, maintenance and the operating costs of maintaining product quality must also be considered. The labour costs are excluded as these would be planned to be the same for both technologies and, as these processes are assumed to be fully automated, labour content would be confined to loading only.

In order to derive a direct comparison between the joining technologies, the process parameters and operating parameters must be considered. The process parameters define the weld capability for each process that, with the OEE, defines the net welding capability of the equipment. The operating parameters define the available production time, the shift pattern and operating lifetime of the equipment. These parameters then allow the calculation of cost per hour, and hence cost per joint, to be derived.

The cost model was structured in such a way as to allow different equipment content specifications to be compared, thus comparing different sub-sets of a common technology, e.g. laser source, delivery and motion systems from different manufacturers and integrators. The cost drivers are listed in Table 11.3, while the costs included within this comparison can be broken down as shown in Table 11.4. The calculated operating costs are listed in Table 11.5.

The cost model was populated with data based on the above parameters and assumptions. Cost data were collected from equipment suppliers and manufacturers. The resource data were based on similar product process and content at the production plant. Equivalent costs using the above methodology were then calculated for resistance spot-welding (RSW), remote fibre laser weld (RFLW), self-piercing riveting (SPR) and close-coupled laser welding (CC). It must be noted that these costs must not be taken in isolation and any conclusion must also evaluate the specific strength or weaknesses of the particular process. There may also be volume drivers, which means that the utilisation figures required to exploit a laser welding process fully, for example, could not be achieved. Therefore this process, although more cost-effective at high-volume production, will not work within a specific low-volume application.

Table 11.3 Cost drivers

Investment costs	Operating costs
Engineering	Production area
Incoming services	Service consumables
Hardware	Process consumables
Process quality control	Spare parts
Implementation	Maintenance
	Quality

Table 11.4 Process and equipment – investment

Cost driver	Item	Self-piercing rivet
Investment costs	Engineering	Process development, robot simulation and programming Power supply from landlord services to cell connection Compressed air supply from landlord services to cell connection
	Incoming services	Cooling water supply from landlord services to cell connection – N/A Proportion of cost of power and compressed air plant wide infrastructure Fume extraction – N/A Six axis robot (Comau NH4) and base SPR electrical control panel, control to six guns SPR gun loom, power, controls and pneumatic supply Standard servo gun with tape feed, 150–300 mm throat depth, no toolchanger
	Hardware	Process maintenance (RSW– electric tip dresser and cutters) N/A Cell 2 m high safety guarding, interlocked access gate Operator load area interlocked rise and fall guard Two position turntable Two medium tooling fixtures with pneumatic clamping Cell control and PLC cabinet, cell wiring and trunking
	Process quality control	RIVMON process monitoring For post–process monitoring the proportional cost of a plant wide NDT, non-destructive weld inspection system
	Implementation	Delivery, installation, commissioning of the equipment and launch of the product. Training and spares provision

The model was also able to provide an indication of the levels of power required to support the application of the specific process, the comparative requirements being shown in Fig. 11.3. Although this is still only a minor part of the overall costs, industry, media, legislative and customer focus means that it plays a

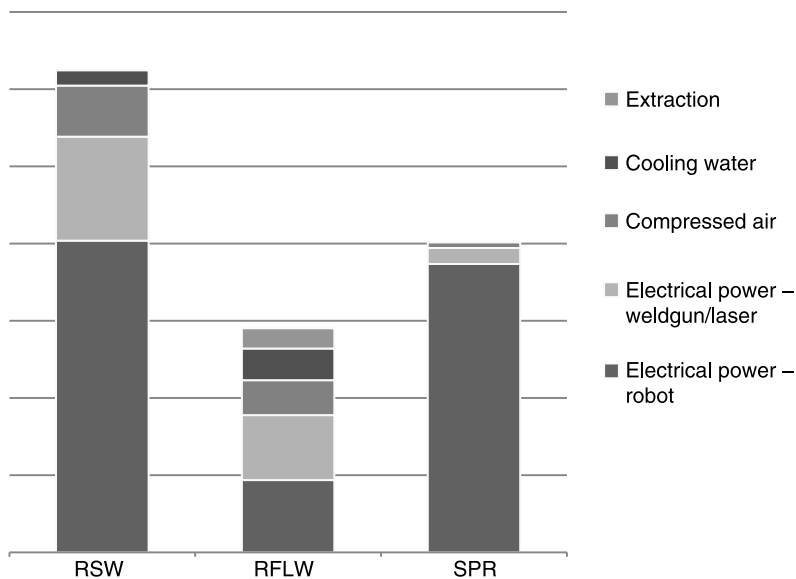
Table 11.5 Operating costs

Cost driver	Item	Self-piercing rivet
Operating costs (per hour)	Production area	Cell floorspace Power consumption of the robot
	Services consumables	Power consumption of the SPR gun Compressed air consumption of the SPR gun and robot Cooling water – N/A Heating cost (specifically replacing warm air extracted due to fumes from the general shop) – N/A Power consumption of local extraction – N/A Shield gas – N/A
	Process consumables	Cost of consumable SPR equipment
	Spare parts	Cost of spare parts to undertake daily running and annual maintenance of the equipment
	Maintenance	Cost of resource to undertake scheduled and unscheduled maintenance of the equipment
	Inspection	Inspection resource required to undertake dimensional and SPR inspection according to the OCC for the product, based on similar product in size and process content

Sunday, February 02, 2014 3:07:23 AM

significant part in process selection. Recent trends in supply costs have also driven manufacturers to direct a greater degree of attention to processes that are not ‘power hungry’.

The cost model compares the various joining technologies, simplifying the benchmarking process by removing the product, process and application variables. In each case the processes have been optimised to ensure a robust capable performance that will provide joints or the required performance when subjected to the anticipated process variation on a representational selection of joint configurations. The cost model confirms the business case for specific processes, but it does not support joint comparison for structural or performance characteristics. This must be carried out separately in order to ensure that the selection will provide the required performance in a specific application.



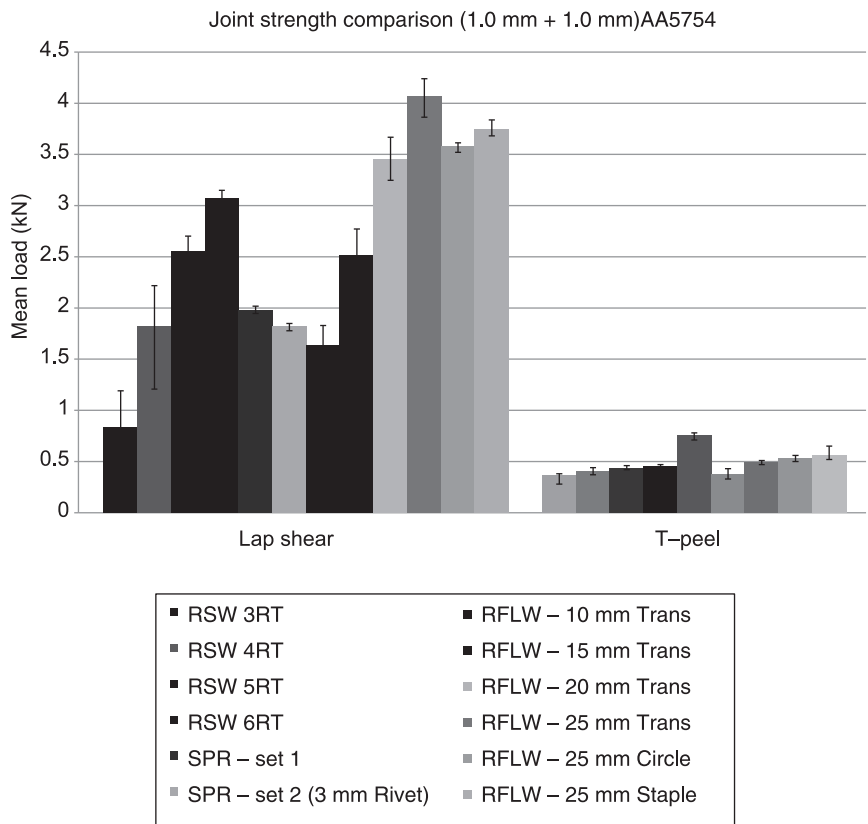
11.3 Comparative power consumption per joint.

11.6 Comparable joint performance

Many studies have tried to identify comparable parameters, then compare the performance of these joining processes via these parameters to demonstrate comparable or dissimilar performance of strength, nugget or joint widths, application times, etc. The approach taken within the above comparison was to use the optimum process parameters, which provided the most robust solution to process variation. This may mean that process time or joint strength would vary, but the overall comparison would take this into account when providing the comparison on a specific nominal component.

In Fig. 11.4 we can see a range of joints all applied to a joint between 1 mm AA5754 and 1 mm AA5754 sheet. The resistance spot-welded joint ranges in nugget size from $3\sqrt{t}$ up to $6\sqrt{t}$, where t is the thickness of the thinnest sheet of material. In general, automotive applications require a minimum nugget size of $4\sqrt{t}$ and Fig. 11.4 demonstrates the range of joint performance available. For self-piercing riveting many different selections of die and rivet type could be made, but for the sake of this comparison a typical selection of rivet and die was made, whilst varying the diameter of the rivet (a choice that is made in some cases if the specific application has a constrained area of application).

We can see when we come to the remote laser welding process that a linear joint has a far more flexible solution that demands a decision on both joint length



11.4 Comparison of quasi-static joint strength for specific joint configurations.

and shape. For this example we demonstrated joint lengths from 10mm up to 25 mm, as well as linear, circular and staple shapes to demonstrate the comparative performance of the configurations. As we found no considerable difference between specific shapes, the costs were based upon a straight stitch of 25 mm, the length being dictated by the accepted industry application standard. It must also be noted that the comparative performance of each joint type will vary, depending on the material and joint stack being evaluated as shown by Han *et al.* (Han *et al.* 2009b).

11.7 Specific process opportunities

The comparison of the joining processes must also take into account the specific benefits of each process, both in terms of range of application and as the specific design benefits that they could support. Self-piercing riveting as a cold joining

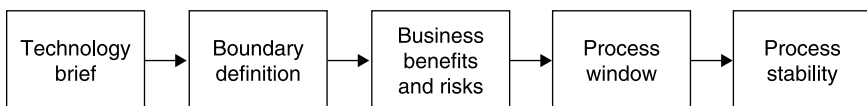
Sunday, February 02, 2014 3:07:23 AM

process will allow the mechanical joining of aluminium to steel, whereas remote laser welding will provide single-sided access to a joint and thus provide the design freedom to join box sections or tubes together. Over the last 10 years the range of materials and design innovation has rapidly matured to meet the structural and weight targets, driving both materials selection and subsequent joining methods. This development is expected to continue with the continued drive to reduce vehicle emission to meet legislation and customer expectations.

The inherent flexibility of a process will have a great impact on the final cost of any facility. Although self-piercing riveting can join dissimilar materials together, each gun with a specific rivet and die combination is effectively tied to a specific range of material, gauge and total thickness combinations. This is not the case with resistance spot-welding as the gun can approach a far wider range of joints, but cannot join together dissimilar materials. Remote fibre laser welding is more flexible still, but in this case its ability to create robust joints is limited by the ability to control the interface within strict parameters to ensure a robust and stable joint. When budgeting for the use of specific joining processes within a production facility the number of application units therefore has to take into account this reduced level of flexibility. Owing to the comparative joint strength of a self-piercing riveted joint compared with a resistance spot-welded one, the total number of joints required within the structure would be reduced. The impact of this constraint will also depend upon the design approach taken within the specific vehicle structure. Some designs have limited the range of materials, gauges and layers within the material stacks to improve the robustness of joining processes, which will in this case reduce the range of self-piercing riveting guns. This impact is felt more significantly within lower volume facilities as each station has a longer cycle time and therefore a greater range of work. This drives the expectation for a greater combination of joints to be approached by each application head, which may not be possible for less flexible solutions.

11.8 Process development

The process development for any joining technique critically needs to ensure that the technique will be capable and robust for the expected application. A process development flow chart is presented in Fig. 11.5. For a cost-effective staged approach, a sequence of evaluation can be used.



11.5 Process development flow chart.

The initial stage is to carry out a literature and market review of the specific process to understand its capabilities, referred to here as a 'Technology Brief', which should cover the following areas:

- Brief description of the technology
- Potential benefits
- Limitations
- Market supply, technology leaders or suppliers
- Cost: initial investment and piece cost
- Volume assumption and application cycle time
- Current applications
- Potential internal application
- Safety implications
- Quality implications to product
- Quality control of process: in-process monitoring, post-process checking
- Process maturity.

At this stage the review would be a desk-top study, taking into account readily available information from suppliers or the web. This can then be compared with the 'Boundary Definition' of the specific application for which the process is being developed, where we will be identifying:

- Volume and cycle time application
- Cost: capital and piece cost targets (ideally with comparative values from competitive processes)
- Quality requirements or concerns
- Specific joint or material combination concerns
- Fallback strategy (if application unsuccessful)
- Process flexibility (volume, material, joint combination, etc.).

The information gathered should now be enough to create the 'Business benefits and risks report', which will provide a baseline from which the decision to investigate the proposed technology further can be made. This analysis should be able to identify within the target application:

- Potential benefits and limitations
- Supplier availability and expertise
- Volume and time cycle restrictions
- Current applications and process maturity
- Safety, ergonomic and environmental considerations
- Facility implications
- Maintenance and operation requirements and training
- Quality implications and solutions
- Design implications
- Target application and business impact

- Risk analysis: process maturity, fallback plan, back up processes, repair options, in field service options, etc.

A conclusion can therefore be drawn about the applicability to the application and the business benefits.

Once a decision has been made to take on the process, further physical trials and a 'Design of Experiments' can then be planned. This can progress in two stages: first, to evaluate whether the process will operate at the design nominal condition, the 'Process Window' phase is carried out followed by the 'Process Stability' phase where the process will be subjected to the anticipated range of process variation to ensure that the process is stable and robust and will still provide a quality product when subjected to this range of variation.

For these tests to take place, the boundaries of the process have to be understood, and may include:

- Material type
- Material thickness
- Material coatings and preparation
- Joint combination (sheet number, thickness and orientation)
- Rivet specification (type, length, diameter, hardness, etc.).

The tests will also have to determine the output measures, for example:

- Shear strength
- Cross-tension strength
- Fatigue strength
- Peel strength
- Corrosion performance.

The initial stage will examine whether the process is viable at nominal conditions and what parameters enable the design conditions to be met. The next stage will subject the process to the anticipated range of variation, which could include:

- Surface contamination
- Oxidation
- Lubricants
- Pre-treatments
- Presence of dirt
- Temperature
- Humidity
- Joint gap
- Voltage or current variation
- Wear
- Rivet variation
- Air pressure variation.

Generally the involvement of existing production and maintenance staff will support the identification of current variables with further key items being identified during trials and development activities. Once these trials have been completed and robust parameters have been defined for the specific application, production line trials can be carried out to ensure that the process is production-capable and can be proposed for a full production implementation.

11.9 Industrial application

The introduction of self-piercing riveting to an existing automotive facility will require training to ensure that the required product design, quality control and process understanding are in place to enable robust process application that is capable of accommodating the anticipated variation within an industrial production facility. The selection of rivet and die combination is critical, especially where a number of different stacks of material (gauge and material type) are to be joined by the same gun. With any joint, there are usually a number of different gun types and/or rivet and gun combinations that are able to produce a robust joint. However, the choice combination can rapidly decrease, depending on the compatibility of the required joints. The key-determining factor is the total stack thickness as this will be a major driver for the required rivet length. The type of rivet and type of die will depend on the material type and mix.

The usual process for joint development is to optimise the rivet and die combination and to ensure the joint buy-off criteria are met on test coupons. Once the die and rivet combinations have been selected, the selection of guns can be made for the particular production facility, bearing in mind access or ergonomic constraints (if manual). The rivet application process is simple to control with only one parameter available for the optimisation of the process' which, depending on the system chosen, is either:

1. velocity-controlled, or
2. displacement-controlled.

The ability to vary this value between joints will depend upon whether a manual or automated facility is installed. Within an automated facility it is simple to optimise each individual joint, as long as the control system has the capability to store the number of different joints. In a manual facility the usual approach is to maintain the same parameters for all the joints produced by an individual gun, ensuring confidence that an incorrect selection has not been made.

The aim of any process optimisation is also not to define the process tolerance too closely in order to achieve a quality joint. The window of application has to remain large so that any variation in material gauge or strength, gap between materials, surface coatings, etc. can be accommodated and the process will still generate a robust joint meeting the design standard required. The typical evaluation criteria for a joint are:

- Rivet head height – this is the depth to which the rivet is inserted into the material.
- Interlock distance – this is the distance that the rivet legs spread into the bottom sheet, creating the effective clamping force holding the sheets together.
- Remaining material thickness – this represents the material thickness between the bottom of the rivet legs and the lower surface of the joint.
- Rivet cracking / buckling – the deformation or weakness of the rivets needs to be maintained within acceptable limits.

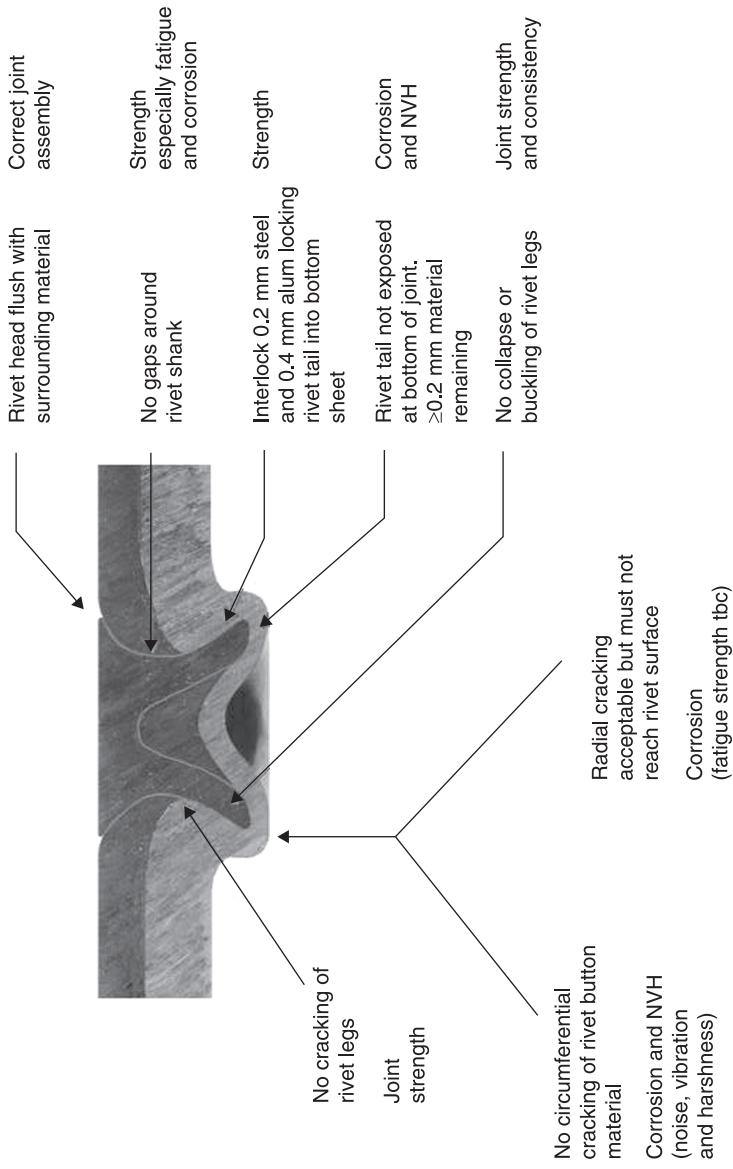
Further criteria are applied, although failure is determined only through multiple irregularities, rather than an individual non-compliance. For example, gaps that are created by the process need to be considered. They include gaps as follows:

- between the rivet head and the sheet material;
- within the rivet shank between the rivet and different materials;
- between sheets around the rivet, although this may be promoted by the application of adhesive within the specific joint;
- cracks within the material;
- asymmetry within the joint – a non-symmetrical joint;
- offset of rivet and die.

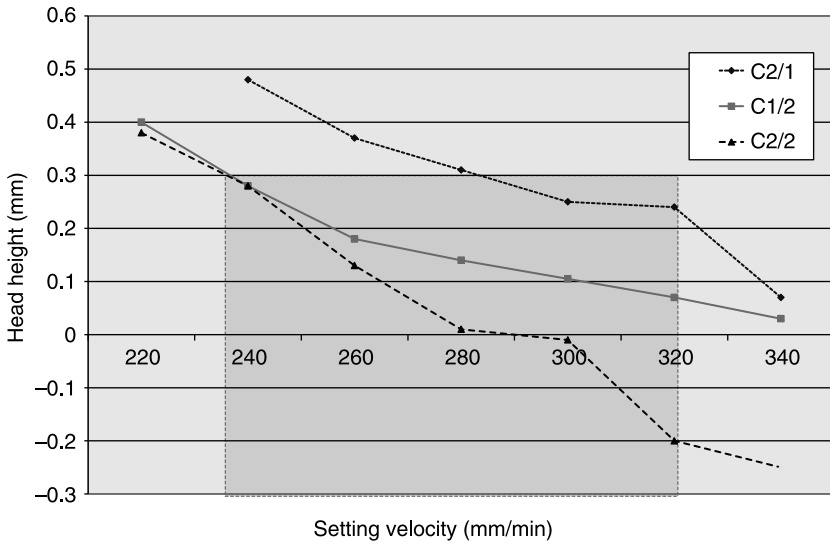
Some of the above problems can point to application and equipment issues, which can be optimised immediately. For example, the offset of the rivet to the button on the back of the joint immediately points to the misalignment of punch to die alignment within the self-pierce rivet gun. The specific gun should be checked and realigned to bring the process back into control. Figure 11.6 provides a quick overview of the requirements for a good self-pierce riveted joint.

The benefit of the self-piercing riveting process is that, once the initial rivet, die and parameter selections have been made, the process itself is fairly repeatable if the compromises made to accommodate the maximum amount of joints within the work of a single gun are not too great. This can be demonstrated by the graph in Fig. 11.7.

The graph shows the impact of different material combinations to process capability within a single gun and rivet and die combination. The three lines relate to the combination of material 1 to material 2, material 2 to material 1 and material 2 to itself. The shaded box outlines the acceptable range of velocities and head heights and we can observe an acceptable head height for two of the materials, but for the third we only just achieve an acceptable condition. For this reason we would either select an alternative rivet and die combination or re-allocate this joint combination to another gun. The comparison between self-piercing riveting, resistance spot-welding and spot friction joining for aluminium automotive sheet is further discussed by Briskham (Briskham 2006).



11.6 Requirements of a good self pierce rivet joint.



11.7 Joint combination compatibility.

11.9.1 Equipment selection

A key stage of industrial implementation is the selection of application equipment and the system specification. The main suppliers of systems to the automotive industry at the present time are Henrob, Emhart Technologies and Böllhoff. These companies can provide different specifications of systems that can be categorised as follows:

- A servo-electric or hydraulic drive system:
 - different options to provide the power for inserting the rivet into the substrate.
- Control philosophy: different suppliers manage the application process in different ways:
 - controlling the rivet velocity;
 - controlling the application force;
 - rivet displacement.

In most cases when comparisons have been made between alternative systems using the same die and rivet on alternatively controlled systems, no significant change in performance has been noted. However, when performing at the limits of the rivet or substrate performance any small change may be critical.

- Application – manual or automated: the application can be manually applied with a unit manipulated by an assembly operative, mounted to a robot or pedestal mounted with the component presented to the static gun either manually or by robot.
- Rivet feeding system – hand-feed, tape, blow-feeding or magazine: the delivery of rivets to the gun will impact on cycle time and also the ability of the gun to access space constrained areas. The hand-feed systems are generally only used where multiple rivet types need to be applied on a single manual unit, which are typically laboratory or rectification units. Production units will typically have tape, magazine or blow feed to enable multiple rivets to be fed before reloading. The different feed types can accommodate different numbers of rivets. The tape-feed can be supplied in spools or cassettes and can store between 145 and 11 000 rivets, depending upon the rivet size. Magazines will store a smaller number of rivets, but will be refilled after each production cycle via another automated feed system; this system has the benefit of fast refill, generally within the transfer time, and a small package space requirement to optimise access capability.
- The gun geometry will generally be defined by the range of application positions specified and will be specified to suit by each manufacturer.

The choice between the available systems depends on the capability of the system to provide the joint requirements on a repeatable basis and on commercial requirements. The main system suppliers in the UK are currently Henrob and Emhart Technologies, with comparable technical performance provided by both systems, even though the feed and control systems offered by the two companies do vary.

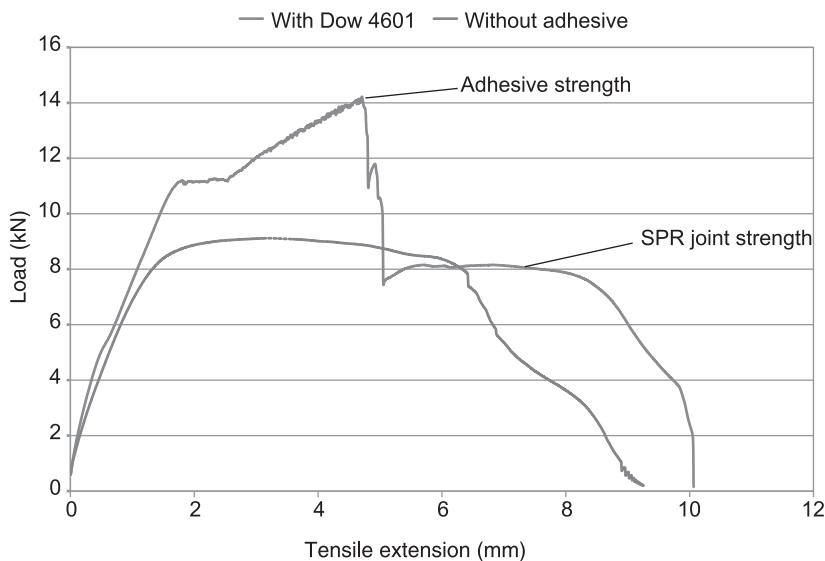
The choice of joining method has generally been made early on in the development of a new vehicle with selection being driven by:

- Design requirements:
 - materials to be joined: single or multiple material types;
 - number of materials within the stack;
 - access available to approach joint;
 - joint performance.
- Production drivers:
 - volume requirements;
 - application speed;
 - equipment cost;
 - piece part cost.

In the UK the selection of joining processes has therefore been fairly polarised, with steel body structures being dominated by resistance spot-welding, supported by MIG/MAG welding. During recent years, laser welding / brazing has also

become more prevalent, where design and volume provide a commercial driver for the high capital cost; this has also been driven by design solutions and the incorporation of high and ultra high strength steels. In the case of aluminium vehicle structures the primary joining method has been self-piercing riveting supported by MIG welding. Other joining methods have been proposed in the form of friction spot joining and resistance spot-welding but, due to cycle time, flexibility in terms of multi-material joints and application robustness, these processes have yet to be taken up to a great extent within aluminium automotive body structures. In most structures the application of adhesive is also used, creating hybrid riv-bonded structures, increasing the strength and stiffness of the joints.

Figure 11.8 shows that the adhesive becomes the dominant of the two joining processes, although once the adhesive joint fails the self-piercing rivet then continues to absorb energy prior to complete failure. The graph demonstrates the performance under quasi-static shear; the adhesive performs favourably in this mode of loading, but when subjected to peel forces the self-piercing rivet will become the dominating means of load-bearing. Comparison of the energy absorption of resistance spot-welded joints with self-piercing riveted joints has shown that the self-piercing rivet joint will deform rather than fracture, leading to higher energy absorption during a crash scenario (Han 2009a).



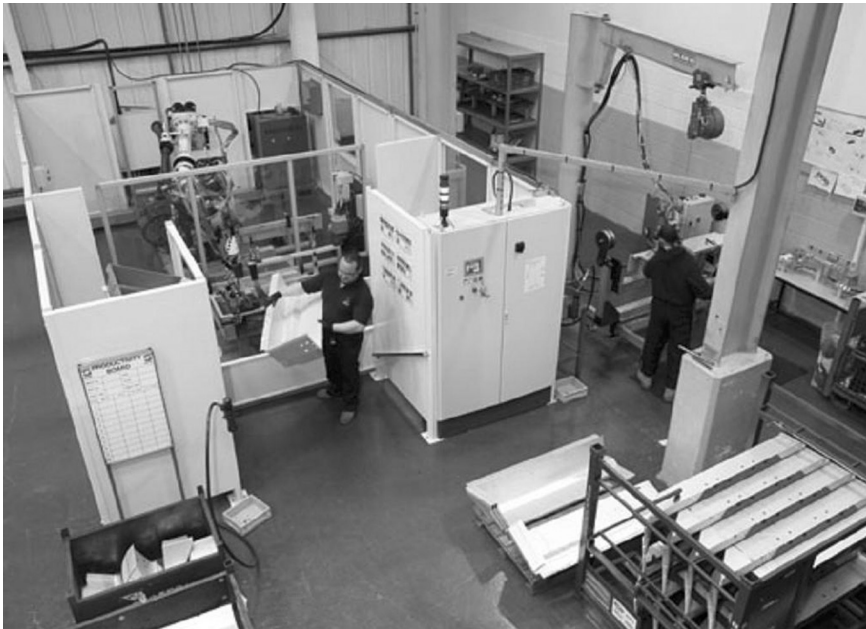
11.8 Influence of adhesive.

11.9.2 Industrial installation

The application of rivets will follow on from the development stages already discussed:

- Design requirements.
- Processes evaluation:
 - cost comparisons;
 - comparable joint performance;
 - design opportunities.
- Process development:
 - robustness to expected process variation;
 - ability to meet key process requirements.

Once the required processes have been selected, the facility can then be designed, manufactured and installed to meet the product and volume requirements. The facility in Fig. 11.9 has been designed to produce a component that contains Aluminium AA5754 to AA5754 joints as well as the incorporation of a high



11.9 Example production facility.

strength low alloy steel (HSLA) reinforcement. In this instance, two processes were chosen to prepare the joints:

1. Resistance spot-welding to prepare the aluminium to aluminium joints.
2. Self-piercing riveting to prepare the dissimilar material joints.

These joints were chosen to meet the specific design requirements of the component. The process selection criteria have been simplified and shown in Table 11.6.

The table is not exhaustive, but does provide an initial guide. For example, the self-piercing riveting process was chosen to provide the required joint strength and also to perform hybrid material joints between steel and aluminium. The level of flexibility provided by the gun was not an issue as this particular assembly had a limited number of different joint stacks and could be performed by a single gun. The resistance spot-welding process was chosen because of the low cost of equipment and the flexibility to approach the range of joint stacks within the assembly. This facility was also being used to prove the industrial readiness of the resistance spot-welding process for high-volume automotive production. Other joining processes could have been used, but they were unsuitable because they did not meet the specific selection requirements. For example, laser welding requires a high-volume application to meet throughput requirements because of the high capital costs of the process, while spot friction joining is unsuitable because of the long processing times and insufficient flexibility of the processing tool to accommodate all the joint stacks within the component.

The volume of joints applied at each stage of assembly, by each process, has also supported the decision to apply the self-piercing riveting process manually and to apply the resistance spot-welded joints in the adjacent area robotically. The

Table 11.6 Process selection strengths and weaknesses

Process	Surface defect
Self pierce riveting (SPR) + Best mechanical properties + Mixed material joints – Ongoing cost of rivets – Gun flexibility	Button
Resistance spot welding (RSW) + Low cost of equipment + Gun Flexibility and automation – Consistency remains to be proven – Tip maintenance	Indent
Spot friction joining (SFJ) + Joining thin materials + Low running costs – Long process time for thick sheet – Gun flexibility	Hole

Sunday, February 02, 2014 3:07:23 AM

decision on whether to automate or not was not one that was driven by the particular process, as the application units are of a similar size, weight and manoeuvrability. Man or robot can handle these units and the use of this equipment in either manual or automated application has been applied in multiple facilities over the last ten years. The benefit of automated facilities over manual application is the repeatability of the application process, with specific benefits around:

- application angle and minimal deviation from perpendicular approach;
- optimised rivet velocity for each joint;
- positional repeatability of rivet location.

Mortimer (Mortimer 2006) has described how Jaguar Cars is assembling aluminium car bodies in the UK using self-piercing rivets and self-tapping screws to join aluminium castings, extrusions and pressings.

11.9.3 A quality control plan

A successful application requires the supplier to confirm to the customer that the quality of the component being produced will meet the required specification. This will be done through a number of stages:

1. Process monitoring – This can confirm that the process is under control and produces joints within the defined tolerance limits (primarily head height with current production systems).
2. Non-destructive testing (NDT) – Visual evaluation of the joint, checking the head height and for the presence of any cracking, break-through, offsetting of the rivet, etc. Currently a reliable ultrasonic, thermal or alternative evaluation tool is not available. Han *et al.* (Han *et al.* 2007) evaluated an ultrasonic inspection tool for self-piercing riveting and demonstrated that for thin sheets as used within automotive applications further development is required.
3. Destructive testing – This involves sectioning of the rivet and provides the performance baseline to confirm the parameter selection for specific joints, including interlock distance, rivet cracking, break-through, axial offset, etc.

A plan is therefore required to demonstrate that the process and the resultant joints, when subjected to appropriate levels of control and inspection, will provide a quality product to the customer. Primarily this is achieved through process monitoring and needs to meet the production specification, followed by confirmation by destructive testing and comparison, to control process trials. Inspection is only required to confirm the process performance baseline being evaluated by process monitoring and should be minimised as confidence in the process improves.

11.10 Conclusions

This chapter has outlined the drivers for moving toward lighter weight structures within the automotive sector in order to reduce emissions. The use of aluminium

alloys for the body structure has been identified as the way forward. The use of aluminium as well as composites and mixed material structures is further driving the use of self-piercing riveting because the technique is ideally suited for joining dissimilar materials. In many cases, the materials are developed to overcome the strength and ductility issues to meet the structural and style requirements of the automotive body with little thought being given to the integration of the component into the existing structure or combination with other materials. The content of the chapter has been directed towards the evaluation of joining technologies and their performance against the design requirements. The comparison between joining processes evaluates performance against the buy-off criteria, cost analysis and the requirements for an industrial application, so ensuring that a robust quality control plan can be implemented to provide customer confidence.

The chapter has therefore concentrated on the comparison of processes and the challenges faced in bringing a new process into a position to be applied within an industrial facility. The application of self-piercing riveting, although embraced by Jaguar Land Rover, Audi and BMW, still has to penetrate into the automotive supply chain and into the higher volume sectors, so the challenge of evaluation and introduction into these new areas is still a key issue.

This chapter aimed to support a robust evaluation, introduction and implementation of new processes, providing a methodology to ensure new processes will meet the design requirements, whilst being subjected to the anticipated production variation. The references provide further comparative analysis between joining processes as well as an overview of a Jaguar Cars production facility that demonstrates the application of self-piercing rivets within an automotive facility.

It has been demonstrated that the use of self-piercing riveting can be justified within an automotive structure. This has been incorporated successfully by Jaguar Land Rover into their model ranges to provide class-leading performance.

11.11 Acknowledgements

I would like to thank the joining team I worked with at WMG at the University of Warwick: Li Han, Nic Blundell, Leigh Smith, Dezhi Li, Martin Thornton, Bob Spittle, Paul Briskham and Ken Young. I worked with this team through a number of joining development projects and the progress would not have been possible without this team. Thanks also have to go to our lead industrial partners and their key contacts: Mike Shergold and Mark White at Jaguar Land Rover; Paul Meeson and Charles Marine at Stadco; Mike Gillett at CovPress; Steve Morley at Sertec and George Mollison at Premier Sheet Metal.

11.12 References

- Barnes, T A and Pashby, I R (1998), 'Joining techniques for aluminium spaceframes used in automobiles. Part II – adhesive bonding and mechanical fasteners', *J. Mat. Processing Tech.*, 99, 72–79.

- Briskham P (2006), Comparison of self pierce riveting, resistance spot welding and spot friction joining for aluminium automotive sheet, SAE International, 2006-01-0774.
- EEC (1999), Regulations (EEC) No 4064/89 Merger Procedure, Article 6(1)(b) Non-Opposition, Date 17/03/1999 – Case No IV/M.1406 – Hyundai/Kia.
- Han L *et al.* (2007), An evaluation of NDT for self-pierce riveting, SAE International, 2007-01-1364.
- Han L *et al.* (2009a), ‘Advanced joining technologies for aluminium assembly for the automotive industry’, *Key Engineering Materials*, 410–411, 105–116.
- Han L *et al.* (2009b), ‘A comparison of the mechanical behaviour of self-piercing riveted and resistance spot welded aluminium sheets for the automotive industry’, *J. Mater. Design*, doi:10.1016/j.matdes.2009.08.031.
- Mortimer J (2006), ‘Jaguar uses castings, extrusions to reduce parts count in new sports car’, *Assembly Automation*, 26(2), 15–200.
- Wheeler M J (1998), ‘Crashworthiness of aluminium structured vehicles’, Alcan International Limited, Canada, Paper Number 98-S1-W-20.

- aluminium A8, 5
- aluminium alloy, 113, 114, 115, 118
- anode, 42
- anodic reaction, 42, 48
- ARCAN test device, 80–2
 - load–displacement curves, 81
 - test and cross-shaped specimen, 81
- ASTM B117-97, 47
- Audi 8, 2, 5
- automated vehicle construction
 - comparable joint performance, 192–3
 - comparison of quasi-static joint strength, 193
 - cost comparisons, 186–92
 - comparative cost analysis, 187
 - comparative power consumption per joint, 192
 - cost drivers, 189
 - operating costs, 191
 - process and equipment – investment, 190
 - welding cell configurations, 188
- industrial application, 197–205
 - equipment selection, 200–2
 - industrial installation, 203–5
 - influence of adhesive, 202
 - joint combination compatibility, 200
 - process selection strengths and weaknesses, 204
 - production facility, 203
 - quality control plan, 205
 - requirements of a good self pierce rivet joint, 199
- joining techniques, 184–5
 - schematic diagram, 184
- material requirements, 183–4
- material Usage within BIW, 184
- process development, 194–7
 - flow chart, 194
- process evaluation, 186
- self-piercing riveting (SPR), 181–206
- specific process opportunities, 193–4
- automotive industry
 - future trends, 180
 - manufacturing considerations, 178–80
 - flange length, 179
 - rivet spacing, 180
 - product considerations, 177–8
 - rivet description, 172
 - self-piercing riveting (SPR), 171–80
 - types of self-piercing rivet, 173–6
 - uses of SPR, 176–7
- Boundary Definition, 195
- brittleness, 74
- business case model, 188
- buttonhole, 53
- C-frame, 3
- cathode, 42
- cathodic reaction, 48
- coach peel loading, 73, 150
- compression riveting, 126
- computer vision, 128–46
 - material measurement, 133–4
 - deep set rivet head, 134
 - high set rivet head, 134
 - rivet button diameter, 145–6
 - button formation post-processing, 146
 - button formation pre-processing, 145
 - rivet head position, 143–5
 - head of a rivet after setting into aluminium sheets, 143
 - measurement diagram, 144
 - simplified array, 144
 - rivet orientation, 131–3
 - extrapolated angular deviation, 133
 - non-vertical rivet orientation, 132
 - tumbled rivet set into aluminium, 132
 - rivet status, 128–31
 - amplitude values of a single rivet, 130
 - bespoke process monitoring software, 131
 - camera position, 129
 - jaws, 130
 - punch imprint in aluminium joining materials, 128

- rivets set into aluminium joining materials, 129
- side material measurement, 135–7
 - camera and laser position, 135
 - laser line threshold and threshold midpoint, 137
 - side laser measurement setup, 135
- stacked aluminium with neutral density and red filters, 136
- stacked aluminium without optical filtering, 136
- top material measurement, 138–43
 - bottom sheet material, 139
 - camera and laser position, 138
 - camera FOV, 141
 - lenses, 141
 - second sheet material, 140
 - stacked measuring materials using the 3.6 mm lens, 142
 - stacked measuring materials using the 16 mm lens, 142
 - third sheet material, 139
 - top laser measurement setup, 138
 - top sheet material, 140
- conventional load frames, 60
- corrosion behaviour
 - building up and failure, 52
 - EDAX analysis, 49, 50
 - effect on the lap shear strength, 52
 - percentage weight change of I.F. steel with aluminium 5182, 47
 - progression in the interfacial area between the rivet and I.F. steel, 51
 - protection, 53–4
 - self-piercing riveting (SPR), 41–54
 - study methodology, 46
 - theory, 42–6
 - electrochemical cell, 43
 - electrochemical series for selected metals, 44
 - mechanism of differential aeration corrosion, 45
- corrosion protection, 53–4
- cost model, 189–91
- coupled damage model, 87
- crashworthiness
 - dynamic tensile tests, 58–62
 - recommended testing procedures, 63–6
 - fixture designs for dynamic tests, 63
 - force and displacement vs. time curves for ID 7, 66
 - summary of the joint populations studied, 65
 - self-piercing rivets (SPR), 56–77
- crevice corrosion, 46, 50
- cyclic load, 35
- damage model, 87–9
 - load–displacement curve and microstructural damage mechanisms, 88
- destructive testing, 205
- die tip height, 35
- differential aeration corrosion, 45
- displacement curves, 70
- dissimilar metal
 - joining, 114–18
 - defects for self-piercing riveting of high strength steel and aluminium alloy sheets, 115
 - joining range for high strength steel and aluminium alloy sheets, 117
 - shapes of rivet and sheets for upper high strength steel sheet and aluminium alloy sheets, 116
 - shapes of rivet and sheets for upper ultra-high strength steel sheet and aluminium alloy sheets, 116
 - shapes of rivet and sheets obtained from experiment of riveting, 118
- double sided access, 185
- ductile failure criteria, 87
- dynamic loading, 70
- dynamic strength
 - dynamic tensile tests, 58–62
 - recommended testing procedures, 63–6
 - fixture designs for dynamic tests, 63
 - force and displacement vs. time curves for ID 7, 66
 - summary of the joint populations studied, 65
 - self-piercing rivets (SPR), 56–77
- dynamic strength test, 61, 66
- dynamic tensile test, 58–62
 - experimental methods for base material property test, 59
- elastic–plastic behaviour, 86–7
- electrochemical cell, 42
- electrochemical corrosion, 42
- electrolyte, 44, 48
- equivalent element, 82–3
 - decomposition of forces on the joint, 82
 - failure criterion of a SPR joint, 83
- failure mode s1, 83
 - schematic diagram, 84
- failure mode s2, 83
 - schematic diagram, 84
- failure mode s3, 83
 - schematic diagram, 84
- failure mode t1, 83–4
 - schematic diagram, 85
- failure mode t2, 83–4
 - schematic diagram, 85
- failure modes, 83–6, 99–102
 - calculated and observed damage field for mixed loading, 101
 - calculated and observed damage field for shear loading, 102

- calculated and observed damage field for tensile loading, 101
- combination of s1 and t1 for mixed loading conditions, 85
- combination of s3 and t2 for mixed loading conditions, 85
- s1 for shear loading, 84
- s2 for shear loading, 84
- s3 for shear loading, 84
- t1 for tensile loading, 85
- t2 for tensile loading, 85
- fatigue behaviour
 - fretting fatigue, 38–40
 - self-piercing riveted joints affecting factors, 35–8
 - HSLA steel and aluminium 5182 with different piercing directions, 37
 - self-piercing riveted vs. resistance spot-welded joints, 34
 - self-piercing riveting (SPR), 33–40
- fatigue failure, 37
- finite element
 - simulations of riveting process, 118–20
 - comparison between cross-sectional shapes of sheets and rivet, 119
 - deforming shapes of sheets and rivet, 119
- fixture, 62
- flange length, 178
- flaring stage, 3
- flexibility, 185
- force–displacement curve, 127
- fracture criterion
 - comparisons of numerical and experimental failure criteria, 102
- fretting fatigue, 38–40
 - fretting scars as a result of fatigue, 39
 - fretting scars on the surface of aluminium alloy 5182, 39
- frictional force, 35
- galvanic corrosion, 53
- G.E.R.I. algorithm, 128–9
- governing metal thickness (GMT), 178
- high strength steel, 114–15
- high-strength/low-alloy steel (HSLA), 6
- hydraulic ram, 64
- hydroxide ions, 42–3, 48
- impact riveting, 126
- industry-wide standards, 62
- inertia, 59–60
- interlock distance, 198
- international standards, 62
- interstitial-free (I.F.) steel, 47
- Jaguar XJ, 2, 6
- joint speed, 185
- ‘kill-element’ technique, 94
- lapshear, 150
- laser-welded joint, 186
- load cell response time, 60–1
- load cell ringing, 60–1
- load train, 62
- load–displacement curves, 99
 - comparisons for different loading directions, 100
 - measured and calculated ultimate forces, 101
- lower die geometry, 103–4
 - initial and optimised geometries, 103
- load–displacement curves of the riveting process, 104
- load–displacement curves on a shearing test, 103
- mechanical plating, 53–4
- mechanical strength
 - ARCAN test device, 80–2
 - equivalent element, 82–3
 - failure mechanisms, 19–22
 - cracking of cast aluminum SPR joint assembly, 21
 - SPR joint assemblies exhibiting rivet head pullout, 19
 - SPR joint assemblies exhibiting rivet tail pullout, 20
 - SPR joint assemblies exhibiting sheet tearing, 20
- failure modes, 83–6
- future trends, 104–5
- mechanical behaviour and damage analysis, 86–92
 - aluminium 5754-O load–displacement curves, 91
 - damage model, 87–9
 - elastic–plastic behaviour, 86–7
 - identification of rivets mechanical properties, 92
 - identified damage parameters, 92
 - parameters identification, 89–92
- numerical modelling, 93–104
- rivet strength optimisation, 22–6
 - piercing direction, 22, 24–6
 - rivet length, 22
- self-piercing riveting (SPR), 11–32
- self-piercing riveting (SPR) modelling, 79–105
- structural adhesive joining, 27–32
- test types, 12–19
 - average static strength for heavy vehicle aluminium cast wrought alloy SPR joint, 16
 - coach peel coupon assembly, 15
 - cross tension coupon assembly, 14
 - joining parameters for single joint SPR specimen assemblies, 17
 - lap shear coupon assembly, 13

- static strength results for various dissimilar material SPR joint, 18
- uniaxial test results for aluminum cast, 18
- narrowband ultrasound spectroscopy (NBUS), 146
- non-destructive testing (NDT), 205
 - computer vision, 128–46
 - current technologies, 126–7
 - ‘Watchdawg’ process monitoring system, 127
 - self-piercing riveting (SPR), 124–47
 - ultrasonic testing, 146–7
- non-impact riveting, 126
- numerical modelling, 93–104
 - mechanical problem, 93–4
 - degrees of freedom for P1 +/P1 tetrahedral elements, 94
 - friction coefficients between the different parts, 94
 - results and validation, 99–104
 - studies, 95–8
 - calculated failure modes, 98
 - damage, 97–8
 - damage influence on the load-displacement curve for tensile test, 98
 - influence of the mechanical history on the mechanical strength simulations, 97
 - mesh size, 95–6
 - mesh size influence on the load-displacement curve for tensile test, 96
 - spatial discretisations, 96
 - SPR process history, 96–7
 - transfer of SPR process solution, 94–5
 - creation of the 3D numerical model from the 2D axis-symmetrical results, 95
- orbital riveting *see* non-impact riveting
- overall equipment effectiveness (OEE), 187, 189
- piercing direction, 22, 24–6, 35
 - joint aluminum and steel assemblies, 26
 - static peak load for 5182-O/HSLA 350 (ID 10) and HSLA 350/5182-O (ID 11), 25
 - static tests energy absorption for 5182-O/HSLA 350 (ID 10) and HSLA 350/5182-O (ID 11), 25
 - strength optimisation, 165–9
 - experimental load *versus* displacement comparison of ID 10 and ID 11, 168
 - fatigue strength comparison of ID 10 and ID 11, 168
 - ID 10: SPR of 2 mm AA5182-O (head)/1 mm HSLA 350 (tail), 167
 - ID 11: SPR of 1 mm HSLA 350 (head)/ 2 mm AA5182-O (tail), 167
 - riveting parameters for ID10 and ID11, 166
 - uniaxial test results for 5182-O/DP 600 (ID 12L) and DP 600/5182-O (ID 13), 26
- piercing stage, 3
- process monitoring, 205
- process stability phase, 196
- process window phase, 196
- quality control
 - current technologies, 126–7
 - ‘Watchdawg’ process monitoring system, 127
 - self-piercing riveting (SPR), 124–47
- quasi-static loading, 80
- quasi-static test, 13
- remaining material thickness, 198
- resistance spot-welded joints, 34
- rivet buckling, 198
- rivet coating, 35
- rivet cracking, 198
- rivet diameter, 35
- rivet feeding system, 201
- rivet hardness, 35
- rivet head height, 198
- rivet head pullout, 19, 152–3
- rivet length, 22, 35
 - comparison of static strength results of 5182-O joined to DP 600, 23
 - joint ID 12 and ID 12L with a 6 mm and 6.5 mm rivet, 23
 - strength optimisation, 159, 161–5
 - cross tension failure mode comparison of ID 12 and ID 12L, 164
 - ID 12: SPR of 2 mm AA5182-O (head)/1.6 mm DP 600 (tail) with 6 mm rivet length, 163
 - ID 12L: SPR of 2 mm AA5182-O (head)/1.6 mm DP 600 (tail) with 6.5 mm rivet length, 163
 - load *vs.* displacement comparison of ID 12 and ID 12L, 164
 - riveting parameters for ID12 and ID12L, 162
 - uniaxial test results for 5182-O/DP 600 SPR assemblies, 24
- rivet shank damage, 21
- rivet size, 179
- rivet spacing, 179
- rivet tail pullout, 19–20, 153–4
- RivMon, 126
- RIVSET system, 126
- self-pierced rivet joint, 186
- self-piercing rivet
 - types, 173–6
 - breakthrough and collapsed rivet, 175
 - semi-tubular rivets, 173
 - semi-tubular rivets setting process, 174
 - solid rivet installation process, 176
 - solid rivets, 175
- self-piercing riveted joints, 34
- self-piercing riveting (SPR), 1–7

- advantages and disadvantages, 4–5
- automated vehicle construction, 181–206
 - comparable joint performance, 192–3
 - cost comparisons, 186–92
 - industrial application, 197–205
 - joining techniques, 184–5
 - material requirements, 183–4
 - process development, 194–7
 - process evaluation, 186
 - specific process opportunities, 193–4
- automotive body application, 5–6
- automotive industry, 171–80
 - future trends, 180
 - manufacturing considerations, 178–80
 - product considerations, 177–8
 - rivet description, 172
 - types of self-piercing rivet, 173–6
 - uses, 176–7
- C-frame, 3
- corrosion behaviour, 41–54
 - building up and failure, 52
 - EDAX analysis, 49, 50
 - effect on the lap shear strength, 52
 - percentage weight change, 47
 - progression in the interfacial area between the rivet and I.F. steel, 51
 - protection, 53–4
 - study methodology, 46
 - theory, 42–6
- dissimilar metal joining, 114–18
- dynamic strength evaluation and crashworthiness, 56–77
 - coach peel load vs. displacement curves for ID 11, 71
 - coach peel strength and energy absorption comparison, 69
 - coupon configuration and fixture design for static tests, 57
 - cross tension load vs. displacement curves for ID 11, 71
 - cross tension load vs. displacement curves for ID 11A, 76
 - cross tension strength and energy absorption comparison, 68
 - dynamic tensile tests, 58–62
 - failure mode for ID 11 coach peel, 72
 - failure mode for ID 11 cross tension, 73
 - failure mode for ID 11 lap shear, 72
 - lap shear load vs. displacement curves for ID 11, 70
 - lap shear load vs. displacement curves for ID 11A, 75
 - lap-shear strength and energy absorption comparison, 67
 - recommended testing procedures, 63–6
 - sheet deformation for ID 11 cross tension, 74
- fatigue behaviour, 33–40
 - affecting factors, 35–8
 - fretting fatigue, 38–40
 - resistance spot-welded joints, 34
- finite element simulations, 118–20
- future trends, 6–7, 120–1
 - aluminium alloy rivets, 121
 - cylindrical aluminium alloy rivets, 121
 - laser assisted for magnesium alloy sheets, 120
- material joining, 112–13
 - joining of sheets, 112
- materials suitability assessment, 111–21
- mechanical strength, 11–32
 - failure mechanisms, 19–22
 - strength optimisation, 22–6
 - structural adhesive joining, 27–32
 - test types, 12–19
- quality control and non-destructive testing, 124–47
 - computer vision, 128–46
 - current technologies, 126–7
 - Directive 70/220/EEC, 125
 - ultrasonic testing, 146–7
- schematic diagram, 3
- similar metal joining, 113–14
- strength estimation, 150–9
 - comparisons of estimated rivet strength and failure mode, 160
 - comparisons of predicted and measured rivet strength, 161
 - head pullout, 152–3
 - Henrob rivet, 151
 - joint coupon for cross tension loading condition, 151
 - SPR of 2 mm AA5182-O (head side)/2 mm AA5182-O (tail side), 156
 - SPR of 2 mm AA5754-O (head side)/2 mm AA6063-T6 (tail side), 155
 - SPR of 2 mm AA5754-O (head side)/3 mm AA6063-T6 (tail side), 155
 - SPR of 3 mm AA5754-O (head side)/2 mm AA6063-T6 (tail side), 158
 - SPR of 3 mm AA5754-O (head side)/3 mm AA6063-T6 (tail side), 158
 - SPR of 2 mm AA5754-O (head side)/1.9 mm HSLA350 (tail side), 156
 - SPR of 3 mm AA5754-O (head side)/1.9 mm SAE1010 (tail side), 157
 - SPR of 3 mm AA6063-T6 (head side)/3 mm AA5754-O (tail side), 159
 - SPR of 1 mm HSLA350 (head side)/2 mm AA5182-O (tail side), 157
 - tail pullout, 153–4
 - validation, 154–9
- strength modelling, 79–105
 - ARCAN test device, 80–2
 - equivalent element, 82–3
 - failure modes, 83–6
 - future trends, 104–5

- geometrical definition of connection based
 - on an experimental cut, 80
- mechanical behaviour and damage
 - analysis, 86–92
 - numerical modelling, 93–104
- strength optimisation, 149–69
 - piercing direction, 165–9
 - rivet length, 159, 161–5
- semi-tubular rivet, 173–5
- shearing force, 82
- sheet fracture, 112
- sheet thickness, 35
- similar metal
 - joining, 113–14
 - self-piercing riveting of automobile body panels, 113
 - self-piercing riveting of five aluminium alloy sheets, 114
- single sided access, 185
- solid rivet, 173–5
- static cross tension test, 167
- static lap shear testing, 36
- static rivet strength test, 163
- strain-gage load cells, 61
- stress cells, 46, 53
- stress state, 87
- structural adhesive joining, 27–32
 - cross tension static test results of joint ID 13 (DP 600/5182-O), 31
 - fatigue test results for dissimilar metal joint ID 13 (DP 600/5182-O), 32
 - fatigue test results for dissimilar metal joint ID 12L (5182-O/DP 600) coupon assemblies, 29
 - lap shear results for joint ID 10, 11, 12L, and 13, 28
 - lap shear static test results of joint ID 13 (DP 600/5182-O), 30
 - uniaxial test results for joint ID 12L (5182-O/DP 600), 27
- Technology Brief, 195
- tensile force, 82
- tensile strength, 154
- tensile yield strength, 154
- tin-zinc coating, 54
- ultra-high strength steel, 115
- ultrasonic testing, 146–7
- uniaxial tension test, 12
- upset force, 38
- Watchdawg, 127
- wave propagation, 59–60
- wet corrosion, 42
- zinc-coated steel, 53
- zinc coating, 54